DEVELOPMENT OF MULTI-CHANNEL ANALYSIS OF SURFACE WAVES (MASW) FOR CHARACTERISING THE INTERNAL STRUCTURE OF ACTIVE FAULT ZONES AS A PREDICTIVE METHOD OF IDENTIFYING THE DISTRIBUTION OF GROUND DEFORMATION.

A thesis submitted in partial fulfilment of the requirements for the Degree

of Master of Science in Geology

in the University of Canterbury

by

Brendan Gilbert Duffy

University of Canterbury

2008

For my lovely wife

Nicci

and our two beautiful children

Ciara (3 yrs)

And

Isabella (1 yr)

I couldn't have done this without you!

Think left and think right and think low and think high.

Oh the thinks you can think up if only you try!

From 'Oh the THINKS you can think!' by childrens author Theodor Seuss Geisel (Dr Seuss, 1904-1991)

ACKNOWLEDGMENTS

This report takes the form of a thesis, which was supported by grants from the Earthquake Commission and Mason Trust, for which I am thankful. Dr Hugh Cowan and Priscilla Cheung at EQC were ever willing to fund my penchant for conferences and the Tauranga Geolsoc conference pushed this project forward immensely.

I wish to sincerely thank my thesis supervisors Mrs Jocelyn Campbell and Dr Michael Finnemore for their assistance in the collection and processing of data and their reviews of this manuscript. Jocelyn's in particular were thorough, insightful and patient. Congratulations on your retirement Jocelyn. Thanks also to Dr Andrew Gorman from Otago University, who was the external thesis examiner. His comments greatly aided preparation of this report. Dr Phil Tonkin not only provided ever-useful advice and assistance with OSL sampling and loess stratigraphy, but also provided timely sanity checks. Erskine visitors Assoc. Prof. Paul Santi and Dr Jim McKean joined me for valuable late stage geotechnical discussions. Dr. Andy Nicol at GNS enthusiastically introduced me to Professor Richard Norris from Otago, whose MSc student became an important collaborator. I hope that Jeremy Kilner derived as much value from the collaboration as did I.

A great deal of thanks is due to the landowners on whose land I have worked. So thankyou to Gary Ferguson, Ian and Elizabeth Turnbull, Preston Allen, Gareth Renowden and Raymond Herber. Of these, three deserve special mention. Gareth, Ian and Elizabeth went beyond the call of duty. Gareth lent me his ride on tractor mower to mow the RD2 site and took a series of photographs for me that helped me greatly. Ian and Elizabeth were also ever welcoming and among other favours lent me valuable family photographs of the site.

Department staff and students helped greatly. Anekant's blunt and welcome intervention moved me in the direction that became this thesis. The other technical staff provided assistance along the way, particularly Vannessa Tappenden and Cathy Knight. John Southward was ever patient with my computer frustrations and Nick Etheridge in the Department of Biological Sciences provided timely workshop assistance. Many students assisted me in the field and their help was appreciated. Field assistants included (in chronological order) Keith Machin (hardly a student), Paul Shackleton (him neither!), Yvette Hobbs, Richard and Kirsty Cooksey, Matt Dodson, Vicky Kershaw, Lucille Tatard

and David Hood. My numerous discussions with Florian Buch were invaluable from my viewpoint and contributed greatly to my understanding of and confidence in my data. Thank you all, good luck with your own studies and apologies and thanks to any I missed.

David Park and his colleagues at the Geospatial Research Centre helped during my abortive experimentation with photogrammetric techniques and made it an intriguing and enjoyable failure. Their expertise is an extremely valuable resource and they will hopefully be key partners in some of the research directions identified in the concluding chapter of this document.

Above all, thanks are due to my family. My parents gave me the education that started it all and supported my decision to return to study. My mother-in-law Gaye-Lynn and her partner Dave Potter were outstanding with their moral support and timely pep talks. My father-in-law Graham Boniface kindly arranged the printing of this volume by Xerox Limited. But most of all, my hugest debt of gratitude goes to my wife, Nicci and my children, Ciara and Isabella, to whom this volume is dedicated. As well as teaching me to touch-type, which greatly aided preparation of my manuscript, Nicci inspired me from the very start of my geology career. Without her support none of this would have been possible.

TABLE OF CONTENTS

LIST OF EQUATIONS, FIGURES AND TABLES

ABSTRACT

Bulk rock strength is greatly dependent on fracture density, so that reductions in rock strength associated with faulting and fracturing should be reflected by reduced shear coupling and hence S-wave velocity. This study is carried out along the Canterbury rangefront and in Otago. Both lie within the broader plate boundary deformation zone in the South Island of New Zealand. Therefore built structures are often, , located in areas where there are undetected or poorly defined faults with associated rock strength reduction. Where structures are sited near to, or across, such faults or fault-zones, they may sustain both shaking and ground deformation damage during an earthquake. Within this zone, management of seismic hazards needs to be based on accurate identification of the potential fault damage zone including the likely width of off-plane deformation. Lateral S-wave velocity variability provides one method of imaging and locating damage zones and off-plane deformation.

This research demonstrates the utility of Multi-Channel Analysis of Surface Waves (MASW) to aid land-use planning in such fault-prone settings. Fundamentally, MASW uses surface wave dispersive characteristics to model a near surface profile of S-wave velocity variability as a proxy for bulk rock strength. The technique can aid fault-zone planning not only by locating and defining the extent of fault-zones, but also by defining within-zone variability that is readily correlated with measurable rock properties applicable to both foundation design and the distribution of surface deformation. The calibration sites presented here have well defined field relationships and known fault-zone exposure close to potential MASW survey sites. They were selected to represent a range of progressively softer lithologies from intact and fractured Torlesse Group basement hard rock (Dalethorpe) through softer Tertiary cover sediments (Boby's Creek) and Quaternary gravels. This facilitated initial calibration of fracture intensity at a high-velocity-contrast site followed by exploration of the limits of shear zone resolution at lower velocity contrasts.

Site models were constructed in AutoCAD in order to demonstrate spatial correlations between S-wave velocity and fault zone features. Site geology was incorporated in the models, along with geomorphology, river profiles, scanline locations and crosshole velocity measurement locations. Spatial data were recorded using a total-station survey. The interpreted MASW survey results are presented as two dimensional snapshot cross-

sections of the three dimensional calibration-site models. These show strong correlations between MASW survey velocities and site geology, geomorphology, fluvial profiles and geotechnical parameters and observations. Correlations are particularly pronounced where high velocity contrasts exist, whilst weaker correlations are demonstrated in softer lithologies. Geomorphic correlations suggest that off-plane deformation can be imaged and interpreted in the presence of suitable topographic survey data. A promising new approach to in situ and laboratory soft-rock material and mass characterisation is also presented using a Ramset nail gun.

Geotechnical investigations typically involve outcrop and laboratory scale determination of rock mass and material properties such as fracture density and unconfined compressive strength (UCS). This multi-scale approach is espoused by this study, with geotechnical and S-wave velocity data presented at multiple scales, from survey scale sonic velocity measurements, through outcrop scale scanline and crosshole sonic velocity measurements to laboratory scale property determination and sonic velocity measurements. S-wave velocities invariably increased with decreasing scale. These scaling relationships and strategies for dealing with them are investigated and presented.

Finally, the MASW technique is applied to a concealed fault on the Taieri Ridge in Macraes Flat, Central Otago. Here, high velocity Otago Schist is faulted against low velocity sheared Tertiary and Quaternary sediments. This site highlights the structural sensitivity of the technique by apparently constraining the location of the principal fault, which had been ambiguous after standard processing of the seismic reflection data. Processing of the Taieri Ridge dataset has further led to the proposal of a novel surface wave imaging technique termed Swept Frequency Imaging (SFI). This inchoate technique apparently images the detailed structure of the fault-zone, and is in agreement with the conventionally-determined fault location and an existing partial trench. Overall, the results are promising and are expected to be supported by further trenching in the near future.

1 INTRODUCTION

New Zealand has a growing population. It is expected to grow by up to 1.3 million people by 2026, which represents a 35% increase on 2001 figures (Statistics-New-Zealand, 2004). This increased population must be provided with safe housing. However, New Zealand's tectonic setting, outlined in 1.3 below, poses challenges to planners attempting to zone land for residential development. Basins such as Canterbury are often afflicted with poor outcrop, indistinct marker horizons and a lack of subsurface data. This adversely affects the resolution at which fault-zones can be characterized using conventional geomorphic and structural mapping (Litchfield et al., 2003). This study will investigate and put forth a method of improving planning efficacy by enhancing the reliability and resolution with which active faults are located in New Zealand's active landscapes.

1.1 Motivation: Present day land use planning in New Zealand fault-zones.

Land use planning within active tectonic settings is fraught with difficulty. Buildings sited across faults that rupture will invariably sustain the greatest damage during an earthquake, closely followed by those buildings in close proximity to the fault (eg Kelson et al., 2001). A 2001 report, entitled 'Building on the Edge: The use and development of land on or close to fault lines' (Williams, 2001, BOE report) and released by the office of New Zealand's Parliamentary Commissioner for the Environment raised concerns about the ability of legislation such as the Building Act 1991 (since replaced by the Building Act 2004) and the Resource Management Act 1991 (RMA) adequately to manage the development of seismically hazardous land. The report was initially motivated by concerns regarding the safety of the Winara Village retirement complex on the Kapiti Coast, where inappropriate provisions in the Kapiti Coast District Plan coupled with scientific uncertainty in determining the location of the fault placed the development in a potentially precarious situation.

Parties consulted in the preparation of the BOE report considered earthquake hazard planning to be a two stage process involving firstly the mapping of active faults and secondly site-specific, pre-development, geotechnical investigations. The latter stage is typically expensive but nevertheless essential. Whilst these parties agreed on a need to prevent construction over active faults, they also expressed concern regarding a lack of consistency of approach in site-specific investigations due to lack of guidance,

appropriate criteria and expertise. The BOE report identified a need for clear guidance on what a site-specific investigation should entail and concluded that it was important for local authorities to base their assessment and management of seismic hazards on accurate and relevant scientific information.

Following on the publication of the BOE report, a working party of relevant professionals developed a set of guidelines to assist New Zealand's resource management planners and these were published as a report entitled 'Planning for Development of Land on or Close to Active Faults' (Kerr et al., 2003, The Guideline). The Guideline sets out a risk-based planning approach based on the three elements of recurrence interval, fault complexity and building importance category.

The second step of this approach after fault identification is creation of fault avoidance zones around active faults. Section 6 of The Guideline defines a fault avoidance zone as a 20 m buffer either side of the active fault trace or likely fault rupture zone, with provision to increase this based on an assessment of fault complexity. Fault complexity in this instance is geomorphically defined but difficulties may arise when attempting to quantify the extent of a fault-zone and its associated deformation, which may be considerably degraded or buried by young sediments (Hart and Bryant, 1997; Similox-Tohon et al., 2006). This problem may directly impact uptake of The Guideline as shown by Becker *et al.* (2005). A key issue raised by their questionnaire returns in a study of uptake of The Guideline was that of justification. An interviewee responded that local authorities had difficulty justifying 'heavy-handed' implementation of the structured guideline approach where fault scarps were not well defined, especially without additional [subsurface] information.

The simple fault avoidance zone specified in The Guideline encompasses a zone 20 m *either side* of the fault trace or likely fault rupture zone. Oglesby *et al.* (1998) however, in a widely cited study, report an asymmetry in expected ground motion either side of dip-slip faults. For instance, they state that, given identical stress magnitudes, the intensity of motion depends on both fault sense (thrust fault ground motions surpass those of normal faults by 100%) and on location relative to the fault (hanging wall motions are larger than footwall motions for both normal and thrust faults). Duan and Oglesby (2005) further report that irrespective of dip sense, horizontal ground motion dominates on the footwall whilst vertical ground motion dominates on the hanging wall. This suggests that fault

avoidance should take greater account of fault geometry, which in the case of a buried fault may be less than clear and requiring information derived by subsurface investigation.

Although The Guideline is limited by the somewhat arbitrary 20 m setback criteria, the problems associated with active fault ground rupture and deformation do at least come within its scope. The Guideline, however, fails to address related issues such as strong ground shaking and liquefaction. The differential high intensity shaking mentioned above will extend beyond the immediate range of a few tens or even hundreds of metres and therefore cannot be completely mitigated by land zoning as such, although strategies reviewed in Chapter 2 have shown significant success in this area by classifying the shaking potential of sites. No such program is suggested by The Guideline and no further guidance is to be found in the Building Code (DBHNZ, 2007), set out in the first schedule to the Building Regulations (1992). The Building Code requires simply that "Buildings, building elements and sitework shall have a low probability of rupturing, becoming unstable, losing equilibrium, or collapsing during construction or alteration and throughout their lives." (Clause B1.3.1). It further states that "Account shall be taken of all physical conditions likely to affect the stability of buildings, building elements and sitework including: ... earthquake" (Clause B1.3.3(f)) with due allowance required to be made for site characteristics and inaccuracy in performance prediction (Clause B1.3.4(d) and (e)). These performance requirements, for building elements imparting structural stability, extend to the life of the building, which unless specified is not less than 50 years (Clause B2.3.1(a)(i)). The Building Code does not however contain any specification of site classifications such as are found in the United States' National Earthquake Hazard Reduction Program (NEHRP) building provisions (BSSC, 2006).

A consideration which deserves more immediate planning attention within a fault-zone is the extent of ongoing and coseismic secondary off plane deformation, particularly in the hanging wall of thrusts and transpressional faults. The internal structure of faults is not limited to a simple planar surface but incorporates a damage zone that may extend to several hundreds of metres within which complex distributed deformation may take place. Kelson *et al.* (2001) carried out detailed surveying of styles of deformation and related structural damage following the 1999 Chi-Chi earthquake in Taiwan. They recorded a deformation zone with a width that was typically 10-20 times the net vertical displacement of up to 4 m. In some instances they observed distributed secondary faulting and folding well into the hanging wall up to 350 m from the scarp. Such well

documented observations demonstrate that the extent of folding, tilting and secondary faulting in a variety of configurations may extend well beyond a 20 m corridor relative to the main rupture plane. A clear planning advantage would be gained by not only identifying the projected position of the fault trace but also identifying the width of the zone of damaged rock caused by off plane deformation.

Control over property development in New Zealand is devolved to the regional councils and the RMA requires regional councils to prepare a regional policy statement on issues including natural hazards. The current Canterbury Regional Policy Statement (ECAN, 1998) predates publication of the BOE report and The Guideline. However, a scoping report released in 2006 (ECAN, 2006) recommends a comprehensive review of the relevant chapter to include more precise policies to guide risk management. In addition, Environment Canterbury commissioned Opus International Consultants Limited to develop a draft risk assessment methodology for Christchurch (Brabhaharan et al., 2005). Although this document only addresses the risk in the Christchurch area from fault sources lying predominantly outside Christchurch, the proposed methodology requires the acquisition of ground shaking and liquefaction data. Both of these factors have been related to S-wave velocities (Anderson et al., 1996; Benjumea et al., 2003; Yunmin et al., 2005) (see section 2.4.3).

Despite the weaknesses of The Guideline, the first of its four planning principles calls for the gathering of accurate active-fault hazard information. The Guideline's authors acknowledge that gathering such information will require specialized scientific knowledge and surveys but note that, given the major effects of such information on any property development decisions, the information must be as accurate as technology and resources permit. A successful outcome of this study has practical application to the identification of obscured fault-zones and the siting of buildings, as well as contributing to fundamental research into the nature of high-level fault processes. It will validate Multichannel Analysis of Surface Waves (referred to throughout the remainder of this document as MASW) as a rapid, low-cost, scientific basis for fault-zone planning that is complementary to, and if necessary independent of, geomorphological interpretation, thus making a valuable contribution to New Zealand's fault risk management practices. Additionally, data generated by shallow seismic characterization of rock mass properties will be attractive in subsequent applications such as building foundation design, waste isolation or water containment in fractured rock.

1.2 Objectives

The primary objective of this study is to prove the utility of MASW to aid fault-zone planning by locating and defining the extent of fault-zones in several typical New Zealand settings, and defining within-zone variability that is readily correlated with measurable rock properties and with the distribution of surface deformation. Fundamentally, the method derives a near surface profile of S-wave velocity variability that is taken as a proxy for bulk rock strength.

This goal is attacked by addressing three secondary aims, including:

1. Investigation of the influence of shearing and cataclasis on the physical properties of a relatively uniform, high compressive strength rock type (Torlesse greywacke), by:
    - Initial definition of a multi-scale velocity structure of the Springfield Fault at Dalethorpe (SFD), Hawkins River Valley, South Canterbury and relation of this structure to fractured Torlesse sandstone engineering rock properties, and
    - Correlation of the interpreted (in terms of structure and rock properties) MASW profiles with the geomorphic expression at the outcrop of the SFD.
2. Exploring the limits of resolution of the method when applied in soft rock and discriminating variance due to primary lithologies from the effects of cataclasis, by:
    - Testing and recalibration of MASW at Boby's Stream Fault, Middle Waipara, where at different locations there is juxtaposition of a range of weaker lithologies including limestone, siltstone and greensand. This culminates in a test of the resolution at a complex site where two different siltstones are separated by greensand between two fault strands, with anticlinal bulging of the terrace between the strands.

   In both 1 and 2 existing river exposures are used to correlate MASW data with both in-situ and laboratory testing, and with the detailed structure of the fault-zones.
3. Blind application of the MASW technique is used predictively to characterise a further fault-zone at Sheehy Road, Macraes Flat, Otago.

The sites have been chosen because they have been subject to previous investigation. Their field relationships are thus known and they fulfill the requirements of the stated objectives.

1.3 New Zealand's tectonic setting

New Zealand's location astride a plate boundary is well documented (Figure 1-1). The Pacific plate rotates anticlockwise relative to the Australian plate causing systematic variation in the orientation and partitioning of convergence along the plate boundary system. This results in along strike changes in deformation styles, from oblique subduction at the Hikurangi Margin and back-arc rifting in the Taupo Rift in the North Island, through an almost purely strike slip transfer zone in the faults of the Marlborough fault system (MFS) of the northern South Island. The MFS links the Hikurangi Margin to the Alpine Fault, where oblique convergence is building the Southern Alps in the central South Island. The onshore New Zealand plate boundary finishes with an opposite-sense subduction of the Australian plate under Fiordland at the northern termination of the Puysegur trench (Pettinga et al., 2001; Wallace et al., 2007).

Active faulting due to accommodation of plate boundary motion poses hazards countrywide, particularly where fault-zones approach or transect inhabited or subdividable areas. This study is based in the central South Island, south of the MFS, north of Dunedin and east of the Alpine Fault (see site localities Figure 1-1). The area is particularly suitable for this research, as faults that offset and/or juxtapose a variety of lithologies, and that display late Quaternary and Holocene activity have been well documented in Canterbury (Cowan, 1992; Howard et al., 2005; Litchfield et al., 2003; Pettinga et al., 2001) and Otago (Litchfield and Norris, 2000; Norris and Nichols, 2004).

1.4 Tectonic setting of central South Island and study sites

According to the NUVEL-1A global plate motion model of DeMets *et al.* (1994), the central South Island accommodates 37 mm/yr of convergence on an azimuth of 071^{o} (calculated at Franz Josef by Norris and Cooper (2001)). This convergence is expressed by varying styles of faulting in Canterbury and Otago. In North Canterbury, the southern boundary of the MFS has migrated south over time and is currently dominated by the Hope Fault. An incipient new southern boundary to the MFS is, however, deforming the northern margin of the Canterbury Plains along a zone of dextral oblique shear that has

been termed the Porters Pass Amberley Fault-zone (PPAFZ - Figure 1-1, Figure 1-2) (Campbell et al., 2003; Cowan, 1992).

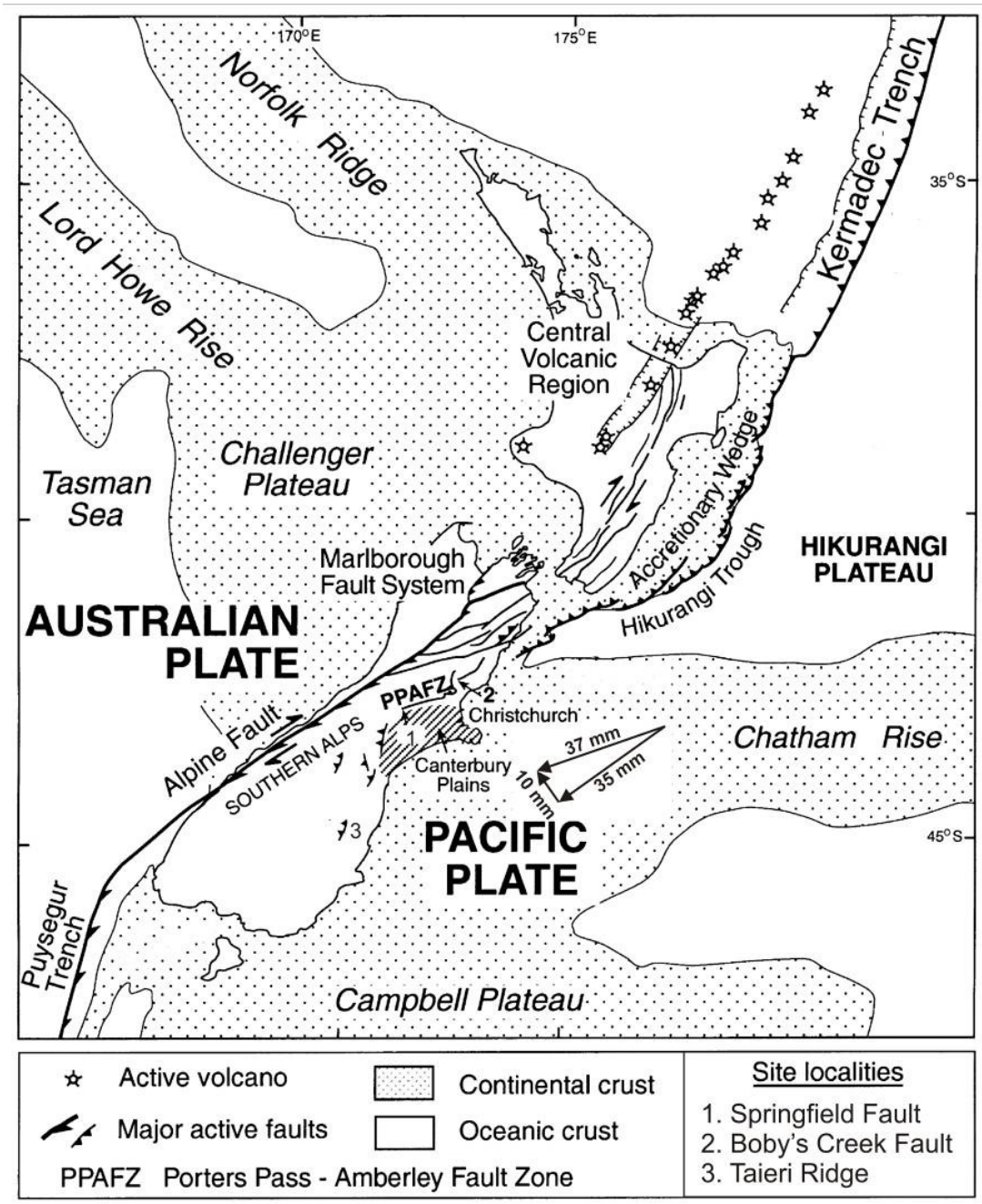

Figure 1-1: Tectonic setting and main structural features of the New Zealand microcontinent bisected by an obliquely convergent plate boundary between the Australian and Pacific plates. Study sites are shown, numbered 1-3. Arrows show rates of relative convergence in mm/yr. Plate boundary motion and partitioning calculated at Franz Josef by Norris and Cooper (2001) according to NUVEL-1A global model (DeMets et al., 1994). Map modified after Pettinga et al. (2001) and Campbell et al. (2003).

Two of the sites investigated in this study lie at opposite ends of the east-northeast trending PPAFZ, a hybrid system of strike-slip and thrust/reverse faults (Pettinga et al., 2001). Study area 1 is a strand of the Springfield Fault outcropping in the Upper Hawkins Basin at Dalethorpe, 7 km south west of Springfield. The mapped fault is a northwest

facing thrust with no evidence of strike slip offsets that falls within the PPAFZ (Figure 1-2 B). Its structure, however, is influenced by its location on a very close domain frontier between the PPAFZ, the Mt Hutt – Mt Peel [thrust] Fault-zone and the South Canterbury Zone as defined in Pettinga *et al.* (2001). The faults in the latter two zones are typically east facing. Lithologically, the Springfield fault juxtaposes different crustal levels of Torlesse greywacke, within the limited area covered in this study.

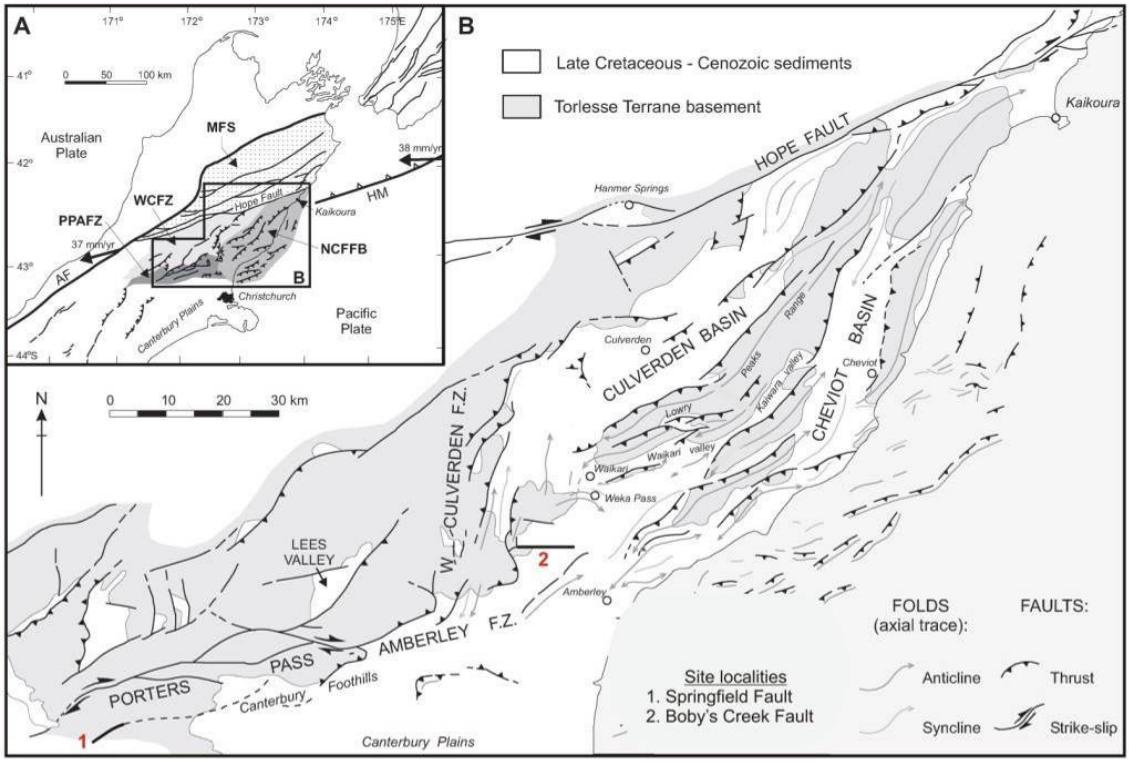

Figure 1-2: Tectonic setting and main structural features of North Canterbury. A) Location relative to the subduction/transpression transition zone between the Hikurangi Margin and the Marlborough Fault System (MFS, stippled). Other zones (after Pettinga et al., 2001) are the West Culverden Fault-zone (WCFZ), the Porters Pass Amberley Fault-zone (PPAFZ), and the North Canterbury Fold and Fault Belt (NCFFB). B) Locations of the Dalethorpe (1) and Boby's Stream (2) study areas at either end of the PPAFB. (modified after Litchfield et al., 2003).

The second study area is the Boby's Stream Fault in North Canterbury. Again part of the PPAFZ but located at the opposite end, this fault is more stereotypical of the domain and is structurally and lithologically dissimilar to the Dalethorpe site. The Boby's Stream Fault is dominantly strike slip with a significant transpressional component of northward thrusting. At various locations along its length it juxtaposes many of the typical lithologies of the South Island Tertiary succession, all of which are significantly softer than intact Torlesse Greywacke.

The third and final study area is located well south of the first two at Sheehy Road, along the Taieri Ridge in the Macraes Flat area (Figure 1-3). This area, which is shortening at ~1.5 mm/year, is characterized by basement schist thrust over Quaternary alluvium and

colluvium and patchy Tertiary remnants (Kilner et al., 2007 ; Norris and Nichols, 2004). The base of the southeastern slope of the Taieri Ridge structure harbours a concealed fault-zone, with no clear indicators of its position. As such it provides an admirable final site on which to test MASW.

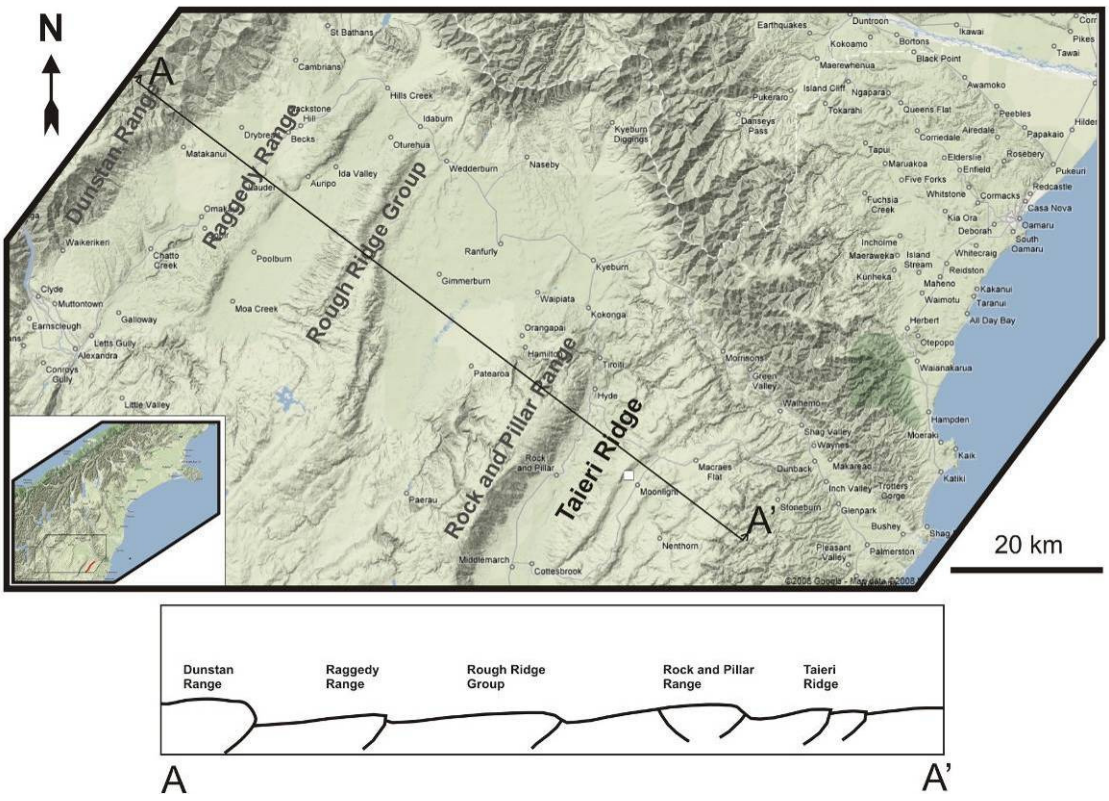

Figure 1-3. Central Otago map with inset South Island location map showing the actively rising northeast trending ranges of Central Otago. The Taieri Ridge is located on the southeastern margin of this system and the study site is marked with a white square. Cross section after Norris and Nicols (2004)

1.5 Study Format

A literature review is presented in Chapter 2 that looks first at the relevance of S-wave velocity data to fault-zone planning. It then outlines the geotechnical applications of S-wave velocities, including a review of the technical bases for correlation of S-wave velocities with geotechnical parameters. This section also encompasses a review of rock mass classification systems for tectonized rock masses and briefly considers photogrammetric characterization techniques. Having established the relevance of S-wave velocity data, the review turns to the techniques by which the data are acquired, concentrating on those relevant to this study.

Chapter 3 outlines the geomorphic, geotechnical and seismic methods employed in the various aspects of this study.

Chapters 4 and 6 present self-contained accounts of the MASW calibrations at Dalethorpe and Boby's Stream respectively. These chapters detail the site context and site-specific geology, review previous work on the sites, present details of the data and results obtained and report the correlations observed at these sites. Chapter 5 presents a structural and paleoseismic analysis of the Springfield Fault at Dalethorpe in the light of the work presented in Chapter 4.

Chapter 7 details a blind-test of MASW at the site at Sheehy Road, Macraes Flat in Otago. Although the test site was originally intended to be in similar lithologies to those encountered in Chapters 4 and 5, the Sheehy Road site presented an unexpected opportunity to expand the range of lithologies whilst fine tuning and blind-testing the techniques developed at the previous sites. It also offered the opportunity to reprocess an existing dataset over a concealed fault that had already been processed as a high resolution reflection survey. Chapter 7, therefore, includes a comparison of the survey methods in terms of data density (hence acquisition time), processing time, interpretability and results. Finally, it presents a first look at a technique developed in this study and not previously reported in the literature that promises to reduce shallow seismic survey times over an active fault by an order of magnitude, whilst providing exceptional lateral resolution.

Chapter 8 presents a general summary of the study and a discussion of the similarities and differences between sites. In addition to discussing points arising from the test sites, it also discusses the relative utility of MASW compared with other geophysical techniques. and makes mention of promising photogrammetric geomorphic analysis techniques being developed at the University of Canterbury's Geospatial Research Centre. It draws conclusions and makes recommendations for further work.

2 SHEAR WAVE VELOCITIES: INTERPRETATION AND TECHNIQUES

A wealth of literature relates S-wave velocities to fault-zones, whether for use as a planning tool, geotechnical interpretation or the application of S-wave imaging techniques in tectonically active areas. This chapter reviews this literature as it applies to this study. Limited methodological details are provided here only where necessary to establish a point or where a particular technique is important in the literature but not in this study.

2.1 S-wave velocities and fault-zone planning

Soule (1907) and Branner (1911) noted the relationship between surficial geology and site earthquake response a century ago (Figure 2-1). Soule (1907) wrote:

> "The destruction wrought by earthquake in its severe effects was proportional in a way to the nearness of the locality of the fault trace, but varied greatly according to the character of the rock and soil formation throughout the disturbed area. [It] amounted to little or nothing in well built structures resting upon solid rock and, all other things being equal, increased in proportion to the depth and incoherent quality of the foundation soil. [Santa Rosa], built upon a deep alluvial soil, was more severely shaken and suffered greater damage, in proportion to its size, than any other town in the state"

B. GENERAL EARTHQUAKE EFFECT ON FRAME BUILDINGS SITUATED ON ALLUVIAL SOIL, HOWARD STREET, SAN FRANCISCO.
Photograph by A. C. Lawson

B. COMPLETE WRECK BY EARTHQUAKE, COURT-HOUSE AND HALL OF RECORDS, SANTA ROSA.

Figure 2-1: Photographs from the San Francisco earthquake of 18 April, 1906 showing the damage associated with low S-wave velocitiy materials in the subsurface (Soule, 1907).

An understanding of these observations has grown with research. Anderson *et al.* (1996), for instance, found that the ground motion responsible for such destruction is influenced to the greatest degree by the S-wave velocity properties of the upper 30 m. This influence

is out of keeping with that zone's thickness as a percentage of the source-to-surface distance. They investigated the relative importance of the surficial, intermediate and deeper velocity structure on vertically propagating S-waves and concluded that similar influence on ground motion is attributable to surficial (<30 m) velocities and to deep (>5 km) attenuation properties. They found little influence attributable to the velocities of the intermediate layers even in an attenuating medium. This makes estimation of shallow shear velocity structure an important component of ground motion estimation and site response characterization (Anderson et al., 1996; Louie, 2001) and therefore of comprehensive earthquake preparedness.

Boore (2004a) cautioned that the question of whether site response can be predicted depends on what kind of site response is being predicted and the accuracy required. He showed that there is a large degree of ground motion variability between sites for a given earthquake and, more importantly, between earthquakes for a given site. Nevertheless, shallow shear velocity structure forms the basis of site hazard classification under the United States' NEHRP building provisions (BSSC, 2006). This classification was shown by Boore (2004b) to have been effective in the case of the 2002 Denali Fault Earthquake in Anchorage, Alaska.

2.2 Factors affecting rock mass S-wave velocity

Land zonation using S-wave velocities must be underpinned by sound geology and geotechnical research. The geometry and the material properties of fractures in a medium dictate its seismic parameters (eg Boadu, 1997; Leucci and De Giorgi, 2006; Rasolofosaon et al., 2000) so achieving the ultimate objective of this study requires definition of within-zone S-wave velocity variability that is readily correlated with measurable rock properties. An early correlation exercise, although not fault-specific, was undertaken by the United States Geological Survey and reported by Fumal (1978). At each site they drilled a hole to 30 m in a wide range of geologic materials to record the site stratigraphy, physical properties and downhole P and S-wave velocities. The study reported strong correlations of S-wave velocity with hardness and fracture spacing. Fracturing dramatically reduces the elastic moduli, often without significantly changing the porosity so that, in well-cemented lithologies, fracture spacing exerts a greater influence on S-wave velocity than does lithology, hardness or primary porosity (Fumal, 1978; Rasolofosaon et al., 2000). Fumal (1978) found hardness to be a proxy for weathering in bedrock material, in which fracturing dominated S-wave velocities. In soft

rock and alluvium, however, he reported that hardness dominated the S-wave velocities. He further reported less strong correlations between these physical properties and p-wave velocities.

Fumal (1978) typically observed three weathering-related velocity zones in his well logs. With increasing depth, these were a layer of unconsolidated residual material, an underlying zone of moderately to deeply weathered bedrock, and relatively fresh bedrock. His results show a close correlation on almost every well log between these weathering zones and the corresponding interval velocities. More significantly, from the point of view of discriminating lithologies based on S-wave velocities, the thickness of individual weathering zones varied between geological units in a given area. Fumal compared the effect of moderate weathering on S-wave velocity for a variety of lithologies. By plotting the velocity *reduction* for weathered rock against the fresh rock velocity at the same site over a range of lithologies, he showed that the velocity drop due to weathering is a direct function of the strength of the fresh rock. Weak rocks will exhibit a greater absolute velocity drop for an equal degree of weathering than will equivalently weathered strong rocks. This suggests the potential to discriminate fault-zones juxtaposing different soft lithologies based on changing vertical velocity gradients.

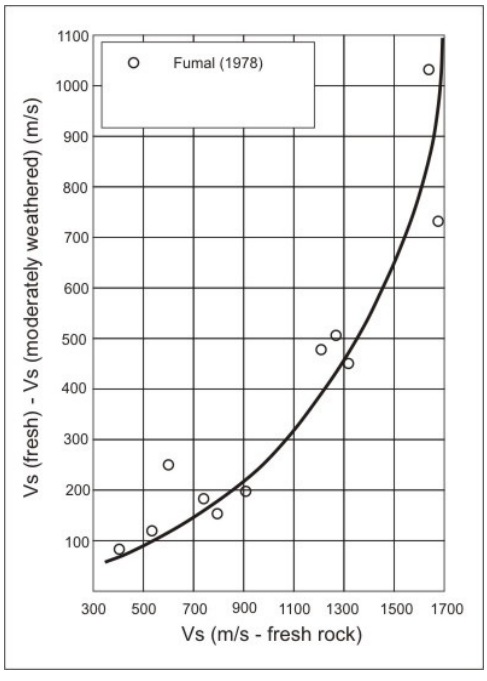

Figure 2-2: Reduction in S-wave velocity attributable to moderate weathering, graphed as a function of the fresh rock S-wave velocity (after Fumal, 1978).

Geotechnical interpretation of S-wave behaviour in a geological medium must be guided by an understanding of the physical relationships between S-wave propagation and rock

mass character. A waveform propagating through a fractured medium is delayed and the high frequencies are filtered, so that the peak frequency in the received signal is shifted toward the lower frequencies. This has been observed in theoretical models (Boadu, 1997), and in laboratory models and the field (Leucci and De Giorgi, 2006). As a wave propagates, an apparent attenuation accumulates because reflections from individual fractures interfere with the propagating wave (Boadu and Long, 1996). This seismic response to fracturing provides a means of inferring fracture density from variations in seismic velocity in and otherwise homogenous medium. Boadu and Long (1996) incorporate linear fracture density into their equations for estimating velocity and attenuation in a fractured medium.

2.3 Potential correlative rock mass classifications

Many parameters have been used to attempt to quantify the condition and mechanical state of a fractured rock mass. Volumetric crack density has been correlated with seismic velocities (Crampin et al., 1980; Leary and Henyey, 1985) but is not easily measurable in field conditions. In recognition of this, Boadu (1997), modelling the effect of fractures on seismic waves, correlated S-wave velocity strongly with *linear* fracture density (fractures per unit length) and rock quality designation (RQD - % of core with fracture spacing >10 cm) among other parameters (Figure 2-3). His correlation, although significant for this study, takes no account of the effects of weathering.

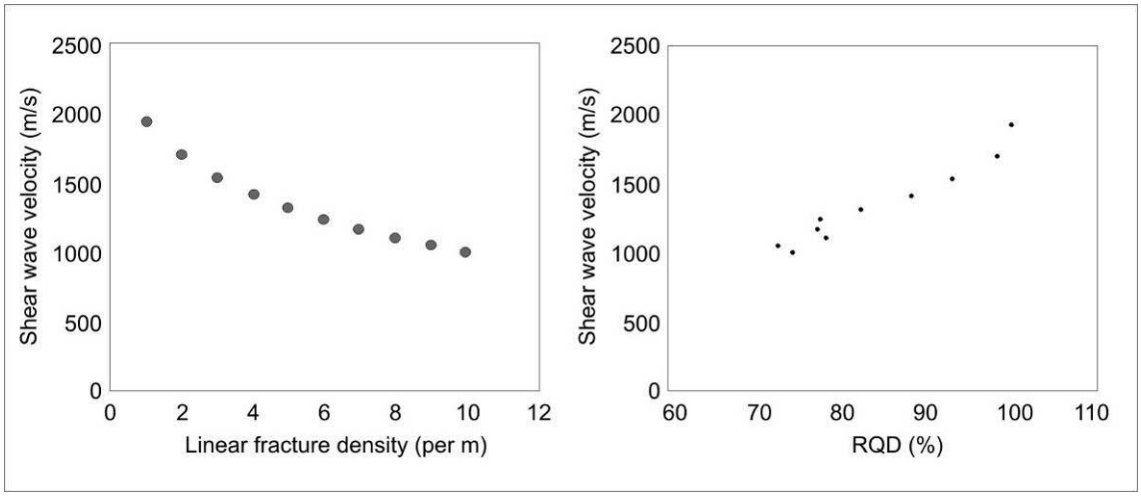

Figure 2-3: Variations of S-wave velocity with fractured rock mass parameters for the model of Boadu (1997). Both parameters exhibit a strong correlation with S-wave velocity.

Rock masses are typically characterised based on intact rock strength and the condition of the rock mass discontinuities (Gokceoglu and Aksoy, 2000; Hoek et al., 1998). Mineralogy of the intact material is only accounted for where it affects intact rock

strength or, as in the work of Gokceoglu and Aksoy (2000), renders the rock mass vulnerable to the damaging effects of water. This characterisation approach implicitly assumes that discrete discontinuities separate *intact* rock, a fair assumption only if core can be recovered from the rock-mass in question to determine the intact material properties of the rock mass itself (rather than the parent material), and if the properties of the fracture fill do not dominate the rock mass.

The commonly-used Hoek-Brown failure criterion was developed by Hoek and Brown (1980) to estimate rock mass properties from intact rock properties and discontinuity characteristics. It was originally dependent on a simplified rock mass rating (RMR) system. Quantitative characterisation and classification of cataclastic rocks using RQD-based systems such as RMR is troublesome due to difficulties in acquiring undisturbed samples for laboratory test procedures such as unconfined compressive strength (UCS). These difficulties persist during sample preparation and testing leading to a very low experiment success rate (eg Habimana et al., 2002). When specimens are successfully tested they are typically not at all representative of the rock mass.

The difficulty obtaining meaningful RQD values in weak rock masses led to the abandonment of RMR in favour of the specially developed and introduced Geological Strength Index (GSI) (Hoek et al., 1992). GSI now forms the basis of parameter selection for the Hoek-Brown failure criterion. It is a classification system for qualitatively estimating the reduction in rock mass strength due to geological conditions. Index values are assigned based on visual assessment of lithology, the degree of interlocking of rock mass components and the quality of the discontinuities indicated by surface roughness and alteration. It therefore takes account of the two major factors affecting S-wave velocity, fracturing and weathering. The original GSI and Hoek-Brown failure criterion system inherently assumed rock mass isotropy and was thus inappropriate where a preferred fabric orientation such as schistosity dominated the mass. Regular encounters with anisotropy have led to the extension of the GSI to allow assigning of values in anisotropic masses where the difference between the strength of the rock and that of the discontinuities is small, such as closely spaced weak schistosity or shear planes (Hoek et al., 1998). GSI has also since been further extended to flysch (Marinos and Hoek, 2001) and modified for cataclastic rocks (Habimana et al., 2002), but is still inappropriate where a single set of discontinuities dominate an otherwise sound rock mass.

In addition to modifying the GSI classification system, Habimana *et al.* (2002) improved the reliability of the Hoek-Brown failure criterion for cataclastic rocks. Hoek and Brown (1997) presented formulae relating the Hoek-Brown failure criterion constants m_b, s and a to the estimated GSI values. Habimana *et al.* (2002), however, found that the failure criterion for cataclastic rocks varies between pure Hoek-Brown for intact rock as the upper bound (un- or lightly tectonised) and Mohr-Coulomb for soil as the lower bound (extremely tectonised). They related these tectonisation degrees to the GSI (Figure 2-4) and substantially modified the formulae of Hoek *et al.* (1998) to account for this transitional behaviour.

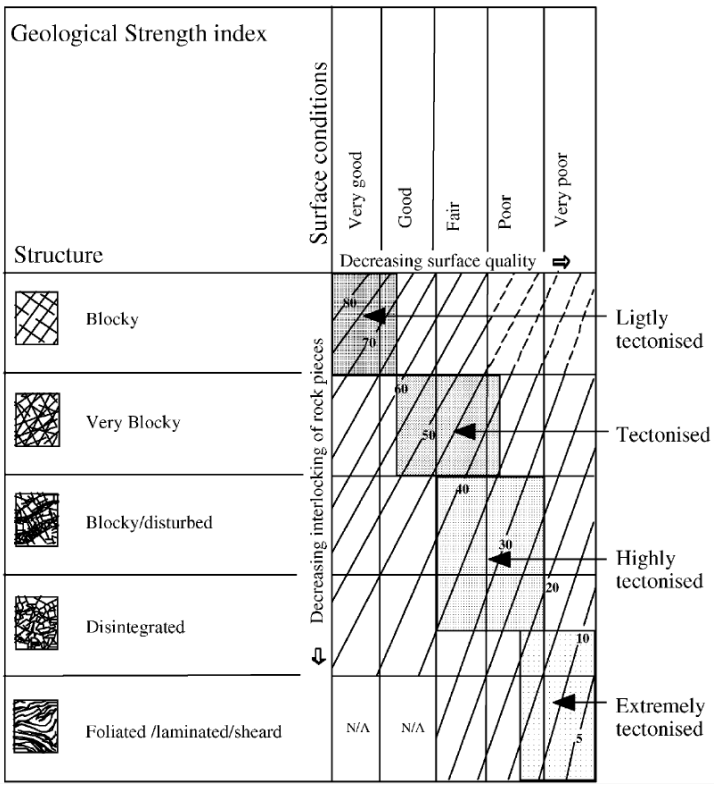

Figure 2-4: Geological strength index modified after Habimana et al. (Habimana et al., 2002)

Based on the observations of Fumal (1978), GSI shows promise as a correlative classification against which field survey S-wave velocities may be interpreted. Such a correlation would feed directly into the geotechnical design via the modified Hoek Brown failure criterion of Habimana *et al.* (2002). However, GSI does not lend itself to laboratory characterization and, as the objective of this study is to relate the laboratory experiments to field data, the most transferable correlative may be linear fracture density as observed by Boadu (1997).

2.3.1 Photogrammetric options

A significant amount of the time invested in site investigations is spent collecting scanline and other geotechnical data at outcrop, and carrying out laboratory work in an attempt to effectively classify the rock mass. This study is no exception and the result is costly in terms of time and money, and almost certainly subject to the skill and experience of the geologist. An early objective of this study was to develop a cheap, rapid and objective photogrammetric technique for rock mass classification. Although such a technique was never developed, considerable time was invested prior to its abandonment, during which several existing packages were investigated for inspiration. One of these packages in particular stood out as a potential tool for fault-zone classification.

Fragalyst is a software package developed by the Central Mining Research Institute in India for explosive excavation optimisation. It is based on a fundamental assumption that rock mass fracturing displays a fractal distribution. A fractal is defined by Hobbs (1993) as 'a shape made of parts similar to the whole in some way'. Fractured rock masses have been shown to display fractal geometries (Chelidze and Gueguen, 1990; Xie, 1993; Xie and Chen, 1988) and rock mass characterization on the basis of this fractal geometry is well established in the literature (Babaie et al., 1995; Bagde et al., 2002; Dor et al., 2006; Gao et al., 1999; Gao et al., 2004; Ghosh and Daemen, 1993; Hamdi and du Mouza, 2005; Lu et al., 2005; Tu et al., 2005). Boadu's (1997) computational analysis, along with his subsequent modelling work (Boadu, 2000) and laboratory work by Leucci and De Giorgi (2006), suggests that simple and valid empirical relationships can easily be developed correlating seismic velocities with fractal rock mass parameters for any given lithology. Leucci and De Giorgi (2006) tested their derived relationships in the field and found good agreement between geological, geomorphological and seismic results.

The Fragalyst system consists of capturing video photographs of a scree pile and its open face using a calibrated video camera. The footage is downloaded and enhanced, calibrated, processed and analyzed to determine the area, size, shape, and sphericity of the fragments on the basis of greyscale difference. The fractal indices are determined from the shape factor (ratio of area to perimetre squared) of fragments for both the scree pile and the in situ rock blocks. Bagde *et al.* (2002) tested the system and concluded that whilst most in-situ rock produced fractal indices lying in the RMR range of 30-40 and beyond, the ratio of the scree fragment dimension to the in situ dimension decreased with increasing RMR. This reflects the rapid disaggregation of an apparently strong rock often

seen with tectonized rock masses. The strong correlation of the dimension ratio with an important rock mass parameter suggests that a single photogrammetrically-obtainable fractal-based number should be sufficient to classify weak rock masses.

2.4 Multi-scale S-wave velocity measurement

Characterization of the within-zone spatial variability in lithology, fracturing, fabric development and cataclasis is necessary to understand past and likely future fault behaviour. These are characteristics that vary at multiple scales and also have been shown to correlate with wave propagation phenomena such as low seismic velocities (Gettemy et al., 2004; Zinszner et al., 2002).

Unfortunately the correlation is scale dependent. Material heterogeneity across a fault-zone may induce apparent dispersion (frequency dependent velocity) due to the significant lithological, fluid and deformation variations that occur at scale lengths from <5mm to >5 m (Gettemy et al., 2004; Mukerji et al., 1995). The dispersion is controlled by the ratio of the wavelength of investigation (h) to the scale length of heterogeneity (a). In general the velocities increase with decreasing values of h/a so that ultrasonic velocities measured at core scale in the laboratory (h is small) are higher than those measured at crosshole or seismic scale and require corrections when changing scales (Mukerji et al., 1995).

This dispersion can be hard to predict without recourse to numerical modelling (eg Gettemy et al., 2004) and this may affect the reliability of interpretations and predictions made based on velocities obtained at seismic survey scale. Nevertheless, this study is conducted at three scales, from ultrasonic laboratory testing to sonic crosshole and seismic surveys averaging velocities over metres to tens of metres and simple scaling relationships will be sought. Each of the methods used is a transmission technique, and therefore suitable for investigating fractured media (Boadu, 1997). The techniques will be reviewed in scale order from smallest to largest.

2.4.1 Laboratory scale: Ultrasonic velocity measurement

Published data on the ultrasonic S-wave velocities of this study's target lithologies will be introduced site by site. However, the objectives of this study demand more than simple laboratory S-wave velocity determination. Fracturing clearly dominates S-wave velocities in competent bedrock (Fumal, 1978), and in fact fracturing dominates other causes of

seismic anisotropy by <100% at confining pressures lower than a few tens of megapascals (Rasolofosaon et al., 2000). What is required for this study is a method of quantifying the effect of fracturing and/or weathering, and the commensurate reduction in rock mass strength, on the characteristic S-wave velocity of a lithology.

Previous studies have approached this question using different techniques but with the same general pattern of results. Shakeel and King (1998) and King *et al.* (1997) investigated seismic wave propagation in sandstone with a system of aligned cracks, which they introduced during measurements using a polyaxial stress loading system. They increased σ_1 and σ_2 to near failure and demonstrated a strong correlation between permeability in the plane of cracks (related to aperture) and S-wave velocities propagating, not only in the direction normal to the plane of the cracks, but also in the plane of the cracks and polarised normal to the cracks. In a similar experiment Wulff *et al.* (2000) investigated the mechanisms involved in the attenuation of seismic waves so as to relate attenuation to fracturing. As with Shakeel and King (1998) Wulff *et al.* measured ultrasonic wave propagation whilst increasing fracturing. They observed similar results and report relationships demonstrating that microcracking due to uniaxial unconfined compression strongly influences velocity and attenuation of ultrasonic waves in dry sandstones.

Both of these studies quantified relationships between cracks and acoustic velocities. Although these types of experiments seem ideal, difficulties arise in trying to reproduce them using simple and limited rock laboratory equipment. Particular difficulties arise in quantifying the incremental intensity of fracturing, hence Wulff *et al.* (2000) used axial strain as a proxy for fracture intensity. A different approach is taken by Nakagawa *et al.* (2002), who modelled elastic wave propagation parallel to an infinite number of plane parallel fractures with equal fracture spacing and fracture stiffnesses. Their results are of limited relevance to this study but, in validating their model data, they used a steel analogue with artificial 'fractures' (Figure 2-5). This concept seems promising for simple laboratory work, with the substitution for steel of parent material 'fractured' normal to the S-wave propagation direction.

2.4.2 Outcrop scale: crosshole velocity measurements

As has occurred in laboratory studies, correlations based on crosshole transmission of seismic energy have been demonstrated between decreasing S-wave velocities and

increases in fracture frequency or density (eg Worthington, 1984). Zhu and Toksooz (2003) used modelling to develop a novel seismo-electric approach to investigate fractures between boreholes. Their technique, unfortunately beyond the scope of this study, records arrival times for an electromagnetic wave induced by a guide wave at a fracture between an acoustic source and receiver boreholes.

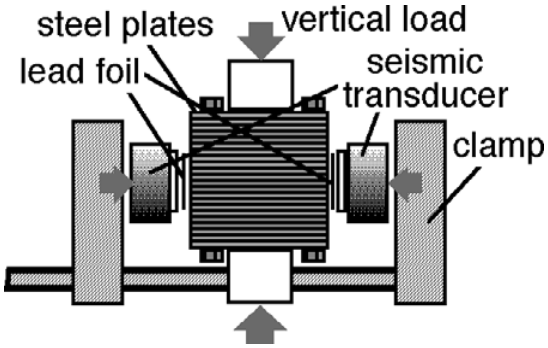

Figure 2-5: Nakagawa et al.'s (2002) experiment was conducted using ultrasonic transducers with waves propagating parallel to fractures in simulated fractured material (steel plates). The lead foil provided acoustic coupling.

Propagation through a fracture causes substantially greater amplitude reduction in a reflected wave than a transmitted wave, so transmission techniques are best for imaging fractured media (Boadu, 1997). Crosshole geometry also allows study of raypaths normal to the strike of fractures. King *et al.* (1986) carried out horizontal crosshole measurements in blast-damaged columnar basalt. Their study however, whilst validating horizontal crossholes for rock mass investigation, used drilling and seismic equipment appropriate to a mining budget and beyond the reach of this study. They did, however, demonstrate a strong relationship in 3 dimensions between S-wave velocity and the intensity of fracturing due to blast damage at the face.

2.4.3 Survey scale: Multichannel analysis of surface waves

Detailed discussion of the method and geophysical principles of Multichannel Analysis of Surface waves (MASW) are reserved for coverage in Chapter 3 and Appendix A respectively. This section will briefly introduce those aspects as necessary for clarity but will mainly be concerned with reviewing the several advantages and applications of the MASW technique, as well as validation studies undertaken and previous uses of MASW in active tectonic environments.

S-wave velocity determination by surface wave inversion has been applied at widely varying scales, from regional full-crustal scale (Surface wave tomography e.g. Behr et al.,

2007), through multichannel near-surface surveys such as Refraction Microtremor (Louie, 2001) and MASW (Park et al., 1999b) to Spectral Analysis of Surface Waves (SASW) soundings (Stokoe et al., 1994), MASW's small-scale predecessor. Surface wave inversion assumes that S-wave velocity dominates layer thickness, P-wave velocity and density in its influence on Rayleigh wave (the direct surface parallel transmission of S-waves) phase velocity and dispersion characteristics (e.g. Xia *et al.*, 1999).

In a seismic survey, more than two thirds of the seismic energy generated is partitioned into ground-roll-generating Rayleigh waves. Propagation through a fracture causes substantially greater amplitude reduction in a *reflected* wave than a transmitted wave, so transmission techniques are best for imaging fractured media (Boadu, 1997). Transmitted Rayleigh wave noise is exploited by the MASW technique, developed by Park *et al.* (1999b) at Kansas Geological Survey, to yield a 2D S-wave velocity profile. The procedure consists of acquiring multichannel records of surface wave events, extracting the fundamental-mode dispersion curves from each record and inverting these curves to obtain 1-D (depth) Vs profiles for each curve. The interpolation of the inverted profiles by contouring software then produces a 2D Vs profile for the length of the survey. The use of multichannel records permits identification and removal of noise prior to dispersion curve extraction. The nature of surface wave surveys favours the use of land streamers because optimal receiver coupling is generally obtainable by pressure contact with the surface rather than labour-intensive planting and recovery (Miller et al., 1999b). The receiver spread is necessarily short to accommodate lateral velocity variation (Park et al., 1999b) and thus easily handled by a minimal team. Geophones are vertically oriented and of the type used for near surface seismic reflection and refraction surveys. This versatile and towable multichannel setup enhances both speed and redundancy in data acquisition, whilst reducing labour requirements.

A fundamental assumption of MASW acquisition and processing is that the subsurface conforms to a laterally homogeneous layered earth model. This assumption can be validated by examination of trace to trace linear coherency, and is best satisfied if receiver spread is kept as short as possible (Park et al., 1999b). This can create issues with dispersion curve extraction, which is optimized by having a *long* receiver spread to separate phase velocities of the multiple modes (see Appendix A). However, given a suitably short receiver spread and successful dispersion curve extraction, the inherent sensitivity of surface wave velocities to lateral seismic velocity changes renders them

particularly suitable for detection of structural features that are characterized by lateral velocity changes in the upper 50 m such as faults (Ivanov et al., 2006).

The MASW method has recently become increasingly popular for a range of applications including the detection of subsurface features such as bedrock topography. Shallow seismic characterization of rock mass fracturing and bedrock topography is attractive in applications such as waste isolation or water containment in fractured rock. Bedrock topography and character has a major influence on subsurface hydrology and may exert significant control over the movement or otherwise of contaminants in the subsurface (Miller et al., 1999b). Miller *et al.* observed large lateral velocity-gradients within their inverted Vs profile that were consistent with drill-confirmed bedrock topography. They also observed localized lateral velocity reductions consistent with low velocity fracture zones and erosional channels. Miller *et al.*'s study was carried out in a manufacturing area with significant cultural and electrical noise but MASW proved largely insensitive to this. Ivanov *et al.* (2006) discriminated two formations of dipping weathered and intact bedrock, the overlying regolith and a concealed fault-zone. Their success at delineating the dip was due to compositionally preferential weathering of the bedrock surface, whilst they attributed their overall success to a half-day of pre-survey on-site calibration to optimize the source offset and shot spacing. The importance of field parameter selection is discussed in Appendix A.

The primary objective of Ivanov *et al.* (2006) was to use MASW to investigate a fault-zone. They imaged an 80 m wide zone with seismic velocities ranging from 400-800 m/s, which coincided with a previously mapped thrust fault. They attributed the reduction in Vs of the fault-zone to a reduction in shear modulus related to fracturing and in-situ weathering. This conclusion is supported by drill logs in the fault-zone, which record blocks of indurated bedrock floating in clay gouge at depths of up to 60 m. A secondary but very important capability demonstrated by Ivanov *et al.* (2006) is discrimination between primary lithological variation and faulting. They were able to distinguish the two juxtaposed formations both from each other and from the intervening fault based on weathering velocities (Figure 2-6). This supports the conclusions of Fumal (1978) (Section 2.2).

Besides bedrock and faults, other features detected include buried pits and trenches (Miller et al., 2000), sinkholes (Miller et al., 1999a) and cavities (Nasseri-Moghaddam et al., 2005; Xu and Butt, 2006). Liquefaction hazards are correlated with S-wave velocity in

the laboratory (Andrus and Stokoe, 2000; Yunmin et al., 2005), and Lin *et al.* (2004) have favourably assessed the utility of MASW for estimating the extent of liquefaction hazards. Geotechnical applications of MASW are particularly promising. Shallow S-wave velocity structure is an indication of stiffness and is used when estimating site response to shaking (section 2.1). By facilitating construction of an S-wave velocity profile MASW can provide critical information for geotechnical site characterization. Specific applications have included non-destructive testing of asphalt or concrete slabs (Rhazi et al., 2002; Ryden and Park, 2005), ground stiffness assessment (Joh et al., 2006; Ryden and Park, 2005; Tomeh et al., 2006) and marine sediment stiffness assessment (Park et al., 2005c). Crice (2005) suggests that the popularity of surface wave methods in general, including MASW, will continue to grow due to their ease of acquisition, processing and interpretation.

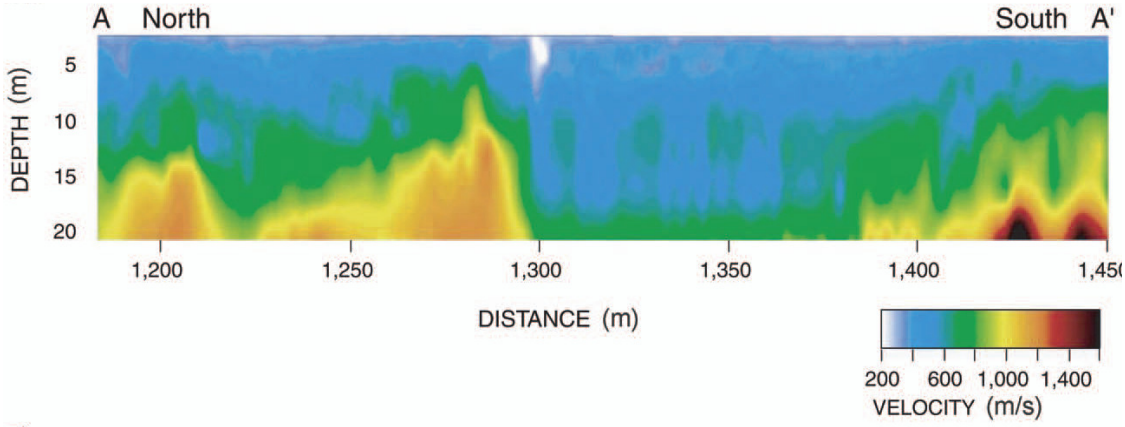

Figure 2-6: MASW 2D Vs profile across an unnamed New Jersey fault-zone. The fault-zone and the dipping and weathered bedrock of the fault bounded formations are clearly imaged to 20m depth. High velocities can be seen south of the fault in the interbedded sandstones and shales of the Stockton Formation. This is in contrast with the mid-range velocities of the weathered massive and laminated mudstones of the Lockatong Formation, which outcrops to the north of the fault (Ivanov et al., 2006).

Despite this popularity and the successful fault study by Ivanov *et al.* (2006 9) little else has been written on the application of MASW to the study of faults. Only three other examples appear in a review of the literature as at June 2008. Seshunarayana *et al.* (2008) used MASW to map shear zones in fractured granite basement. Of the remaining two, one is a preliminary study (Parrales et al., 2003) on which nothing further has been published to date and the other (Karastathis et al., 2007) made only very limited use of MASW, using it as a tool to provide velocities for other shallow seismic techniques. Neither provide details or discussion of the results of the MASW surveys, leaving Ivanov *et al.* (2006) as the only comprehensive published literature on application of MASW to active faults.

Several studies have been published independently validating the S-wave velocities produced by inversion of surface wave data using the MASW and other surface wave techniques (Joh et al., 2006; Stephenson et al., 2005; Xia et al., 2002; Zhang and Chan, 2003). Of these studies, Stephenson *et al.*'s (2005) blind study achieved matches of S-wave velocity averaged to 30 m (V_{s30}) within 15% on all four boreholes and within 3% on two of the four. Xia *et al.* (2002) similarly achieved less than 15% variance from borehole data on their 8 well study, although only one well was matched blind. That well achieved a calculated overall difference of only 9%. Stephenson *et al.*'s (2005) study also included a comparative evaluation with the refraction microtremor (ReMi) method of Louie (2001). They concluded that neither method was consistently better and suggested that both MASW and ReMi were appropriate tools for hazard assessment. These positive results, however, require well constrained fundamental mode dispersion curves and deteriorate rapidly with poor data and/or processing (Zhang and Chan, 2003). Such issues surrounding data acquisition and processing and are covered further in Chapter 3 and Appendix A. A proposed quality index for classifying dispersion curves is appended at Appendix B.

3 STUDY METHODS

The stated objective of this study can be broken down into three major components. The first of these is to prove and optimize the utility of the MASW technique to locate and define the extent of fault-zones. The second component is to correlate the MASW data with standard rock mechanics measures of fracture intensity. The third and final component is to correlate MASW and rock mechanics data with the distribution and character of ground deformation as a predictive tool. Following a brief outline of mapping methods, the structure of the remainder of this chapter reflects the order of those objectives. A variety of techniques were used repeatedly during this study, each selected to best achieve the study objectives. The use of these techniques is reviewed and the methods employed are outlined in the necessary detail here. Methodological details are then omitted in subsequent chapters.

3.1 Mapping

The two selected calibration areas were mapped in detail to establish the geological and geomorphic relationships. The general site geomorphology, emphasising tectonically significant features, was mapped in the field using a combination of the 1963 Aerial Mapping Limited air photos and the 1995 orthophotos from Land Information New Zealand. The older photographs were used because the study areas were significantly less vegetated at that time. A2 sized maps were prepared at scales of 1:5000. No field work was carried out for the blind test at the Taieri Ridge site.

3.2 Survey scale seismic investigations – MASW

The primary objective, outlined in section 1.2, was served by carrying out extensive MASW surveying. The MASW procedure is summarized in Figure 3-1 and its theory expounded in Park *et al.* (1999b), Xia *et al.* (1999) and Appendix A. Stages in the technique include data acquisition, pre-processing, dispersion curve extraction, and surface wave inversion and contouring.

3.2.1 Surface-wave Data Acquisition

3.2.1.1 Acquisition parameters

Data-acquisition parameters were chosen to optimize recording of ground roll signals. The choice of near offset (*x1* – Figure 3-2) is normally critical, as it is best to record both

high frequency and low frequency planar (as opposed to cylindrical – Appendix A) surface waves. This allows the best combination of near surface resolution (high frequencies) and penetration (low frequencies). Another critical parameter in this regard is geophone spacing. Reducing geophone spacing can increase the amount of high frequency energy that is collected at far offsets. Surveys in this study were acquired initially with spacings of 1 m and later surveys with 0.5 m spacing. The relative merits of the two geometries will be discussed in Chapter 8.

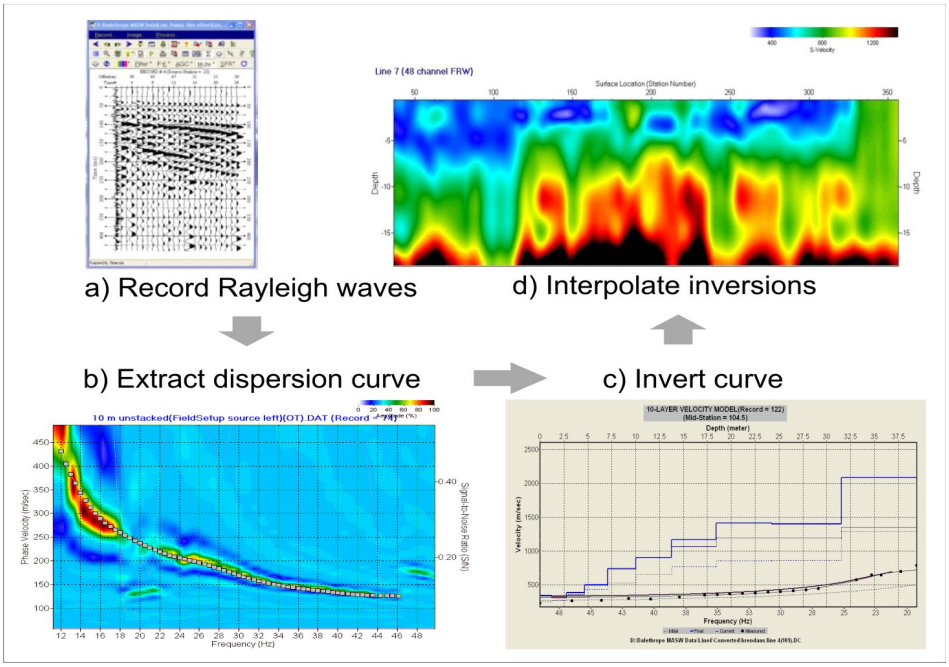

Figure 3-1: Basic steps in the MASW method.

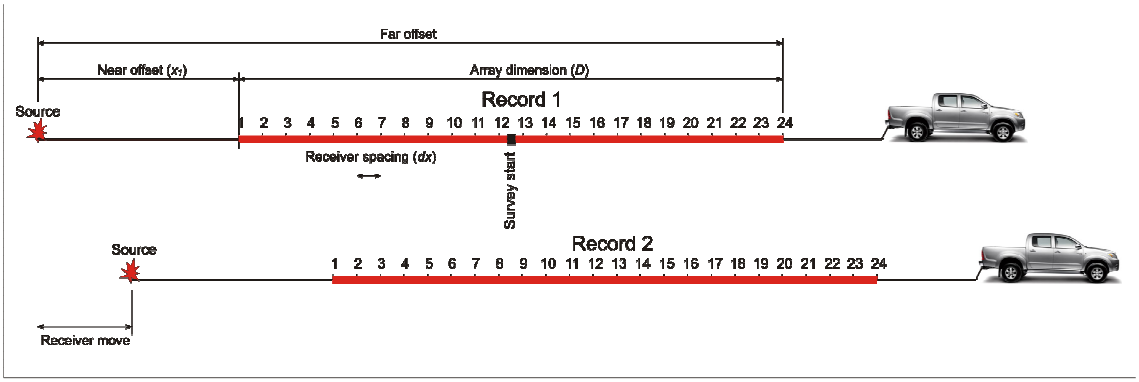

Figure 3-2. MASW survey geometry using a land streamer. Key acquisition parameters are illustrated and selection of these is discussed in the text.

Some sites are amenable to optimization of acquisition parameters by examining a swept frequency record from a full wavefield profile. In this study setting, however, this was found to be of limited use and collection of data for 48 channel walkaways proved more effective and versatile. Where this was possible, greater freedom could be taken in

selection of the near offset. Literature is available on optimal parameters for soil sites (Park et al., 2005a) but is probably of limited use for bedrock floored sites. This study's conclusions will include recommended near offsets for the lithologies encountered.

3.2.2 Equipment and settings

Multichannel shot records were collected in a CDP roll-along type survey using an end-on string of 24 8Hz geophones mounted on steel ground-contact sleds connected together in a land-streamer (Figure 3-3). As a minimum, the start and finish position of the array centre were recorded by a theodolite survey relative to the local site survey pegs. Array centres were surveyed where topographic correction was needed. The array was towed by a 4wd vehicle, which was switched off between shots. Additionally, the vehicle was rolled back slightly at each position to avoid transmission of noise from the vehicle to the geophone string along the tow cable. An 8 kg sledgehammer was used to provide an impulse source and an accelerometre on the hammer handle triggered data collection. Shots were recorded using the first 24 channels of a Geometrics Strataveiw 48 channel seismograph. They were then transferred to a laptop computer for processing using Surfseis software from Kansas Geological Survey. Recording time and sampling intervals varied between surveys. No filters were used and a variable number of shots were vertically stacked at each location. A table of acquisition parameters is included for each site in the relevant chapter.

Figure 3-3. Land streamer carrying 24 channel 4Hz geophone string. The streamer is towed by the vehicle in the photograph, which is switched off between moves.

3.2.3 Data Pre-processing

The data were preprocessed within the Surfseis setup and display utilities as described in the manual (KGS, 2003). Steps included

- Converting the data from SEG-2 to KGS format. This was done as a batch process for standard surveys. In addition, files to be used as part of a walkaway record were individually converted.
- Walkaway construction where necessary. Both fixed receiver (FRW) and fixed source walkaways (FSW) (Vincent et al., 2006) were used at various locations. Walkaway pairs were selected as shown in Figure 3-4.

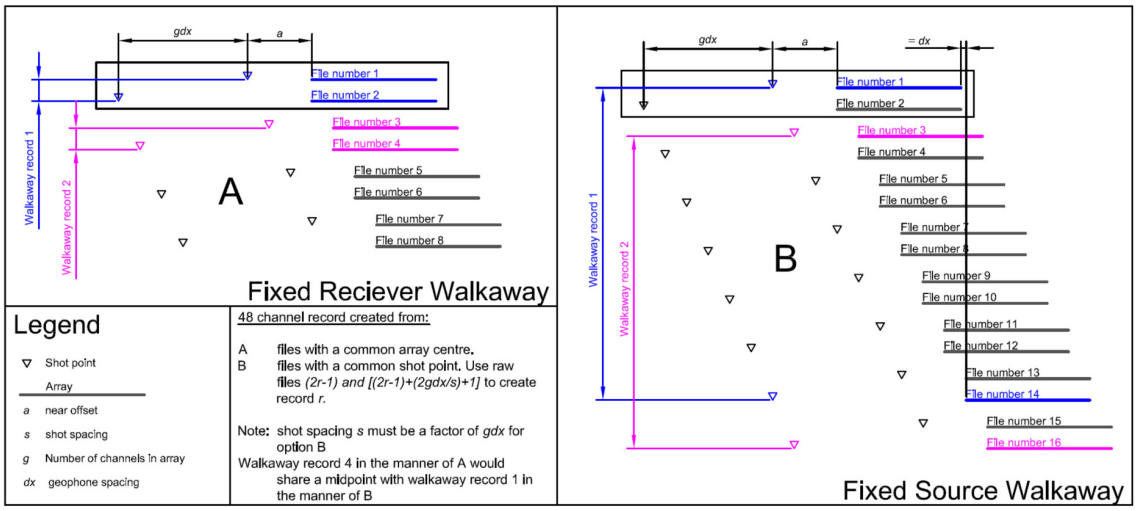

Figure 3-4. MASW survey configuration for walkaway construction.

- Application of field geometry to the converted files, based on field survey observer records of source and receiver locations. FRWs were assigned a field geometry with the source 'relocated' such that the '48 channel' array centre was located at the true array centre.

The following three steps are essentially preprocessing but were carried out record by record during the data analysis process, rather than batch processed prior to analysis, because of the variability between records.

- Swept frequency analysis to determine frequency ranges over which velocities are coherent and to determine velocities of body wave and higher mode contamination.
- F-K filtering to remove backscattered and/or body wave contamination.
- Muting of the first arrival to improve surface wave signal to noise ratio.

If large sections of a survey are expected to be internally laterally homogenous, steps 4, 5 and 6 can be batch processed prior to analysis.

3.2.4 Dispersion curve extraction

This stage of MASW includes the following steps.

1. Overtone analysis to determine the frequency and velocity ranges of surface waves and to examine the dispersion image for the presence of modes.
2. Where higher modes were observed existing alongside fundamental modes, modal separation before dispersion curve extraction using a combination of
   - F-K filtering if the modal velocity fields are not critically overlapping or
   - Offset-time domain muting of higher modes (Ivanov et al., 2005). Muting higher modes also mutes low frequency fundamental mode energy so this method requires separate extraction of low and high frequency dispersion and combination of the curves. Fundamental and higher modes propagating at slightly different velocities are more easily visually distinguished at far offsets, so this technique is more easily carried out on records with a greater number of channels (Figure 3-5). This is the main reason for the use of walkaways in this study.

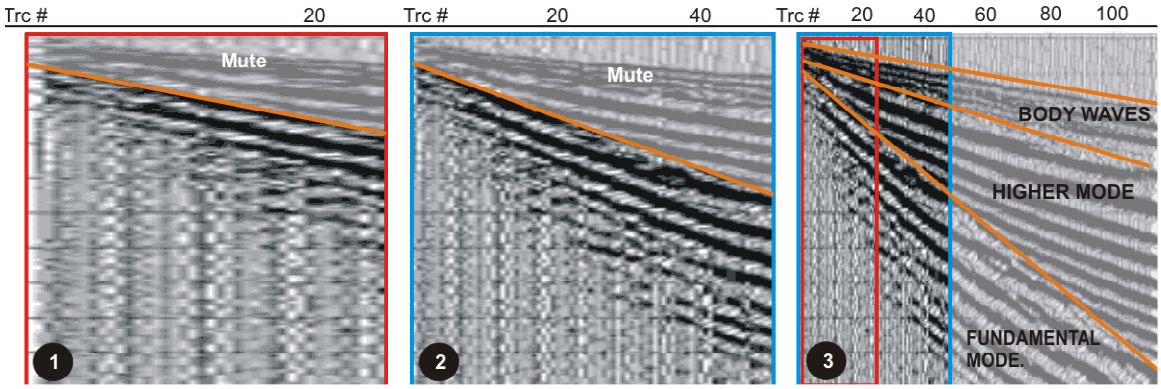

Figure 3-5. Relationship between ease of differentiation of fundamental and higher mode rayleigh waves and the length of the geophone string. The longer the array, the easier to visually identify higher mode and body waves. A short 24 channel array (1) shows very poorly the diverging velocities of fundamental and higher modes compared with a 120 channel array (3) at a similar near offset. A 48 channel array (2) collects significantly more fundamental mode energy, facilitating differentiation and muting.

3. Dispersion curve extraction from the overtone image. Fundamental mode surface wave velocities were picked by user guided automatic picking at 0.5 Hz point to point intervals over the full fundamental mode range present in the record, followed by manual editing of the picked curve.

Removal of higher modes was not always, or even often, possible, which typically limited the highest frequencies for which a dispersion curve could be picked and thus the near surface resolution (see Appendix A).

3.2.5 Surface wave inversion and contouring

Dispersion curves were batch inverted in Surfseis to generate a map of S-wave velocity with depth (Xia et al., 1999). The profile consists of interpolated soundings, each located in the middle of the receiver spread. Default initial models defined by Xia *et al.*'s algorithm were used as they generally converged to geologically acceptable models with an acceptable dispersion curve fit, typically 5-15%. The number of layers chosen was 10 for all models. The thickness of each layer varies based on the depth of investigation and the recorded bandwidth (see Appendix A).

Where significant topography was encountered during a survey, the velocity text file was imported into Surfer8 contouring software to allow topography to be incorporated in the contoured profile. This was done by first altering the text file in Excel to correct the depth to each layer relative to the surveyed elevation of the array centre. The Excel file was then gridded and contoured in Surfer8. Surfer produces rectangular maps so an extra 0 m/s layer was added at the surface elevation to highlight the topography and to prevent extrapolation of surface wave velocities into the air. Overall, this technique has the effect of shearing the 1D soundings but should produce a much closer fit with the real earth model than no correction at all (Figure 3-6).

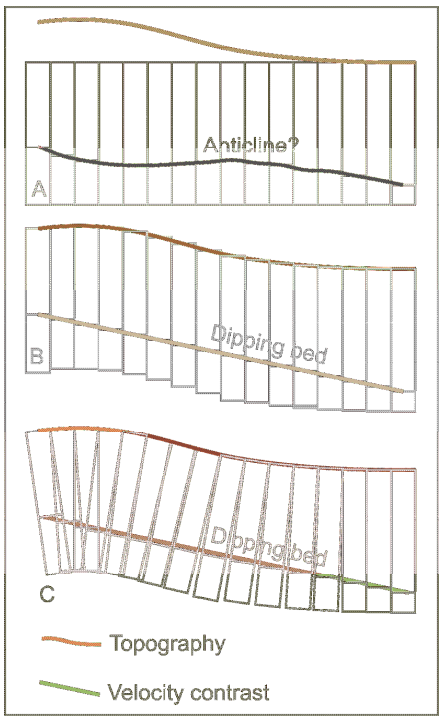

Figure 3-6: MASW profile map with velocity contrast (A) with no topographic correction and (B) with soundings sheared in Surfer8. Profile B compares favourably with the earth model (C) whilst profile A produces structurally misinterpretable artefacts.

3.3 Outcrop scale geotechnical and seismic investigations

3.3.1 Rock mass characterization

Standard scanline surveys, mainly consisting of fracture counts, were done along scanlines at all outcrops, whether hard or soft rock. Schmidt hammer testing was carried out at the Boby's Stream site only. In addition, a novel nail penetration technique was trialled at Boby's Stream for in-situ determination of rock strength for soft rocks. Description of the nail penetration test is reserved for the laboratory methodologies (Section 3.4.1).

3.3.2 Crosshole velocity measurements

Horizontal holes, 32 mm in diametre and ranging up to 0.7 m deep, were drilled in outcrops for the purposes of making crosshole velocity measurements. The holes were located so as to sample as closely as possible tectonic or stratigraphic units that were internally geotechnically homogenous. Each hole was drilled into the face and sleeved using 1 m lengths of 32 mm electrical conduit. Where possible the holes were drilled parallel with each other, but where the face had significant topography this was often not possible. In these cases the holes were drilled normal to the face and the orientation of the conduit sleeve was recorded in terms of trend and plunge. The location of the protruding ends of the conduits, was recorded relative to each other and to the site using EDM equipment, allowing the drill holes to be incorporated into a 3D model of the site and the source-receiver distance to be calculated.

Beginning at one end of the outcrop, a specially developed slide hammer (Figure 3-7) was inserted in one hole to provide a seismic source whilst a geophone was inserted in the adjacent hole. The slide hammer was set up as both source and trigger. For each hole-pair the source and receiver hole numbers, the depth of penetration of the slide hammer and the depth of the geophone were recorded. The slide hammer was operated both into and out of the face, twice in each direction, and the signals recorded using the equipment illustrated in Figure 3-8. Each measurement was recorded as a text file. These files were imported into a Microsoft Excel spreadsheet and signal voltage was graphed as a function of time. S-wave arrival times were picked visually and crosshole velocities computed using the calculated source-receiver distance.

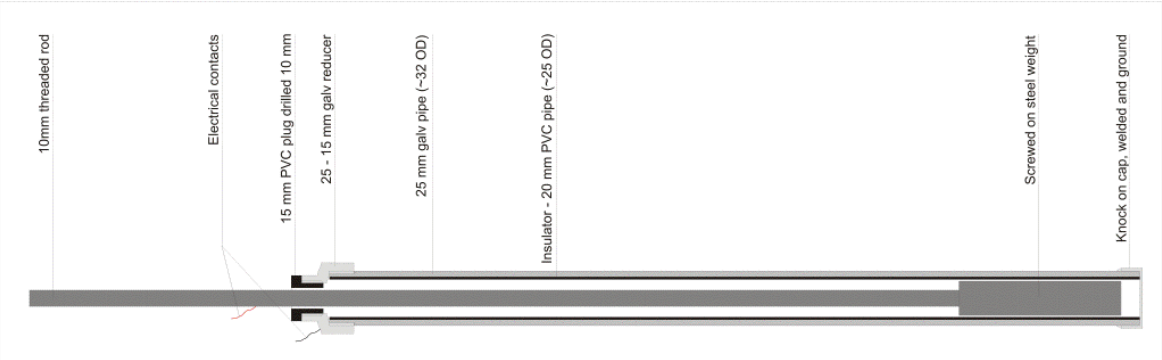

Figure 3-7: S-wave seismic source manufactured to fit 32 mm drill holes. The rod and steel weight of the slide are insulated from the casing along the entire length and contact is only possible at the two ends. By attaching a cable to both casing and slide, the impact of the weight is used to trigger data collection. Shear coupling is assumed to be concentrated at the knock on cap. The handle is insulated to prevent static transfer of a 0-5V 'signal' triggering data collection.

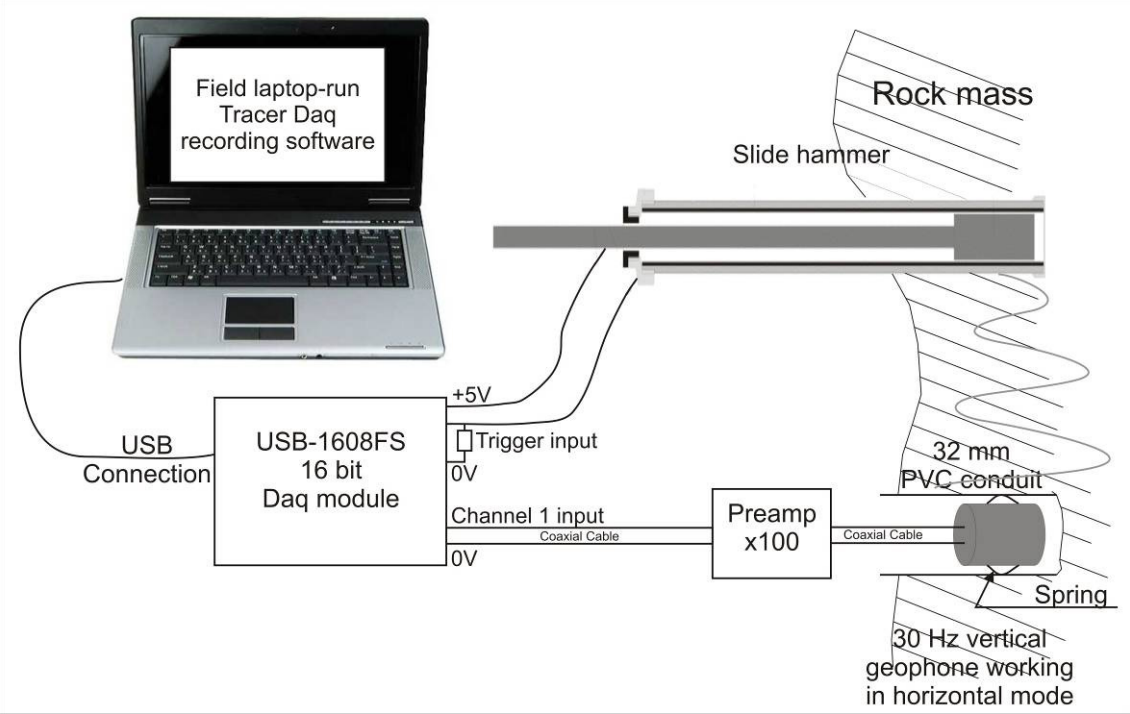

Figure 3-8: Horizontal crosshole velocity measurement equipment setup.

3.4 Laboratory scale geotechnical and seismic investigations

Field classification of tectonized rock masses is difficult and may be somewhat subjective. In order to soundly underpin any apparent correlations, a laboratory programme was undertaken to explore calibration of S-wave velocities to measurable rock properties. As no standard method is available for such a programme, development of the programme is important, both as a stand alone methodology and as a tool to ensure the success and validity of this study as a whole.

This study produced seismic data at core scale in the lab, drill-hole scale at the outcrop and survey line scale on the terraces and/or roads. A key objective is to undertake laboratory calibration and upscale the data to crosshole and survey scale. The upscaling process needs to account for any lack of weathering in lab samples and correct for scale-dependent apparent dispersion due to the different input signal wavelengths of core-scale and survey-scale work. Simple scaling techniques were developed site by site and are discussed in the relevant chapters.

3.4.1 Laboratory investigations

Laboratory experiments were carried out to investigate the effect of fracturing on S-wave velocity for relatively intact specimens and to relate the S-wave velocity to the physical properties of tectonized specimens. The 'intact' specimens were simply the largest blocks that could be found on site representative of each lithology. Where locally sourced large blocks from which core could be recovered were unavailable, the best alternative was used. Examples include use of a river boulder for Torlesse greywacke and use of a quarry block taken from further off the fault plane for Amuri and Weka Pass Limestone. At least three 50 mm diametre cylindrical core specimens were recovered from each specimen, preferably sampling in three mutually perpendicular directions, and the ends were ground square to the core axis. The specimens were then oven dried for at least 24 hours. The axial S-wave velocities of the intact cores were measured using the *GCTS Testing Systems* ULT-100 ultrasonic velocity measurement system. The full waveforms are recorded by CATS ultrasonics software and velocity is determined by pulse travel time. Coupling was improved using either superglue or petroleum jelly and the measurements were taken at increasing uniaxial stress. The three groups of measurements for each lithology were plotted together to look for evidence of S-wave splitting.

The individual cores were then incrementally 'fractured' (sawn) at regular intervals normal to the core axis and S-wave velocity was measured after introduction of each fracture with correction for length lost from the saw cut thickness (Figure 3-9). These velocities were all measured at a nominal axial stress determined from the initial testing to be the minimum required for coupling to be achieved. The thickness of the sawn disc was recorded to allow calculation of a running tally of fracture spacing as well as fracture density. Fractures were introduced until S-waves were completely attenuated.

Figure 3-9: Example of fractured greywacke core. Fractures were introduced from right to left. The core is numbered 1/9/1 using the system adopted for this study (sample 1/core 9/orientation 1).

Where possible, physical properties were determined using core, for which volume is simply calculated. In many instances however, such as for Torlesse Greywacke, even the best site samples were too internally fractured to yield any core at all. In this case irregular blocks, whose size was limited by the disaggregation of the sample along preexisting fractures, were sawn and their volume determined by the immersion method. Volume by this method is given by:

$$V = \frac{(M_{ssd} - M_{ss})}{\rho_w}$$

Equation 3-1

Where V is the volume in m^3, M_{ssd} is the surface dried saturated mass and M_{ss} is the submerged saturated mass, both in kg, and ρ_w is the density of water in kg/m^3. Density and porosity were determined for all specimens, whether core or irregular.

Uniaxial Compressive Strength (UCS) was determined for any cores not required for the fracturing experiment following the ISRM guidelines (ISRM, 1979). The ISRM requirement for 2:1 length to diametre ratio was prohibitive for the purpose of characterizing weak and/or tectonized rocks, which typically broke into short lengths during core drilling, so short cores were often used. Short cores are stronger than long cores for a given diametre so the measured UCS was corrected using the relationship proposed by Turk and Dearman (1986), which averages three very similar relationships (ASTM, 1980; Protodyakonov, 1969; Szlavin, 1974). To avoid unacceptable scatter of results, no core was tested with a length to diametre ratio > 1. This approach has been shown to keep all results within ±5% of values obtained using cores with L:D of 2:1 (Turk and Dearman, 1986).

Point load strength (Ghosh and Srivastava, 1991; ISRM, 1985) was determined for all irregular blocks. Where possible, S-wave velocity was also determined for these irregular

block samples, although it was noted that factors such as non-parallel faces and incomplete fit of the transducer on the contact face would probably lead to systematic errors in the data.

A late change to the laboratory and field program was the inclusion of hardness determination because of problems characterizing soft rock on the basis of fracturing. Hardness was measured for the Boby's Stream test site using both a Schmidt hammer and the nail penetration technique mentioned earlier. The latter was trialled with the objective of developing a field test, more reliable than the Schmidt hammer, that would be useful for low strength lithologies to bridge the range from soft to harder rock, and that could be readily correlated to a standard estimate of rock strength such as UCS. Indentation testing is already used to good effect to determine hardness in metals, alloys and even rocks (Szwedzicki, 1998) but the published standard testing procedure includes application of a standard indentor, specification of a standardized loading rate, criteria for test termination, specification for the properties of the cementing agent and application of continuous data logging (Brown, 1981).

These are difficult conditions to comply with whilst testing in-situ rock masses in inaccessible locations. Nail penetration testing was carried out in both laboratory and field using a Ramset nail gun, firing 220 green, .22 calibre x 0.825 low power cartridges and 75 mm nails. The gun was loaded and placed against the test surface to release the safety mechanism (Figure 3-10). The gun was fired and the nail's protrusion in mm was recorded and converted to a penetration figure.

3.5 Geomorphological investigations

Quantitative analysis of geomorphology is widely used to derive structural and tectonic data. Downcutting streams in an uplifting catchment reflect an interaction between variables that include climate, sediment load, tributary contributions, lithological variations and tectonics. River gradient, pattern, valley morphology and downcutting history are particularly sensitive to faulting and deformation within the floodplain (Local examples include Bull, 1996; Campbell et al., 2003; Litchfield et al., 2003; Nicol and Campbell, 2001). It follows that interpretation of the tectonic history of a landscape must be underpinned by an understanding of how tectonic perturbations act on a fluvial system, and how the tectonic signal can be separated from other factors. For complete coverage of

most tectonic geomorphologic concepts the interested reader is referred to Bull (2007), Bull (1991) and Burbank and Anderson (2001).

Figure 3-10: Ramset gun being fired at a Waikari Siltstone outcrop, Waipara River.

Detailed topographic surveys were carried out using a Trimble Geodimeter 5600 semi-robotic total station. Base stations were surveyed in as necessary to provide line-of-sight coverage and the positions of at least two stations per site were fixed using differential GPS. These peg locations, together with previous data where possible, were integrated with the survey data in Trimble's Terramodel 10.41 survey software. South Island contour shapefiles were clipped in ArcMap for the various study areas and the clipped files imported into Terramodel. The completed dataset was exported to AutoCAD in the New Zealand Map Grid coordinate system. Where survey data were sufficiently dense, localised small interval contour maps were generated in Surfer8 and exported to AutoCAD for incorporation in the site model.

As this study is primarily intended to prove the utility of MASW, 3D topographic profiles were created that showed lateral geomorphological variation in spatial context and could be easily correlated along-strike with 2D MASW profiles. Although 2D longitudinal profiles of river channels are presented, their spatial distortion made them of limited use in this study. Surveyed features include river thalwegs and topographic profiles. The latter included valley cross sections, fault scarp and terrace edge profiles, terrace surfaces and

straths, although not for all sites. As far as possible, profiles were surveyed approximately normal to the strike of the local structures. This strategy was to avoid incorporating complex non-tectonic gradients. In AutoCAD, the integrated survey data were georeferenced to the site orthophoto and used to render accurate maps of the geomorphic features of interest, A new coordinate system (the structural UCS) was defined in AutoCAD for each site, which placed the fault structure contours as close as possible to parallel with the Y axis. This allowed the surveys to be viewed orthographically from the top, front and side relative to the structure.

3.6 Correlation methods

Site layout factors such as topography, ground conditions and access generally constrained the location and orientation of the MASW survey lines. The lines thus varied between strike normal and variably oblique to the structure being investigated. In order to locate and define the extent of fault-zones using MASW and to spatially correlate the profiles with each other and with geomorphological and geotechnical data, the MASW profiles were interpreted in 3D using AutoCAD. The profiles were imported into the geomorphology drawing previously created from survey data and hung in a vertical plane from the geophysical lines defined by EDM surveying of their starts, ends and intermediate positions. These profiles could then be viewed along the structure contours using the structural UCS defined in 3.2. In order to enhance visual identification of changes in surface gradients the entire dataset was exported as an AutoCAD block and inserted into a new drawing with vertical exaggeration of up to x10.

4 CALIBRATION OF MASW TO THE SURFACE EXPRESSION AND ENGINEERING PROPERTIES OF FAULTED TORLESSE GREYWACKE AT DALETHORPE

4.1 Introduction

The presence of a significant upstream-facing fault scarp on a strand of the Springfield Fault at Dalethorpe, Canterbury (the SFD) has hazard implications for Canterbury as a whole and particularly for the nearby rangefront town of Springfield, 70 km west of Christchurch on State Highway 73 (Figure 4-1). The scarp strikes to the northeast across and displaces a flight of glaciofluvial terraces in the Upper Hawkins Basin, labelled from A to C with increasing elevation and age. Its along-strike projection passes almost directly under Springfield, some 7 km distant. In keeping with the basin's rangefront location the views from the displaced terraces are outstanding and the area would undoubtedly attract significant attention if the landowner were to subdivide. On initial inspection the fault-zone appears well defined with the fault only obscured for a short distance under the lowest terrace.

4.1.1 Scope and objectives

This chapter reports on the field and laboratory exercise to correlate laboratory, survey and outcrop scale S-wave velocity structure with the underlying rock-mass properties of the SFD and to relate these properties to detailed geomorphic indicators of faulting at this locality. A number of MASW surveys are used to locate and define the extent of the SFD, and to define within-zone variability. The S-wave velocities obtained from the surveys are compared and correlated with geotechnical and sonic/ultrasonic seismic data derived from outcrops and in the laboratory. The MASW surveys are also compared and correlated with detailed topographic surveying of ground deformation.

4.1.2 Previous work

The fault-zone of the SFD has been the subject of several unpublished previous investigations. Speight (1928) identified and mapped the fault. Evans (2000) investigated

the paleoseismicity of the SFD. A further review of his work is reserved for Chapter 5, but of relevance to this chapter is that he was unable to positively identify any additional faults in the area other than the Bell Hill Fault, for which good outcrop evidence was available (Figure 4-1).

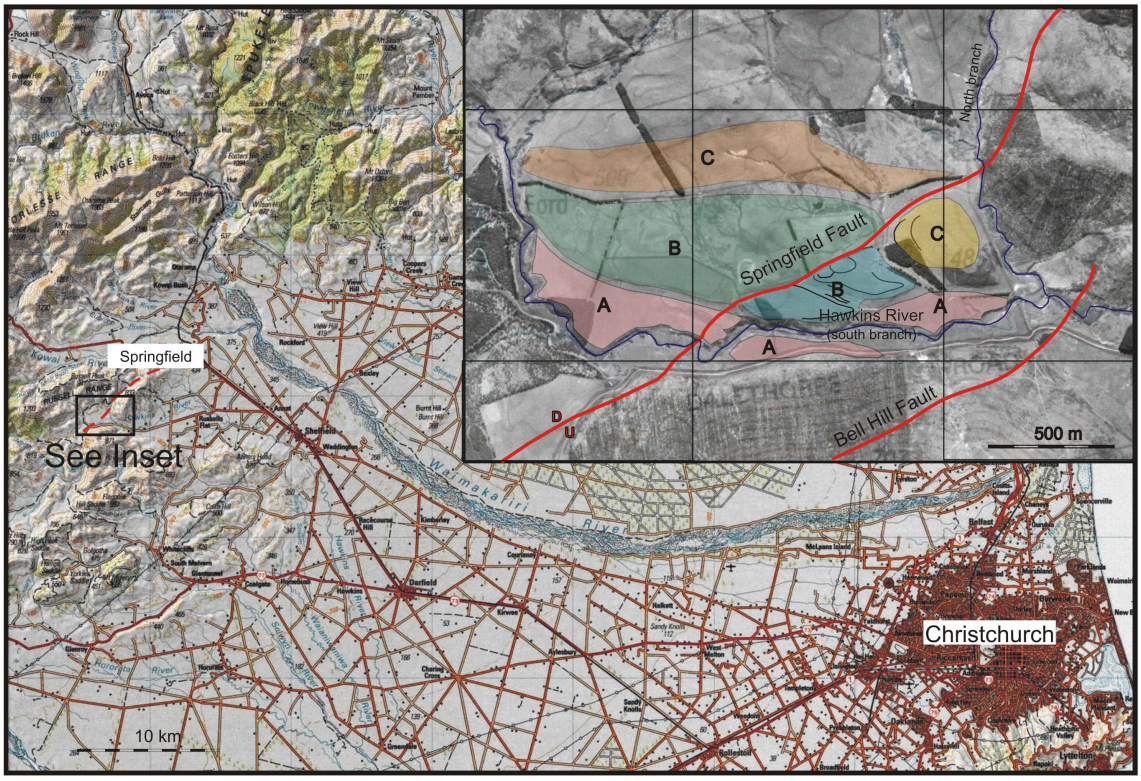

Figure 4-1 Location map for Dalethorpe study site with inset airphoto detail of the Upper Hawkins Basin. A, B and C refers to the flight of fluvial terraces. The mapped fault's surface trace is shown.

A field party from the Swiss Federal Institute of Technology (ETH) in Zurich carried out a seismic reflection survey at Dalethorpe. Limited processing of the survey revealed little of interest and the data were shelved (Green, 2004). Corboz (2004), also from ETH, used ground penetrating radar (GPR) and resistivity tomography (Figure 4-2) to survey the terrace above the projection of the Springfield Fault through Terrace A (Figure 4-1). The survey resolved three discrete shear zones in the overlying, visually undisturbed, gravels but does not resolve shears below the bedrock interface at ~5 m. Paleoseismic implications of the Corboz study are covered in Chapter 5. The easternmost of these shears is thought to outcrop just west (left) of outcrop D1 (Map 1, Figure 4-1) where heavily sheared Torlesse sandstones are exposed (see Figure 4-15). The size of the survey was, therefore, limited both in extent and in penetration by the use of GPR and covers only a fraction of the area covered in this study (See Figure 4-3).

4.1.3 Geomorphology and geology of study area

The SFD transects the Upper Hawkins Basin, which is surrounded by the bedrock hills of the Canterbury rangefront (Figure 4-1). The underfit Hawkins River ('the south branch') and minor tributaries feed the Upper Hawkins basin from the west and northwest, hugging the western and southern sides of the basin. A larger tributary (the 'north branch') flows southward into the basin along its eastern boundary. Only minor drainage is found in the central basin. The basin drains through a gap in its southeast corner, from whence the Hawkins River eventually joins the local baselevel of the Selwyn River, perched on the outwash terraces above the incised Waimakariri River. The south branch shows some interesting gross characteristics in the vicinity of the fault trace, most notably a series of northeast trending doglegs separated by eastward flowing reaches (Map 1 and inset-Figure 4-1).

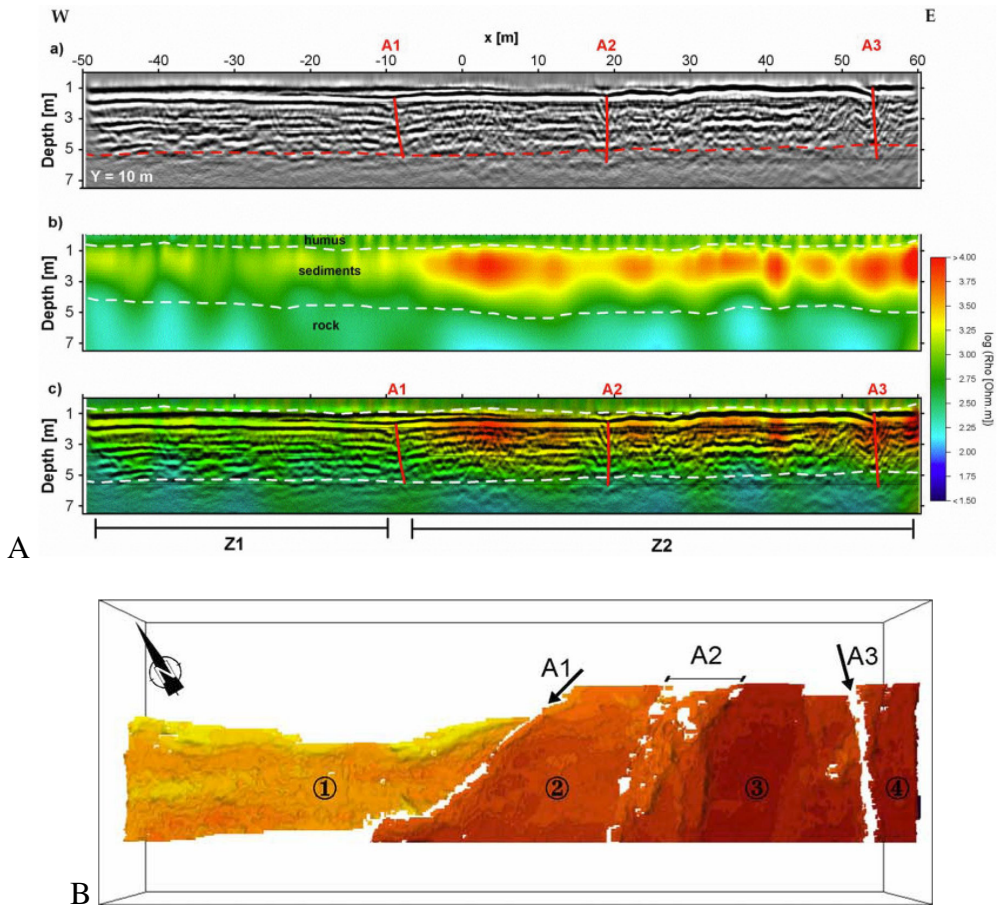

Figure 4-2: A) Integration and interpretation of GPR and resistivity tomography at Dalethorpe (Corboz, 2004). Corboz delineates boundaries between three subhorizontal units. High resistivity values to the east (Z2) correspond to dry sand and/or gravel seen above outcrop D1, whereas lower resistivities to the west (Z1) indicate higher water content (near the swamp) and/or silt/clay content. Bedrock is invoked to explain both the limited penetration of GPR and lower resistivity values at > ~5 m depth. B) 3D GPR 'cube' showing the time to a major GPR reflector. Shorter times are darker indicating uplift to the east.

A narrow deeply incised reach is located just downstream of the projection of the obvious fault trace. The bedrock geology of the area is dominated by the Rakaia subgroup of the Jurassic to Lower Cretaceous Torlesse Supergroup (Andrews et al., 1976). In this area the unit comprises the typical turbidite sequence of interbedded massive quartzofeldspathic sandstones and argillites. The beds are steeply inclined as is typical of Cantabrian Torlesse, and strike approximately north-northeast, subparallel to the strike of the SFD. An outlier of Cretaceous Broken River Coal Measures and View Hill Volcanics (Speight, 1928) is found in fault contact with Torlesse in the NE of the study area, but beyond providing evidence of faulting it is not significant in terms of this study. Clear bedrock exposure of the SFD is limited to a single outcrop in the south branch, where the river meanders across the fault and cuts in hard against the valley side. At this location the fault-zone comprises at least two sub-vertical foliated shear zones separated by intensely fractured zones that display low angle thrusts. These thrusts can be seen in several places to offset attenuated, boudinaged and folded argillites (Figure 4-15, section 4.3.3).

Above the river, particularly to the north, glacio-fluvial terraces comprising variable thicknesses of gravels on bedrock strath surfaces occupy the majority of the central basin. The terraces are labelled by decreasing age from C through A (Map 1 and inset Figure 4-1) and step down southward toward the modern south branch. The intersection of the fault with these terraces forms a fault scarp that increases in elevation and offset away from the modern river channel. Details of this geomorphology are discussed further in the next chapter. Most importantly for this chapter, the youngest and lowest of these terraces (Terrace A) does not have an apparent scarp, other than ponding due to impeded drainage that has created a swamp on the terrace tread above the outcrop of the fault in the south branch on terrace A, although the GPR shows shearing in the gravels. This terrace conceals the fault-zone that is evident both to the north and south and is the surface used for this chapter's geophysical investigations, to test the efficacy of the technique to define hidden fault-zones.

4.2 MASW profiles

4.2.1 Data collection

Seven MASW surveys were carried out across and approaching the SFD over a period between December 2006 and July 2007. The lines were run to investigate the previously-mapped fault and fold, the apparent lack of footwall deformation and to look for within-

fault-zone variability. Together they cover an interpretable area of approximately 42 hectares relative to the strike of the fault (Figure 4-3).

Lines 1 and 2 were acquired as a pilot trial in April 2006 by a class of graduate students and overlap across what was then considered to be the projection of the SFD through outcrop D1. Line 1, run on terrace A immediately north of the south branch of the Hawkins River, approaches and crosses the SFD from the footwall side. It intersects the projection of a major shear zone that outcrops in the river bed (outcrop D1 – see section 4.3.3.1 Crosshole velocity testing) and is roughly aligned with the projection of the fault trace. Line 2, run along the Dalethorpe road (a metalled single lane farm road on the south side of the river), approaches the SFD from the hanging wall oblique to Line 1, and ends 145 m away.

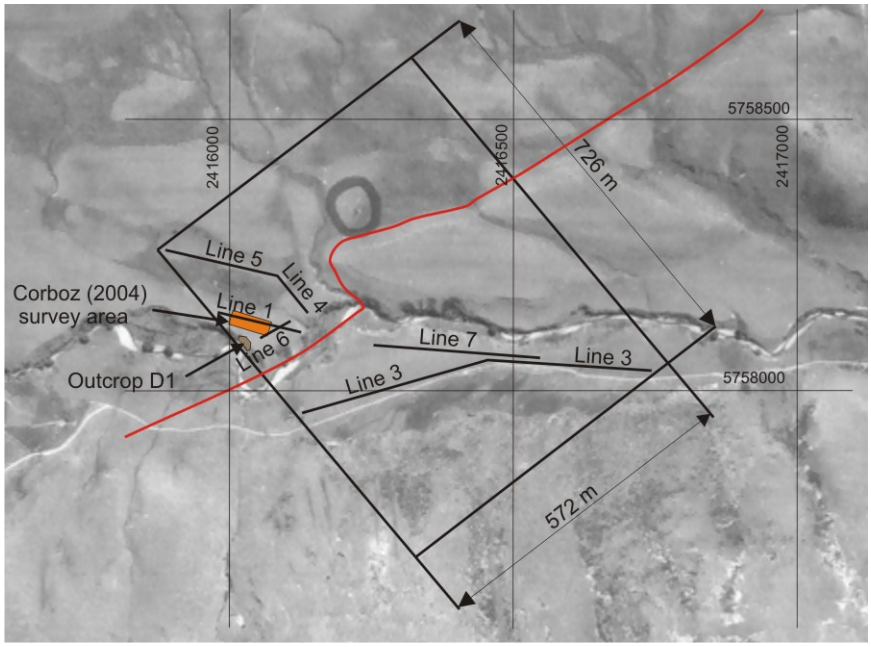

Figure 4-3: The Dalethorpe surveys covered an area of 726 m by 572 m relative to the strike of the fault. The western end of Line 3 (labelled twice) overran and replaced Line 2. The outside of the meander in the river bend at the SW end of line 6 exposes a shear zone (outcrop D1). No obvious scarp is developed in the terrace crossed by the lines. The orange square indicates the area surveyed by Corboz (2004) using GPR.

Lines 3-6 were surveyed in December 2006. Line 3 was run from east to west. Almost 700 m long, it took less than 6 hours to survey. It replicates line 2 and extends it further east along the Dalethorpe road into the hanging wall to look for evidence of folding and/or faulting. Lines 4, 5 and 6 were acquired with a further 8 hours work in the vicinity of line 1 on a grassy, sometimes boggy or tussocky, surface comprising predominantly Holocene fluvial gravel with little soil development. The terrace is mapped as being underlain by Torlesse greywacke bedrock, but this is uncertain because of the possibility

of Cretaceous outliers in the footwall. Surface waves behave unpredictably where the topography is of a shorter scale length than the far offset so these lines were surveyed with shorter near offsets in order to survey as close to the bounding terrace risers as possible without needing to change the source position mid-survey. Lines 4 and 6 for instance, though relatively short, closely approach the terrace boundary at both ends. Line 4 was run from SE to NW, orthogonal to the strike of the fault trace so as to sample normal to the fractures. At the NW end of Line 4 the streamer was rotated around its centre point to form the start of Line 5, which continues westward parallel with the terrace edge and with line 1. Line 6 was sited to investigate within-zone variability in S-wave velocity and was run parallel to the strike of the fault from NE to SW at right angles to line 4, finishing directly above the shear zone outcrop.

The final line, line 7, was surveyed from east to west on a windy day in July 2007. Although inconvenient, the wind provided an opportunity to assess the utility in common Canterbury conditions. The wind was westerly, gusting to 55 km/h, and blew strongly around and through the steel geophone sleds. The line was run on terrace A on the south side of the river, beginning parallel to and 8 m north of line 3 and then diverging from it. Whereas line 3 had followed the bend in the road, line 7 ran due west in a straight line. This line had multiple objectives. Firstly, it was run to investigate whether the near surface high velocities seen in Line 3 were influenced by the coincident change in direction of the line. Essentially, was there directionality in the velocities due to factors such as a preferred fracture orientation? Secondly, processing the earlier lines had highlighted the difficulty in separating the fundamental mode when surveying with a short geophone string (see section on Dispersion Curve Extraction). Line 7 provided an opportunity to experiment with larger near offsets whilst also acquiring walkaway records. Two shot points, one at 12 m and one at 36 m, were used at each array position. This yielded four separate datasets including fixed receiver (FRW) and fixed source (FSW) walkaways. Line 7 also forms the basis of an assessment of the repeatability of the technique.

All surveys were acquired following the roll along methodology outlined in Chapter 3. No site calibration was carried out and the near-offset was the primary parameter that varied between surveys (Table 4-1). Cultural noise was limited to mostly-distant livestock movement and the main environmental noise source was wind.

4.2.2 Dispersion curve extraction

The seismic records were preprocessed, walkaway records were constructed and dispersion curves were extracted following the methodology outlined in Chapter 3. Received bandwidths varied widely but were typically between 10 and 50 Hz. Within this range, coherent dispersion in some cases covered ranges of only 10 Hz. Although coherence was typically low, the surface wave energy generally dominated the records (Figure 4-4). The quality, dispersiveness and phase velocity of the seismic records were variable but often noticeably systematic. For example, dispersion curves evaluated from records acquired at the eastern end of line 3 were typically moderately dispersive and displayed low phase velocities and a high signal to noise ratio. These records were collected in the distal hanging wall relative to the mapped fault.

Table 4-1. Acquisition parameters for Dalethorpe MASW surveys.

Survey line	1	2	3	4	5	6	7a	7b	7c	7d
Acquisition	24 ch	24 ch	24 ch	24 ch	24 ch	24 ch	24 ch	24 ch	48 ch	48 ch
Walkaway construction	None	None	None	None	None	None	None	None	FSW	FRW
Aperture/ Array dimension (D)	23 m	23 m	23 m	23 m	23 m	23 m	23 m	23 m	47 m	’47 m’
Near offset (x1)	8 m	8 m	12 m	10	10	10	12 m	36 m	12 m	12 m
Shot spacing	5 dx (5 m)	5 dx (5 m)	4 dx (4 m)	4 dx (4 m)	4 dx (4 m)	4 dx (4 m)	4 dx (4 m)	4 dx (4 m)	4 dx (4 m)	4 dx (4 m)
Sampling interval (ms)	0.25	0.25	0.5	0.5	0.5	0.5	1.0	1.0	1.0	1.0
Recording time (ms)	1500 ms	1500	1000	1000	1000	1000	1000	1000	1000	1000
Number of records	59	41	157	21	48	13	81	81	81	81
Survey length	295	205	624	84	192	52	324	324	324	324

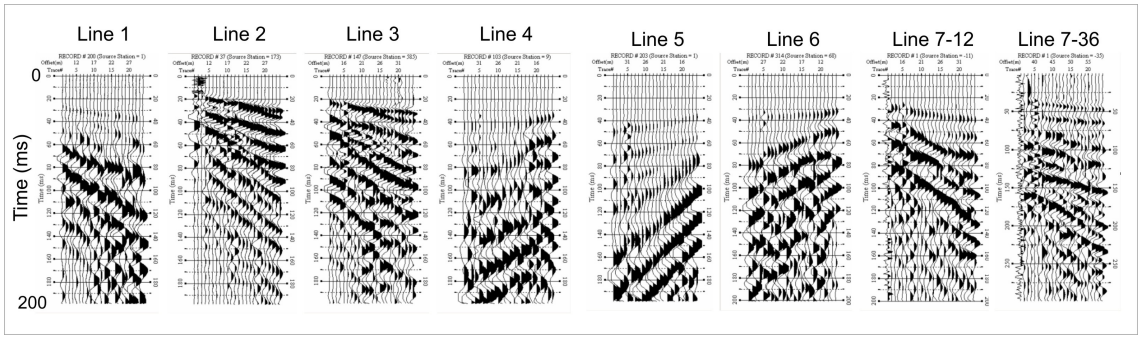

Figure 4-4. Examples of records from each survey line. Surface wave energy is dominant in all records but records are adversely affected by wavefield scattering. This is particularly noticeable for line 4.

An abrupt change in record character occurred at shot records 70+ (Dispersion curves 170+, Figure 4-5), which were acquired in closer proximity to the mapped fault. These records proved to be strongly dispersive but had poor signal to noise ratio. They displayed higher phase velocities, greater wavefield scattering and reduced coherence together with

a change in recorded surface wave bandwidth. They also ubiquitously exhibited a bimodal amplitude spectra with a second peak at frequencies of 80-120Hz that was absent from the lower phase velocity records. Noise and scatter in these fault-proximal records often took the form of surface wave diffractions, amplitude attenuation at some frequencies or within-record backscatter. Backscatter occurs where surface waves propagate after reflection off a velocity contrast. This results in reverse dipping events in the shot gathers, which together with other noise suggests significant lateral velocity variations.

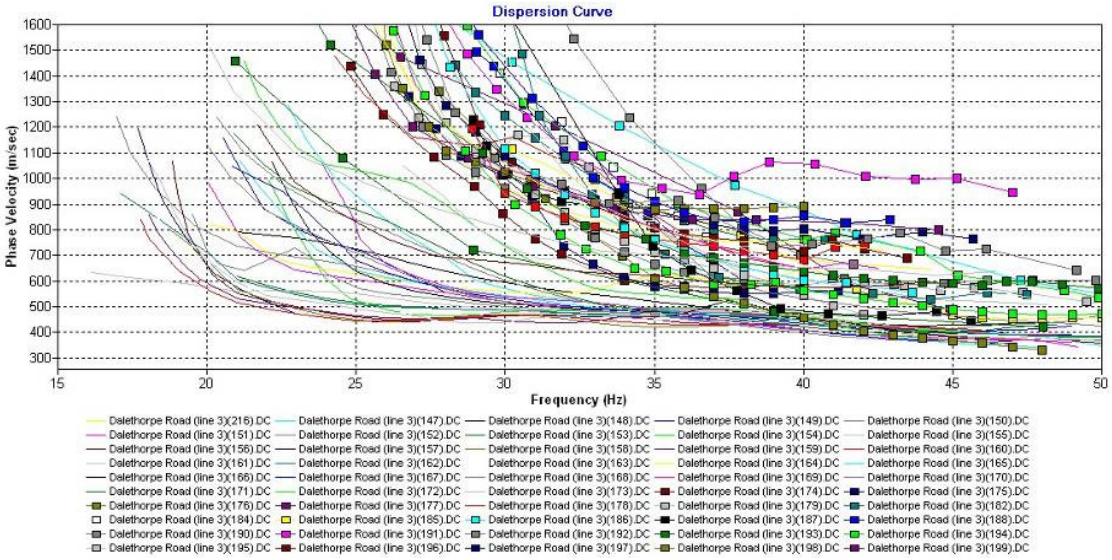

Figure 4-5. Contiguous dispersion curves taken from the centre of line 3. A noticeable shift in dispersion occurs at record numbers greater than 170. Some of the lower frequency Rayleigh wave phase velocities are excessive suggesting body wave contamination of the records. Dalethorpe data were the first to be processed during the course of this study and techniques mentioned in Chapter 3 were subsequently adopted to deal with this problem.

A further record character change occurred over the final 100 m of the line. This was marked by a second shift in the average position of the dispersion curve. The SNR improved and the curves flattened out to become only slightly dispersive. This character was then maintained for the remainder of the line.

Line 7 was also acquired on the hanging wall. Most notable in processing the Line 7 records were the relative ease of processing 24 channel and corresponding 48 channel walkaway records. Modal separation was difficult on the 12 m offset records and un-remediated higher mode contamination led to further difficulties with processing and exaggerated phase velocities on the dispersion curves. The 36 m offset records proved useless as a standalone dataset but were invaluable for modal separation using walkaway records. Both FRWs and FSWs were constructed, with the latter proving to be the better option for this site (Figure 4-6). The FRW records were badly affected by repetition of systematic noise and probably also by static errors introduced by walkaway construction

(see Appendix A). The FSW records, however, facilitated modal separation and provided a stable result. Line 7 followed a very similar progression of record and dispersion characteristics to Line 3.

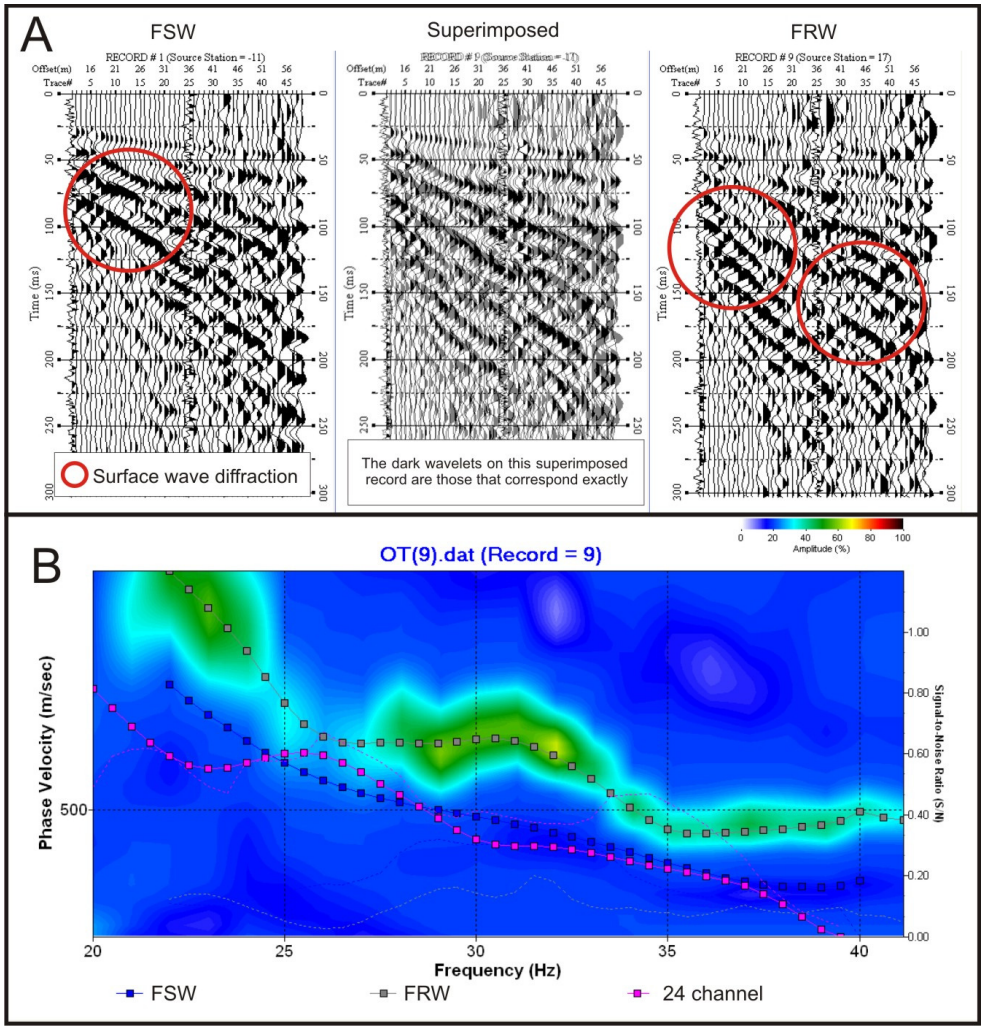

Figure 4-6. A) Comparison of fixed source and fixed receiver walkaway records centred over the same point in the subsurface. Using FRWs is shown to result in repetition of systematic noise, particularly obvious for diffractions. B) Direct comparison of dispersion curves generated using a 24 channel records with both types of 48 channel walkaway records. The 24 channel dispersion curve is generated using the first half of the FRW. The higher mode jump seen in the 24 channel curve is not present in the FSW curve, because the modes were more effectively separable at far offsets. The FRW curve, however, exacerbates the modal jump. Phase velocity differences between the 24 and FSW curves are probably due to bulk averaging over a longer distance that includes higher velocity material outside the 24 channel record.

The third hanging wall line, Line 4, overran the projection of the sheared outcrop in the river, and it predictably produced the least coherent records. Even the best records were significantly backscattered (Figure 4-7) and dispersion curves were difficult to extract with poor signal to noise ratio. They generally displayed relatively high phase velocities, but were extremely variable. The fault parallel survey Line 6 was similar in most respects to Line 4.

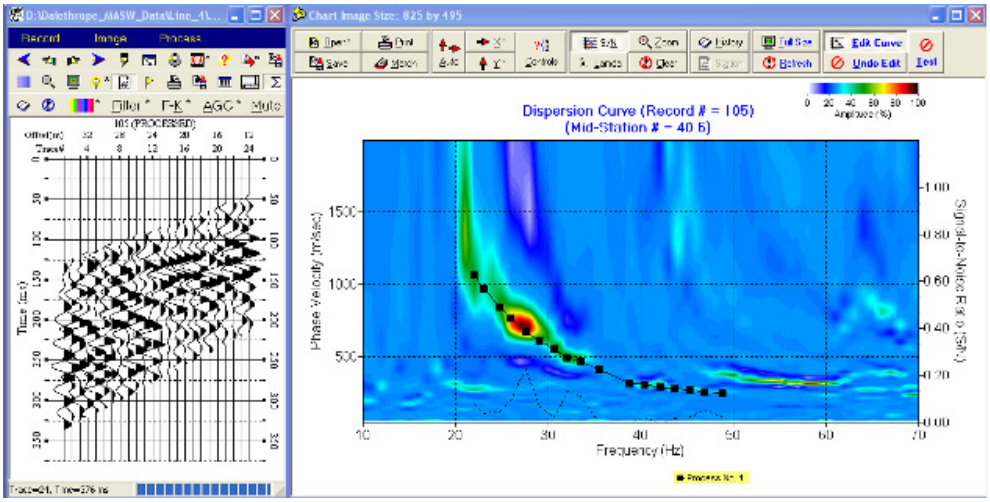

Figure 4-7. Example record and dispersion curve from Line 4. Note strong backscattered events across traces 1-4 and 7-12.

Lines 1 and 5 were dominantly on the footwall of the mapped fault. Their records were typically moderately dispersive and only weakly coherent (Figure 4-8).

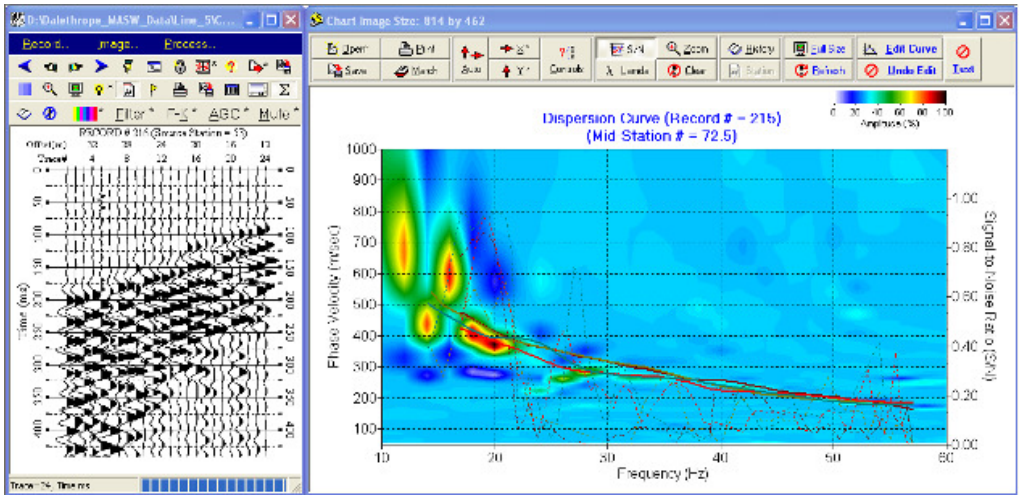

Figure 4-8. Line 5 was typically weakly coherent and moderately dispersive.

4.2.3 2D S-wave velocity sections

For each survey line, the dispersion curves were inverted and 2D S-wave velocity sections were produced. As depth of investigation is a function of the longest wavelength (Appendix A), variability in bandwidth caused variability in the depth of Vs profiles. Results are presented first for the initial surveys (Lines 1, 3 4, 5 and 6, Figure 4-9) and then for the subsequent survey (Line 7, Figure 4-10).

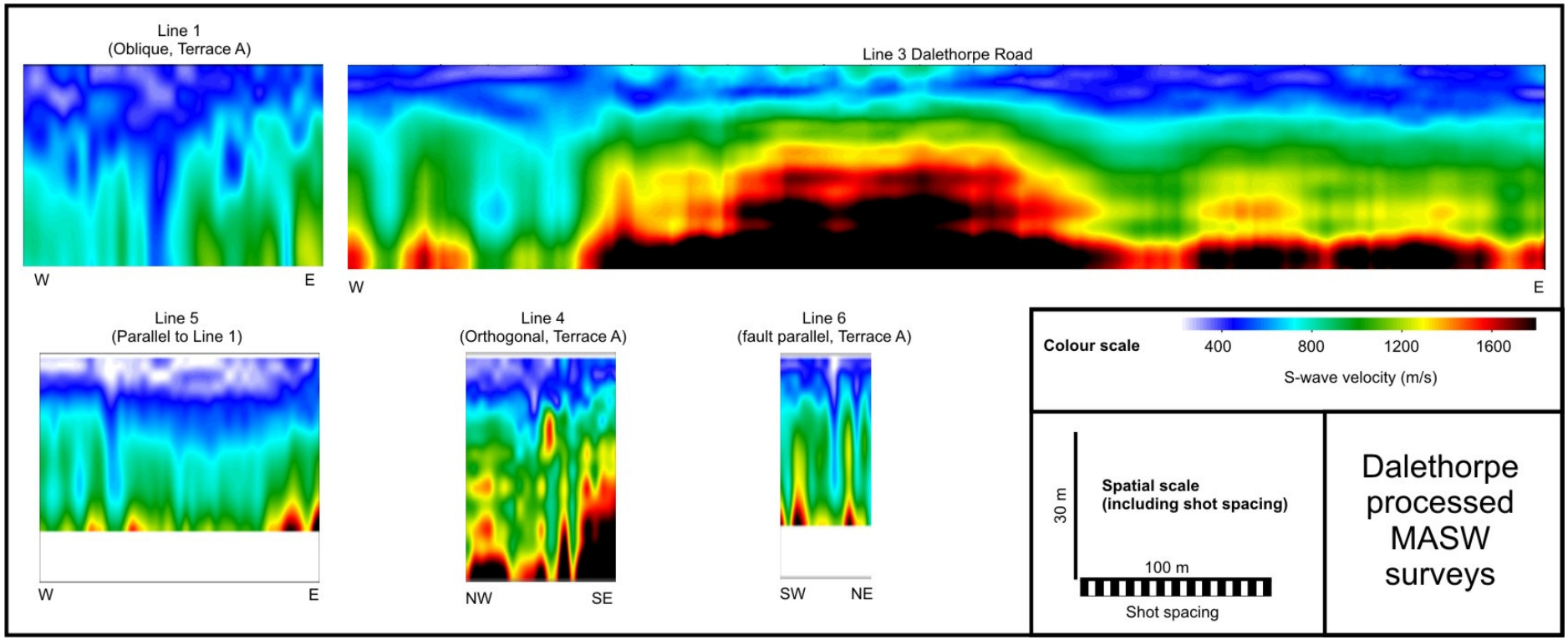

Figure 4-9. Same scale S-wave velocity profiles for all but line 7. 1D inversions contoured to produce these images are spaced at the shot spacing indicated on the scale bar.

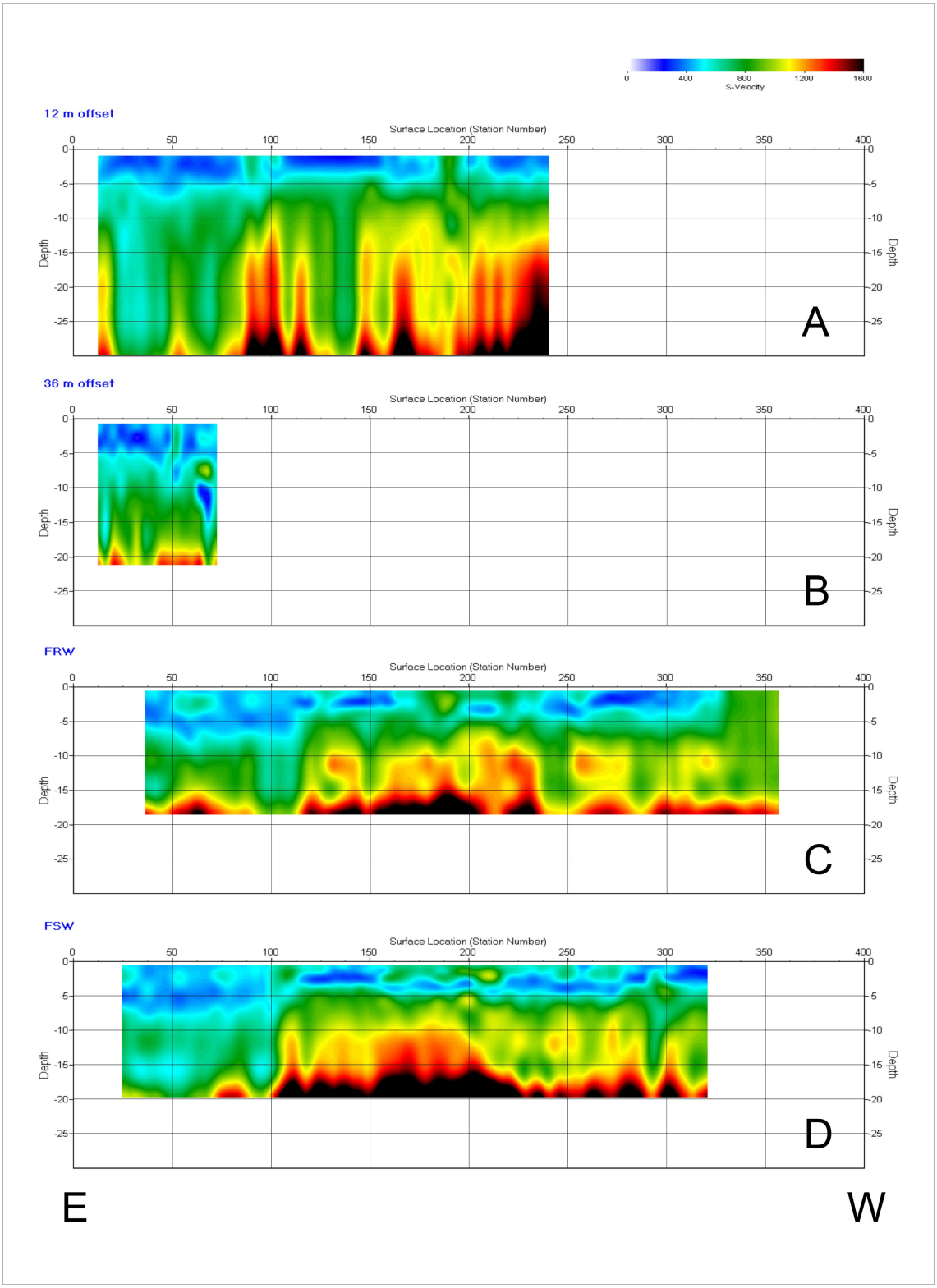

Figure 4-10. Comparison of results over the same ground using different survey parameters and walkaway constructions. A) 12 m offset 24 channel. B) 36 m offset 24 channel. C) Fixed receiver walkaway. D) Fixed source walkaway. Shot/inversion spacing is 5 stations.

The transition from cover material into completely weathered Torlesse can be inferred at S-wave velocities of around 500 m/s (Perrin, 2008 #260 Perrin). Weathering in this case refers to the processes of in ground alteration due to fluid migration through fractured

rocks. In the sections presented here this boundary typically occurs at slightly less than 5 m depth, which agrees with observations on site and with the geophysical interpretations of Corboz (Corboz, 2004). Velocities in excess of 1200 m/s or 1300 m/s, however, are unlikely in the upper 100 m of Torlesse greywacke (Buch, 2008; Perrin, 2008, pers. comm) (Table 4-2). This suggests that some of the MASW data presented here are contaminated with body waves. This problem generally only exaggerates the lower frequencies and hence the velocities close to and within the halfspace. Dispersion curves with low frequency Rayleigh wave phase velocities higher than the expected S-wave velocity, such as are seen in Figure 4-5, are almost certainly contaminated by body waves.

Table 4-2. Torlesse greywacke data, presenting shallow surface S-wave velocities for Torlesse argillites and sandstones for different degrees of weathering/fracturing, after (Perrin, 2008, pers. comm).

Torlesse argillites and sandstones (shallow surface S-wave velocities, upper 100 m)	
Degree of weathering	**S-wave velocity v_s**
***CW* (completely weathered)**	500-550 m/s
***HW* (highly weathered)**	550-750 m/s
***MW* (moderately weathered)**	750-1000 m/s
***SW-UW* (slightly to unweathered)**	1000-1200 m/s

Notwithstanding the high velocities in the halfspace, the velocity gradient at depths >5 m vary significantly across the site even though the entire survey area is underlain by Torlesse greywacke. This can be caused by spatial variations in either one or a combination of weathering, effective stress, pore space and fracturing (Fumal, 1978). On a site such as this a combined effect is most probable.

Above the high and mid velocity strata interpreted as bedrock is a low velocity layer extending from the surface to depths of 5 m. The velocity in this layer is typically higher in line 3 than in line 7, probably due to running line 3 on a well-used metalled road. These low velocities are interpreted as being the weathered greywacke gravels that are immediately encountered when attempting to auger the soil profile on terrace A. No loess profile was encountered (Phil Tonkin, 2007 pers comm.). Mid-velocities are notable at the surface in both of lines 3 (Figure 4-9) and 7 (Figure 4-10D), and these relate to an area of the terrace surface littered with boulders, that are probably the products of mass wasting of the hill to the south.

4.3 MASW correlations

The inverted MASW profiles were correlated with each other and with geomorphological, geotechnical and smaller scale seismic data. This section outlines the results of those correlations.

4.3.1 Geomorphology

A wealth of surveyed topographic profiles has been amassed at Dalethorpe, both during this study and by Evans (2000) and their locations are shown in Figure 4-11. This section details the strong and often surprising correlations that were observed throughout this study area between these profiles and the 2D MASW profiles. Correlations were made using a structural UCS defined by structure contours on the mapped fault. The contours align with the repeated doglegs in the river.

4.3.1.1 General correlations

A site-wide along-strike correlation of the MASW profiles with topographic profiles is presented that agrees strongly with much of the structure predicted by field and structure contour mapping of the fault trace and associated geomorphology (Figure 4-12). Additional structures can, however, be identified. The structure of the fault-zone will be covered in detail in Chapter 5, but several points relating to structural interpretation of depth to bedrock on the S-wave velocity profiles must be made here. The approximate strath profile is drawn in assuming a transition into completely weathered Torlesse at 500 m/s (Section 4.2.3, Table 4-2). Much of this surface would originally have been a continuous, evenly graded bedrock strath below the A surface. The uplift rates make it improbable that any ancestral channels exist below the visible strath.

The velocity-based depth to the strath is indeed relatively flat across a great deal of the site, at an average depth of about 5 m, but several significant departures can be seen. Three areas of deep low velocity can be seen below the strath and are interpreted as fault damage zones (Figure 4-12). The central damage zone is located in the hanging wall of the main mapped thrust. Although the surveys could not cover the projection of the mapped fault through the dogleg in the river, the width of the damage zone appears to be greater in the hanging wall.

Figure 4-11: Location of topographic profiles and their relationship to MASW profiles. Image rotated 51˚ to place fault strike (051) in 'N-S' orientation. Topographic profiles 1-24 after Evans (2000). This figure is formatted to fold out for ease of reference whilst reading this chapter and Chapter 5.

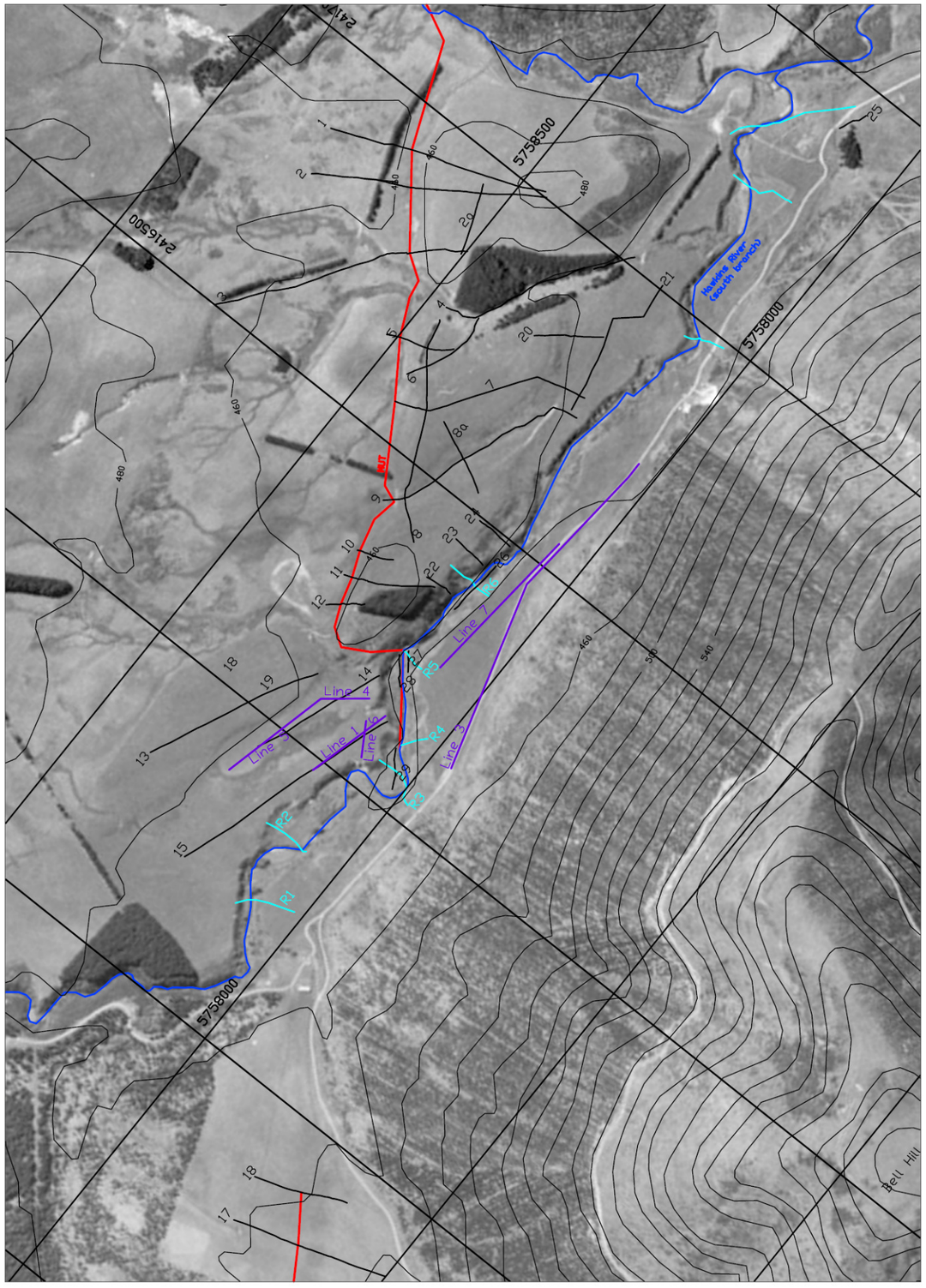

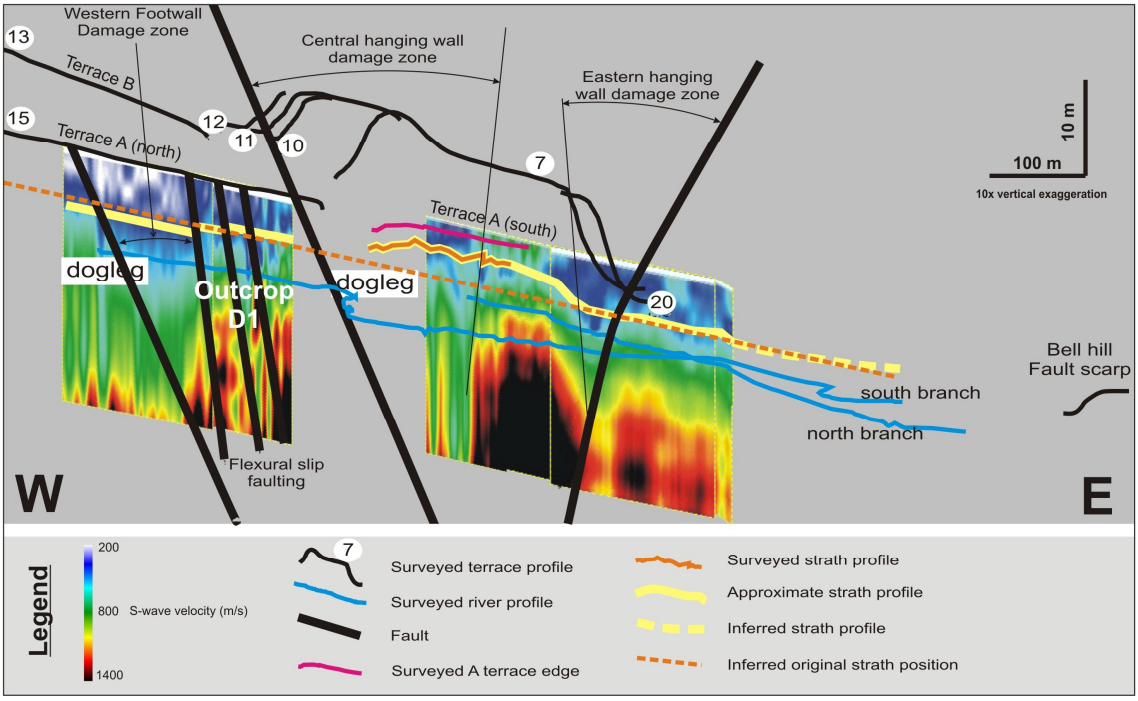

Figure 4-12: A northeast facing across site correlation of the MASW profiles with detailed geomorphological surveys and structural interpretations. Significant detail is evident here of shear wave velocity variability within the wider fault zone that can be closely correlated with individual shears and secondary faulting or off-plane deformation. Features to note include the upwarped surface of Terrace B(13) along the fault scarp profiles (7, 10-12), lesser warping of the younger Terrace A strath and subtle gradient changes in the modern river bed coinciding with the high velocity s-wave zone of differentially uplifted bedrock. These features are indicative of persistent deformation for 300-400metres east of the obvious scarp. The shear zone extends well into the footwall. Note: Fault dips exaggerated by 10x VE. Also, a regional gradient to the NE affects precise superimposition of corresponding surfaces.

The western footwall damage zone underlies much of MASW line 5, between eastings 2415918 and 2416059 (Map 1). It is of similar width, depth and velocity to the mapped fault's (central) damage zone, suggesting that the causative faults are of a similar scale. It is interpreted as being related to a previously unmapped imbricate thrust in the footwall of the main mapped fault. Assuming the imbrication damage to be similarly concentrated in the hanging wall, the projection of that thrust passes through the dogleg west of outcrop D1, beyond which there is a steady rise in velocity. There is no other geomorphic expression. Although the fault was not previously mapped the river dogleg would certainly suggest a mapped-fault-parallel structure at that location.

The eastern damage zone indicated in Figure 4-12, however, is unlikely to have been noticed without MASW. It lies some 290 m southeast of the previously mapped fault scarp. The major westward shift in the dispersion curves in lines 3 and 7 (Figure 4-5), towards higher phase velocity for a given frequency, occurs at this location. This shift is modelled in the inverted profiles as a large and sudden eastward reduction in velocity or

depth to bedrock. The beginning of the velocity reduction correlates with a knick-point in the thalweg profiles of both the north and south branches of the river. The step is more obvious in the north branch, which is a smaller 1st order stream and where it can be measured at 0.72 m in height. Once again assuming the damage to be concentrated in the hanging wall, a fault is mapped here passing through the base of the terrace riser, and through the river just downstream of the knickpoint. The central and eastern damage zones bound a zone of elevated velocity where the surveyed location of the strath correlates closely with the interpreted depth and both indicate that the strath is clearly warped up by ~2.5 m.

The eastern damage zone is mapped as a major downstream facing thrust fault (termed the Main Downstream Thrust – MDT) based on the sense of motion indicated by the strath warping. The fault is not visible in outcrop, but its presence has a strong effect on the local geomorphological development. The location of the fault on MASW line 7 coincides exactly with the location at which the array crossed a small structurally-controlled gulley. The gulley approaches the survey line from the road, intersects the line and disappears into the river. The MASW inferred damage zone and the gulley are correlated along strike with a matching gulley on the opposite side of the river and with the southeastern B – A terrace riser, which is significantly higher than the same terrace riser upstream on the footwall side of the previously mapped fault (see profiles 7 and 20, Figure 4-12, Figure 4-13). On this basis, the terrace riser is remapped as a fault-controlled scarp, modified by river erosion during synchronous deformation and downcutting of the river from terrace B-A as the river flowed diagonally across the valley floor to the northeast. The nature of the processes operating here are discussed more fully in the next chapter.

In addition to low velocities below the inferred original strath position, up-warping of the strath can be observed between the central and eastern damage zones.

4.3.1.2 Detailed correlations

A particular surprise was the correlation observed between lines 3 and 7 and detailed topographic surveys. This correlation supports the identification of at least 2 and possibly a third previously unmapped faults in addition to the MDT, none of which display any immediately obvious surface displacement. Figure 4-13 shows the location of the mapped fault (Evans, 2000) (northwestern-most fault Figure 4-13 A) and the locations of the four newly mapped faults including the MDT. The new faults are numbered on the elevation

view (Figure 4-13B) from 1-3, northwest to southeast. Fault 1 shows up as a deep velocity low in the MASW profile, which correlates closely with a deep pool in the riverbed. It also correlates with an eastward step up in the strath profile. This indication of upthrow to the southeast is confirmed by the river profile. East of this fault the river grades to a higher upstream level than the upstream reach of the river, confirming that the fault is upthrown to the east. This fault is visible in river bank outcrop but its sense is not obvious.

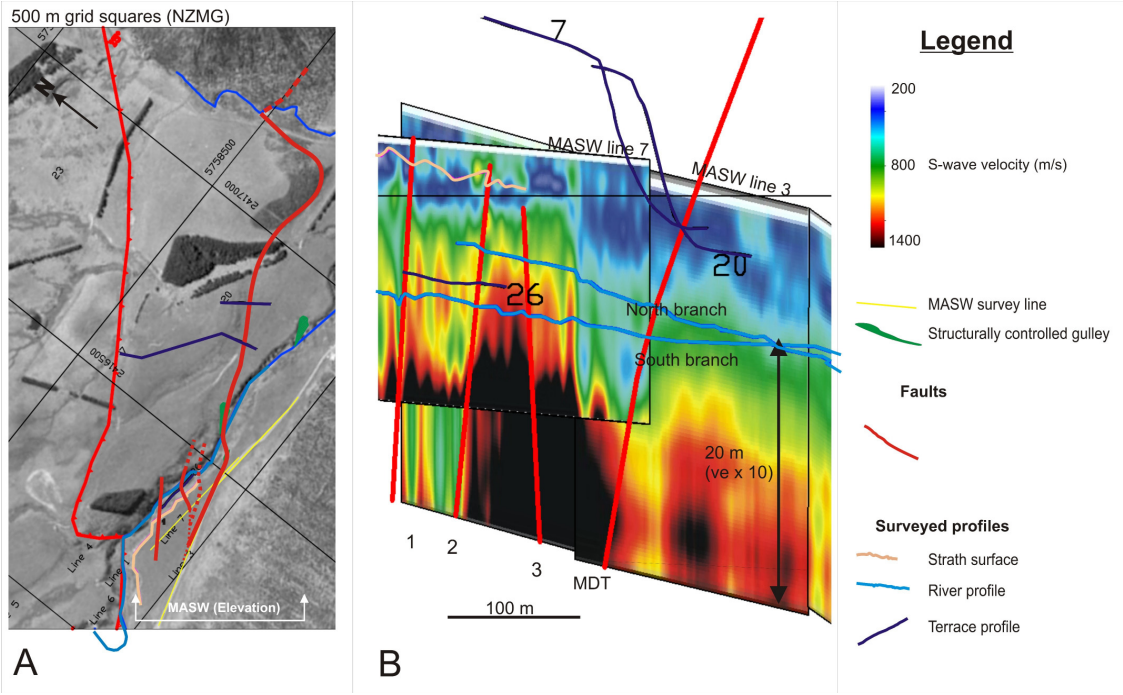

Figure 4-13. Detailed map (A) and MASW pseudo-section view of lines 1 and 3 (B) in the central part of the Dalethorpe structure showing newly mapped faults. For discussion see text.

This fault also correlates with an embayment in the terrace edge on the south side of the river. Fault 2 is picked out by a significant eastward velocity increase that correlates closely with an eastward flattening of the river profile observed in both the north and south branches of the river. Again, this suggests up-throw to the southeast. This is borne out by a correlative up-warping of about 0.5 m in a very young inner terrace profile (profile 26, Figure 4-13), and an eastward step up in the strath profile. The inner terrace appears to be an isolated degradational feature coinciding with this uplifted reach. A northwestward dipping shear zone is visible in outcrop on the north side of the river, but again its sense is unclear.

Identification of the third fault is rather more tenuous. The fault is inferred based on an eastward velocity reduction that correlates with a knickpoint in the river profile. Although not mapped as such here, there is some suggestion of a similar structure approximately

20 m further west. Neither structure is visible in outcrop but outcrop is typically scarce and highly degraded in this section.

The high velocities recorded above the strath surface in Figure 4-13B are probably related to a bouldery deposit, which litters the present terrace surface at this location only. These relatively intact and unweathered boulders have higher velocities than the underlying weathered and fractured bedrock strath.

4.3.2 Line to line correlations

A significant question to address when first applying a technique such as this is repeatability. Can a survey be repeated with confidence? The proximity and orientation of line 3 relative to line 7 facilitated a simple investigation of the repeatability of the technique (Figure 4-14). The lines were run on different days with different teams, survey parameters, locations, orientations and ground and weather conditions. Their commonality was that they both investigated the same part of the structure. Along strike lateral correlation between lines 3 and 7 is very strong, which is especially surprising in view of the differences in orientation and location between the lines (see Figure 4-11). The location of the eastward rise in velocities at Figure 4-14 [3] coincides clearly, as does the drop in velocity into the MDT (Figure 4-14 [2]) and the velocity recovery in the footwall of the MDT (Figure 4-14 [4]). The strong lateral correlation of diverging lines testifies to the along strike linearity of the structure.

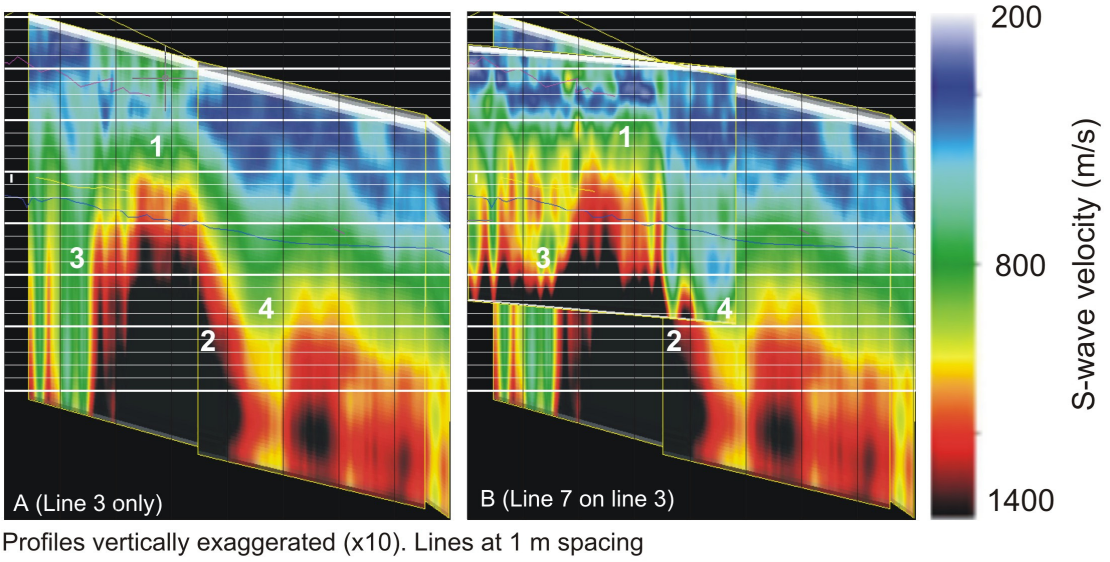

Figure 4-14: Along-strike comparison of MASW line 3 alone (A) with line 7 superimposed on line 3 (B) to investigate repeatability of the technique. The vertical exaggeration is x10 and the horizontal lines are at 1 m spacing. Both MASW profiles can be seen to record some major similarities.

Depth correlation is also strong between lines 3 and 7. The elevation of the low velocity contours across the top of the uplift at Figure 4-14 [1] varies by only ~1 m between lines, and even this is likely to be due to either natural variance or southwestward plunge of the anticline structure between faults 1 and 4. The elevation of velocity contours >1000 m/s coincide almost exactly across the uplift. A significant depth variance is, however, seen at (3) where line 3 extends the low velocity zone to an unrealistic depth compared with line 7. This is probably a processing artefact, caused by the use of a 10 m near offset on line 3 with no farther offset shot to allow walkaway construction.

4.3.3 Rock mass character

4.3.3.1 Crosshole velocity testing

In addition to MASW profiles, horizontal crosshole velocity data were acquired at an outcrop (D1) close to the main thrust, at the southwestern end of line 6. Table 4-3 presents a summary of the physical properties and associated S-wave velocities at the outcrop. The velocities vary from 63 to 450 m/s and generally reflect the structural element being sampled (see Figure 4-15 to Figure 4-17). Large reductions in V_s are apparent in the two major shear zones relative to surrounding rock, and in the sheared argillite. The highest velocities were recorded on either side of shear zone 1 (holes 8-9). The extremely low velocity between holes 11 and 12 may be due to hole 12 being drilled at a low angle to the face to follow the strike of the argillite. This made the hole over-loose and caused poor coupling of the geophone with the base of the hole without noticeably impairing the performance of the slide-hammer.

As shown in Figure 4-15, outcrop D1 exhibits a strong damage asymmetry. The visual appearance of the media either side of shear zone 1 appears different and one would expect to see this reflected in the velocity structure (e.g. Dor et al., 2006). Unfortunately no strong trend emerged, possibly due to the amount of sheared argillite sampled on the SE end of the outcrop.

When the crosshole velocities obtained at outcrop D1 are correlated with lines 1 and 4, several well defined low velocity zones can be seen within the strike-perpendicular range of outcrop D1 (Figure 4-17B). The spacings and locations of these velocity lows are very similar to and closely associated with shear zones seen in outcrop. This appears to emphasise the structural sensitivity of the technique but the results of Corboz (Corboz, 2004) show that the major shears in this vicinity are not linear over the distance between

the outcrop and Line 4, at least in the gravels (Figure 4-17A). The structural correlation with line 1 is, however, solid. Two well developed velocity lows can be observed that correlate exactly with the foliated shear zones observed in outcrop between holes 1-2 and 8-9 (Figure 4-17C). The incipient shear zone between holes 4-5, which is highlighted by a low crosshole velocity, is not obvious in the MASW profile but is also not foliated in outcrop.

Table 4-3 Near-surface physical properties and S-wave velocities at outcrop D1, Dalethorpe.

Hole pair	Structural element	Distance (cm)	Number of fractures	Minimum fractures/m (density)	Maximum spacing (mm)	V_s (m/s)
1-2	Foliated gouge	58	>106	185	5.4	81
2-3	Fractured and faulted	168	>186	110	9	253
3-4	Fractured and faulted	205	>175	86	11.7	259
4-5	Incipient shear zone.	220	>250	114	8.8	184
5-6	Fractured and faulted	265	>145	55	18.3	255
6-7	Fractured and faulted	245	>130	54	18.9	255
7-8	Fractured and faulted	340	>224	65	15	450
8-9	Foliated gouge	190	>212	111	9	174
9-10	Massive sandstone	260	>198	76	13	434
10-11	Sheared argillite	105	>175	167	6	157
11-12	Sheared argillite	105	>180	167	6	63
12-13	Sheared argillite and sandstone	190	>160	84	12	272

Velocity value correlation between line 1 and outcrop D1 is reasonable although the maximum values in outcrop are generally some 200-300 m/s slower than those observed in the survey. This discrepancy is almost certainly due to a combination of enhanced fracturing and greater fracture aperture at the unconfined surface of the outcrop, and the shallow depth of the crossholes. Shakeel and King (Shakeel and King, 1998) found that blast damage loosened material to a significant depth, which resulted in a noticeable decline in velocity towards the free face. The properties of the D1 rock mass show significant fault-related damage (Figure 4-15), and the foliated zones are noticeably spongy in outcrop.

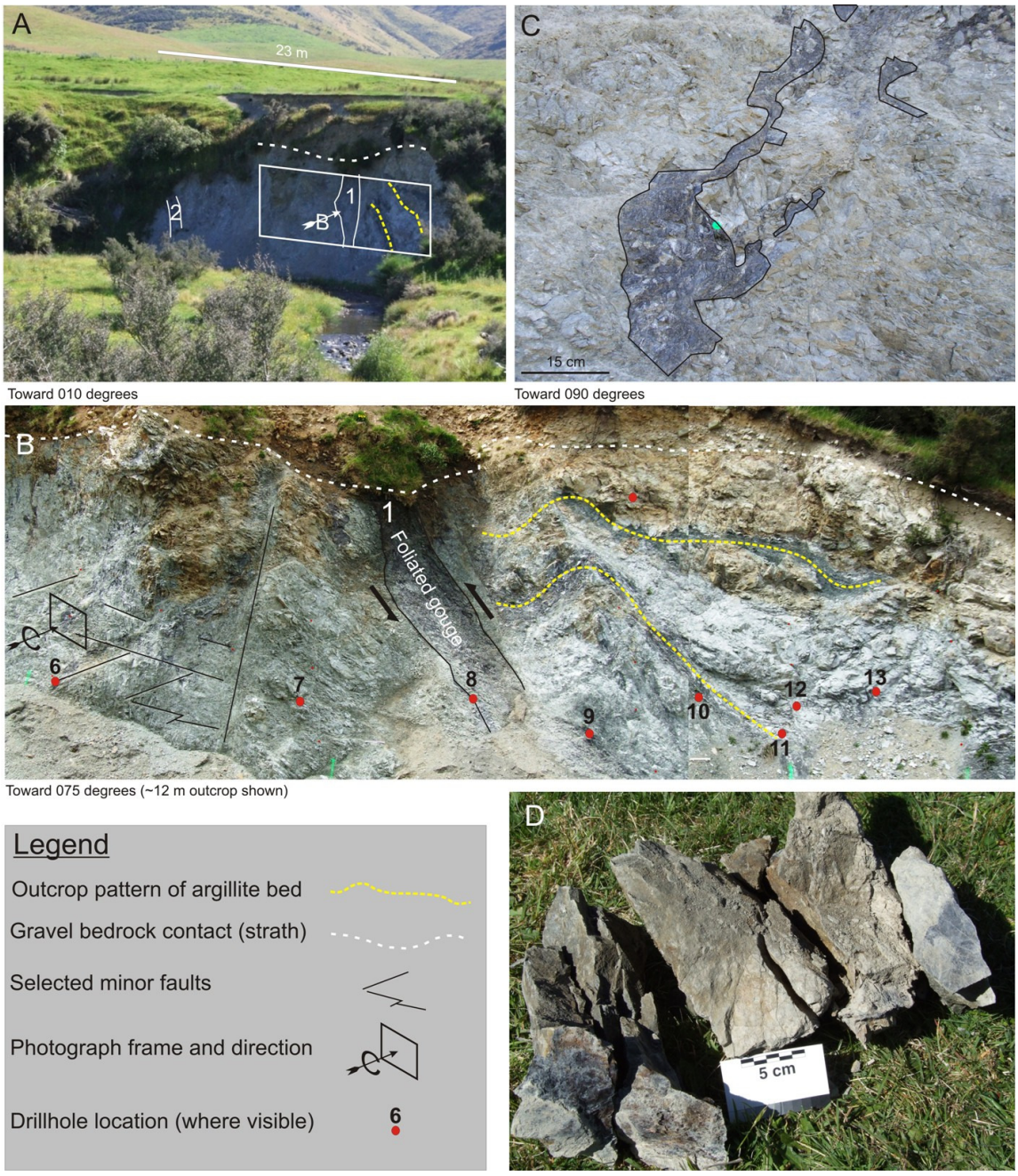

Figure 4-15: Gross features of outcrop D1 (for location see Figure 4-3 or Map 1). A) General view of fault-zone outcrop cut by meander in south branch of the Hawkins River. B) Close up of outcrop. The footwall is intensely brittley deformed by multitudes of low angle thrusts, a few of which are shown along with a major 1 m wide foliated shear zone. The outcrop is more massive and less shocked on the hanging wall where most of the deformation is concentrated in the argillites. The yellow lines pick out the sheared argillite beds, which are oriented approximately 010/65SE. C) Close up of ductile deformation: Isoclinally folded and boudinaged thin argillite layer within footwall forward of shear zone 1. Elsewhere, the folds are crosscut by low angle thrusts. This is in direct contrast to the continuous but sheared argillite beds on the more intact hanging wall side of the shear zone. D) The hanging wall scree contains significantly larger blocks of sandstone than does the footwall scree (see B). The blocks do not however transport well and typically fall apart as shown when disturbed.

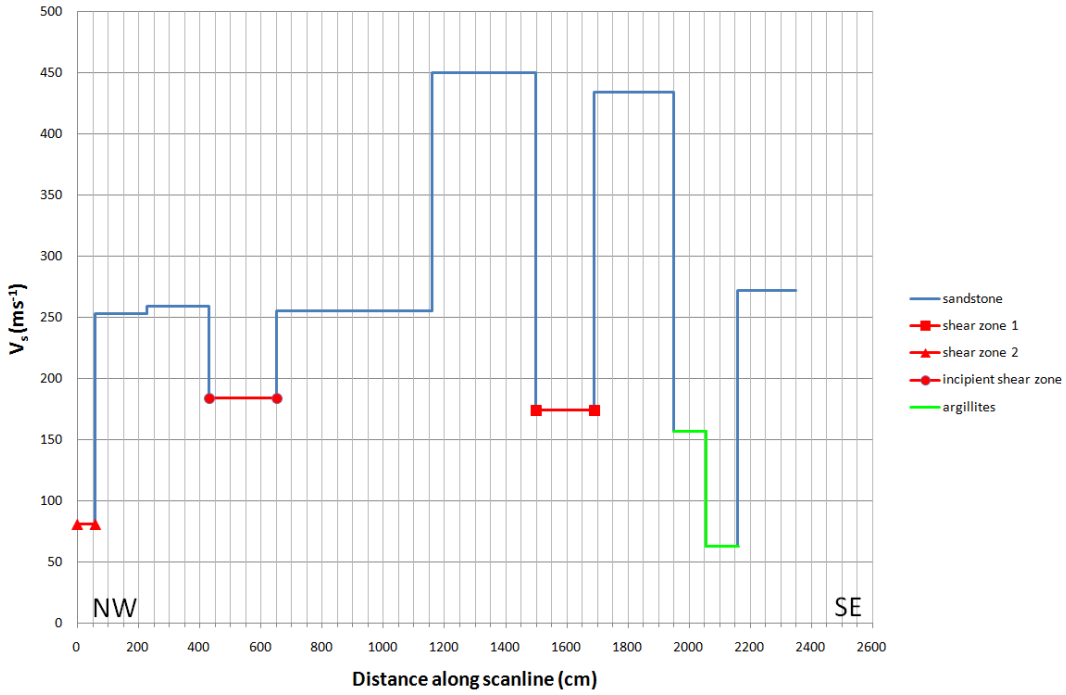

Figure 4-16: Graph of V_s with distance along scanline for outcrop D1. No obvious velocity asymmetry is apparent to match field observations but this may be skewed by the predominance of argillites sampled at the SE end of the outcrop.

Section 4.3.2 demonstrated strong MASW line-to-line correlations whilst lines 1 and 4 appear to belie that claim, in terms of velocity if not structure. This may be due to processing artefacts, the location of line 1 close to an unconfined, actively eroding terrace edge, S-wave splitting or along-strike velocity variability. Leaving aside processing artefacts, unconfined edge effects should not result in low velocities below ground so can probably be discounted. At a given pressure, S-wave splitting in foliated media results in lowest velocities perpendicular to foliation (Okaya et al., 1995). Line 4 is closest to orthogonal to the fault and displays the *highest* velocities, so S-wave splitting is unlikely to be responsible. That leaves along-strike variability, which is investigated in line 6. The intersection of lines 1 and 6 certainly appears to occur at a low velocity zone that is common to both lines (Figure 4-18).

4.3.3.2 Scanline surveys

Apart from outcrop D1, downcutting of the Hawkins River exposes Torlesse greywacke basement rocks in many places along the river's course. Several of these outcrops, marked on Map 1 from D2 through D7 are also investigated and classified in this study and their properties are correlated with S-wave velocities inverted in the MASW studies (Figure 4-19A). Outcrops D3 and D4, which are outside the fault-zone as defined in

Figure 4-13, are characterized by wider fracture spacings and are moderately to completely weathered.

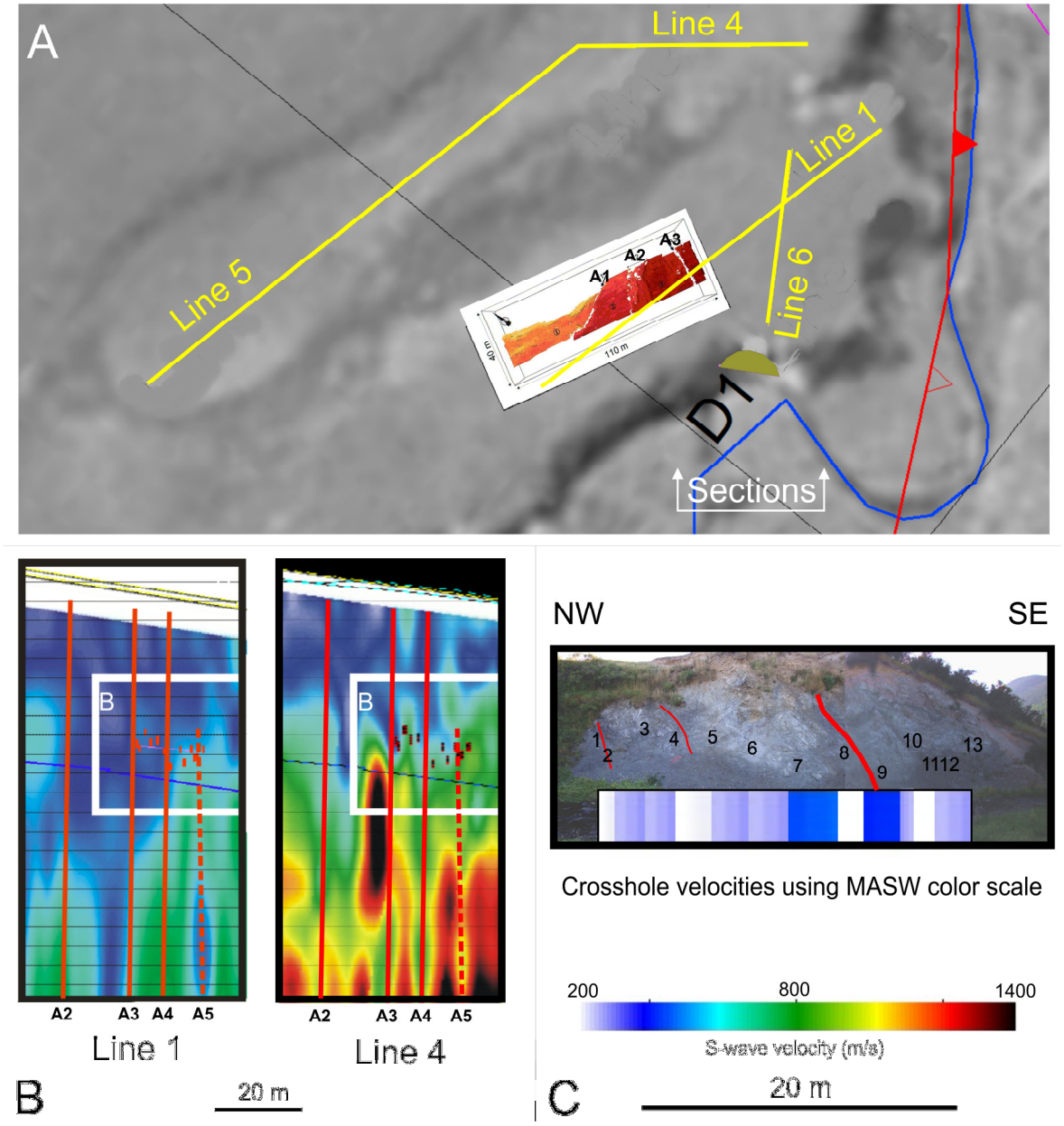

Figure 4-17. Relationship for outcrop D1 between crosshole S-wave velocities and those derived from MASW. (A) Detailed map view showing MASW lines in structural orientation. A GPR data cube imaging three shears, numbered A1-3 (Corboz, 2004 and Figure 4-2B) is shown in position. Shear A3 can be seen to trend towards crosshole 1 at the NW end of outcrop D1, where it outcrops. (B) S-wave velocity profiles for line 1 and 4 with crosshole locations and low velocity zones marked. Line 1 displays significantly lower velocities, probably due to its proximity to an unconfined edge. Both lines display a deep set of low velocity zones, which are numbered as per Corboz (2004). (C) Marked up photo of D1 showing crosshole locations, shear zones and crosshole velocities according to MASW colour scale. The velocities are clearly more representative of Line 1 than of the more distant Line 4.

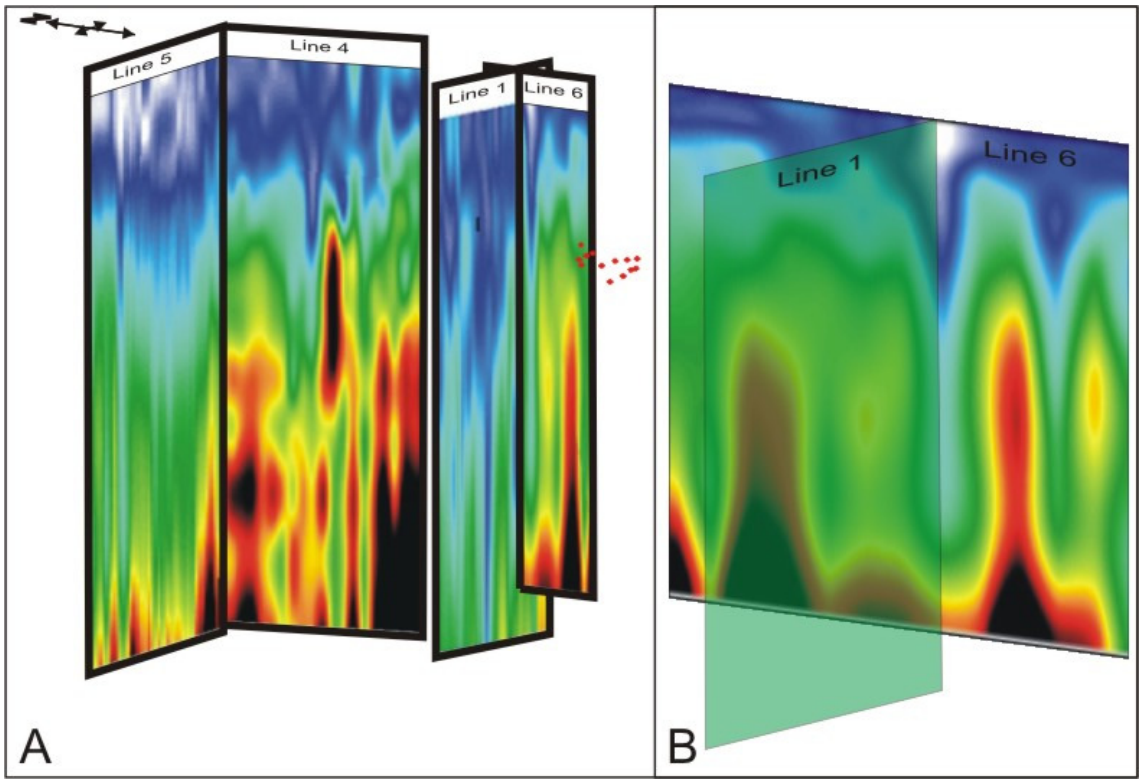

Figure 4-18: (A) Perspective view of lines 1 and 4-6. (B) The low velocities in line 1 correlate closely with a low velocity zone in line 6 at the intersection of the lines. Line 1 is shown without velocities in B so that line 6 can be seen behind line 1. The lensoidal character of the velocities in line 4 particularly may be partly due to the low angle shears seen in outcrop D1 (Figure 4-15)

Outcrops D2 and D5, which are inside the fault-zone, are more closely fractured but the material is only moderately weathered. Outcrop D1, which is close to the main trace of the mapped fault, is completely to residually weathered, often strongly foliated and everywhere intensely fractured. The outcrops were characterized by Geological Strength Index (GSI) (Figure 4-19B) using the scheme of Hoek *et al.* (Hoek et al., 1998). Geological strength indexing provides an estimate of the reduction in rock mass strength based on degree of interlocking and joint surface quality. The indices were then plotted against the S-wave velocities obtained in the MASW survey, yielding a linear relationship for the range of GSI and S-wave velocities covered (Figure 4-19C).

A linear relationship such as this seems unlikely and this conjecture is borne out by integrating all crosshole, MASW and scanline data for the Dalethorpe area. The crosshole data from D1 and D2, together with the MASW velocities correlated with outcrops D3 and 4 (outside the fault-zone), plot linearly on a semi-log plot (Figure 4-20). MASW

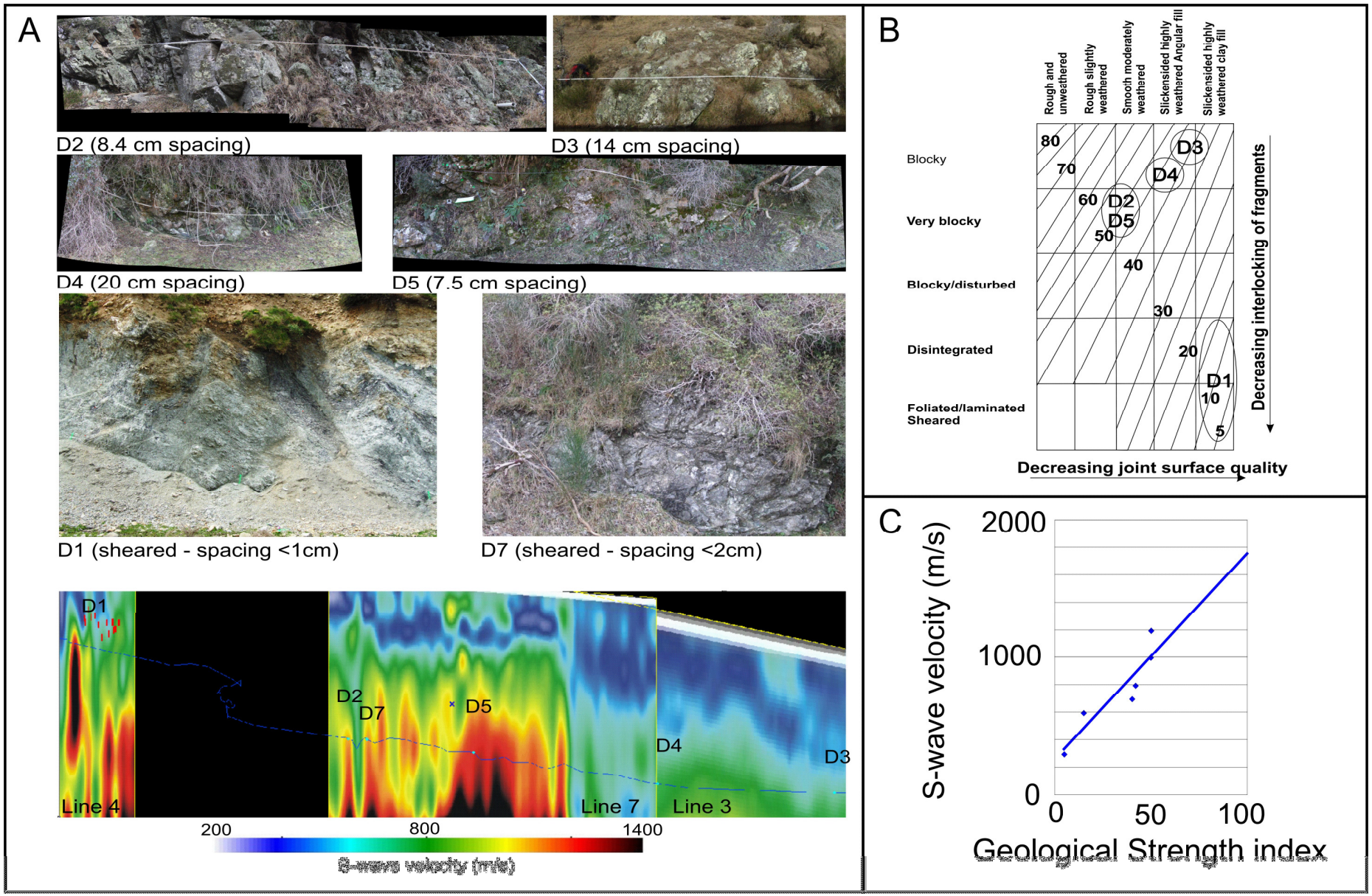

Figure 4-19. Correlation of geological strength index (GSI) with MASW S-wave velocities. (A) The location of the photographed outcrops is shown on the MASW profile. (B) Geological strength indices derived in the field for the outcrops in A. (C) Plot of GSI against S-wave velocity for the outcrops in A and B. A strong, apparently linear correlation can be observed.

velocities for outcrops D2, 5 and 7 define a similar trend at higher velocity values but these outcrops fall within a part of the MASW survey considered likely to be dominated by higher mode surface waves (Figure 4-20). It is thus likely that use of velocity data from both contaminated and uncontaminated sectors accounts for the 'linearity' seen in the GSI trend (Figure 4-19).

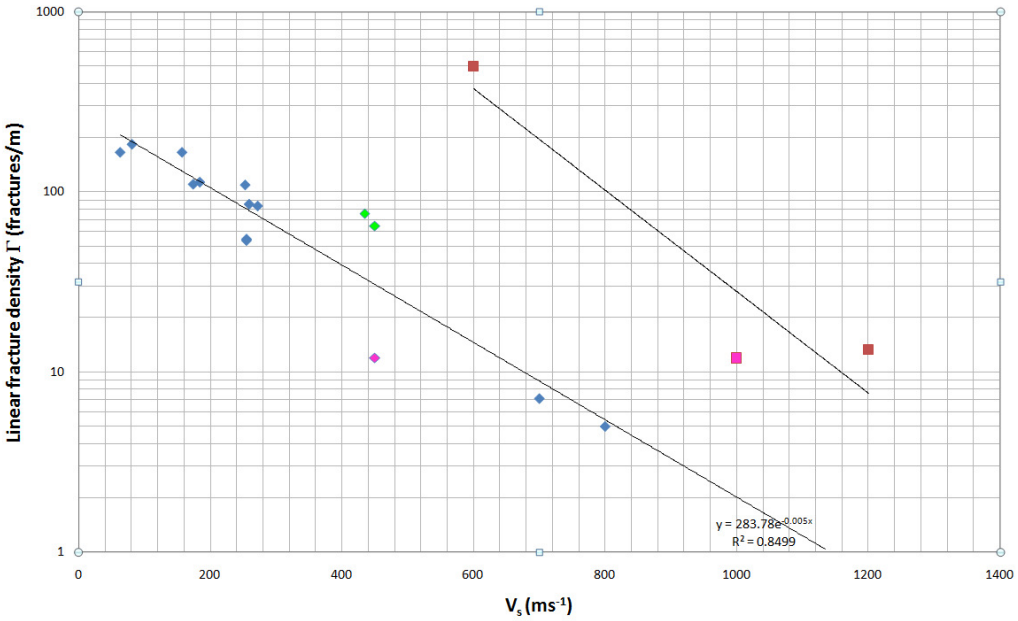

Figure 4-20: Integrated scanline (fracture spacing) and velocity data for Dalethorpe. Crosshole data from Outcrops 1 and 2, and MASW velocities for outcrops 3 and 4 (all diamonds) define a trend that agrees with the data in Table 4-2. MASW data from outcrops 2, 5 and 7 (squares) all lie within the area shown by Figure 4-5 to be potentially higher mode contaminated, and this is reflected in their elevated velocities. Magenta markers are velocities for outcrop 2, green markers are for velocities adjacent to shear zone 1.

Fracture spacing is known to exert a greater influence on S-wave velocity than does lithology, hardness or primary porosity in well-cemented lithologies (e.g. Fumal, 1978; Rasolofosaon et al., 2000). Fracture aperture is also significant. The crosshole velocity from D2 is suggestive of a linear fracture density that is double that observed at outcrop but this anomaly is influenced by the wide fracture apertures of between 2-3 mm, with little or no fill. Conversely, the velocities measured adjacent to the major shear zone is suggestive of a fracture density half of that observed, probably due to fracture closure due to local stress regimes.

Based on the data presented, Torlesse S-wave velocities, including those inverted from fundamental mode Rayleigh waves, can be confidently related to fracture spacing such that

$$\Gamma = 283.78e^{-0.005V_s}$$

(Equation 4-1)

where Γ is the linear fracture density in the subsurface. This relationship even appears to hold for the sheared argillites sampled in outcrop D1 suggesting that fracture density does indeed dominate S-wave velocities in Torlesse sediments.

4.4 Laboratory testing

This section presents the results of an ultrasonic analysis of artificially-fractured parent material. The objective of this laboratory work was to supplement the outcrop data and potentially to provide an alternative method of calculating an empirical relationship between fractured rock-mass parameters and S-wave velocities. Samples taken from outcrops D1 and D2, as well as from an intact boulder from the Hawkins River, were tested in the laboratory to determine a range of physical properties including density, porosity, unconfined compressive strength, point load strength and S-wave velocity.

The river boulder had been selected for apparent homogeneity but, in the first instance, several cores were drilled in three mutually perpendicular directions and tested to determine their intact S-wave velocities. 10% unconfined S-wave velocity anisotropy was shown that reduced slightly with increasing uniaxial stress (Figure 4-21).

Still using the intact boulder, an artificially fractured core was tested to determine the effect of fracturing on the ultrasonic S-wave velocities of Torlesse greywacke. This experiment predictably produced the strongest relationship observed in the laboratory (Figure 4-22). S-wave energy was completely attenuated across sawn fractures until coupling was improved with uniaxial stress. This dry attenuation was due to frictional sliding of the fracture surfaces (Wulff et al., 2000). Once uniaxial stress was applied the S-wave velocity for a given specimen was seen to decline dramatically with increased fracturing, especially at lower uniaxial stresses.

Microcracking due to uniaxial unconfined compression strongly influences velocity of ultrasonic waves in dry sandstones. The experiment depicted in Figure 4-22 began with 12 fractures and the number of fractures was reduced at the start of each run.

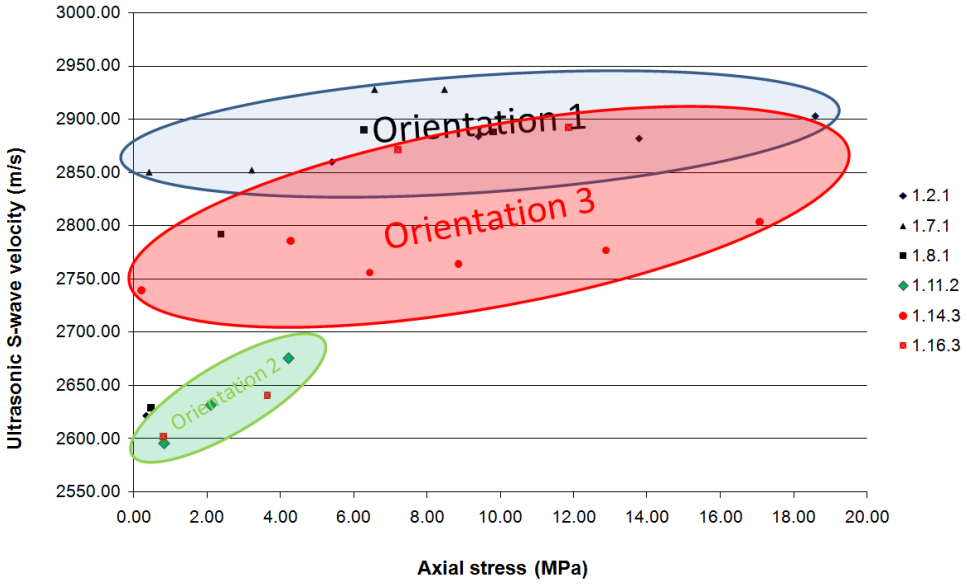

Figure 4-21: Intact S-wave velocities for specimens cored from Torlesse greywacke river boulder sourced from the Hawkins River catchment at Dalethorpe. The unconfined S-wave velocity is slightly anisotropic [10% using Okaya et al's formula (V_{max} - V_{min})/V_{ave} (Okaya et al., 1995)] but this appears to reduce with compression. For the purpose of this study the unconfined intact S-wave velocity is taken as 2750 m/s.

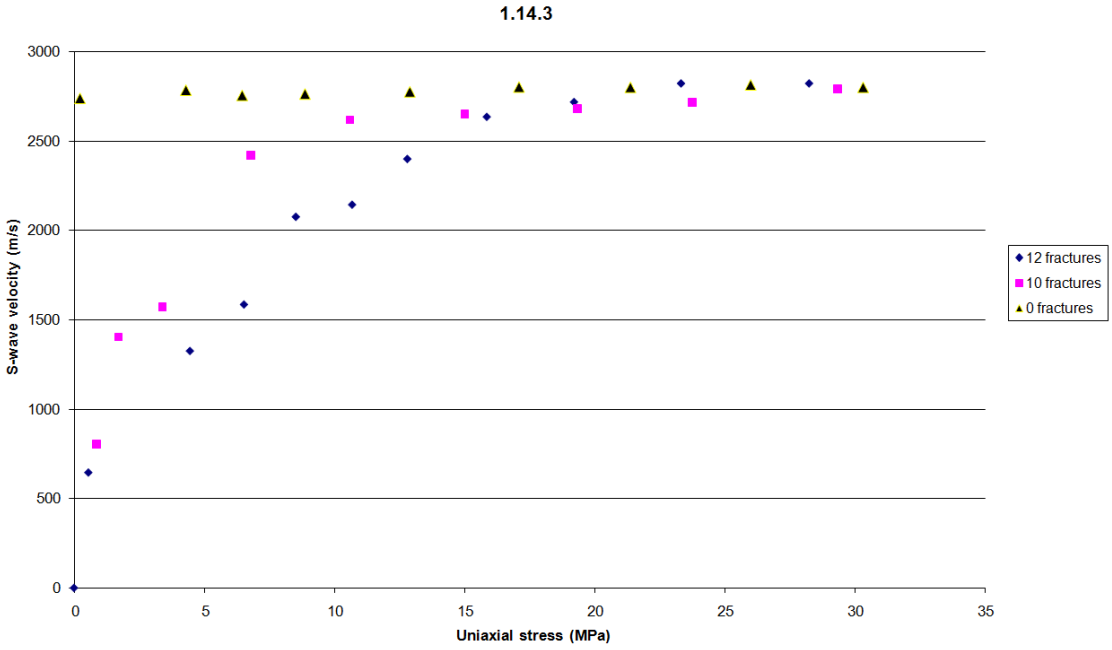

Figure 4-22. Ultrasonic S-wave velocity plotted as a function of uniaxial stress for an un-fractured specimen (triangles) and the same specimen with saw cut 'fractures'. The specimen was cored in orientation 3.

When the fracture number was reduced to 8 following the 10 fracture run the velocities suddenly dropped to unrealistically low values. These velocity changes are explainable by

the creation of cracks located in the grain contact areas during the preceding test cycles (Wulff et al., 2000).

Following this experiment, all subsequent testing was done using only minimal uniaxial stresses of <5 MPa to avoid creating unaccounted for fractures. One specimen from each orientation was fractured at regular intervals from a point part way along its length and S-wave velocities measured with increasing linear fracture density. Plotting the results for this ultrasonic data alongside the sonic data revealed no obvious relationship (Figure 4-23A), a problem probably related to the differing ratios of investigation wavelength to heterogeneity scale length (Gettemy et al., 2004; Mukerji et al., 1995). An improved fit of the two datasets was achieved by plotting linear fracture density against the velocity decline relative to the theoretical maximum for the wavelength of investigation (Figure 4-23B). This approach yielded a reasonable fit (~20% misfit) between the lightly loaded ultrasonic data and the sonic velocity data.

The suboptimal fit can be significantly improved if the maximum theoretical velocity is increased to 3500 m/s, a figure that would agree with the work of Okaya *et al.* (Okaya et al., 1995). Either alternatively or in conjunction with this, the misfit may reflect the influence of weathering on S-wave velocity. The boulder was relatively unweathered, and it could be conjectured that weathering has a greater influence on S-wave velocity at low fracture densities, whilst fracturing dominates the velocities at higher fracture densities. This might explain the convergence of the data at higher fracture densities.

No cores were obtainable from outcrop samples so the physical properties of irregular blocks were determined. Some reasonably strong trends emerged from this testing. S-wave velocity in Torlesse greywacke material is shown to be related to specimen porosity (Figure 4-24A). This suggests that the porosity of Torlesse hand specimens may be a useful indication of volumetric fracture intensity because intact boulder porosities are typically less than 0.5%. A less strong relationship was observed between S-wave velocity and point load strength (Figure 4-24B), although the relationship between porosity and point load strength was very strong (Figure 4-24C).

In all cases, the velocities and physical properties measured for irregular blocks yielded a larger data spread than those determined using core. This scatter can be rationalized. The difference in velocity spread is caused by measuring velocities across non-parallel faces of roughly rectangular blocks rather than along cores. The scatter in physical property estimates is probably due to errors in volume determination using the immersion method.

Comparisons of core and block data in the plots of V_s against porosity and point load strength suggest that the irregular block methods consistently over-state S-wave velocities and other physical properties. Use of the block method is unavoidable given the degraded nature of the outcrops, from which no core is recoverable. It should, however, be possible to account for overestimation during data analysis. If the relative core to block

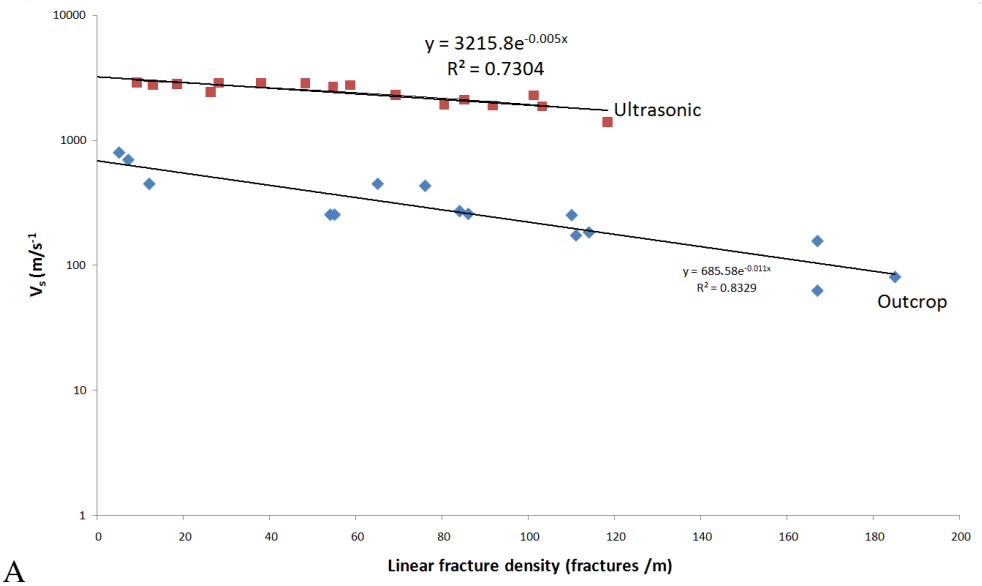

A

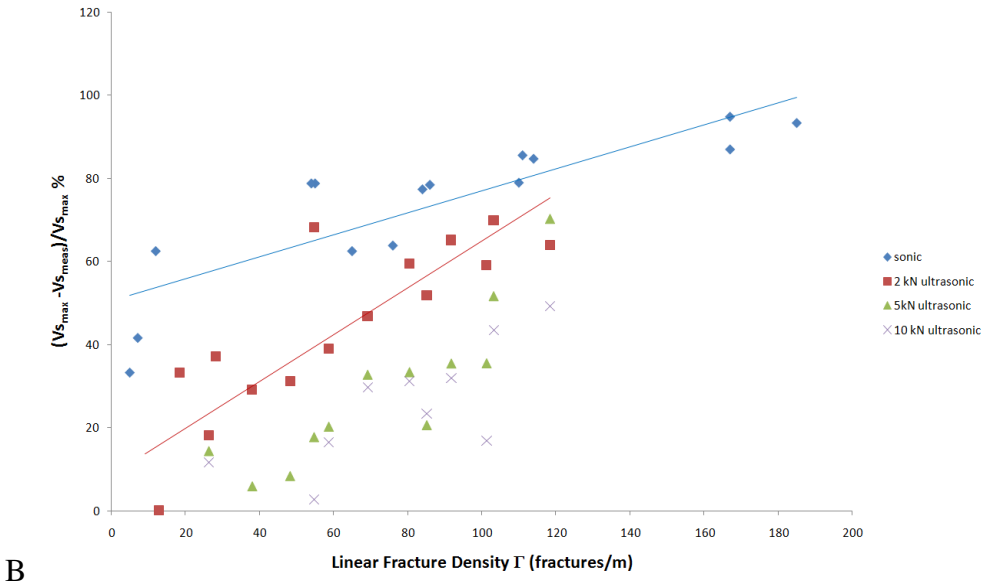

B

Figure 4-23: Comparison of sonic and ultrasonic velocity relationships to linear fracture density. A) Both ultrasonic and sonic (outcrop) velocities decline linearly with fracture density over the range tested. Ultrasonic and sonic velocity fields are widely separated. B) Percentage velocity decline from a theoretical maximum plotted against linear fracture density. A better fit can be seen between the sonic velocity field and the lightly loaded ultrasonic data. Maximum sonic velocity was set at 1200 m/s (Table 4-2) and ultrasonic at 2750 m/s (see Figure 4-21).

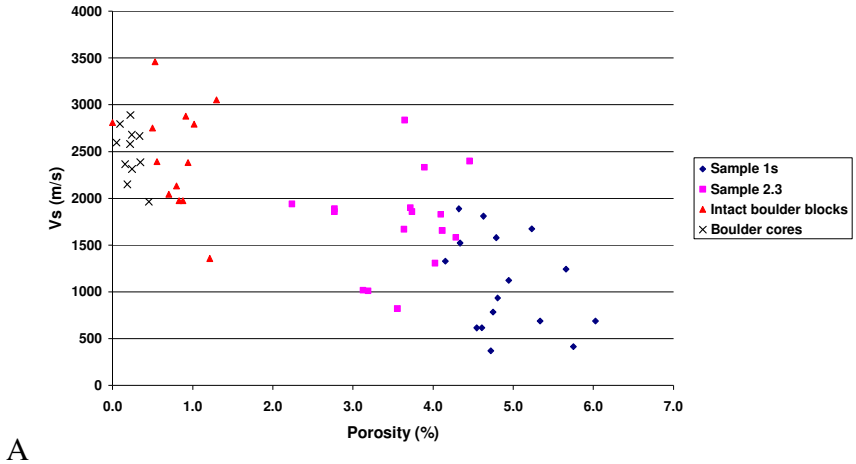

A

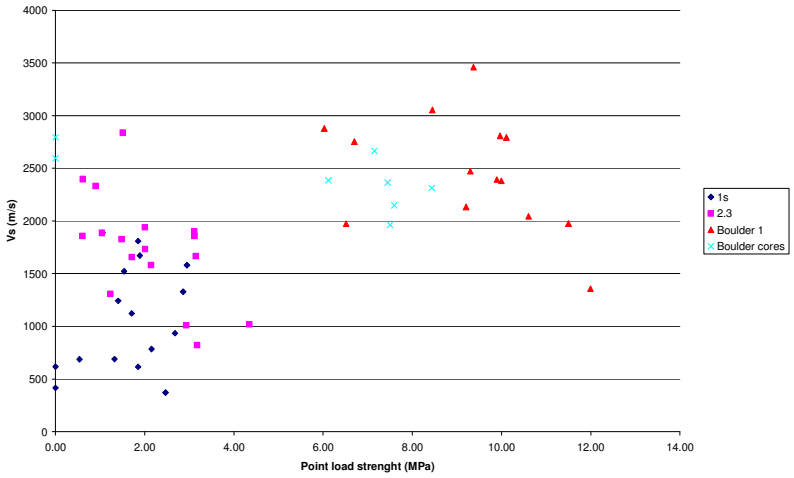

B

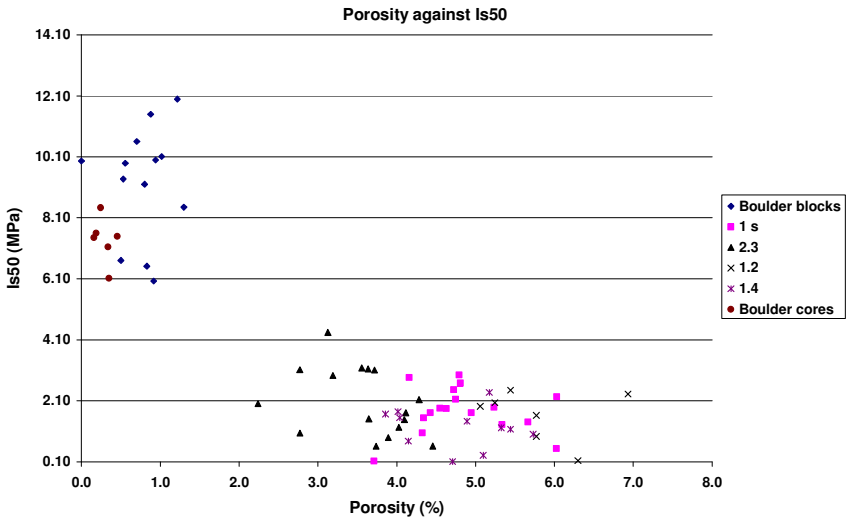

C

Figure 4-24: Relationship between A) ultrasonic S-wave velocity and porosity, B) ultrasonic S-wave velocity and point load strength and C) Point load strength and porosity for specimens from intact boulders and tectonised outcrops of Torlesse greywacke.

errors for intact rock reflect the likely errors in the data from the tectonized specimens, derivation of any empirical relationships should be guided based on the relative spreads of block and core data. Many of the observed relationships would also be improved if the block cutting was more accurate and if it were possible to cut larger blocks with parallel faces. In this instance, however, quantity has superseded quality due to equipment limitations.

4.5 Discussion

The close correlations of geomorphological, geotechnical and seismic techniques exceeded expectations for this site. Despite the smearing effect of MASW and the non-uniqueness of 1D inversions (Xia et al., 2005), structural and geotechnical boundaries within the Dalethorpe Fault-zone correlate closely with changes in S-wave velocity measured at both tomographic (MASW) and crosshole scale. The MASW velocity variations are damped by the range of S-wave velocities within the structural element below the array. However, the magnitude of velocity contrasts in faulted Torlesse creates sufficient perturbation in the average velocity that even subtle features can be detected. Gross features can definitely be clearly detected.

Field parameter selection for future surveys over Torlesse-floored sites should be simple. Examination of hundreds of records suggests that the optimal near offset, beyond which near-field effects are absent, appears to vary between 12 and 14 m. As near field effects do not adversely affect dispersion curve extraction, the 12 m option should prove acceptable in most cases, thus limiting the potential for higher mode contamination of high frequencies at far offsets. In this study such contamination was contributed to by the use of a 23 m array at 1 m geophone spacings. The strategy employed to best effect was filtering by muting (Ivanov et al., 2005) using 47 m, 48 channel walkaway records to highlight higher modes. Recent commercial application of MASW in Torlesse, however, demonstrated the remarkable improvements obtainable using a 48 channel array with a reduced geophone spacing of 0.5 m (Duffy et al., 2008). Such records can be cut to remove both near and far field effects following examination of a swept frequency record. This is not possible with 1 m spacings without significantly reducing the surface wave energy in the cut record.

The higher mode contamination in lines 3 and 7 is probably due to the shallow depth to bedrock (O'Neill and Matsuoka, 2005) and as such is not a significant hindrance to using

MASW to locate the fault-zone. It does mean that care should be taken during acquisition and processing if engineering use is to be made of the inverted velocities. A subjective scale and other strategies for grading survey quality are appended that should be used in engineering applications of MASW data.

The integration of field and laboratory seismo-technical relationships in Figure 4-23 provides a strong basis on which to infer geotechnical parameters from MASW S-wave velocities. The major issue that remains is that of determining whether velocity changes relate to fracturing, weathering or both. In an area with differential uplift it is not reasonable to assume that vertical velocity gradients are weathering related whilst horizontal gradients are fracture related.

4.6 Conclusions

Spatial variability in the wavefields, the dispersive nature of the MASW data and the magnitude of inverted velocities correlates with the geological and geomorphic context of the survey lines. Overall, a strong correlation is observed between the MASW data and topographic profiles. The transition into and out of the fault-zone is strongly correlated with quantitative assessments of ground deformation, with the river thalweg proving the most sensitive measure of deformation. On the basis of these correlations the extent of the SFD has been re-defined and significantly extended. The within-zone variability that is seen in the MASW images is correlated with crosshole velocity measurements and measurable rock properties particularly linear fracture density. This correlation is refined by laboratory testing and a scheme is proposed to relate both laboratory and field derived velocities with the same measure of S-wave velocities. The laboratory testing also correlates the S-wave velocity of a variety of Torlesse material with secondary porosity in addition to visible fracture density. This additional parameter provides a measure of volumetric fracture density and with refinement could potentially be correlated with bedrock acquifer porosity and permeability.

5 STRUCTURE, KINEMATICS AND PALEOSEISMICITY OF THE SPRINGFIELD FAULT, DALETHORPE

5.1 Introduction

The broad geological and geomorphological setting of the Springfield Fault Dalethorpe (SFD) was detailed in the introductory chapter and in Chapter 4. The MASW data presented in Chapter 4 established the existence of a second major strand of the SFD that lies between the Main Upstream-facing Thrust (MUT) and the Bell Hill Fault studied by Evans (2000). This provides a key starting point for quantifying the fault-zone's hazard potential using structural, kinematic and paleoseismic analyses. This chapter integrates the MASW profiles from Chapter 4 with the detailed geomorphology of the SFD and should be read in conjunction with Map 1.

5.1.1 Scope and objectives

The detailed geomorphology of the Upper Hawkins Basin was mapped with the objective of elucidating the sequence of channel occupation, deformation and abandonment in the uplifted terraces, and placing them in the context of local structural development. Particular attention was paid to delineating and characterizing:

- the fault scarp.
- the extents, gradients and relative ages of the major glacio-fluvial surfaces and subsequent degradational terraces.
- the evolving relationship between SFD and the past and present watercourses occupied by the Hawkins River.
- the strath surface underlying terrace A.
- the river bed elevation as a sensitive indicator of bedrock faulting that may or may not be expressed by the mapped fault trace.

The survey detail is drawn together in Map 1.

This chapter begins with a description of the structure of the fault-zone (Section 5.2) that defends the cross section (Section A-A', Map 1), followed by a review of the

geomorphological character, evolution and paleoseismic history of the fault-zone (section 5.3). This includes a general description of the tectonic geomorphology of the Upper Hawkins Basin. 3D analyses are used to isolate individual event traces and determine their relative timing and the magnitude of their coseismic displacements. Samples were collected for optically stimulated luminescence (OSL) dating and the results are presented. Long term slip rates and recurrence interval are calculated based on the OSL dating and number and magnitude of events recorded. Paleoseismic analysis is followed by a geomorphological investigation of the kinematics of the fault-zone (section 5.4), discussion and conclusions.

Reconstructing the paleoseismic history of the site is outside the primary objectives of this study, since MASW is not directly useful as a tool for this purpose. However, it is an important step in the reconstruction of the geometry and history of the uplift of the hanging wall structure. This is relevant to the question of predicting the likely distribution and style of off-plane deformation within a fault zone, and as such is an important objective of this study in the context of land use planning considerations.

5.2 Fault-zone structure

The fault trace geometry and structure of the SFD was integrated 3 dimensionally with surface mapping and topographic data in AutoCAD (Map 1 and cross section A-A`). The MUT has a clear-trace length of at least 3.8 km in the study area, over which distance it is obscured for only ~0.5 km. The fault plane was defined by drawing structure contours on the fault trace, which exactly parallels the dogleg in the river between MASW lines 1 and 7. Based on the elevation view in Figure 5-1, the fault trace is relocated from the work of Evans (2000) to pass along the dogleg rather than simply projecting under Terrace A and through outcrop D1. Although Figure 5.1 shows a large apparent deviation in the fault trace, this is probably largely due to burial of the fault trace to depths of <2 m by fan debris and swamp deposit accumulation. This conjecture is supported by soil augering, which encountered an indeterminate thickness of fan debris in the area. Evans (2000) also suggests that even the clearest scarps are significantly modified. The modification adversely affected his diffusion modelling, which failed to produce reliable ages. The MUT has a dip of only 15°, upthrown to the southeast. Despite the regular sinistral sense doglegs in the river, there is no unequivocal field evidence of strike slip offset.

The minor relocation of fault 1 leaves the steeply dipping foliated shears observed in outcrop D1, and in the GPR imaging of Corboz (2004), reassigned as part of the footwall structure. The presence and orientation of these shears must be accounted for in a fault model. Sheared and truncated argillite bedding in outcrop D1 (Figure 4-15) is oriented at approximately 010/65SE, in line with the average orientation of most local Torlesse bedding. The steeply dipping shears that truncate the bedding are strike-parallel. These two orientations are both reflected in the GPR survey of Corboz (2004) (shown on Map 1), where his south-eastern shear zone (A3) is similarly oriented to the truncated argillite beds, A1 is strike parallel and A2 appears to represent a diffuse interaction of the two. The shearing observed in the argillites is interpreted as flexural slip thrusting on favourably oriented bedding planes, whilst the strike-parallel shears represent the evolution of the internal structure of the footwall into a set of through-going shears. Subhorizontal shears were also noted (Figure 4-15B), often offsetting the steeper shears and accommodating the forward component of thrust motion.

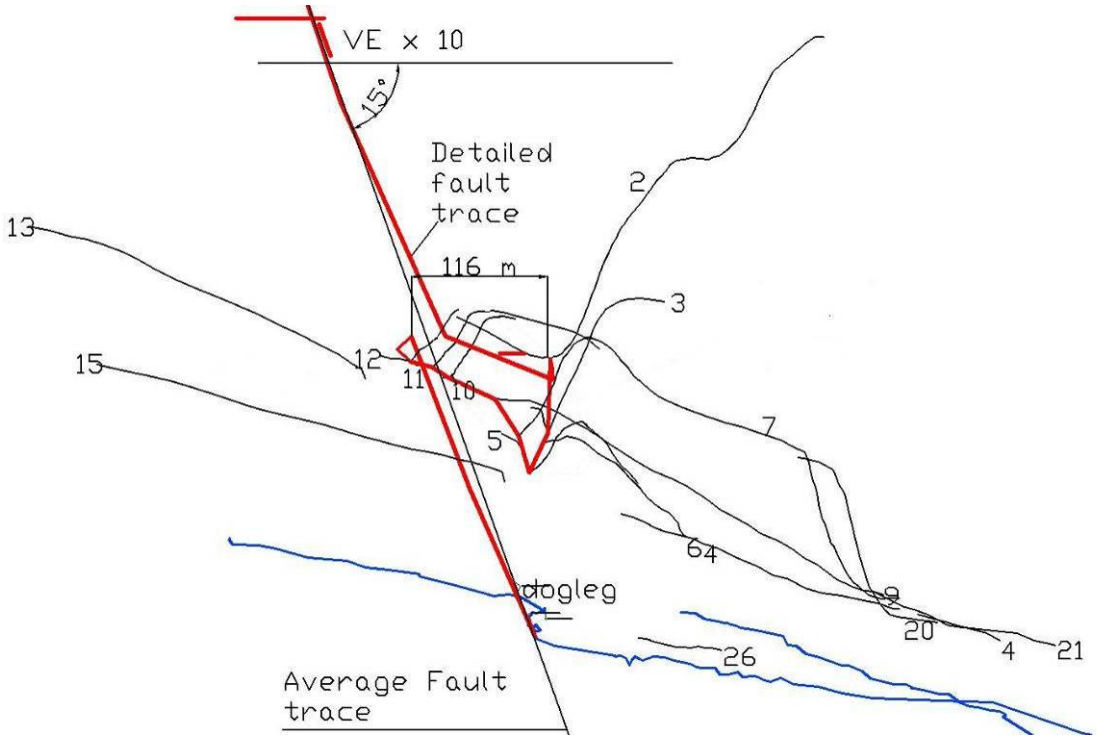

Figure 5-1: Topographic and river thalweg profiles viewed viewed towards 51° showing the detailed and average traces of the main upstream facing thrust. Profile 13 is run on the B terrace, Profiles 15 and 21 on the A surface (see Figure 4-11). This 10x vertically exaggerated elevation shows a fault dip of 15° to the SE. The dogleg is seen in this elevation as the sudden decrease in the elevation of the riverbed, due to the river flowing along strike. The apparent re-entrant angle in the projected fault profile reflects the gradient on terrace B and consequential drop in the elevation of the base of the fault scarp.

The western damage zone in Figure 4-12 was interpreted in section 4.3.1.1 as a thrust that breaks out through the river dogleg west of the MUT. It is not directly related to the MUT since outcrop D1 is forward of that thrust and has higher velocities. The flexural slip shearing discussed in the previous paragraph, together with the adjacent meander in the Hawkins River, suggest a significant amount of strain is partitioned in growth of a footwall syncline and this conclusion is supported by the rate and shape of the velocity increase in the MASW profiles in Figure 4-12. With its lack of topographic expression, the fault could be an out of syncline thrust with not much movement on it. Such a fault is unlikely to account for the degree of damage suggested by the velocities so an alternative and favoured interpretation is as a previously active splay forward of the main thrust.

The location and apparent sense of faults 1 and 2 are intriguing. Evans (2000) carried out a detailed analysis of slickensides in shear zones of the Bell Hill Fault on the NW face of Bell Hill. He recorded data that appeared suggestive of a component of normal faulting and conjectured that the slickensides may represent normal faulting on the oversteepened hanging wall of the fault. Both faults 1 and 2 are upthrown to the southeast, the same as the main upstream facing fault. The warping of the young terrace profile (profile 26) over fault 2 suggests thrusting, but no such warping is observed at fault 1. For this reason, fault 1 is interpreted as a normal fault, supporting the conjecture of Evans (2000).

The Main Downstream-facing Thrust (MDT) is the largest newly identified fault in this study. As outlined in the previous chapter a scarp previously mapped as the terrace riser between B and A picks out the fault as it strikes to the northeast. Trimming by the Hawkins River during downcutting to terrace A and fans exiting the antecedent stream channels modify the scarp morphology. Other indicators are structurally controlled gullies to the north and south of the south branch and knickpoints in the beds of both the north and south branches of the Hawkins River. The MDT has a significantly shorter topographic expression than the MUT (only 540 m), with a further 300 m confidently inferred based on thalweg-to-thalweg and thalweg to MASW correlations of both the north and south branches of the Hawkins River. The fault is upthrown to the northwest and appears to dip steeply in that direction, which together support interpretation as a backthrust off the MUT. Together the MUT and MDT bound an uplifted block (the pop-up wedge).

At the southeastern limit of the MASW surveys the profiles of both rivers show a marked increase in gradient that correlate along strike with each other and with a same-sense,

though less obvious, gradient change in profile 21 (Figure 5-1). These features also correlate with an eastward decrease in velocity in MASW profile 3 (Figure 4-13). When seen in a long river profile (Figure 5-2) this gradient increase is preceded by a gradient reduction that creates a 1.3 m high anomaly relative to the average elevation of the riverbed.

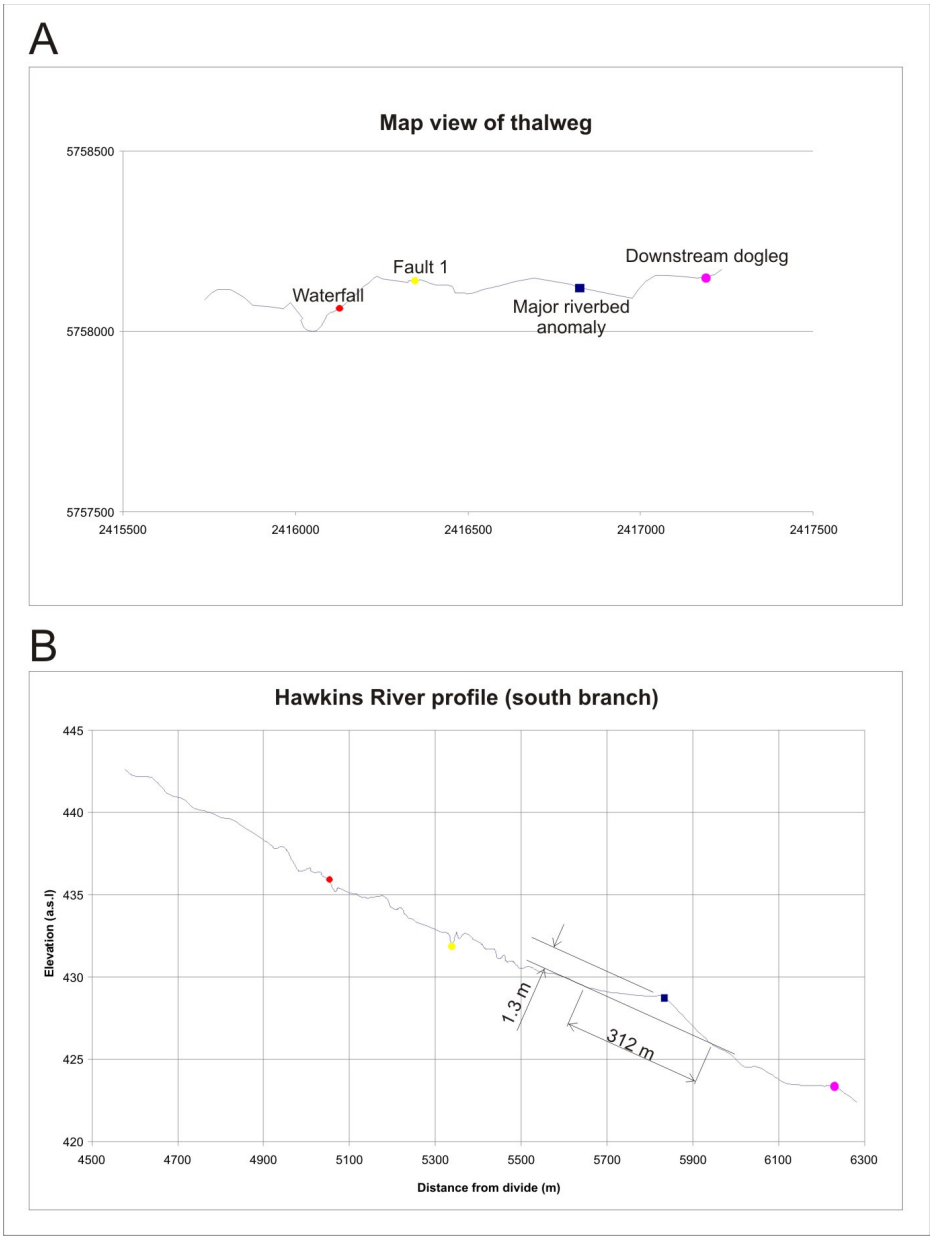

Figure 5-2: Map (A) and profile (B) views of the thalweg of the south branch of the Hawkins River. The most notable feature of the profile is the 1.3 m high, 312 m long anomaly in the river bed at 5830 m from the divide.

The vertical expression of the riverbed anomaly is paradoxically greater in the active river bed than on the abandoned A terrace immediately above. One probable explanation is to invoke folding rather than faulting. Local river and basin characteristics, discussed later in sections 5.3.1 and 5.4 respectively, suggest that a footwall syncline is actively growing in

association with the Bell Hill fault scarp further downstream. Although the river bed anomaly may represent a fault, it is more probably a very small parasitic anticline formed by compression along the inner free surface of the syncline developing in the greywacke slab. A fault with 1.6 m of expression in the river bed is unlikely to leave little trace on the abandoned terrace above. The gravel cover on a fold, however, would deform considerably differently to the underlying bedrock and the strain would be more easily disseminated. For this reason, a syncline is mapped at this location.

The Bell Hill Fault forms a well preserved, upstream facing scarp that cuts across the Dalethorpe Road in the easternmost section of the study area. Selective erosion picks out the fault's plane on the hillside on the northeastern side of the Hawkins River, at the confluence of the north and south branches. This allows a reliable projection of the strike and dip of the fault and its southwestward trace across the north face of Bell Hill using structure contours. The constructed trace coincides with the projected position of the fault located by Evans (2000) outcropping in forestry roads high up on Bell Hill. It also seems to account for the roughly west-east trending lineations observed on the 163 (pre-forestry) aerial photographs of the study area (Figure 5-3).

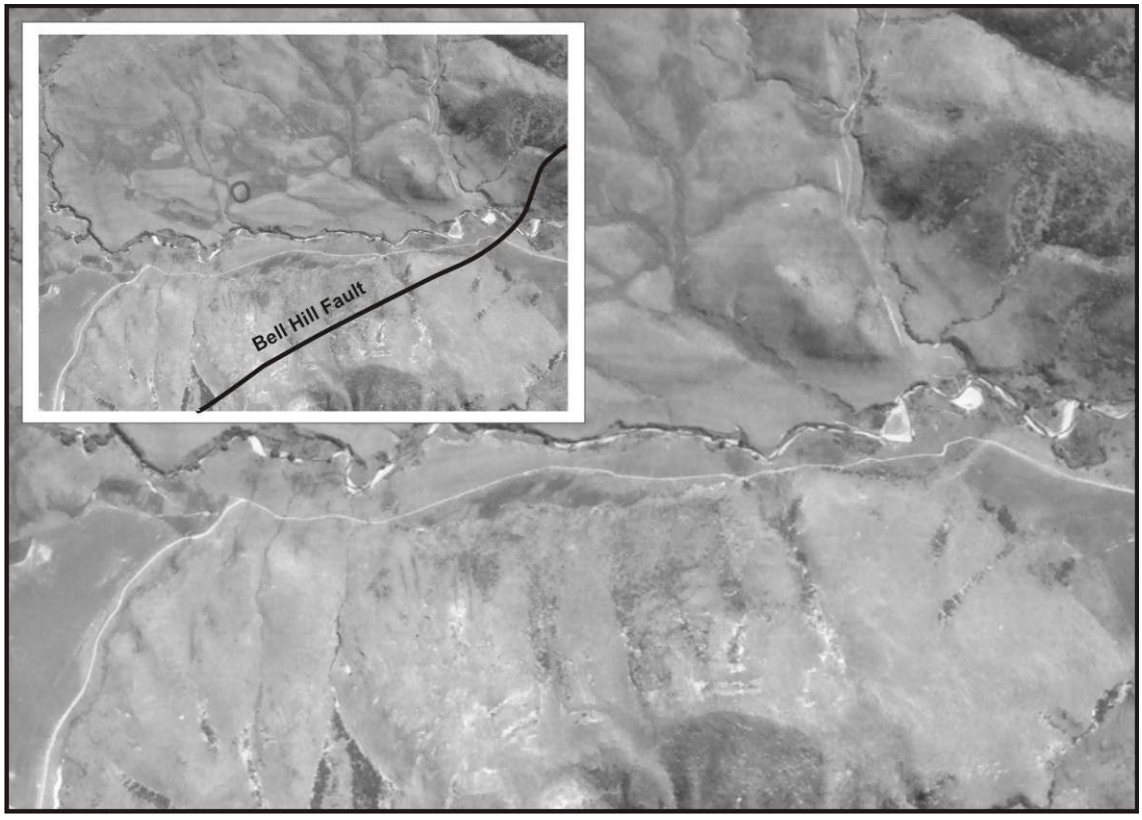

Figure 5-3: Detail from 1963 Ashburton-Kowai River aerial photograph 3706-3, showing lineations (main picture) and inset the trace of the Bell Hill Fault. The meandering of the Hawkins River as it approaches the fault can be clearly seen, as can its increased sinuosity as it approaches the MUT upstream.

5.3 Fault-zone history

5.3.1 Geomorphological principles and observations

Before continuing to a detailed geomorphological description of the study area, it is necessary to outline several fundamental concepts about the genetic nature of terraces. Three types of terraces are understood (Bull, 1990) and all three are present in this area. Firstly, climatic terraces form due to climatically controlled aggradation followed by degradation leaving a fill terrace known as an aggradation surface. An aggradation surface is entirely climate controlled because base level of erosion cannot be attained during a climatic aggradation event. Conversely, tectonic terraces are major straths bevelled at the base level of erosion by streams in dynamic equilibrium with tectonic uplift. Climate and tectonically-controlled responses are not, however, independent of each other and flights of complex response terraces are found below or between major aggradation or strath surfaces. These terraces form in the vertical space provided by uplift of the channel, whether by aggradation or by tectonic uplift. Differentiation between tectonic (major) and complex response (minor) straths is difficult as tectonic straths may be completely backfilled leaving only exposure of the complex strath below (Bull, 1990).

As outlined in the previous chapter, the SFD fault-zone transects the Upper Hawkins Basin. Within this fault-zone, the wedge bounded by the MUT and MDT vertically offsets a flight of glaciofluvial terraces that step up in elevation northward with increasing age. These terraces, designated A through C with increasing age and elevation by Evans (2000), record a history of southeastward migration of the Hawkins River through distinct climatic cycles. Although referred to here as aggradation surfaces, the accumulated gravels are only of moderate thicknesses of a few metres and rest on eroded bedrock straths. Even so, the modern Hawkins River and its catchment are underfit to represent the source of the gravels. The source of the gravels is speculatively related to the Rakaia glaciations via glaciation of the Selwyn catchment that lies beyond the saddle southwest of Bell Hill. This area, however, merits investigation well beyond the scope of this study because there is presently a 200 m elevation difference between the top of the saddle and the headwaters of the Selwyn River below.

The highest, C, surface is best preserved in the west of the basin, where it wraps around the south of the bedrock ridge that occupies the northwest of the study area. Further east toward the MUT it becomes thoroughly degraded and dissected by small streams. The

streams issue from the bedrock ridge and deposit fans on the B surface below. A correlative surface is mapped in the pop-up wedge. Directly north of the uplifted C surface, the downthrown surface is obscured by a debris flow deposit, although a surface remnant remains that, based on its elevation, is an intermediate surface from the incision down to the B surface.

An extensive original B surface (B0) is also well preserved in the west of the basin on the north side of the modern river. This surface is correlated with multiple displacements in the pop-up wedge, each of which is recorded by remanant surfaces incised into the wedge. These surfaces record a waning flow, from a period during which the river had sufficient excess stream power to plane a wide surface across most of the basin. During later uplift events the pop-up wedge was dissected by a much smaller flow than that which planed the B3 surface. At that stage the river was still slipping southward around the nose of the propagating Eastern Russell Range Anticline and had probably begun cutting down to the A surface. The modern downthrown B0 surface in the centre of the study area is extensively buried by the fan and debris flow deposits issuing from the bedrock ridge through a network of streams incised into the degraded C surface. The limits of this fan are unclear as it is considerably degraded.

A well defined terrace riser separates the B and A surfaces in the west. The A surface is the lowest of the surfaces and the only surface preserved on the south side of the Hawkins River. It appears undisturbed but several tectonic signals are apparent. Firstly, drainage appears trapped at the back of the A terrace and flows east parallel to the river, toward the major structural dogleg that defines the trace of the MUT. This trapping of drainage, along with the trimming of a steep A terrace riser north of the river (Figure 5-4), seems to be caused by recently reversed tendency for the river to slip northward since abandonment of the A terrace. Prior to abandonment, the river was trapped on the south side of the basin against Bell Hill, to where it had migrated over the three aggradation cycles preserved in the terrace flight. Secondly, a fault-strike oriented impediment visible on the air photo has further confined the already-trapped drainage just short of the dogleg and led to the creation of a swamp. This feature was mapped as a fault displacement in the gravels by Corboz (2004) (Figure 4-2B, located on Map 1). Thirdly, the aforementioned dogleg is repeated about 300 m upstream of D1 but without the marked increase in sinuosity.

These observations lead naturally to a discussion of the site river channel morphology, which is of considerable interest. At the western end of the basin the valley width of the south branch abruptly increases, along with the river sinuosity. The river cuts a wide strath with a sharp double meander bend as it approaches and passes outcrop D1. This behaviour has been observed elsewhere including on large rivers such as the Rakaia (Yousif, 1987) and on smaller rivers such as the middle Waipara (Campbell et al., 2003; Nicol and Campbell, 2001). Campbell and Nicol (2003), reporting very similar circumstances, make a distinction between the response of the Waipara River to coseismic uplift and to long-term deformation of the bed (see also Chapter 6).

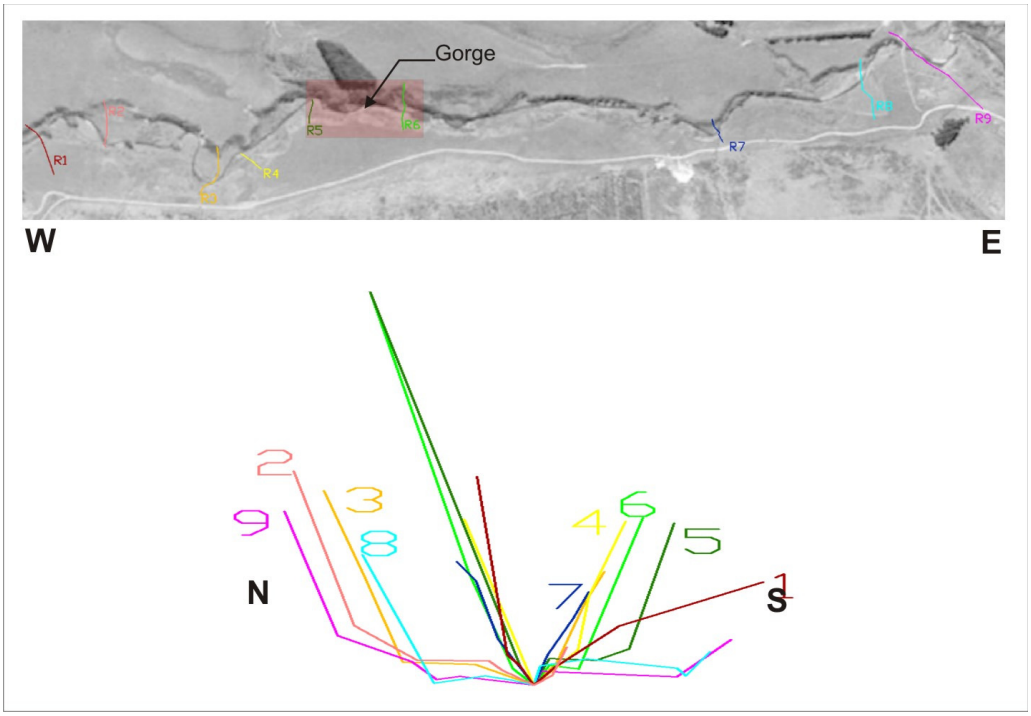

Figure 5-4: Locations and section views showing the valley shape at surveyed sections across the south branch of the Hawkins River (ve x5). The northern bank can be seen to be almost ubiquitously steeper except in the gorge, where it is higher but of roughly equal gradient. Sections 2, 3, 8 and 9 are located very similarly relative to active faults and are all distinctly wider due to meandering. With the exception of the gorge profiles all profiles end on the edge of the A surface.

Meandering is not simply a response to coseismic uplift. Modern drainage configurations can be interpreted in terms a competition between stream power and upstream deposition rates on one hand, and bedrock resistance and rates of crestal uplift and fold widening on the other (Burbank et al., 1996) The spatial and temporal interplay of these variables controls geomorphic thresholds, across which a river must change its channel form in order to remain in dynamic equilibrium with the uplift. A channel's form is an independent variable controlling water and sediment discharge over short time scales ($10<10^2$ years) (Moseley and Schumm, 2001). Only over longer timescales does the

channel form become a dependent variable that must respond to and keep pace with the growth of emergent structures. Where uplift and folding weigh heavier, an antecedent stream will be defeated. The timescales required for channel form adjustment suggest that the meander bend in the Hawkins River is forming in response to ongoing deformation over the width of the meander. Just downstream of the double meander bend the channel morphology changes again to accommodate greater uplift rates. This significantly straighter reach incises a deep gorge in the hanging wall of the MUT (Figure 5-4). The long river profile (Figure 5-2B) suggests that the river in this rapidly incising reach, and in the western half of the basin, is presently in dynamic equilibrium with the uplift.

Downstream of the MDT the river channel widens and the southern bank returns to the slip off type of morphology seen upstream of the MUT. It is in this reach that the anomaly occurs that is interpreted as a parasitic anticline in the Bell Hill Fault footwall syncline. This morphology must be of recent origin. It has certainly developed since the formation of a wide bedrock strath underlying the extensive surface of Terrace A, since which period there is no evidence of significant displacement on the major fault strands. Downcutting of 11 m through Torlesse bedrock has since occurred along the whole length of the river, which is a combination of local effects superimposed on regional uplift or base level fall. Any older events affecting the river should by now have been completely eliminated from the thalweg profile. A small meander has begun to develop across the uplift but no significant incision has occurred at that location, suggesting that the anomaly may be of the order of only very few hundred years old. The river may take some time to adjust. For example, the Mississippi River has yet to adjust fully to the uplift of 190 years ago in the New Madrid Seismic Zone and is still wider and shallower across the uplift (Guccione et al., 2002).

A very similar progression of channel forms can be seen still further downstream in the southeast of the study area and these are similarly located with respect to structure. The broad slip off surfaces are present south of the river as is a steep riser to terrace A immediately north. The river, which has maintained a relatively straight path since entering the gorge, begins to meander again within 2-300 m of the Bell Hill Fault, as it obliquely crosses the rising limb of the footwall syncline. The river has incised through the 2.5 m high upstream facing scarp of the Bell Hill Fault, which displaces the A surface at the exit of the river from the Upper Hawkins Basin.

Just as the modern river reflects modern activity on the faults and folds, the drainage history of the uplifted wedge between the MUT and MDT records a long history of uplift. The height of the MUT fault scarp increases to the northeast with the age of the terraces and the emergent scarp is cut in at least 3 places by significant incised drainage channels other than the modern north or south branches. These channels, labelled from east to west as *ch1, ch1a* and *ch2* (Map 1), record a history of episodic downcutting and drainage disruption that is not seen in the only slightly perturbed, mainly aggradational, terraces on the footwall. The uplift and incision of the wedge, particularly during and post the river occupation of the B surface, therefore directly records a local tectonic signal governed by the magnitude and frequency of local co-seismic ground-rupture events. This coseismic signal is almost certainly overprinted by folding on the anticline but, if the MDT has been operating over the whole period of the terrace record in the uplifted wedge, the influence of folding on the relative terrace elevations is probably limited because, even at modern low flows, the river rapidly trims down to grade equilibrium. The spatial and temporal relationships between the various surfaces on the wedge, and between the wedge and its footwalls, therefore provide an opportunity to establish the paleoseismic and kinematic history of this fault by direct measurement of coseismic slip and by constraining the ages of the various surfaces and by direct measurement of rotations.

Whilst the influence of folding on relative terrace elevations may be limited, it has clearly had a marked effect on the channel morphology, particularly in the gorge. Given the south branch's present dynamic equilibrium and its 11 m of post-terrace A downcutting, the narrowing and steepening of the gorge in response to only 2.5 m of additional local folding in the pop-up wedge is perhaps a little surprising. It may be that the combined uplift, coupled with the decreased erodibility in the area of the gorge shown by the higher S-wave velocities, pushes the river across a critical geomorphic threshold above which planation is not possible at the present stream power. The north branch of the river is responding to the same base level and uplift signals and is not in dynamic equilibrium, having developed a marked convexity (see for example Figure 5-1) that is exaggerated by its sudden fall to join the local base level of the south branch.

5.3.2 Coseismic slip estimation

The reliable identification of individual events and measurement of their coseismic slip is an important factor in determining paleomagnitudes, slip rates and recurrence intervals.

The major surfaces upstream of the wedge were progressively abandoned following the climate driven aggradation events to which they were responding. Their abandonment is a complex downcutting response to glacio-climatic and tectonic lowering of regional baselevel. They are unlikely to have been abandoned due to local neotectonics because such activity would have dammed the river and is more likely to have caused revisitation of previously abandoned surfaces. They are also free of intermediate complex-response degradational events, quite the opposite of what is observed on the hanging wall. This situation allows one to reliably infer from the footwall the inter-surface elevation difference attributable to out-of-basin forcings. The remainder of any elevation difference seen in the wedge must have accumulated by tectonic displacement.

The reader is now advised to open Map 1 and pull out Figure 4-11 (profile locations – p. 52) and Figure 5-5 (p. 89) for ease of reference whilst reading this section.

The influence of original gradient and apparent rotation of the wedge block made measurement of the individual downcutting events difficult. To simplify matters a plane was constructed on the most extensive surface (surface B3, Figure 5-5) and rotated to place the surface horizontal. The elevation differences between each surface were then measured perpendicular to the B3 plane. Datum surfaces are numbered alphanumerically, beginning with the parent terrace identifier and followed by a number where 0 is the peak-aggradation parent surface and *n* represents the *n*th increment of downcutting during occupation of the downthrown parent surface. As it is the risers that record events, the base of any channel is also recorded as a surface.

An early challenge in this exercise was to identify the original correlative surfaces within the wedge for the footwall aggradation terraces (B0 and C0). This exercise is complicated by the similarity of the loess sheet on the C-B slip-off surface with the loess profiles on the B3 surface and the downthrown B0 surface. The loess on these surfaces is all of similar stratigraphy and thickness, suggesting no great age difference since the onset of loess accumulation. The downthrown slip off surface is clearly higher than any projection of the downthrown B0 surface but not as high as the C0 surface. Its gradient suggests it is a relic slip off surface between C and B and the measured slip off is within a metre of the C-B downcutting measured in the west of the basin. The upthrown C-B slip off surface has a very similar gradient but records a smaller amount of slip off. The back of the terrace is only 5 m above the highest point on the downthrown side, well less than the total uplift recorded in the B surfaces. It can therefore only be loosely correlated within

the time period represented by the downthrown slip off surface. As shown on Figure 5-5, there is also almost certainly uplift recorded within the C-B interval so the exact elevation of the upthrown B0 surface cannot be calculated based on the data. It seems likely, however, that it is at a higher elevation than the mapped B1 surface.

Accurate determination of coseismic slip is further complicated at Dalethorpe by what appears to be concurrent activity on two bounding faults. It was not possible to distinguish events on the wedge-bounding faults from each other so uplift increments presented here refer to wedge uplift on either one or both of the bounding faults. Some uncertainty is also introduced by the preservation of only one extensive surface (designated B3) and several smaller scraps of surfaces within the wedge. Although at first sight the extent of the B3 surface might be interpreted in terms of recurrence interval as reflecting a period of quiescence, the broad swath over which the surface is planed off suggests that the full flow of the Hawkins River was operating across the area, whilst the small channels (*ch1a, ch2*) were cut by a much lower flow. Because the younger A surface is similar in extent to the B surface, this can only mean that between events 3 and 4 the river had relocated southward to a lower elevation, probably during the process of incising down to the strath below the aggradational surface A. This would have left the smaller channels draining only the small hills to the north and northwest, much like the present day, and controlled at the downstream end by the progressive downcutting of the main river to the level of surface A. The reduction in streampower across the wedge that accompanied this shift has contributed to improved preservation of the record of individual events.

This observation opens the door to inferring further, unrecorded events prior to the cutting of the B3 surface. The likely response of the aggrading ancestral Hawkins River to episodic scarp emergence across its alluvial plain would have been to pond behind the scarp, depositing sediment and quickly aggrading to the level of the scarp. This would result in the river being perched significantly above the correlative downstream surface, which together with the abrupt upstream aggradation would increase the streampower of the flow across the MDT, the downstream boundary of the wedge. In this situation, the reconfigured low-gradient meandering river crossing the wedge would immediately begin mining its banks and depositing the sediment downstream in order to re-attain dynamic equilibrium with the regional aggradation event. Modelling suggests that dynamic equilibrium could rapidly be regained for a river encountering a fault of this type in its alluvial plain (Ouchi, 1985), leaving the river free to bevel a cut-fill terrace and remove

all traces of the higher cut-fill surface(s). The time to achieve equilibrium would, however, have been greatly increased once bedrock emerged in the wedge. Auger investigations of the B3 surface suggest that it is draped in loess over gravel or weathered Torlesse, whilst augering of the B4 surface shows that it is probably underlain by weathered Torlesse bedrock. On this basis it seems likely that the uplift event that led to the cutting of the B3 surface was the last event before the southwestward propagation of the anticline and the consequent exhumation of bedrock pushed the river further south. There it began incising down to the strath underlying terrace A in response to regional base level lowering.

The ultimate relevance of this discussion lies in the choice of event numbers for calculating likely recurrence interval. The relative elevation changes within the B surfaces are all less than the elevation of the A-B riser on the footwall, so the surfaces can be safely inferred to be coseismic degradational event markers. Only six individual surface remnants are preserved below the C-B slip off surface, each of which probably records an increment of coseismic slip. The first of these (B1) is some 7 m below the C-B slip off surface (Figure 5-5). Surface B1 is seen as a small knob bounded to the northwest by the fault scarp and to the south and east by the broad planar surface of B3. To the west it is bounded by an airgap tributary to *ch2,* designated *ch2a*. *Ch2a* is now well above the level of the swamp and channels *ch2* and *ch2a* are separated by a planar surface (B2) which is itself at a lower level than B1 but above the extensive B3 surface. Given the measured elevation differences between surfaces B1, B2 and B3, it is extremely improbable that the 7 m interval above surface B1 represents a single event. It more probably includes an unknown series of several unpreserved events, all traces of which have been removed due to the efficiency of the river in recycling alluvium from the wedge prior to exhumation of bedrock. The mean increment of coseismic uplift recorded by the five subsequent events is 2.234 m. If this is characteristic, the 7 m interval would yield almost exactly 3 events rather than 1, bringing the total number of events since occupation of the preserved section of C-B slip off surface to eight.

Channel *ch2,* which occasionally still drains the swamp, is incised below surface B3 and its sides record further increments of downcutting. These are best preserved at the mouth of the channel as remanant surfaces B4 and B5. Both of these surfaces are also preserved in the triangle defined by the MUT fault scarp and channels *ch1* and *ch1a*. Within this triangle the B4 surface can be clearly seen to have been planed off at a lower level than

B3. As seen in Figure 5-5, surface B5 is an airgap partly defined by the highest point of *ch2* where it warps over the MUT fault scarp. Therefore, B5's preservation above the channel floor at the southeastern end of *ch2* suggests that the 6th event at least involved simultaneous movement on both wedge-bounding faults. The lack of convergence of surfaces B4 and B5 in *ch2* further suggests that this coincidence was characteristic of this system. Ongoing, perhaps simultaneous, movement on both bounding faults goes some way to explaining the paradoxically smaller tilts observed on the higher surfaces of the wedge when compared to more steeply inclined lower surfaces, although the latter are also probably chasing the dropping baselevel at the downstream end (see also section 5.4 below).

Of the 6 preserved surfaces, the lowest (B6) is not a surface as such but rather the present day topography. This event is inferred based on a displacement of the B surface but is assigned within the time marked by occupation of the A surface. Although no obvious active trace of the MUT crosses terrace A immediately north of the river, GPR imaging shows that the last rupture occurred during occupation of terrace A (Corboz, 2004). This is supported by the profile of *ch2* (profile 9), which along with *ch1a* clearly grades down from the last MUT rupture to the downstream A surface. This demonstrates that the A surface was indeed already occupied prior to the last rupture. The channels, which by that stage would have been draining the B surface only, rather than the Hawkins catchment, were warped and blocked by the rupture, leading to their virtual abandonment, although *ch2* still occasionally carries water. This evidence supports the remapping of the MUT through the river dogleg (Section 5.2), where the rupture could best be disguised, leaving only minor displacements on the flexure slip faults that cut through the A surface and outcrop D1. Because fan and swamp deposits have accumulated against the scarp on the upstream footwall, this last event (B6/A0) was measured relative to a projection of the well preserved footwall B0 surface onto the scarp of the MUT. The measurement yielded a slightly lesser uplift estimate than could be derived by measuring the elevation difference between *ch1* and *ch1a* as they cross the scarp of the MUT.

Table 5-1 summarizes the individual uplift events associated with the event horizons discussed above and illustrated in Figure 5-5. In addition to the coseismic slip events recorded in the terrace sequence, a 2.5 m displacement of the strath underlying surface A has been documented, over and above the regional incision (Figure 4-12). Apart from noting that the warping postdates the cutting of the strath, the timing and rate at which this

strain accumulated is unclear, but nevertheless significant. Ekstrom *et al.* (1992), for instance, documented a pattern of aftershocks following the 1985 Kettleman Hills, California, earthquake that corresponded with readjustment of the anticline core following coseismic strain. Figure 4-13 suggests that much of the warping documented on terrace A is probably accommodated by shuffling on minor faults. Unfortunately, no fault-normal topographic profiles, that may have indicated the degree of warping of the terrace surface, were run along the A terrace on the south side of the river. However, it is probable that in this instance the 2.5 m up-warping of the strath is produced by a combination of co- and immediately post-last-seismic activity, and pre-next-seismic activity.

Table 5-1 Riser heights and calculated characteristics for incision events at Dalethorpe.

Event	Occupied surface	
	A	B
B1 – B2		2.2 m
B2 – B3		0.95 m
B3 – B4		2.65 m
B4 – B5		2.4 m
B5 – B6/A0	2.97	

Net uplift	11.17 m
Net uplift since abandonment of B3 surface	8.02 m
Overall average uplift/event	2.234 m
Uplift per event averaged since B3	2.67 m
Characteristic fault plane slip	1.2 – 1.5 m (for derivation see below)
Coseismic folding	0.8 – 1 m
Pre-seismic warping	0.8 m

Unfortunately, the net uplift events recorded as terrace offsets do not appear to provide a realistic direct measure of co-seismic fault-plane slip. A 2.2 m vertical coseismic uplift on a 15° fault, that was purely slip-generated, would require a massive fault-plane displacement of 8.5 m, which is unlikely on this or any other reverse fault; Wells and Coppersmith (Wells and Coppersmith, 1994), for instance, do not speculate on earthquake parameter relationships for reverse displacements >3 m, and even then only for rupture lengths greater than 100 km (see Figure 5-9 in section 5.3.6 below). This raises the question of what constitutes a reasonable partitioning of pre-seismic strain, coseismic folding and coseismic slip for the SFD.

Answering the question above requires assumptions to be made regarding the model of thrust faulting and hence the distribution and relative contributions of the various components of strain. The fault zone structure as summarized in the cross section on Map 1 has already been defended above, so this section addresses the strain partitioning. Assuming that pre-seismic strain is not released at rupture, it is unlikely to account for more than 1/3 of total uplift (Nicol and Campbell, 2001 and references therein) and may be up to an order of magnitude less than co-seismic strain (Ruegg et al., 1982). The pre-seismic component preceding each rupture should be recorded in the apparent uplift ascribed to the previous rupture. The overall slip history in Table 5-1 suggests a characteristic total uplift of ~2.2 m from one event to the next, with the final event recording the largest 'uplift' at 2.97 m. This last event is temporally correlated with, and has a similar magnitude to, the 2.5 m apparent warping of the strath. Both must record all three components of uplift mentioned above, assuming that they are all expressed here. Given their magnitudes compared with previous events, it thus seems likely that much of the pre-seismic strain preceding the next event has already accumulated. Assuming this to be the case, and further assuming that pre-seismic strain accounts for a full 1/3 of the total uplift, a pre-seismic strain magnitude of ~0.8<1 m is estimated based on the last event and the warped terrace. This leaves 1.6<2 m of coseismic strain, partitioned between co- or immediately post-seismic folding and co-planar fault slip.

The amount of coseismic deformation expressed as surface fault slip in a thrust earthquake may be a small fraction of the overall deformation. The 1980 El Asnam, Algeria, earthquake for instance was accompanied by intense surface folding and reduced surface rupture compared with calculated fault slip at depth, such that the surface displacement was a maximum of half the total slip inferred from horizontal and vertical geodetic displacements (e.g. Philip and Meghraoui, 1983; Ruegg et al., 1982). Due to a lack of trench data, this study will therefore assume that fault slip accounts for 0.8-1 m of uplift. On a 15° fault this amounts to a coseismic surface displacement estimate of between 1.2 and 1.5 m. Wells and Coppersmith (1994) note that average *sub*surface displacement typically falls somewhere between the average and maximum surface displacement, however the stacked assumptions required to reach the 1.2 – 1.5 m estimate still render its validity questionable.

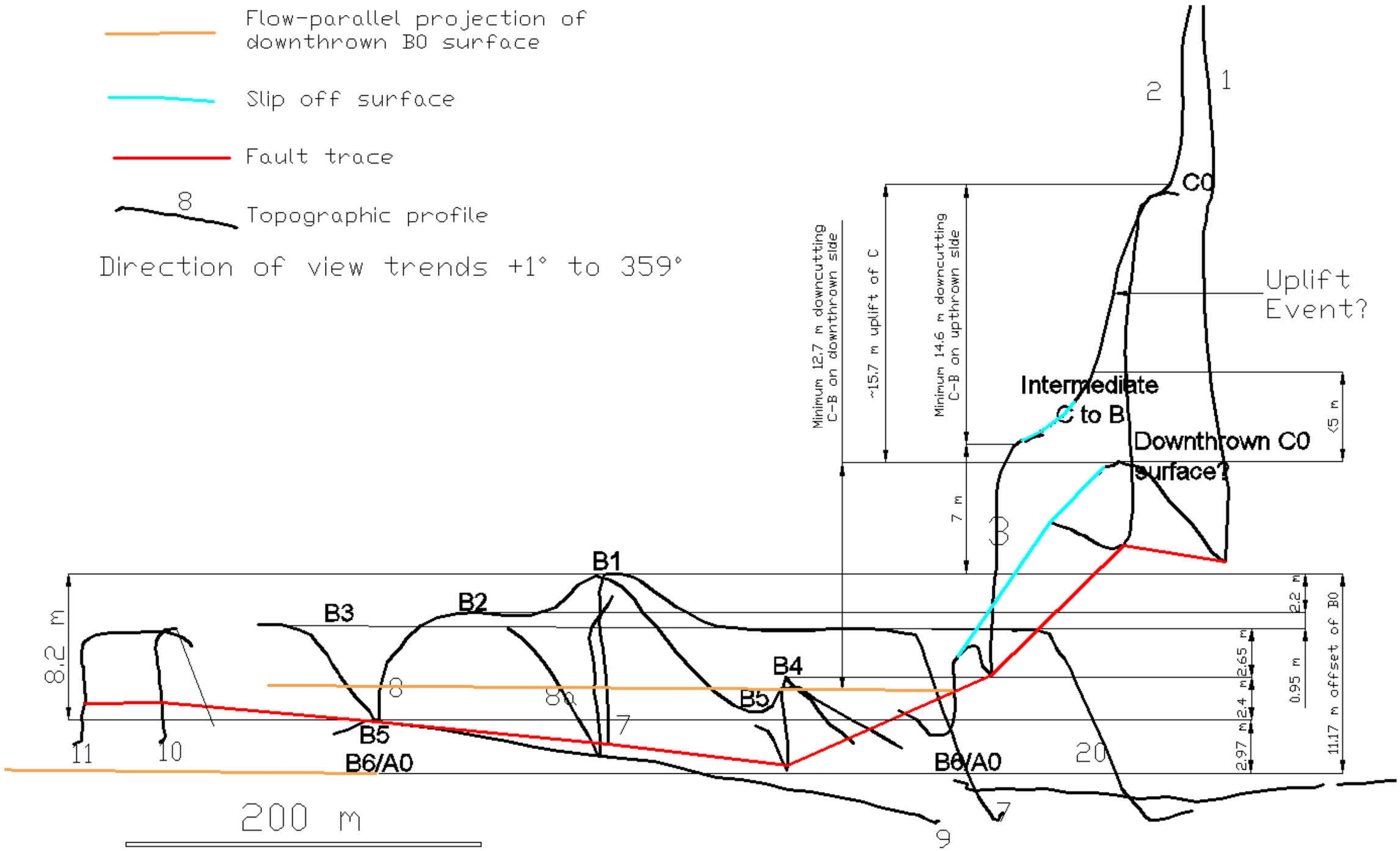

Figure 5-5: Oblique elevation of topographic profiles (numbers shown) showing coseismic uplift markers at Dalethorpe. Vertical exaggeration x10, all dimensions in metres. B0 and C0 represent the correlatives of the B and C surfaces on the downthrown side. Surfaces B1-4 and B6/A0 record periods of quiescence and varying degrees of lateral planation separating coseismic uplift events that led to abandonment of the previous surface. B3, shown horizontal, is the most extensive and best preserved of these surfaces. For profile locations see Figure 4-11.

5.3.3 Timing of paleoearthquakes

In order to determine long term slip rates it is necessary to establish the cumulative slip on the fault over a given time interval covering several events. Slip rate variability is best resolved if the slip accumulation can be traced back through several dated markers. Due to the pop-up nature of the uplift, a clear altitudinal separation of 2.3 m per event is achieved between each degradation surface suggesting that formation of terrace soils should be synchronous across the marker surfaces and clearly separated from markers above and below within the resolution of the climatic system. Aggradation or complex response surfaces such as these often provide an ideal opportunity to study a soils chronosequence (Bull, 1990; Tonkin and Almond, 1998).

The soils at Dalethorpe have been investigated by Tonkin (pers. comm.). The soils on the uplifted terraces are developed in loess and are classified as firm brown soils that are generally similar to two other firm brown soils. Of these, the Pleistocene Peel Forest soils incorporate shards of the 22.5 ka Kawakawa Tephra, whilst the Holocene to Late Pleistocene Gorge soils have a basal age of 12-14 ka. Dating of the fluvial / aeolian transition should provide a minimum age for coseismic uplift of a surface out of the floodplain and resolve this ambiguity. OSL sampling was thus carried out to constrain the minimum uplift age of the extensive B3 surface, for which the total uplift has been measured, by dating the loess deposits at the transition from fluvial to aeolian deposition.

The loess could not be directly sampled in the usual way because trenching of suitable locations was not permitted. To overcome this obstacle samples were collected using a sediment corer in a vertical auger drillhole. This technique is difficult because sampling is blind so the sampler has no feel for the proximity of the sampling tube to the gravel/loess interface. Apart from being a time line, this interface is also a dose rate boundary so it was important to remain clear of it when sampling. Two reconnaissance holes were drilled one metre apart using an Idaho auger and logged to determine the thickness of the loess based on the depth to the first fluvial gravels. Both holes produced markedly similar logs so a third hole was drilled and logged midway between the first two (Figure 5-6). The first gravel had been encountered at a depth of around 1.2 m in both reconnaissance holes so the samples were targeted for collection from the 0.5-0.7 m and 0.9-1.1 m intervals. Dating of two samples from the same hole was used as an indirect way of extrapolating

the age at which loess began accumulating on the stable surface without inadvertently sampling across the boundary. The hole was drilled to the upper limit of the sample depth and a sample was extracted using a 20 cm long, 5 cm diametre stainless steel sediment sampling tube attached to a push rod. The cleaned auger was then used to carefully extract a bulk sample from the same interval and the procedure was repeated for the deeper target depth. The hole was then drilled until gravels were encountered at 150 cm.

The samples were processed at the luminescence dating facility at Victoria University, Wellington, New Zealand and returned ages and 1σ confidence limits of 10.7 ± 0.6 ka for sample 1 and 18.7 ± 1.1 ka for sample 2. These ages extrapolate to an age of 22.7 ± 1.95 ka at the first gravels and 28.7 ±3.23 ka at the base of the hole on the B3 surface (Figure 5-7). Gravel may be pulled up into the loess by the action of frost or falling trees (Tonkin, pers. comm.) so without direct inspection it is not possible to determine what thickness of transition zone may be present before reaching primary fluvial gravel. In the light of this uncertainty, the extrapolated 22.7 ± 1.95 ka age of the first gravels is used as an indication of the latest date for abandonment of the B3 surface.

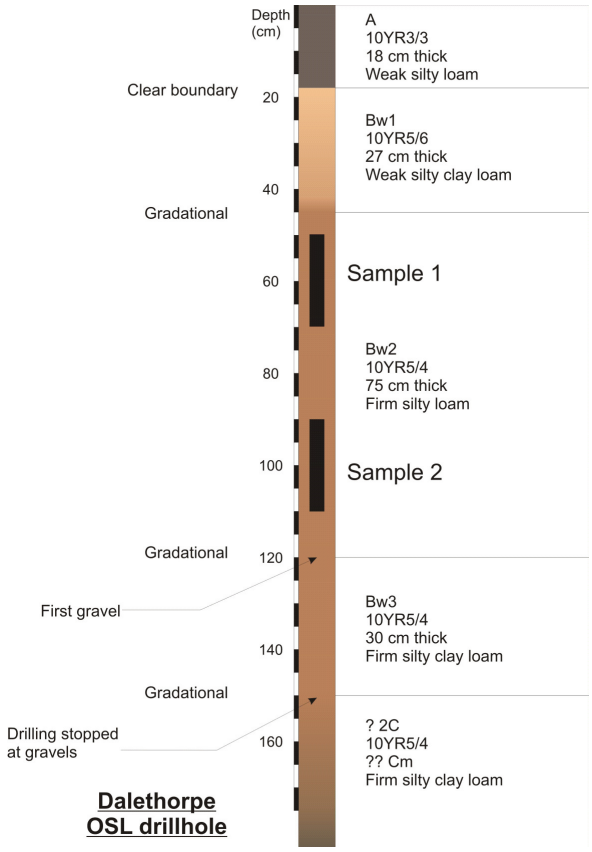

Figure 5-6. Auger hole log for OSL sample taken from surface B3 south of fault trace. Auger-hole log shows horizons, colours, thicknesses and textures, as well as sampling depths. Both samples are taken from the same auger hole.

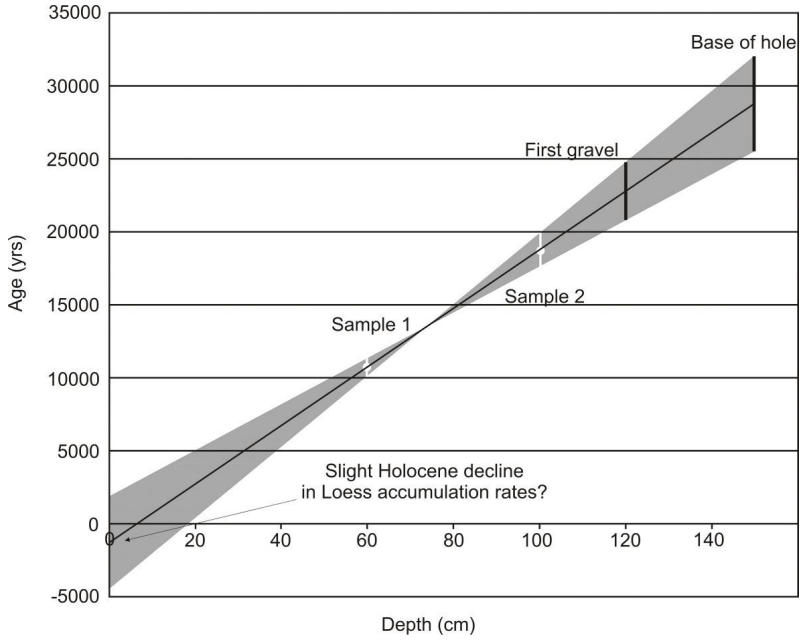

Figure 5-7: Extrapolated age of B3 surface, assuming fluvial / loess transition at first gravels

Dating of the abandonment of the B3 surface provides one part of a chronology that should ideally include dating of the last event. However, in the absence of robust dating of the last surface rupture on the SFD its timing can only be inferred. The SFD has certainly not ruptured since European settlement and the timing can be further constrained by considering the fault-zone morphology. The A terrace appears undisturbed but slip could be disguised by the fault passing through the dogleg that separates the north and south A surfaces. There is, however, no evidence of alluvium upstream of a sill of anything close to the characteristic 2.3 m in the modern river. Rather, the river is actively cutting a meander across bedrock suggesting long term folding in the footwall. The strath surface within the wedge, which is relatively flat elsewhere, is warped up by 2.5 m (almost exactly the same as the characteristic slip) over a distance of only 200 m and the river has incised a deep gorge through the uplift, which again suggests significant strain accumulation. This warping is interpreted in 5.3.2 above as including a large percentage of any pre-seismic folding.

Taken together the evidence suggests that no discrete displacement event has occurred since abandonment of the A surface. The last slip on the flexural slip shears forward of the MUT, as imaged on the A surface by Corboz (2004) are probably coeval with the last event. The slip occurred during occupation of the A surface but the river did not

immediately abandon the surface because the shears do not propagate to the surface. This probably reflects aggradation to raise the level of the river above the fault scarp dam. Shortly thereafter the river began incising, since which time it has incised >13 m into the wedge and < 11 m elsewhere.

If the timescale of the incision could be constrained it would provide a minimum age for the last event, although the observation above, that much of the likely pre-seismic strain appears to have already accumulated, suggests that the fault is nearing the end of its cycle.

Unfortunately, only ~40 cm of soil covers terrace A, which is unsuitable for OSL dating. The soil characteristics, however, suggest affinities with mid-Holocene soils (Tonkin, pers. comm.). The likely age can be rationalised somewhat by considering the river morphology. Campbell and Nicol (2003), working in the area of the Boby's Stream Fault (see review Chapter 6) documented accelerated incision rates of 100 mm/yr during precursor folding in soft Tertiary lithologies in the middle Waipara. The rate and width of precursor folding and a river's power to incise through it will vary with tectono-climatic setting and the lithology and rock mass character in the uplift. At the SFD, the Hawkins river is at least 2/3 smaller in flow than the Waipara River, whilst fresh Torlesse greywacke is almost 3x harder than any of the Tertiary cover sediments. Incision of 100 mm/yr is thus improbable and figures of 10mm/year probably represent a maximum. This reasoning suggests that a minimum of 1300 years must have elapsed since abandonment of the A terrace shortly following the last event. 2.5 m of warping in 1300 years would require fold growth of 2 mm/yr in the centre of the uplift. Weathering rind dating of boulders on the A terrace south of the river (Campbell, pers comm. - in progress) should further clarify the age of the onset of incision.

5.3.4 Uplift and slip rates

The net uplift recorded by the Dalethorpe terrace sequence over a minimum of 3 events since occupation of the dated B3 surface has been established to be 8.02 m (Table 5-1). This displacement yields a minimum calculated uplift rate since abandonment of the B3 surface (22.7 ± 1.95 ka) of 0.35 ± 0.025 mm/year. In the absence of a better understanding of the relationship between the base of the loess and the first gravel, this rate is based on the extrapolated age of the first gravel. Improved confidence in calculation of uplift rates would be served by dating a second marker. Nevertheless, the question of how the local uplift rate relates to slip rates on the fault itself remains uncertain.

5.3.5 Recurrence interval

Estimation of a recurrence interval (RI) for a fault implicity assumes that a particular site has a characteristic earthquake interval that is a function of a constant strain rate, and a characteristic fault strength and coseismic strain drop (Figure 5-8a). Unfortunately, however, these parameters are rarely truly characteristic. The strength of fault-zone rocks varies temporally due to such factors as fluid migration, which may lead to aseismic creep (Haney et al., 2005; Kanamori and Brodsky, 2004; Losh and Haney, 2006). Strain rate also exhibits temporal variability. Although the regional strain rate may remain uniform, large stress changes may occur on a fault due to activity on adjacent faults. This may dramatically affect the local rate of strain accumulation. Together, changes in fault strength and strain rate may conspire to produce short term variations in the long term RI trends (Kanamori and Brodsky, 2004) (Figure 5-8b). The long-term trends themselves may also be affected by regional tectonic perturbations such as plate vector changes.

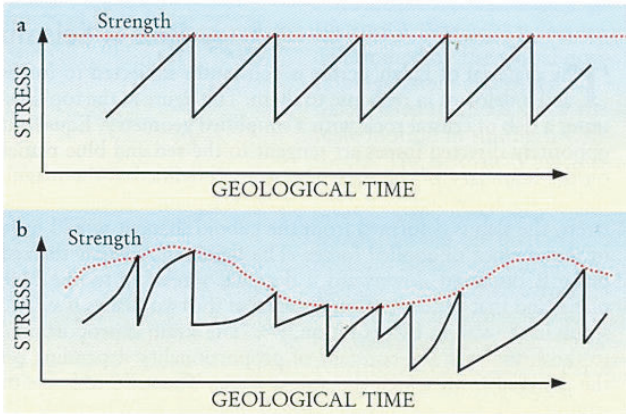

Figure 5-8. Stress changes and earthquake sequence. (a) Regular sequence. (b) Irregular sequence caused by the changes in loading rate and temporal variations in the strength of crust (after Kanamori and Brodsky, 2004, p.1437)

RI estimation is based on determination of the number of ground-rupture events within a given time frame, and the placing of constraints on that time frame. The validity of estimates is strongly dependent on acquiring a long, well constrained chronology of past events on a fault, although statistically the typical RIs of major earthquakes at a given site in a plate boundary setting are 100-1000 years (Kanamori and Brodsky, 2004). This site is clearly not typical as only 3 co-seismic events are recorded in 22.7 ka.

The recurrence interval is calculated here by simply dividing the calculated uplift rate (0.35 ± 0.025 mm/year) into the characteristic surface displacement. If the characteristic displacement is based on the last 3 displacements (2.67 m, Table 5-1), which postdate the dated surface, the recurrence interval is calculated at 7620 ± 500 yr. If the B3 terrace

was abandoned 22.7ka, this places the last event at approximately $22.7-(3\times 7.62)\approx 0.16\pm 1.5ka$. The proximity of these dates to the present day suggests that the system is just beginning a new cycle. This is not in agreement with field observations of extreme downcutting since abandonment of the A surface. If the long-term average displacement of 2.234 m is used instead, the recurrence interval becomes 6380 ± 430 yr, placing the last event at approximately $22.7-(3\times 6.38)\approx 3.5\pm 1.3ka$. This figure suggests the fault is well through its cycle and is in better agreement with field observations.

5.3.6 Paleo-magnitude

Published empirical relationships relate moment magnitude (M), surface rupture length, and maximum and average displacement per event (Wells and Coppersmith, 1994). These published relationships are used here to estimate the probable magnitude of events on this system (Figure 5-9). Based on the Wells and Coppersmith relationships, a surface rupture length of 11 km should produce an event of around M6.3 regardless of fault sense, whilst a characteristic displacement of 1.5 m on a reverse fault suggests a slightly larger event of M6.6, but is statistically related to longer faults with surface traces of >30 km. On this basis, the likely magnitude of previous events is thought to be approximately M6.35 ±0.15.

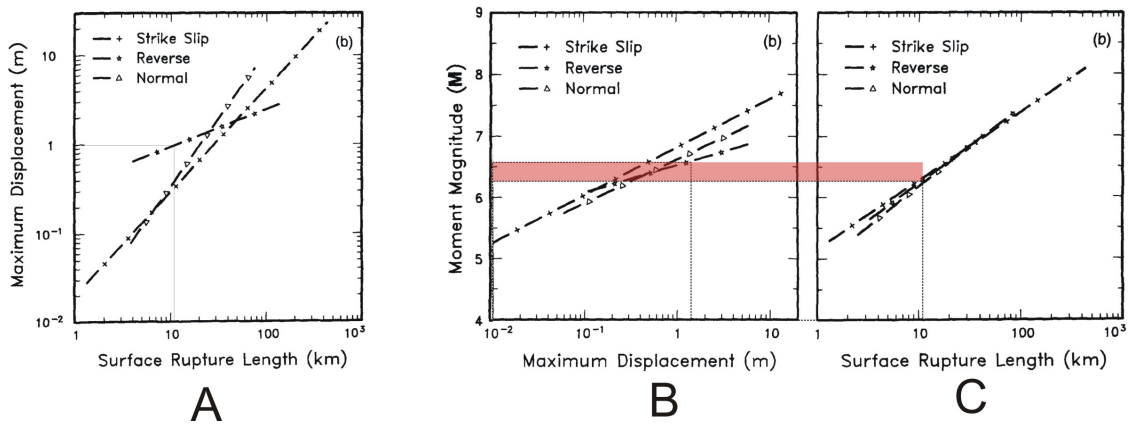

Figure 5-9: Selected fault/earthquake parameter relationships after Wells and Coppersmith (1994). A surface rupture 11 km length on a reverse fault is related to displacements of 1 m (A), and a rupture magnitude of M6.3 (C), not greatly different to the M6.6 magnitude associated with a displacement of 1.5 m (B). On this basis, a likely earthquake magnitude is M6.35 ± 0.15.

5.4 Kinematic observations and discussion

A greater understanding of the kinematics of the fault-zone, i.e. the spatial and temporal components of fault motion, can be gleaned from observation and analysis of the geomorphology although the level of survey data detail required for kinematic analysis is only available for the MUT/MDT wedge block.

A differential tilt, suggestive of rotation on one or both fault planes, can be observed and measured between the B surfaces of the MUT footwall and the surfaces on the wedge. The B3 surface on the wedge, for instance, is planar and continuous across most of the wedge and grades down to the southeast in what is clearly a combination of original gradient, uplift and tilting. It is defined by a strike and dip of 035/2.5SE. Even though the extent of the B3 surface suggests that the river achieved equilibrium prior to the subsequent event, there is a noticeable difference in orientation between it and the footwall B0 surface, which is oriented at 026/1.7SE. The 0.9° differential tilt angle between the poles to the two surfaces lies on an almost vertical plane normal to the strike of the fault oriented at 135/89.5SW. This suggests rotation of the pop-up wedge on the fault plane.

In addition to this differential tilting, both the modern and antecedent channels of the Hawkins River have asymmetric cross sections suggesting tilting to the north, a conclusion in agreement with the observations of trapped drainage on terrace A. This is in stark contrast to the lack of B and C surfaces in the south of the Upper Hawkins Basin, which show that the course of the river slipped steadily south until the river was cutting up against Bell Hill to the south of Dalethorpe Road. This south-slipping trend has been reversed since the abandonment of the A surface and the river is now developing slip off surfaces on the south side and cutting in hard against the abandoned surfaces to the north (Figure 5-4). This is probably due to the growth of a syncline in the footwall of the northwestward thrusting Bell Hill Fault.

Although the MDT is confidently mapped on the basis of a low velocity damage zone and structurally influenced geomorphic features, an alternative explanation that may explain both the high velocities in the wedge and the terrace attitudes has been proposed by Jocelyn Campbell (2008, pers. comm). Some of the apparent rotations on the terraces may be related to the listric ramp and flat geometry of the fault plane as shown in the cross section on Map 1. The nature of Torlesse greywacke is such that it will deform as a thick slab rather than as a layered cake. If a river such as the Hawkins is cutting straths across a

fault in a thick slab of Torlesse greywacke, which is passing up a listric thrust from a low angle decollement , the entire thickness of the slab will have to deform internally, and the straths will be complexly deformed rather than simply tilted as they pass round the bend. Typically such faults also flatten out as they break onto the ground surface forming a compound curve on the fault plane (Section AA', Map 1). In this case the internal deformation of the slab is further complicated as elements of the strath pass through the transition between the inner and outer arcs across the neutral surface from compression to extension. The result of this scenario is illustrated by a photograph of a sponge analogue on which straths have been sequentially drawn during increments of translation of the slab up a listric surface (Figure 5-10A). This physical analogue does not include flattening of the emergent leading edge, which would probably bow down the leading edge of the deformed strath. An AutoCAD drawing created by sequentially rotating points about through two rotation centres simulating a compound curve similarly produces the observed change from downstream convergence to downstream divergence, even though it fails to account for the neutral surface change (Figure 5-10B).

A key stumbling block in this study has been accounting for the apparently unrealistic magnitudes of observed coseismic uplift as measured by conventional techniques. This problem is related to the ambiguity surrounding the real fault model as discussed in the previous paragraph. Addressing these problems would thus be best served by constraining the geometry and kinematics of the fault at depths beyond a few tens of meters. Earthquake records may help. For instance, recent minor earthquakes in the Dalethorpe area suggest that displacement is progressing by creep of the upper plate, presumably currently terminating at the locked upper segment of the fault. If this is the case, how and when is that strain transferred into the emergent fault complex? Questions such as this provide abundant fodder for future researchers in this area.

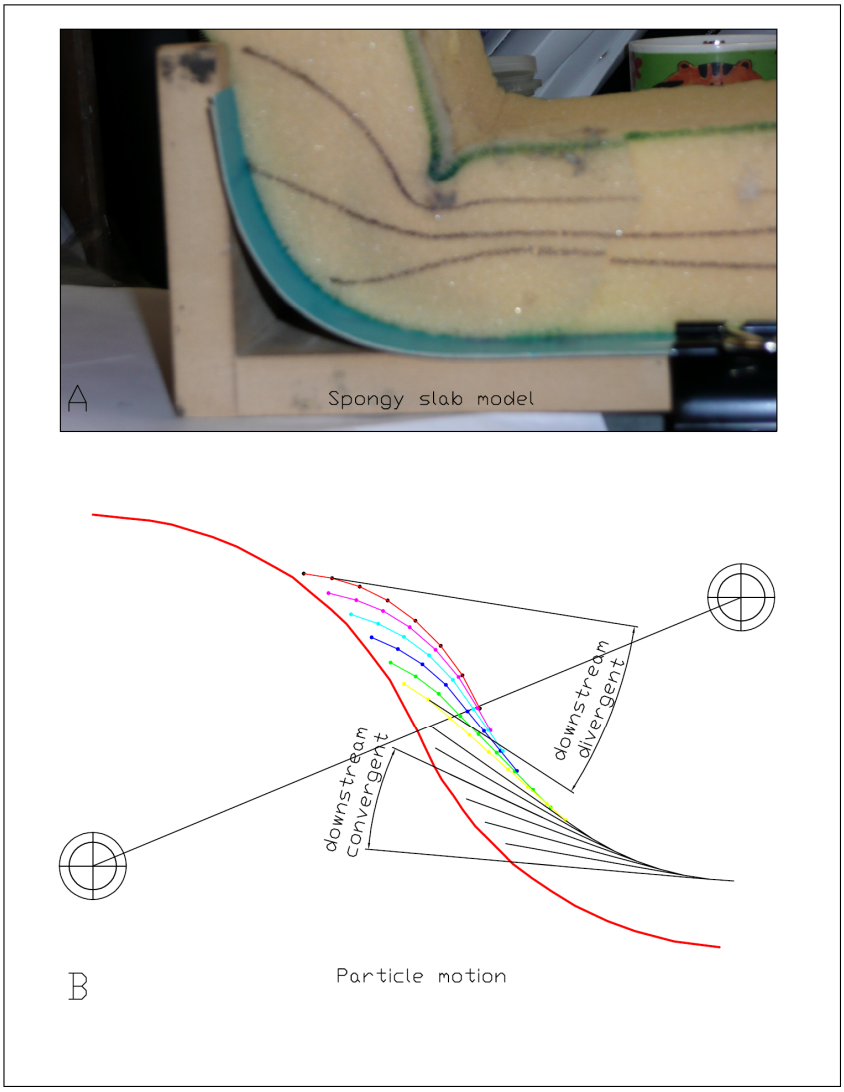

Figure 5-10: A) A slab of sponge as an analogue for a deforming slab of greywacke. The top two lines on the face represent the progressive deformation of a strath originally derived from a river profile graded across the slab at intervals during translation of the slab up the fault plane. Note the rapid steepening of the upper strath in the compression zone, compared with surfaces cut close to or below the neutral surface. B) particle motion drawing showing the behaviour of incrementally deformed straths close to the neutral surface. The effect is similar to that seen in the sponge analogue.

5.5 Conclusion

This chapter has presented a description and interpretation of the tectonic geomorphology of the SFD, leading to a first partial paleoseismic analysis indicative of the general level of activity. However, much remains to be done to better constrain the paleoseismic history. For instance, the elapsed time since the last event should have been determined. Achieving this is dependent on locating a reliable and datable trace of the last event. Unfortunately, landowner guidelines for our activity on the land presently preclude trenching of any suitable sites. This event timing is, however, probably closely related to the age of incision into the A surface, so any future last event determination will be based

on weathering rind dating of the A surface. This will in turn provide a starting point for paleoseismic analysis of the Bell Hill Fault, which bears heavily on the paleoseismicity of the fault complex as a whole. Once this work is complete, and once other selected surfaces have been dated with OSL (in progress), a more robust paleoseismic characterization of the SFD may be possible.

The paleoseismic characterization is also dependent on interpretations of the geometry of the structure, which is somewhat subjective. However, the deformation of the terrace sequence shows that an anticline or pop-up having this general style must be involved, whilst a broad imbricated deformation zone in the footwall is the interpretation most compatible with the distribution of low velocity material and the GPR evidence of deformation under the A terrace. The penultimate paragraph of section 5.4 above illustrates the uncertainties inherent in interpreting a model of faulting using conventional techniques, even in an area with apparently good exposure. This problem, together with the difficulty establishing a robust paleoseismic history, especially in terms of coseismic slip, provides a cautionary tale for land use planners. Prediction of the likely style and distribution of off-plane deformation will never be easy in such an active environment without considerable expense or recourse to historic earthquake data for the fault. Nevertheless, the concept of a 20 m setback can be seen to be fundamentally flawed. This conclusion is supported, not only by this study, but by work on the Algerian El Asnam earthquake (e.g. King and Vita-finzi, 1981; Ruegg et al., 1982; Yielding et al., 1981) and on the more recent Chi-chi earthquake (e.g. Kelson et al., 2001) among others.

6 MASW CALIBRATION AT THE BOBY'S STREAM FAULT, WAIPARA

6.1 Introduction

The previous chapter focussed on the investigating influence of shearing and cataclasis on the physical properties of a relatively uniform, high compressive strength rock type, Torlesse greywacke. The successful application of MASW to fault location is predictable in a setting where large velocity declines are likely but the same cannot be said in a setting where rocks are of a low initial strength. Fumal (1978) reported that velocity decline due to fracturing was related to the intact velocity. Soft, low velocity rocks should therefore show a lesser cataclastic velocity decline, which raises questions about the potential lower limit of resolution of a S-wave velocity-based technique such as MASW. In order to address this issue this chapter reports an exercise to explore the resolution of MASW when applied in soft rock and the potential for discriminating variance due to primary lithologies from the effects of cataclasis.

6.1.1 Geological setting and previous work

The Boby's Stream study area is located northwest of Amberley (Figure 6-1) and links into the Porters Pass Amberley Fault System (PPAFZ, Cowan, 1992) in North Canterbury, which is situated on the southeastern margin of the Marlborough Fault System (Figure 1-2). Several workers have previously studied this area or related faults (eg Campbell et al., 2003; Cowan, 1992; Cowan et al., 1996; Nicol, 1992; Nicol et al., 1994; Nicol and Campbell, 2001)) and their work demonstrates that the Waipara area of North Canterbury is presently being deformed as part of the plate boundary system. Measurable deformation probably postdates conformable deposition of the Plio-Pleistocene Kowai Formation (Cowan, 1992; Nicol, 1992) and may have initiated as late as within the last 1Myr (Nicol et al., 1994). Despite the youth of deformation in this area, present day strain rates in North Canterbury and especially along the PPAFZ are high (Wallace et al., 2007).

Figure 6-1: Location map for the Boby's Stream study area in North Canterbury.

Although measurable surface deformation is relatively recent, the Tertiary rocks of the Boby's Stream area record a history of at least three phases of deformation through the Tertiary. The Haumurian (Nicol) Broken River and Conway Formations of the Birch Hollow Basin were deposited in a half graben developed by continental crustal extension along the ancestral Birch Fault. The extension ceased before deposition of the Loburn Formation but only up to 30 Ma after the Gondwana breakup (Nicol, 1993). The Boby's Stream Fault is almost certainly a similar inherited structure now inverted from normal faulting to dextral oblique thrusting (Campbell et al., 2003). The Oligocene Amuri and Weka Pass Limestones, in the middle of the Tertiary cover sequence, are multiply fractured and faulted and contain abundant stylolitic pressure solution seams. These structures record a further two stages of deformation (Nicol, 1992) that is summarized in Table 6-1. This tectonic history and structural development has implications for the mechanical and elastic properties of the lithologies at Boby's Stream.

Surface faulting associated with plate boundary deformation in North Canterbury is dominated by NE striking reverse faults, many of which are closely associated with asymmetric folds. The northwestern limbs are typically steep (60° to overturned) and often faulted whilst the southeastern limbs are shallower, dipping at 10-30° (Nicol et al., 1994). A typical example is the Karetu Thrust, which shears out the steep NW limb of the Doctors

Anticline. These structures lie just to the west of the study area and are closely associated across the McDonald Syncline with the east facing Mt Grey Thrust.

Table 6-1: A summary of the brittle microstructures developed in Oligocene limestones of North Canterbury, their relative sequence of development, and estimated ages (after Nicol, 1992).

Tectonic structure	Estimated age	Deformation event
Fractures at low angle to bedding	Mid-Late Oligocene	Weak tectonic, NNE subhorizontal shortening associated with major extension in western New Zealand
Bedding parallel pressure solution seams	Pliocene	Lithostatic loading by overlying sedimentary cover
Orthogonal joints	Late Pliocene – early Pleistocene	Uplift associated with onset of northwest-southeast shortening at the outer edge of the plate boundary zone
Bedding normal solution seams and stylolites	Late Pliocene – early Pleistocene	Regional northwest-southeast principal horizontal shortening. Uniaxial strain.
Macrofractures, mesofaults and folding	Early Pleistocene – Recent	Folding associated with local north-south and east-west shortening and fracture development. Joints, fractures and bedding planes activate and become mesofaults.

The inverted Boby's Stream Fault is now a secondary, discordantly oriented structure of the Mt Grey/Karetu system that functions as a transfer fault (Campbell et al., 2003). It is north facing and strikes east-west along the steep northern limb of the Onepunga Anticline for >6 km east of Mount Grey. It terminates to the west at the Mount Grey Fault and at its eastern end disappears a few hundred metres to the east of a property known as The Deans. A 2 m high scarp can be seen outside the study area on a high terrace east of the The Deans, just before the fault disappears and a smaller 1m scarp on the low terrace at The Deans. Further west a high scarp crosses the Claremont property. The total throw of the fault and the amplitude of the anticline increase to the west (Nicol and Campbell, 2001) as the fault progressively overrides the companion syncline north of the fault. These secondary folds locally reverse and deflect the regional bedding orientations, which are otherwise related to the gentle <30° dip of an extensive Tertiary sequence southeastward at off the eastern flank of the north-striking Doctors Anticline (Nicol, 1992; Nicol and

Campbell, 2001). Along its length the Boby's Stream Fault breaks into several strands that offset, juxtapose and incorporate duplex blocks of the mainly soft Tertiary cover sediments.

The Boby's Stream Fault is closely coupled with the Mt Grey, Karetu and Birch faults. For instance, the broad convergence of evidence presented by Nicol and Campbell (2001) with that of Cowan *et al.* (1996) suggests that at least the most recent event on the Boby's Stream Fault at a little over 300 yr, and possibly another at a little over 2 kyr, were rapidly sequential to almost synchronous with events on the other three faults. The most recent event swarm falls within a window of 300-400 years BP on all four faults and landslide evidence presented by Campbell *et al.* (2003) places the Boby's Stream event at the younger end of this window.

In addition to that rupture, paleoseismic evidence has been documented for at least one and possibly two more events, including one at around 1000 yr based on trenching carried out on the Claremont property adjacent to Boby's Stream (Jocelyn Campbell (1995) unpublished data). Three trenches were excavated and a simplified log of trench 2, which is closest to the Randolph Downs study area, is provided in Figure 6-2B. Two shears are exposed, the southern of which has not moved recently. It dies out in clean gravels on the upthrown side that are not exposed in the full >2 m depth of the trench at the on the northern (downthrown) side of the second shear. The overlying gravels suggest that the rupture on the southern shear occurred whilst the river was still operating on the surface. The northern strand clearly offsets swamp fill silts that had to have accumulated on the downthrown side of an existing scarp. The sand lenses in the gravels below the swamps suggest that the river area was affected by residual flow and overbank incursions for a while after the river left this surface, presumably following shortly after the seismic event and the onset of rapid downcutting (Jocelyn Campbell, pers. comm.).

Geophysical imaging of the Boby's Stream Fault had been carried out prior to excavation of the Claremont trenches using ground penetrating radar (GPR) (Figure 6-2A) (Nobes and Campbell, 1994 - unpublished data, for location see Map 2). This is an area where bedrock lithology consists of Waipara Greensand on both sides of the imaged fault strand but it is unclear from the trenching how much bedrock penetration was achieved if any. The GPR images show significant reflector disturbances but although the resolution is good, the

reflections are open to (mis) interpretation. The approximate location of the easternmost GPR line was later trenched and the GPR to trench correlation was reasonable although the line had clearly been over-interpreted (Figure 6-2). The GPR also gives no indication of lithology.

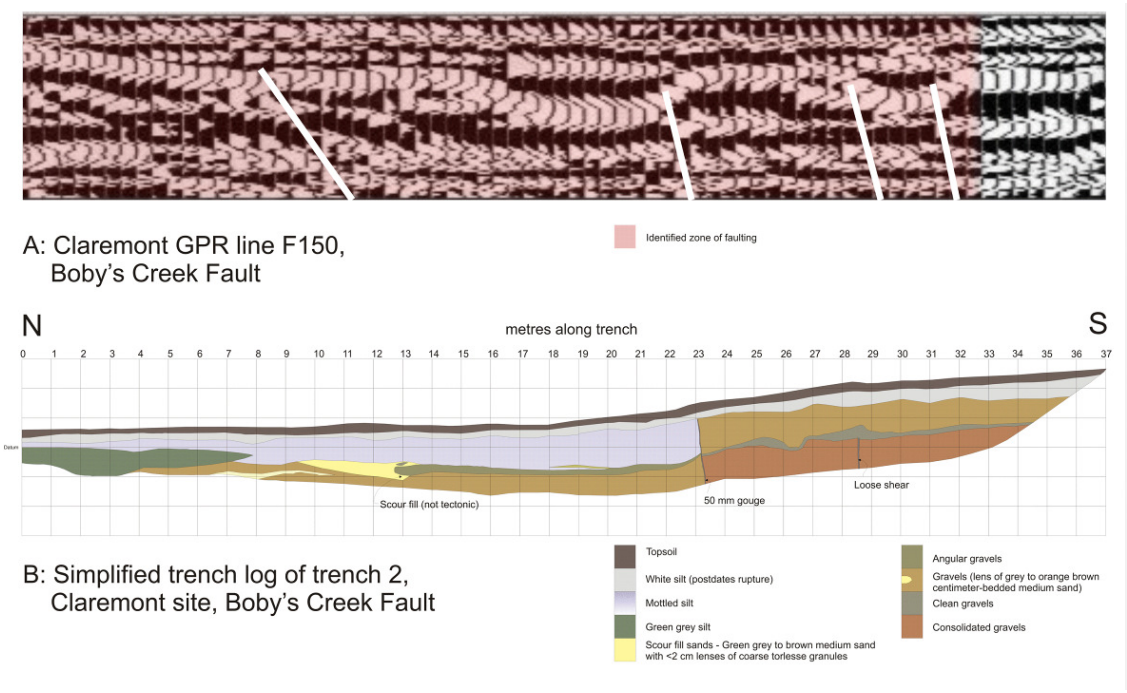

Figure 6-2: Same-scale GPR profile and trench log across the Boby's Stream Fault. Faults were inferred over a considerable distance along the line including at the locations marked in A. Two of these are clearly discontinuous sand lenses.

6.1.2 Scope and objectives

This geographically compact, structurally complex and lithologically variable setting was selected with two major objectives in mind. The first is to extend the calibration of MASW to rocks of the South Island Tertiary succession by using similar procedures to those used in Chapter 4. The second is to explore the limits of resolution of the MASW technique when applied in soft rock and to determine the potential for discriminating variance due to primary lithologies from the effects of cataclasis. This chapter thus reports an exercise to correlate the detailed S-wave velocity structure of the Boby's Stream fault-zone with the underlying rock-mass properties of the range of weak Tertiary lithologies and to relate the S-wave structure and rock mass properties to detailed geological mapping and geomorphic indicators of faulting and folding. The laboratory results are used to suggest general

relationships between S-wave velocity and rock mass properties by combining data from both this site and Dalethorpe. In order to allow a logical order from development through to evaluation of geotechnical/S-wave-velocity relationships, the rock mass characterisation programme is presented first. New approaches are also presented to characterization of soft rock and these are refined with appropriate laboratory testing. Derived relationships are then evaluated in the light of survey results by comparing laboratory results and predictions with survey S-wave velocities as they relate to the geological mapping. A geomorphological correlation is then presented, followed by discussion and conclusions.

6.2 Rock mass and material characterisation

No crosshole velocity testing was carried out on the Waipara soft rocks due to equipment failure during the fieldwork phase of the Boby's Stream study. A programme of laboratory testing similar to that carried out for Torlesse Greywacke was, however, carried out. The programme consisted of ultrasonic velocity testing of both intact and artificially fractured rock material from the various lithologies found at Boby's Stream. Laboratory testing was also carried out to establish relationships, if any, between rock properties and Ramset gun nail penetration, used as a measure of hardness. Lithologies not tested (reasons in parentheses) were the Broken River Formation (not found in the field area), Conway Formation (no intact samples obtainable except from concretions) and the Loburn Formation (no intact samples obtainable at all). Intact samples were collected for each of the other formations present in the field area and these were subjected to laboratory testing. 300 mm^2 blocks of mortar of variable strengths were moulded in plastic cubes to increase the amount and range of 'soft rock' available for nail penetration testing. The results of the laboratory testing programme are presented below.

6.2.1 Rock property determinations

Physical properties were determined for all core successfully drilled and the specimens were then reserved for UCS and fracture testing. The physical properties of the various lithologies are summarized in Table 6-2. Velocity anisotropy (S-wave splitting) was only investigated for two lithologies due to the difficulty obtaining sufficient core from three

Table 6-2: Summary of mean laboratory-determined physical properties of soft rock lithologies from the Boby's Stream Fault, with values from Rewanui mudstone (Campbell, 2008) and Torlesse greywacke (this study) for comparison. The predicted sonic S-wave velocity is calculated by subtracting the ultrasonic velocity percentage below 2750 m/s (Torlesse maximum ultrasonic velocity – this study) from 1100 m/s (fresh Torlesse sonic velocity). This assumes that ultrasonic velocities for intact rocks fall on a common strength-related trend and any decline is reflected by sonic velocity decline.

Unit	**Waipara Greensand**	**Amuri Limestone**	**Omihi Formation (Weka Pass member)**	**Waikari Formation**	**Mt Brown Formation**	**Mortar 1**	**Mortar 2**	**Mortar 3**	**Mortar 4**	**Mortar 5**	***Rewanui mudstone***	**Torlesse**
Lithology tested	Unusually well-indurated sample	Limestone	Limestone	Siltstone	Sandstone	mortar	mortar	mortar	mortar	mortar	*Mudstone*	*Greywacke*
Internal friction angle	31	30	36	34	35	46	35	43	43	40		*24*
UCS (MPa)	35	24	26	27	12	0.7	10.9	6.5	9.4	10	*47*	*82*
Schmidt hammer rebound	30	34	29	29	22	0	23	16	16	20	*40*	*54*
Ramset nail penetration	31	29	39	41	52	95	41	50	64	49	*20*	*5*
Bulk Density (kg/m^3)	2041	2065	1783	2083	2089	1560	1907	1890	1802	1853	*2546*	*2687*
Porosity	16	20	21	15	20	26	20	18	25	22		*0.2*
Intact P wave velocity	2283	2828	2419	2117	2049	1226	2275	2194	2513	2505	*3324*	*4850*
Intact S-wave velocity	1486	1571	1482	1408	1490	386	1480	1428	1455	1477	*2078*	*2750*
% below 2750 m/s	46.0	42.9	46.1	48.8	45.8	86.0	46.2	48.1	47.1	46.3	*24.4*	*0.0*
Predicted fresh unconfined sonic S-wave velocity	594.4	628.4	592.8	563.2	596	154.4	592	571.2	582	590.8	*831.2*	*1100*

orientations. The samples collected were typically-fractured fault-zone rocks and did not stand up well to drilling. No S-wave splitting was observed in Amuri Limestone or Waikari Siltstone, but the individual velocities were strongly related to the specimen UCS. The single exception was a high velocity Amuri specimen that failed along a pre-existing defect (Figure 6-3). Looking at the complete dataset including Rewanui Mudstone (provided by Campbell, 2008) and Torlesse values (this study), the relationship between S-wave velocity and UCS appeared weaker but could be improved by splitting results into two fields . The smaller field lay below a UCS value of 20 MPa and was dominated by the mortar specimens but included all the Mount Brown specimens and two Amuri specimens that had failed along pre-existing defects. The larger field lay above 20 MPa and included all the other specimens in a strong relationship. The fields are separated by up to 500 m/s. A direct comparison of Figure 6-3 with Figure 6-4 suggests that the scatter within the larger dataset is caused by lithology-specific trends that fall within the larger trend.

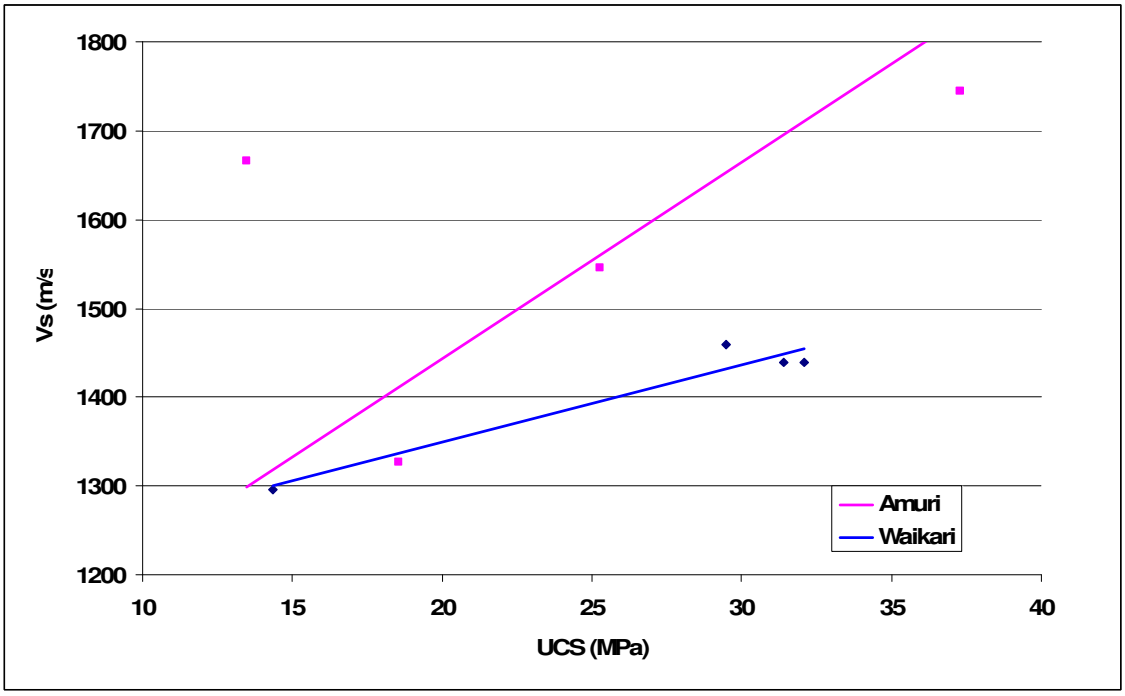

Figure 6-3: Correlation of ultrasonic S-wave velocity with UCS for four specimens cored from samples of Amuri Limestone and Waikari Siltstone. The Amuri outlier at 13.5, 1670 failed in UCS testing along a pre-existing fracture.

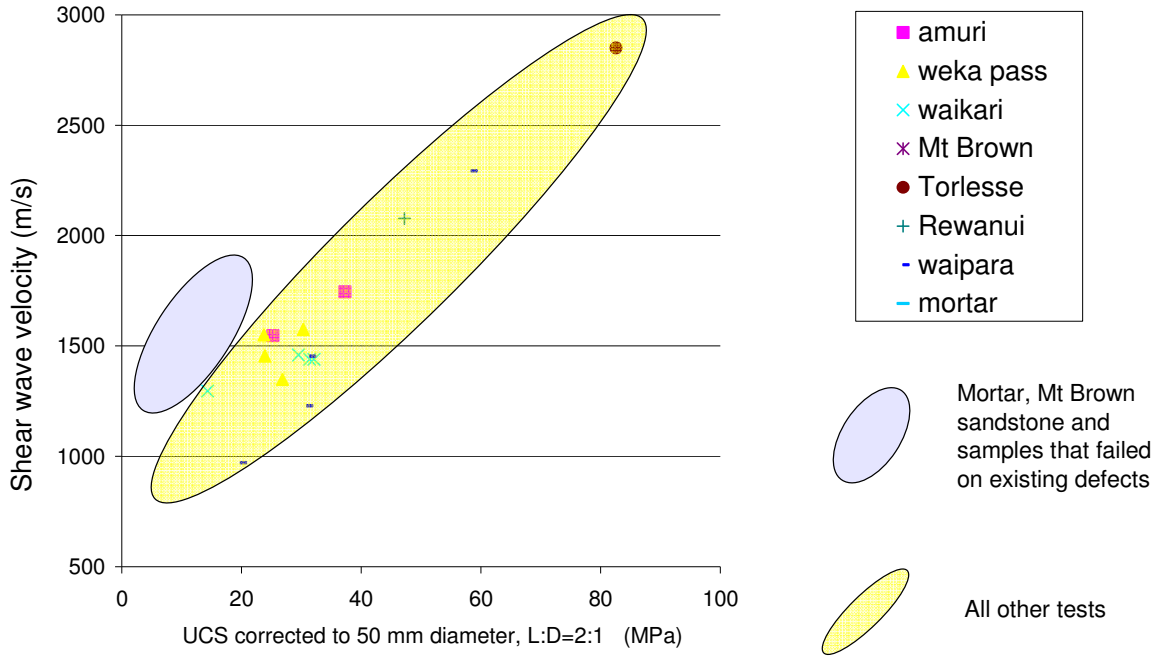

Figure 6-4: Correlation of ultrasonic S-wave velocity with UCS. The relationship splits into two fields, one dominated by the mortar and Mt Brown sandstone specimens. For discussion see text.

Predictably, the degree of S-wave velocity dependence fracture on fracture density demonstrated for Torlesse Greywacke could not be reproduced for any of the soft rock lithologies. In the cases where fracture dependence was shown it was significantly less clear than was demonstrated for greywacke. In the soft rock experiment the signal became completely attenuated at lower fracture densities, which limited the extent of fracturing possible in the experiment. Nevertheless, fracture-dependent velocity declines were observed that were compared with the decline observed in Torlesse and related to the strength of the specimen remnant left at the end of the fracturing experiment (Figure 6-5). The resultant plot shows unequivocally that S-wave velocity decline with fracturing is strongly dependent on the UCS of the specimen, supporting the work of Fumal (1978). The Weka Pass 1 specimen, however, behaved anomalously and displays a trend of increased velocity with increased fracturing. This may reflect strain hardening of the specimen in the uniaxial test rig controlling the ultrasonic S-wave velocity.

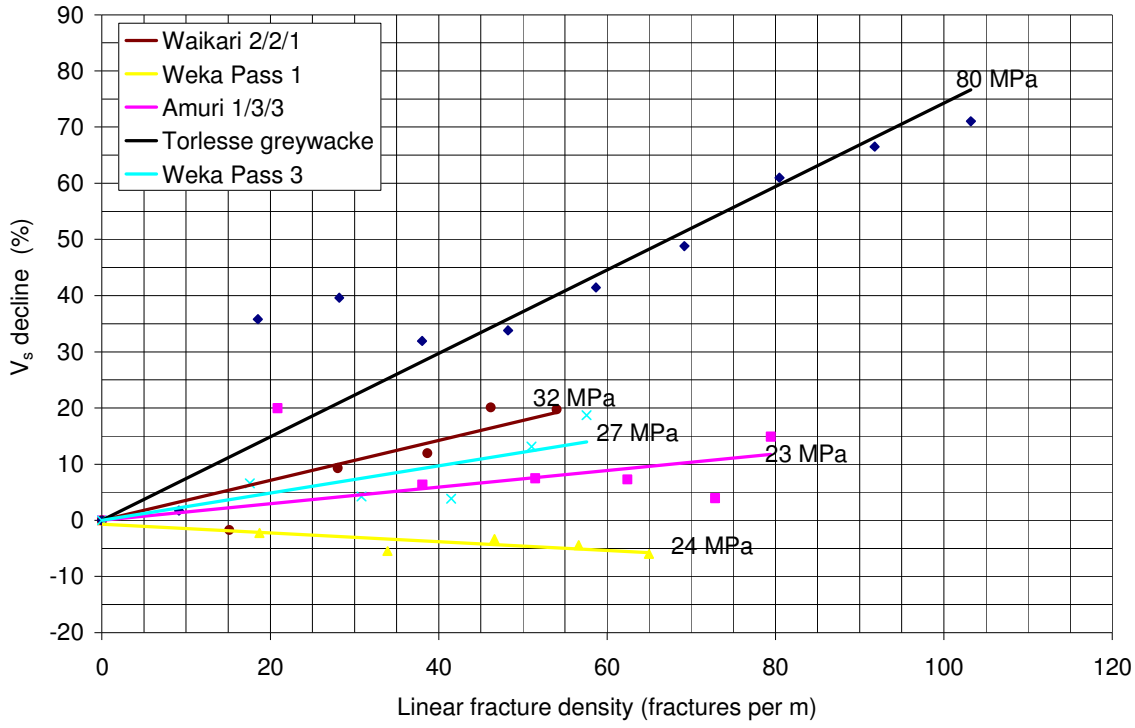

Figure 6-5: Observed velocity declines due to incremental increases in fracture density for three soft rock lithologies and comparative data for Torlesse Greywacke. Each trend is accompanied by the UCS of the sample remnant tested after the fracture experiment.

The data presented in Figure 6-5 were re-plotted using the final UCS values as the independent variable and an (arbitrarily chosen) percentage velocity decline at 50 fractures per metre as the dependent variable (Figure 6-6). The plot clarifies the suggestion in Figure 6-5 of a threshold UCS value above which the influence of fracturing becomes dominant and places that threshold at a UCS value of around 20 MPa. This figure was the UCS value across which the velocity field separation occurred in Figure 6-4. That separation was initially thought to indicate the unsuitability of mortar for this experiment, although it may be simply another expression of the 20 MPa UCS value of the fracture-hardness threshold. The plotting of the >20MPa field below the <20MPa field in Figure 6-4 can be rationalized by speculating that existing micro-fractures and other defects in the stronger intact samples are acting to reduce their S-wave velocities (eg Wulff et al., 2000). Such defects are ubiquitous in the soft rocks of the middle Waipara area (eg Nicol, 1992). If this reasoning is followed, the low 2750 m/s velocity of the greywacke relative to the 3500 m/s velocity published by Okaya *et al.* (1995) can be inferred to be probably due to micro-fracturing of the boulder.

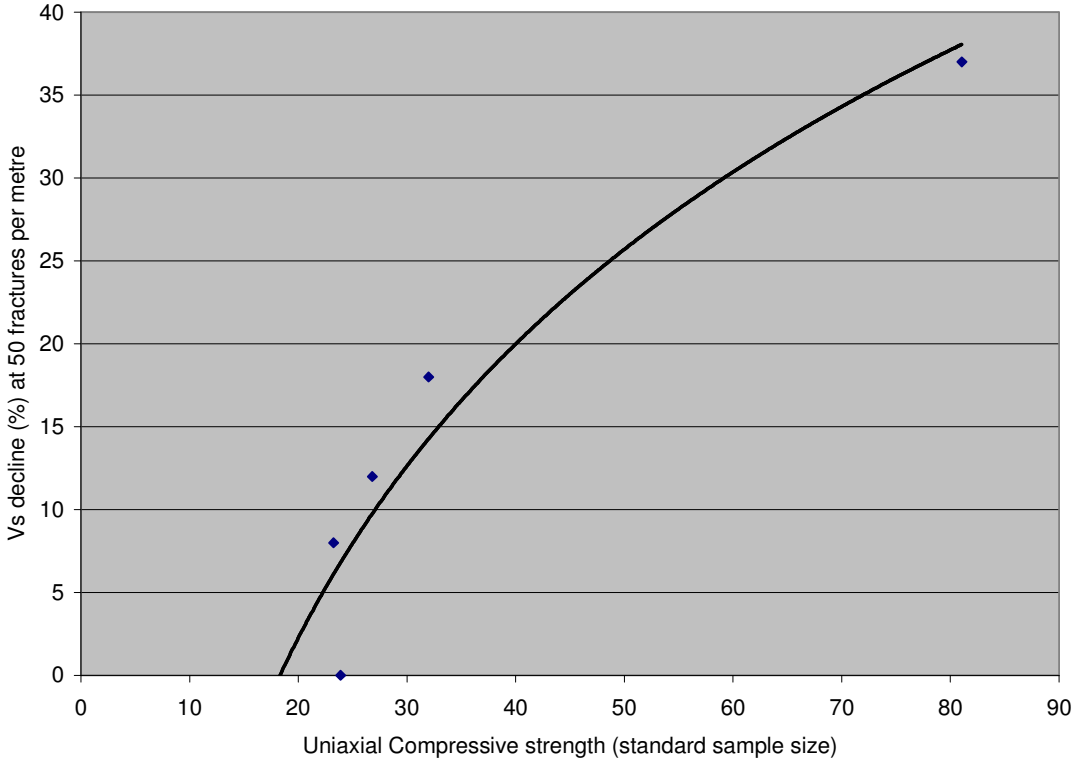

Figure 6-6: S-wave velocity decline at fracture density of 50/m, plotted as a function of uniaxial compressive strength. This plot suggests that a threshold exists at around 20 MPa, above which fracture density rapidly exerts a controlling influence on S-wave velocity and below which S-wave velocities are otherwise controlled.

A singularly useful relationship to establish would be one between sonic S-wave velocity and UCS and just such a relationship is proposed in Figure 6-7. The sonic S-wave velocities are calculated by subtracting the specimen ultrasonic velocity percentage below 2750 m/s (Torlesse maximum velocity – this study) from the Torlesse maximum near surface sonic velocity of 1100 m/s. This assumes that the ultrasonic velocity decline directly reflects the sonic velocity decline. Figure 4-24 in Chapter 4 suggests that the two are related and are probably separated only by weathering. In this instance the samples were not well rounded river boulders such as were used for much of the ultrasonic testing of Torlesse greywacke. Rather, they were taken directly from outcrop and carry the weathering signature of the outcrop.

6.2.2 Ramset gun calibration

The use of a Ramset gun is a new departure in geotechnical characterisation of rock material and masses and the tool was selected because of its potential to provide data in soft rock conditions where the Schmidt Hammer is less than effective. The technique was used alongside the Schmidt Hammer both in the laboratory and in the field. Laboratory

data (Figure 6-8 and Table 6-2) suggests the relationship between UCS and nail penetration can be defined as:

$$UCS = -29.567Ln(d) + 130.07 \qquad (5mm<d<90mm)$$

Equation 6-1

Where d is the penetration of the tip of a 65 mm nail driven by a Ramset 220 green cartridge.

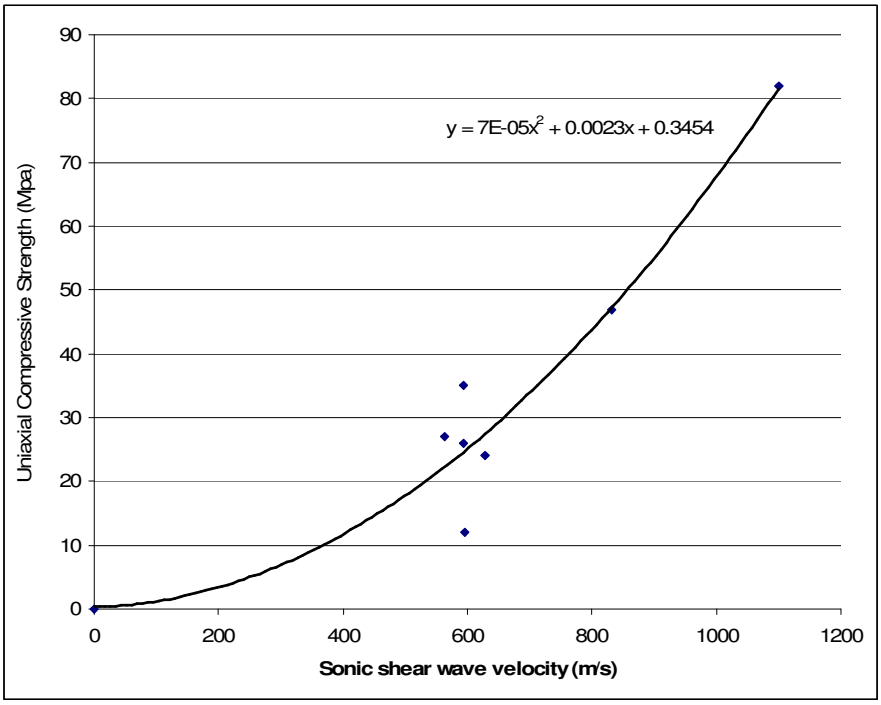

Figure 6-7: Proposed relationship between fresh sonic S-wave velocity and UCS. This graph is plotted using the predicted velocities in Table 6-2. These will be compared later with the MASW survey velocities.

Based on the discussion of relationships detailed above, it should be possible to predict nearest surface weathered S-wave velocities based on outcrop nail gun characterization using the relationship in Figure 6-9. Because nail penetration is strongly correlated with UCS, the threshold effects described earlier are noticeable on the plot. Predictions of weathered unconfined S-wave velocities are thus made for all lithologies but may be somewhat under-estimated for rock types that fall below the threshold. The weathered velocities are combined with the predicted fresh unconfined velocities from Table 6-2 to yield an unconfined velocity range for each lithology (Table 6-3, Figure 6-10), which can be compared with the near surface MASW velocities. Prediction of the velocity increase with depth is less feasible because the reason for velocity increases is not clear, although

they may be related to changes in effective stress and/or porosity due to increased overburden load (Fumal, 1978).

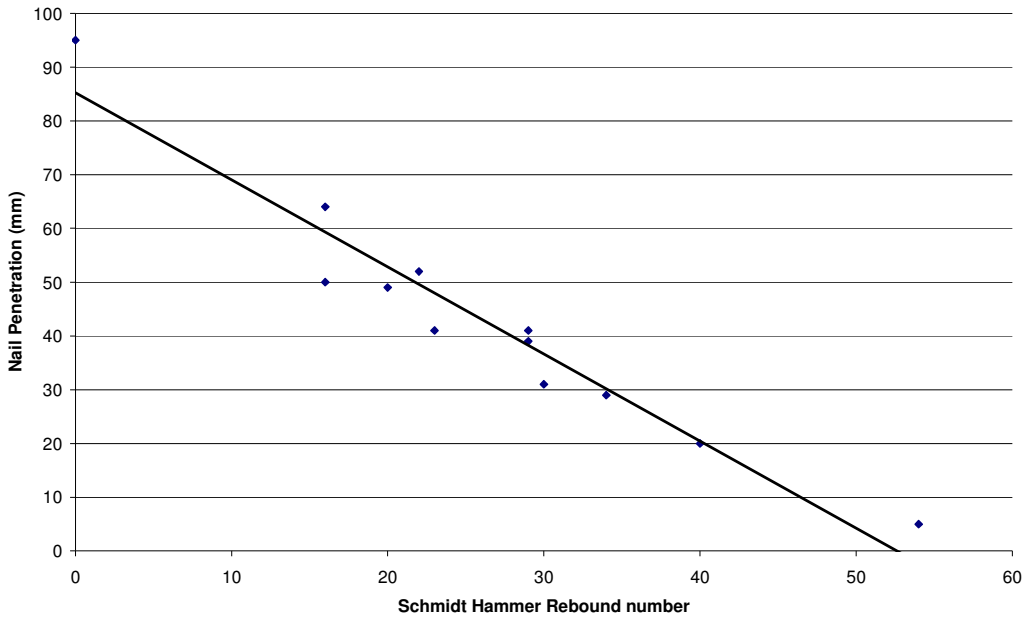

A

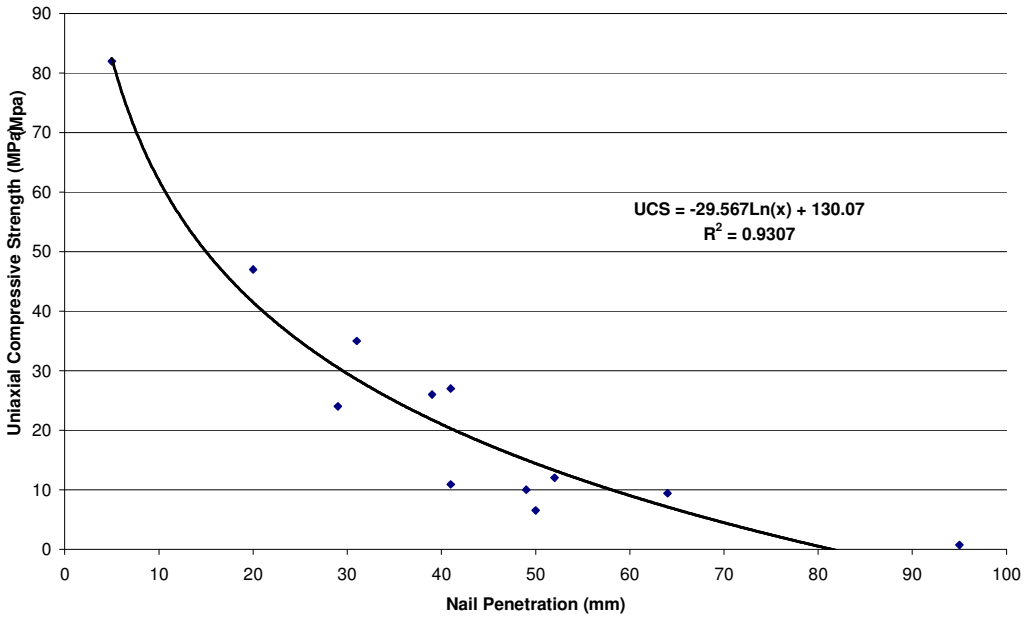

B

Figure 6-8: A) Nail gun penetration displays an almost linear relationship with Schmidt Hammer rebound number in laboratory testing. B) A strong relationship is also seen between UCS and nail penetration.

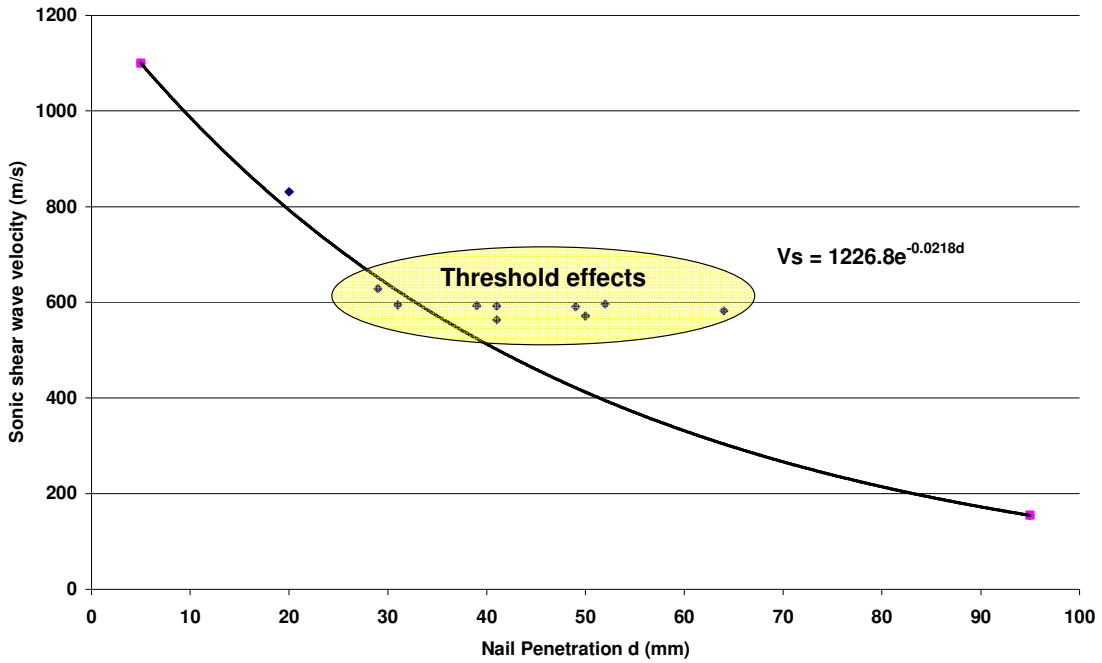

Figure 6-9: Predicted exponential relationship of S-wave velocity to nail penetration. This relationship does not, however account for threshold effects, which may perturb the velocity decline with nail penetration.

Table 6-3: Predicted unconfined S-wave velocity ranges based on laboratory velocity testing and nail gun penetration tests at free outcrop faces.

Unit	Average penetration	Predicted Weathered velocity	Predicted fresh velocity from Table 6-2
Weka Pass Limestone	64	302	593
Mt Brown sandstone	77	227	596
Amuri Limestone	83	202	628
Waikari Formation	86	190	563
Waipara Greensand	103	130	594
Loburn Formation	116	98	no data
Conway Formation	150	47	no data

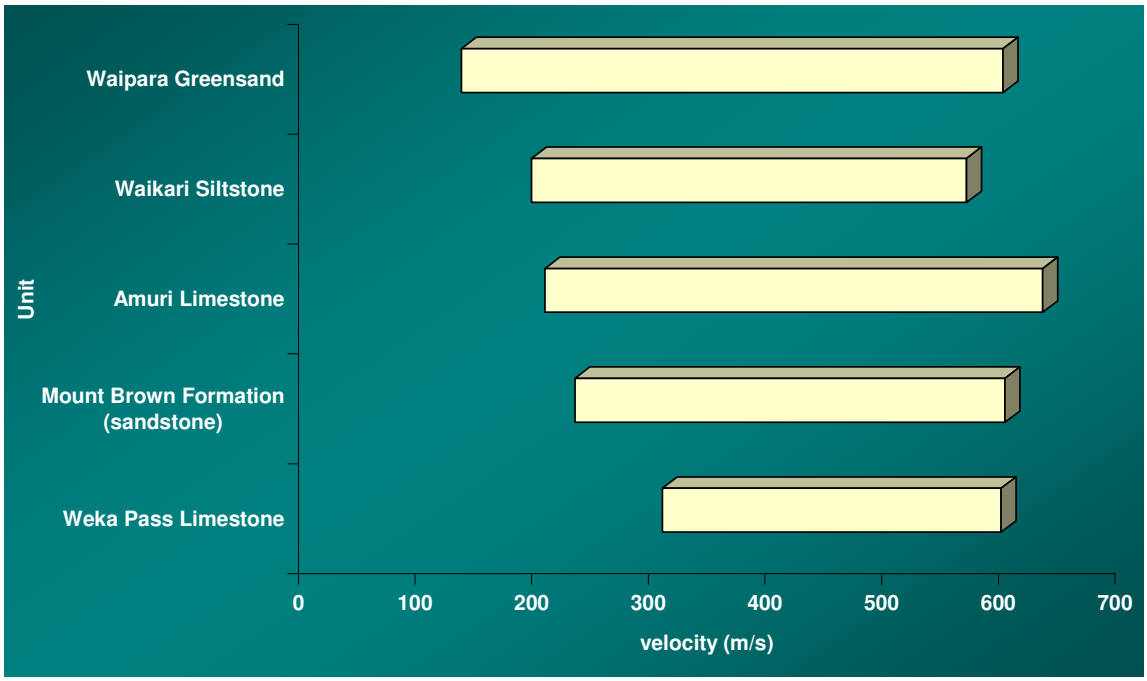

Figure 6-10: Summary figure for Table 6-3. These velocities straddle the higher alluvium and lower bedrock near surface velocities reported by Fumal (1978) and do not fit comfortably in either field.

6.3 MASW profiles

6.3.1 Site selection, geology and geomorphology

Six MASW surveys were carried out at three sites along the Boby's Stream Fault Locations are shown on Map 2 and Figure 6-14. The site characteristics and the reasons for site selection are summarized below. Figure 6-14 is located on p. 119 for ease of reference whilst reading this section.

6.3.1.1 The Deans

The easternmost study site is located at The Deans, a property that straddles the Waipara River downstream of the gorge in an area where a history of deep incision following the Pleistocene aggradation is recorded in a flight of degradation terraces preserved in the core of a modern meander (see Map 2, area of Detail B). The incision history at The Deans has been thoroughly documented (Campbell et al., 2003; Nicol and Campbell, 2001) using Torlesse Greywacke weathering rind data. It is strongly influenced by the growth of structures related to the Boby's Stream Fault. In summary, the early post last-glacial-maximum (LGM) downcutting was slow enough to plane the wide Mid-Waipara

surface over both the upthrust bedrock and the fault angle wedge of late Pleistocene aggradation gravels associated with the Boby's Stream Fault at The Deans. The significantly higher rate of incision, however, commenced ~2000 years ago and trapped the Waipara River in its present course (Campbell et al., 2003). This incision accelerated post 800 a and achieved its maximum rate between 250 and 400 a, during which period the most recent Boby's Stream Fault rupture occurred (see section 6.1). The rupture at The Deans occurred on a single strand, which is well defined on the high terrace and concealed on the low terraces. Within the area of the seismic surveys this strand juxtaposes Waikari siltstone on the hanging wall against a Pleistocene gravel wedge that overlies Mt Brown sandstone in a fault angle depression. The Deans is the only site selected in this study area where a well known fault scarp is preserved.

The bedform of the Waipara River at The Deans has been said to be more influenced by folding than by fault displacement (Nicol and Campbell, 2001). Before and after the last earthquake event the river incision that cut the high terraces was driven by aseismic folding and there are still strong indicators of active tilting. For instance, the slip off direction of the high terraces north of the river and those preserved closer to the modern river level appear to record a progressive southeastward migration of the meander by slipping off of the river away from the trace of the active fault. The river is still actively cutting southward and a deep hole has formed at the base of the cliffs on the outside of the meander bend. North of the fault trace the high terraces are visibly deformed and the treads seem to be tilting northeastward. This appears to be the underlying cause of the preferential erosion taking place in gullies located along the east side only of the high terraces. Trapped drainage is being constrained by tilting to flow eastward along the base of the terrace risers.

The trace of the fault does not disturb the lower terraces and its location as it passes through The Deans homestead is unclear. The area surrounding the homestead was in the active floodplain of the river until 230 ± 40 yrs BP (Nicol and Campbell, 2001) and the fault trace has been comprehensively removed. A small degradational terrace scarp strikes northeastward across the north side of the landowners house. Its location just north of the strike projection of the fault has caused significant light-hearted speculation as to its nature. A large isolated block of Mount Brown Formation limestone, of unclear origin, looms over the house a few metres south of the scarp. A block dropping from the ridgeline above the road is unlikely to have survived, not only intact but at a reasonable approximation of its original bedding orientation and carrying its gravel cap. An alternative explanation requires the block to be transported several hundred metres along the strike of the fault in a small duplex. Careful mapping of the

inferred along-strike extension of the fault confirms that this is probably the correct interpretation. An undisturbed landslide deposit lies across the projection of the fault approximately 50 m east of the house. This landslide was cited by Nicol and Campbell (2001) as stratigraphically constraining the youngest date for the rupture that created the scarp on the high terraces.

The close association of the river and the fault at The Deans location provides an excellent opportunity to satisfy the requirements for MASW testing and calibration. This site also provides an opportunity to address the issue of whether or not MASW can be used across a fault scarp. Two MASW surveys were run at this site. The first survey (D1) was run across the fault scarp on the high terraces, thus tackling the outstanding issue of whether or how topography impacts adversely on a shallow surface wave survey. The second (D2) was run along the driveway at The Deans homestead, parallel to the river. This was sited to potentially intersect the projection of the fault trace and also to cross the small scarp along the front of the house and thus confirm its nature.

6.3.1.2 Limestone Hills

West of The Deans, the fault sub-parallels a meander bend in the channel of the Waipara River before passing westward out of the river bed and crossing the road to the north of the Limestone Hills homestead. Like The Deans, the Limestone Hills location is closely associated with the river, but it is lithologically distinct. Just to the north of the Limestone Hills homestead an active strand of the fault can be seen thrusting limestone over the same Pleistocene fault angle gravel wedge seen at The Deans (Figure 6-11), but this time the gravel overlies Waikari Siltstone. A single line, LH, was run along the road at this location. Geological mapping shows that where the active strand crosses the road a small amount of greensand may lie between the limestone and the fault in the core of the Onepunga Anticline. Unlike the single strand mapped on The Deans, a second vertical strand in the hanging wall is mapped through the limestone and greensand and must also cross the seismic line. The fault scarp or scarps are not preserved at this location although the along-strike projection of both strands of the fault through the seismic line can be confidently inferred based on river outcrop and mapping. Limestone Hills has the added advantage (or challenge) of providing an opportunity to test the technique on a public tarmac road.

Figure 6-11: View looking east of Amuri Limestone thrust over Pleistocene gravels at Limestone Hills. The MASW survey was run along the road that can just be seen in the bottom right of the photograph. For photo location see Figure 6-14.

6.3.1.3 The Quarry

A short line (line Q, Figure 6-14) was acquired in the quarry just south of the fault. The quarry was originally excavated to recover Amuri Limestone for agricultural lime and is more than 30 m deep. Weka Pass Limestone can be seen capping the western wall of the quarry, which together with the depth of the quarry suggests that Karetu Sandstone is not far below the surface. Wrapped around the eastern side of the hill into which the quarry is excavated is an artificial fill terrace comprised of waste quarry rock. An MASW profile was run partly on the quarry floor and partly on the artificial fill terrace. It was run to facilitate correlation of the quarry rock mass properties with the seismic velocities but proved extremely difficult to process, particularly where the array was centred over fill material. Nevertheless, the results are presented to allow an evaluation of the reasons for the problems and the utility of MASW on cut and fill sites.

6.3.1.4 Randolph Downs

West of Limestone Hills the fault crosses a slight saddle to the north of the quarry before swinging slightly to strike parallel with Boby's Stream. The fault and the hinge of the Onepunga Anticline are repeatedly crossed by the antecedent Boby's Stream over the next few kilometres. The first crossing west of the saddle is the third location chosen for MASW surveying at the Boby's Stream site. Four strands of the Boby's Stream fault are mapped crossing the site (Figure 6-14), which is complex and selected to provide the ultimate test of resolution for the technique in a logistically, geologically and topographically challenging site with limited space (Figure 6-12). All four strands are considered likely to be close to or below

the resolution limits of the MASW technique. Two overlapping seismic lines were run because no clear path was available to transect the full width of the fault-zone. The southern strand of the fault, which crosses the centre of line RD1, is completely contained within outcrop of the Loburn Formation, a soft, grey, thoroughly sheared jarositic mudstone (Figure 6-13). A second strand, thrusting Loburn Formation northward over Waipara Greensand, crosses a small, steep-sided terrace remnant at the northern end of line RD1. This terrace remnant is a difficult site for seismic surveying due to the likelihood of backscattered noise from the terrace edges and is also challenging due to the similarly soft nature of the juxtaposed lithologies. Line RD2 crossed the third and fourth faults, a small Amuri Limestone duplex separating the Waipara and Waikari Formations in an abandoned meander several metres below RD1.

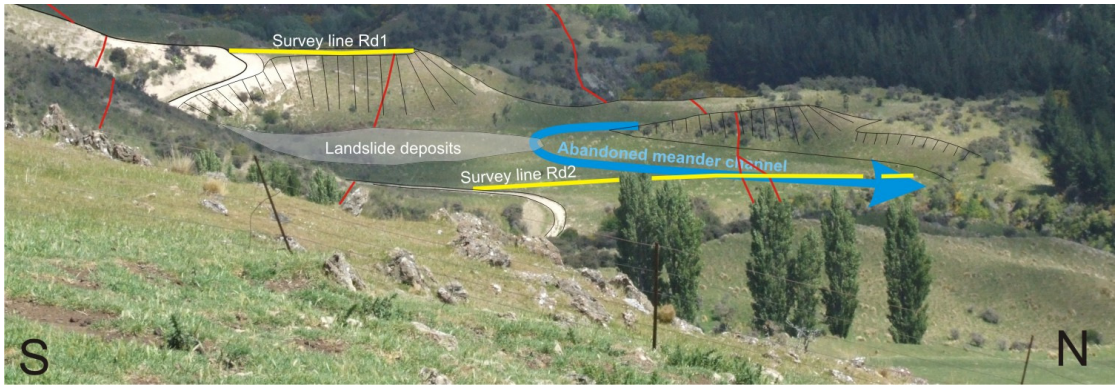

Figure 6-12: Photograph looking west along the Boby's Stream Fault at the Randolph Downs site and illustrating the complicated (from an MASW perspective) topography and structure. The visible section of survey line RD1 is about 30 m long.

Figure 6-13: Photo towards 90° of sheared Loburn Formation showing sheared relict bedding planes at <1 cm spacings picked out by limonitic weathering. The whole outcrop is chopped up by small to medium scale conjugate shear planes that render it virtually isotropic (white circle shows typical debris), but discrete folded shear planes such as the white line can be traced through the outcrop. A fault juxtaposing SE dipping Conway formation against the steeply north-dipping Loburn Formation is located just outside the right of the main photograph. For photo location see Figure 6-14.

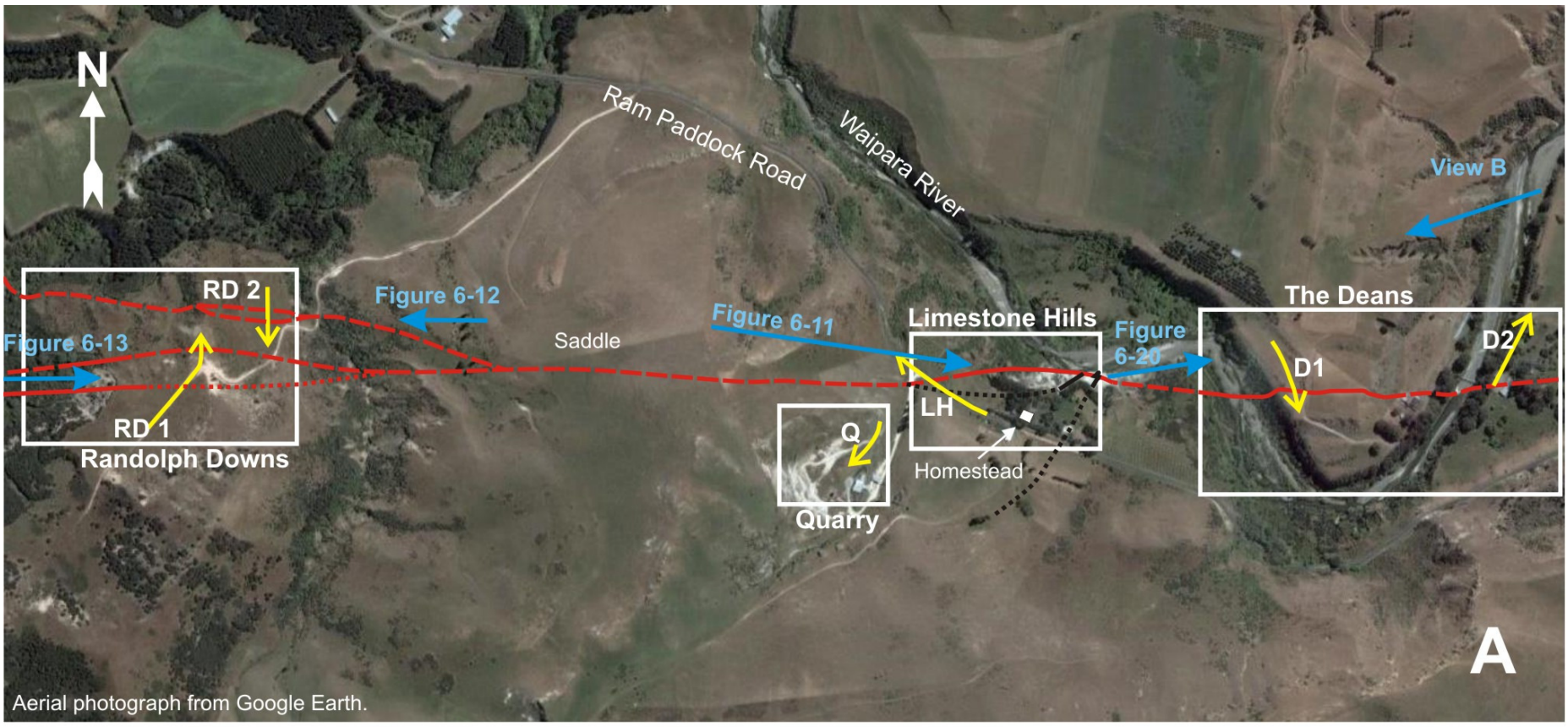

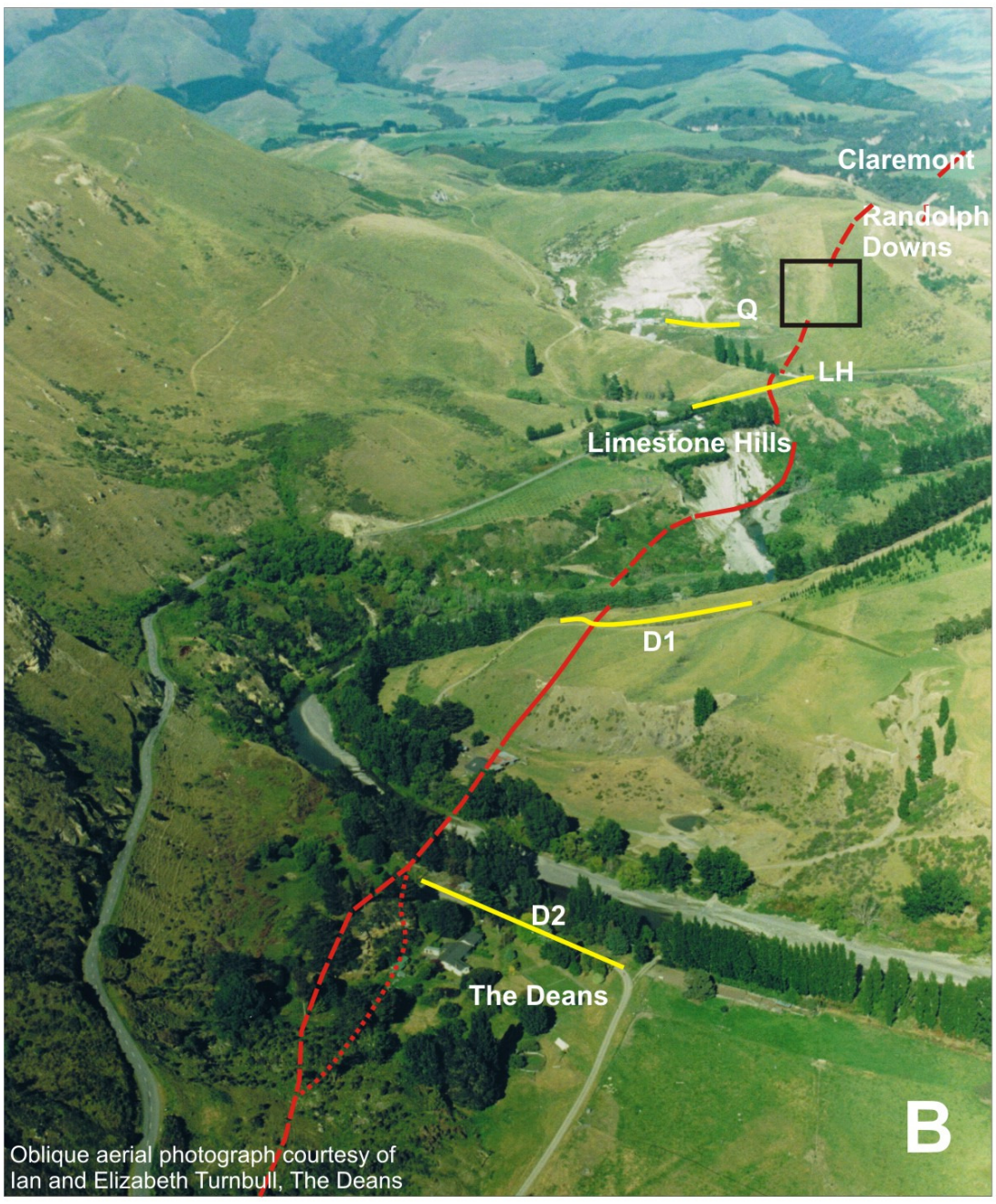

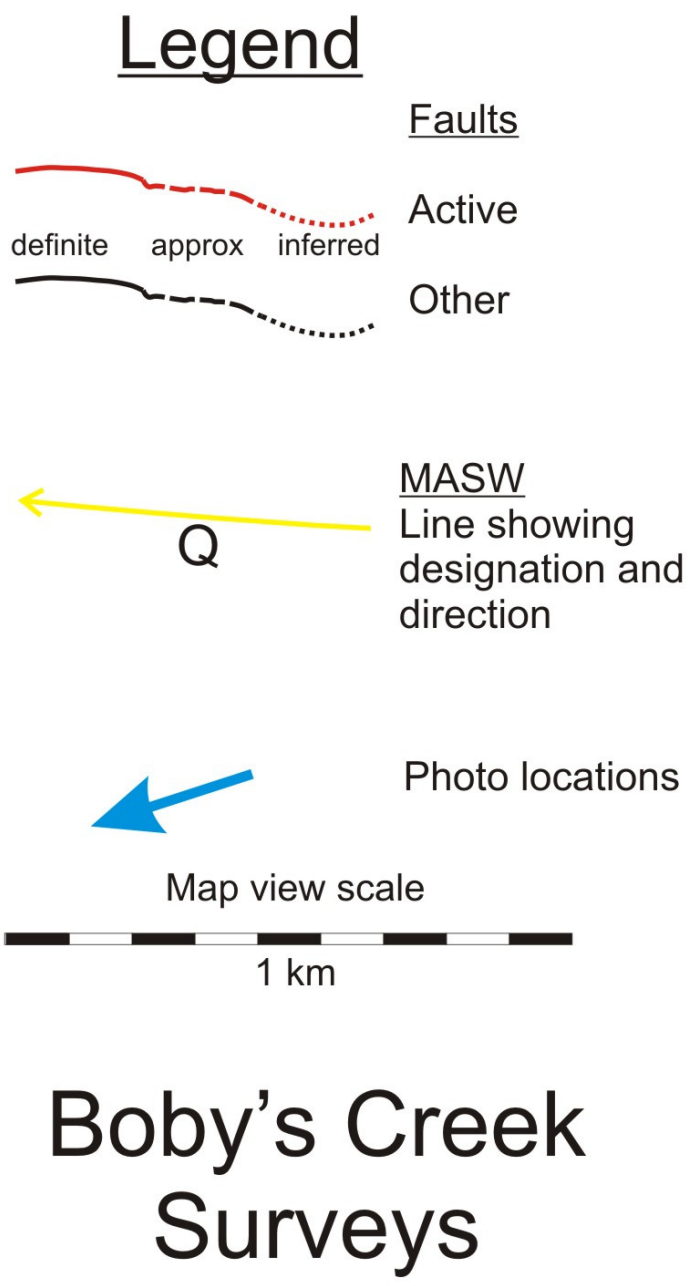

Figure 6-14: Aerial (A) and oblique aerial (B) photographs of the study area. The Deans homestead can be seen in the foreground with the duplex block of Mt Brown limestone south (left) of the house. Beyond The Deans, the fault passes through the large river outcrop in the middle distance below the Limestone Hills homestead. The fault then passes up the hill to the north (right) of the quarry, cresting the hill just south (left) of the Mt Brown limestone bluffs. As it passes up the hill the fault marking on the oblique photo is interrupted at the black rectangle to highlight a change in vegetation colour across the fault between Amuri Limestone (left) and Waikari Siltstone (right).

6.3.2 Data collection

The seismic data for the six survey lines were acquired over two two-day periods, an interval made overly long because it included an attempted active/passive survey on Ram Paddock Road in conjunction with the LH survey. The passive component of the survey was unsuccessful due to incorrect acquisition procedures so only the active component of the LH survey was processed. Where two lines were run close together they were run in opposite directions (Figure 6-14). Most of the surveys were carried out using the land streamer but the condition of the tussock on the site of the RD2 survey was unsuitable for simple pressure coupling, even after mowing the survey line with a light tractor and slasher. At this location the streamer was used as a towable tape measure and the geophones were dismounted and planted (Figure 6-15). The mowing paid dividends because small geophone spacings could be reliably maintained. Where the RD1 survey negotiated a tight bend the array centre points were pre-painted and the array was incrementally manually rotated along with the shot point to keep the survey linear.

Figure 6-15: View looking south along the mowed path of survey line RD2. The site was thickly grassed with springy tussock and pressure coupling using the land streamer was ineffective. Field assistants Rob and Hoody are planting the geophones next to the sleds on the towed streamer. The streamer is located on Waipara Greensand whilst the outcrop in the background is sheared Loburn Formation mudstone.

The lines acquired over the first two day period (LH, Q, RD1) were surveyed with 1 m geophone spacing but, following processing of the Taieri Ridge line (Chapter 7) in the interim period, the array was shortened to 0.5 m spacing for the remaining surveys. All surveys were acquired following the roll along methodology outlined in Chapter 3 and no on-site calibration was carried out. Cultural noise included several stock trucks (LH) and a minimal amount of stock movement (D1 and 2). The survey acquisition parameters for the Boby's Stream surveys are laid out in Table 6-4.

Table 6-4: Acquisition parameters for Boby's Stream MASW surveys (with ref to Fig 3.4).

Survey line	D1	D2	LH	Q	RD1	RD2
Acquisition	24 ch	24 ch	24 ch	24 ch	24 ch	24 ch
Receiver spacing (*dx*)	0.5 m	0.5 m	1 m	1 m	1 m	0.5 m
Aperture/ Array dimension (*D*)	23 m	23 m	23 m	23 m	23 m	23 m
Near offset (*x1*)	10 m	10 m	10 m	10 m	10 m	10 m
Shot spacing	8 dx (4 m)	8 dx (4 m)	4 dx (4 m)	4 dx (4 m)	4 dx (4 m)	8 dx (4 m)
Sampling interval (ms)	0.25	0.25	2	1	1	0.25
Recording time (ms)	1000 ms	1000	1000	1500	1500	1000
Number of records	35	30	38	18	39	25
Survey length	136	116	148	72	152	96

6.3.3 Processing

The seismic records were pre-processed and dispersion curves were extracted following the methodology outlined in Chapter 3. Received fundamental mode bandwidths varied widely and are given in Table 6-5. Surface wave coherence was generally better than was observed at Dalethorpe. Once again, however, systematic trends could be observed in the raw data that were reflected by the subsequent variations in the processability of the data. The records from the D1 line, for instance, fell into 3 categories. In category 1 were the majority of records from the centre of the line, which were linearly coherent and produced normal dispersion curves (Figure 6-16A). Category 2, the expected scattering and phase velocity drop in the proximity of the fault scarp materialized only on record 253 (Figure 6-16B). Swept frequency records for record 253 and 243 (20 m away from fault) showed little obvious variation (see again Figure 6-16) but the dispersion curve picked for record 253 showed reduced phase velocities. The third category was the records displaying the lowest phase velocities to depth, which were recorded from similarly scattered records at the opposite (northern) end of the line.

A Table 6-5: Typical fundamental mode bandwidths for Boby's Stream MASW surveys. Coherent energy in many cases covered ranges of only 10 Hz within these ranges.

Survey	Min Hz	Max Hz	Surface lithology	Range Hz	Comment
D1	15	40	Kowai Formation Waikari Siltstone	25	
D2	5	30	Recent alluvium	25	
LH	10	30	Waipara Amuri Weka Pass	20	
Q	20	35	Fill Amuri Limestone	15	Not processable
RD1	5	40	Loburn Formation	35	
RD2	5	40	Waipara Greensand Waikari Siltstone	35	

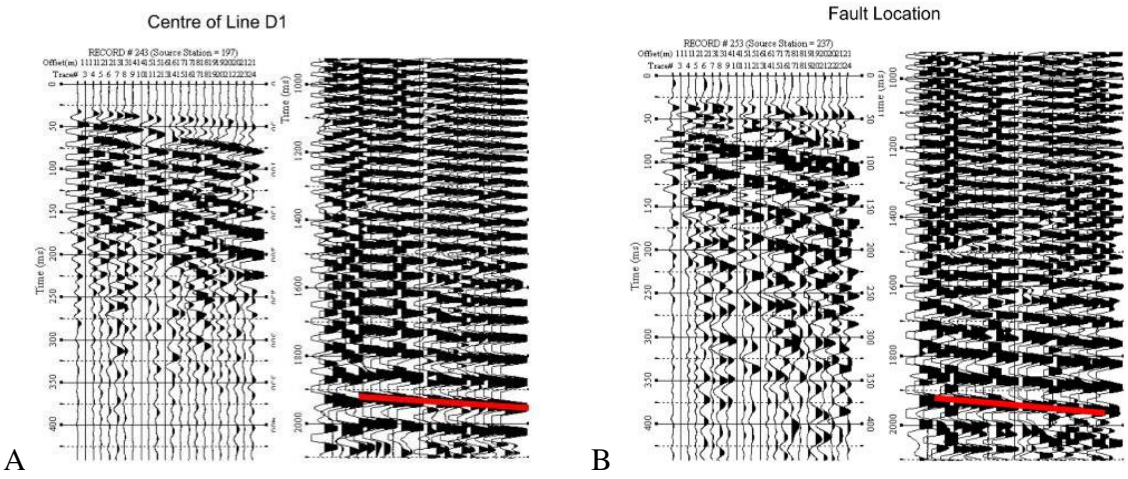

Figure 6-16: Shot records and associated swept frequency records from D. A neutral position in the line at shot gather 243 (A) shows little scatter compared with the fault related scattering of record 253, collected astride the fault (B). The scattering has little apparent influence on the velocities (event slopes) in the swept frequency record.

Although clear systematic changes were observed on the D1 line, the general lack of scatter aided dispersion curve extraction. The D2 line on the other hand was more difficult to process. The records were scattered for most of the line and higher modes dominated at frequencies greater than 30 Hz. Two sections of the line, centred on stations 40 and 140, were affected by higher modes at frequencies >10 Hz, although the fundamental mode velocities were low enough that the higher modes could be effectively removed by f-k filtering.

The records from the Ram Paddock Road line (LH) lost coherence over two sections, one early in the line between records 4 – 8 and one over an almost 30 m wide zone between records 17 – 23. The first zone was reflected by a change in Rayleigh wave phase velocity but dispersion curve velocities varied little across the second zone. The dispersion trends in the second zone were similar to but significantly more scattered than those observed on the undisturbed parts on the line to either side.

The quarry line yielded useful dispersion curves only for the first few records, specifically those acquired over fill material rather than the quarry floor. Although the signal was very scattered in the fill, it generated a weak but coherent dispersion curve (Figure 6-17A). The curves generated for the quarry floor, on the other hand, had strong signals but displayed large abrupt modal (velocity) jumps of up to 100% in the middle of the frequency range. At higher frequencies the dispersion returned to fundamental mode (Figure 6-17B). This type of response has been shown to be caused by large velocity reversals or contrasts causing the layered system to vibrate anomalously and higher modes to propagate with significant energy (O'Neill and Matsuoka, 2005) (Figure 6-17C and D). Such an effect may explain why the quarry floor responds so differently to the fill. The Karetu Sandstone, a greensand unit, is mapped just a metre or two below the Amuri Limestone of the quarry floor and this may result in a high velocity cap such as is seen in Figure 6-17D. The fill velocity will be much closer to and probably less than that velocity of the greensand, and thus significantly less than the velocity of the hard limestone. The effect thus disappears for the section surveyed on fill.

The mapped location of the southern strand of the duplex crossing line RD2 at Randolph Downs was confirmed by a major and abrupt contrast in the shot records and dispersion characteristics, such that the fault could almost have been located without further processing. The RD1 line, on the other hand, also crossed two mapped faults but displayed significant interference in the shot records that was not clearly reflected in the dispersion characteristics. For instance, a vertical fault is mapped in the field in the meander west of RD1 that offsets the contact between Conway and Loburn Formations. The eastward strike projection of that fault intersects the RD1 line about 1/3 of the way along its length. The southeastward dip of the Conway Formation at the fault outcrop (RDa – Map 2) suggested that the fault would be within the Loburn formation for most if not all of the penetration

depth at the fault's intersection with the seismic line. The surface wave events were clearly noisy and backscattered at the expected fault position (Figure 6-18) but the phase velocity did not change significantly across the contrast.

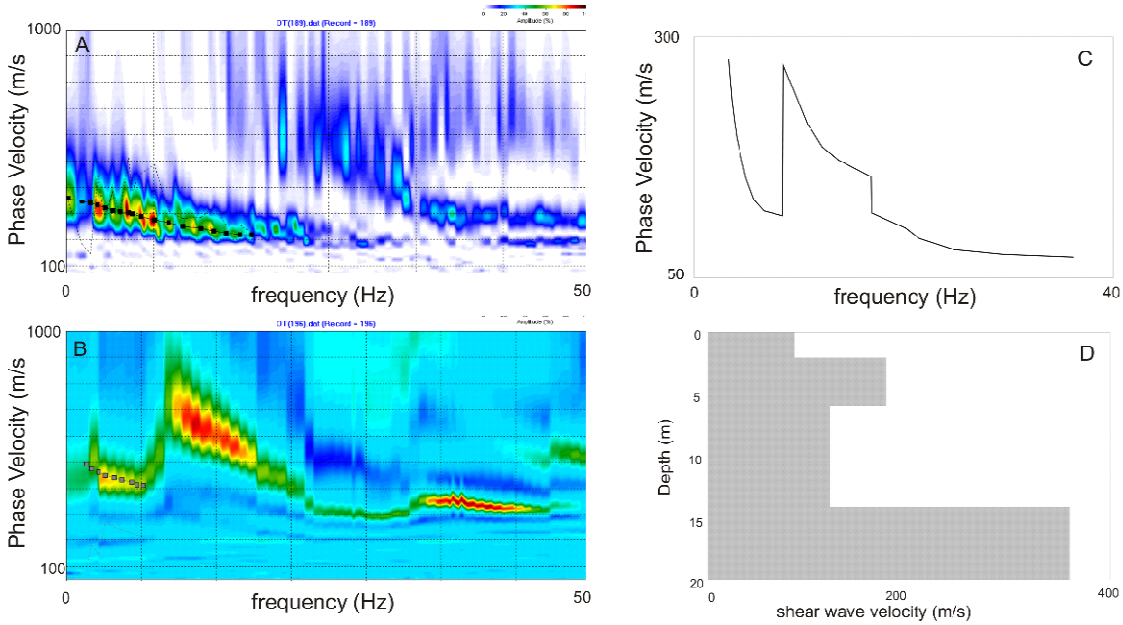

Figure 6-17: Quarry dispersion curves extracted from records acquired over A) fill and B) the quarry floor. The response seen in B is comparable to dispersion curve (C) (after O'Neill and Matsuoka, 2005) modelled using the synthetic layered earth S-wave velocity model (D) of Tokimatsu et al. (1992). The high velocity cap between 2 and 5 m in the layer model causes excitation of higher modes with significant energy over the corresponding wavelengths.

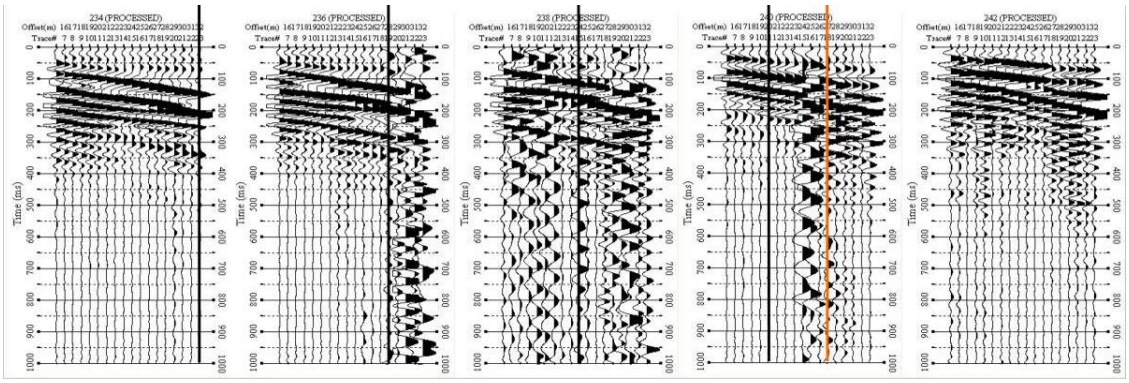

Figure 6-18: Progression of 5-40Hz bandpass filtered surface wave records from seismic line RD1. The array moved from left to right and the heavy black lines are an arbitrarily chosen common point. The red line is the source of the backscatter, which has greatest amplitude when the array butted up to the red line. Backscatter and noise quickly disappears after the array passes over the backscattering contrast, located at station 80.

6.3.4 2D S-wave velocity sections

For each survey line, the dispersion curves were inverted and 2D Vs sections were produced using the built-in contouring software in surfseis. Several of the profiles (LH and D1 in particular) crossed significant topography so the profiles were also corrected and contoured in Surfer8. The resulting S-wave velocity profiles are presented in Figure 6-19, contoured between 100 and 600 m/s on the basis of laboratory-based predictions presented in Figure 6-10, (reproduced in Figure 6-19 to facilitate comparisons). Apart from actual velocities, the main prediction taken from the field and laboratory rock property determinations is that it will be challenging to distinguish either primary lithological changes or fracture density variations in the soft rock of this study area and even more challenging to discriminate between them. This is borne out by the S-wave velocity profiles, which show velocities clustered as predicted in the 100-600 m/s range, rather than the 100-1100 m/s range seen in the Dalethorpe greywackes.

Overall, the velocity sections show reasonably good agreement with geological mapping. Evidence of faulting is, however, predictably equivocal in many of the sections, with a couple of notable exceptions. The RD2 line was run across a mapped duplex of Amuri Limestone trapped between Waipara Greensand and Waikari Formation siltstone and shows two distinct velocity contrasts that are confidently interpreted to represent the bounding faults. In this instance the velocities of the Waikari and Amuri lithologies are as predicted virtually indistinguishable from each other. A fault damage zone is clearly expressed between the Amuri and Waikari units, which both have intact strengths above the 20 MPa threshold in Figure 6-5 and Figure 6-6.

No such well defined damage zone can, however, be observed separating the Waipara Greensand and the Amuri Limestone across the southern of the two faults. This is a predictable result given that the velocities in the Waipara Greensand are typically around 150 – 300 m/s with occasional excursions to 450 m/s. This is >50% lower than the predicted maximum of 600 m/s, probably because that velocity was based on testing of an exceptionally well indurated sample collected from near the contact with the Loburn Formation at outcrop RDb. The Waipara Greensand is in general extremely poorly

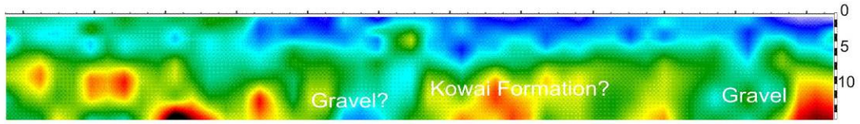

D2 - The Deans Driveway

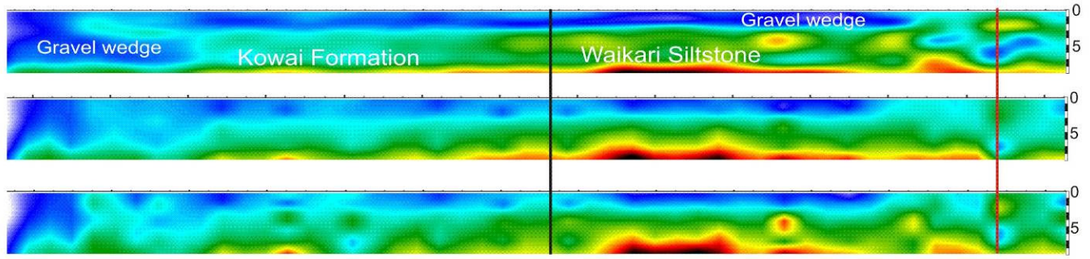

D1 - The Deans high terrace

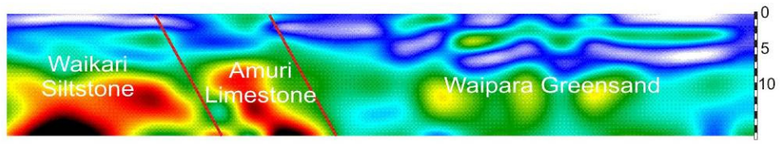

RD 2

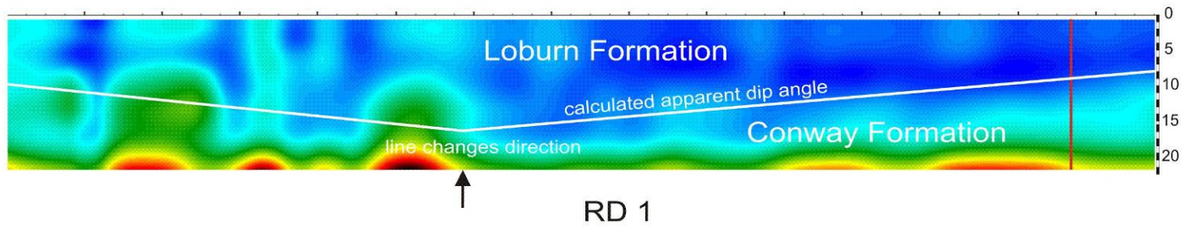

RD 1

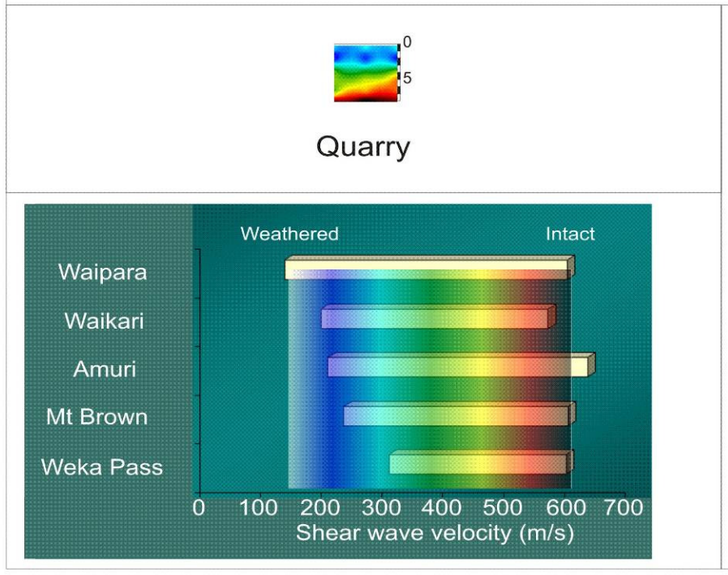

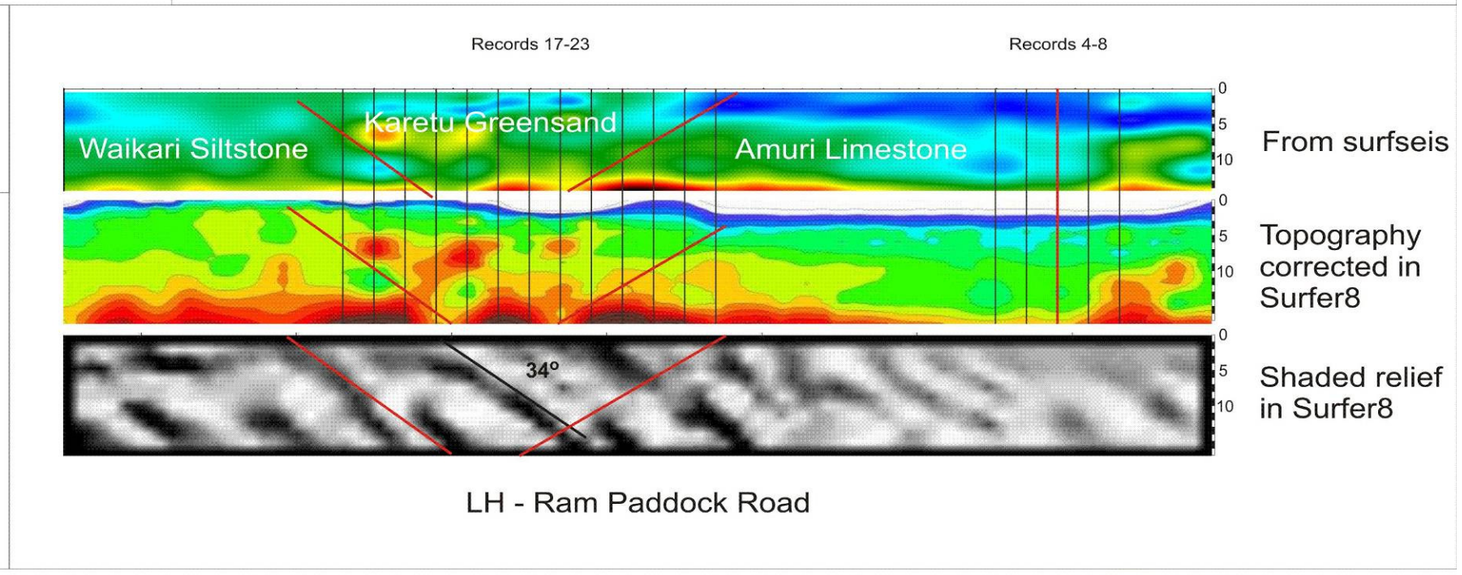

LH - Ram Paddock Road

Figure 6-19: Boby's Stream MASW profiles and laboratory-predicted, weathered through intact S-wave velocities for comparison. Contouring is in Surfseis unless otherwise indicated. 3 separately processed profiles are presented for D1, to demonstrate the repeatability of the technique. All profiles contoured between 100 and 600 m/s. S-wave velocity colour scale shown is for Surfseis profiles only. Not all Surfer-corrected profiles are shown.

indurated and the survey velocity highs can probably be considered more characteristic of the unit than can the laboratory predictions.. The observed sonic S-wave velocities of 150 – 300 m/s, together with outcrop nail penetration of ~100 mm (Table 6-3) suggest rock mass strengths of <10 MPa, well below the damage influence threshold, which explains the absence of an obvious damage zone in this lithology.

Remaining with the Randolph Downs lines, S-wave velocities of 200 m/s in the Loburn Formation (line RD1) are in strong agreement with the nail penetration testing carried out on outcrop RDa (seen previously in Figure 6-13). This muddy unit had an average nail penetration of 116 mm (Table 6-3) which yields expected unconfined velocities of 100 – 150 m/s (Figure 6-9). The appearance of slightly higher velocities at the surface may be due to higher modes excited by vehicular consolidation of the farm track on which the survey was run. The Conway Formation at outcrop RDa is dominated by friable, silty sands and is even weaker than the Loburn with an average nail penetration of 150 mm. On this basis it should exhibit lower velocities than the Loburn Formation but nowhere does this line encounter unconfined Conway Formation to allow direct comparison. The Conway formation is indicated on the velocity section based on field mapping and the correspondence of the velocity boundary with the calculated apparent dip in the direction of the line, rather than on velocity characteristics.

Little sense can initially be made of the velocities at the northern end of line RD1, north of the direction change. Once again there seems to be a broad correspondence with the calculated apparent dip but several velocity lows and highs are apparent with little order. These may, however be related to faulting through the fluid conduit effects of the faulting. The iron oxides seen throughout the Loburn formation at the RDa outcrop are indicative of long term hydrogeological processes that have been shown to increase S-wave velocities (Fumal, 1978). It is probable in this instance that the high velocities are due to iron cementation by the action of water flowing in the fault-zone. The low velocities are thus interpreted as discrete faults, where differential movement has countered the strengthening effects of iron cementation. This fault-zone cementation may also be responsible for the exceptionally high S-wave velocity of the Waipara Greensand sample obtained from the RDb outcrop, less than 10 m from the northern end of the RD1 line.

Further reasonably strong evidence of faulting is seen in the LH line, run on Ram Paddock Road. A southward velocity increase below record 5 at the southern end of the line images an apparent 5 m vertical offset in the S-wave velocities. This feature is located directly below an area mentioned in Section 6.3.3 as having weakly coherent records. The locations of the affected records are marked on the S-wave velocity section. These locations suggest that the damage is concentrated on the northern footwall side of the fault.

The second zone of scattered surface waves, from records 17 – 23, appears to be terminate northward at a velocity decline, interpreted as a fault, that coincides with a low velocity south-dipping damage zone. It is unclear from this profile whether the damage is concentrated in the footwall or hanging wall. The footwall Waikari siltstone at this location appears to have a gentler velocity gradient than is seen in line RD2, but this is probably because the velocities are offset downwards due to the overlying thickness of gravels. No gravels overly line RD2.

The fault juxtaposing Waikari and Karetu units on line LH is <100 m west of an outcrop of the fault where Amuri Limestone is thrust over Pleistocene gravels sitting on Waikari Formation (Figure 6-11). Karetu Sandstone is, however, mapped underlying the Amuri Limestone on the hanging wall in a gulley between the outcrop and the road. A significant thickness is also mapped on the quarry side of the road, hence the Karetu designation on the profile.

Experimentation with various mapping options in Surfer8 during topographic correction of line LH provided an unusual perspective in the form of a shaded relief map of the velocities. By highlighting relative velocity highs and lows the shading appears to image a north-dipping fault offsetting bedding with an apparent dip of 34° to the south. The bedding dip at least is in strong agreement with field observations. The road runs along the hinge of a sharply-swinging anticline that turns bedding orientation from 070/24 SE in the quarry to 180/40 E in outcrop LHa below the Limestone Hills residence. An angle of 34° thus almost certainly reflects the true dip of bedding below the road.

Three separate profiles are presented for Line D1, which is run dominantly across Waikari Formation siltstone and Kowai Formation. The three profiles represent three separate processing attempts, as a means to assess the repeatability of the technique in soft rocks.

The three profiles are markedly similar, with variations mainly concentrated in the low velocity zones at either end of the line.

The formations marked on D1 are based on mapping of The Deans point bar. No laboratory work was done on Kowai Formation samples but they are clearly of lower velocity than Waikari Formation but well discriminated from the overlying Pleistocene gravels. The low 100-250 m/s velocity cover that occurs at the surface over most of the line is truncated in the south by a 100 m/s increase in S-wave velocity in the vicinity of the fault scarp. This base of this low velocity zone coincides with the base of the Pleistocene gravels and is interpreted as such. The southward truncation coincides with the crossing of the fault scarp and with a poorly defined low velocity zone to depth. This velocity low is attributed to fault damage in the Waikari Formation. The damage zone is not as clear as that which was seen on RD2. The penetration depth on RD2, however, was twice that of D1 so the full extent of the damage zone may not have been revealed on D1. The northern end of line D1 is also marked by a low velocity zone to depth. This appears to be a attributable to a gravel wedge accumulated against another fault (Figure 6-20).

Figure 6-20: Marked up photograph towards 90°of the visible (solid black line) and approximate (dotted black line) base of the Pleistocene gravel cover on The Deans point bar. The Mount Brown/Waikari contact is marked in white and is upthrown to the south by the fault in the centre of the picture, which crosses the northern end of Line D1 (purple line). For location see Figure 6-14. [Photo taken from Limestone Hills homestead by Gareth Renowden, Limestone Hills].

The final line to discuss is the line run on The Deans driveway. This line is remarkable mainly for its generally low velocities and for the two deeper low velocity zones within the line. The origin of the deep lows is unclear but both coincide with zones of intense higher mode excitation mentioned in section 6.3.3. The southern of the two velocity lows also coincides with an outcrop of bouldery gravels (outcrop Db) in the track leading down to the Waipara River from The Deans homestead (Figure 6-21).

Figure 6-21: Photo towards 90 °of bouldery gravels outcropping against residually weathered Mt Brown Formation in a farm track adjacent to The Deans homestead. Limestone boulders are deposited over greywacke cobbles. The gravels terminate ~2-3 m to the right of the photograph where they give way to sands. A band of limestone boulders can be seen outcropping in the driveway above, which is level with the wagon wheels.

6.4 Geomorphological correlations

The MASW profiles were correlated with each other and with geomorphological data to aid structural interpretation. A similar wealth of topographic profiles was amassed at Boby's Stream as at Dalethorpe and the locations of relevant profiles are shown in the back pocket supplement to the correlation diagram at Figure 6-22 .This section details the correlations that were observed throughout the study area between these profiles and the 2D MASW profiles. The strike of the Boby's Stream Fault varies slightly either side of E-W so this orientation was selected for correlations. Separate correlation diagrams for The Deans and Randolph Downs ends of the study area are presented together in Figure 6-22.

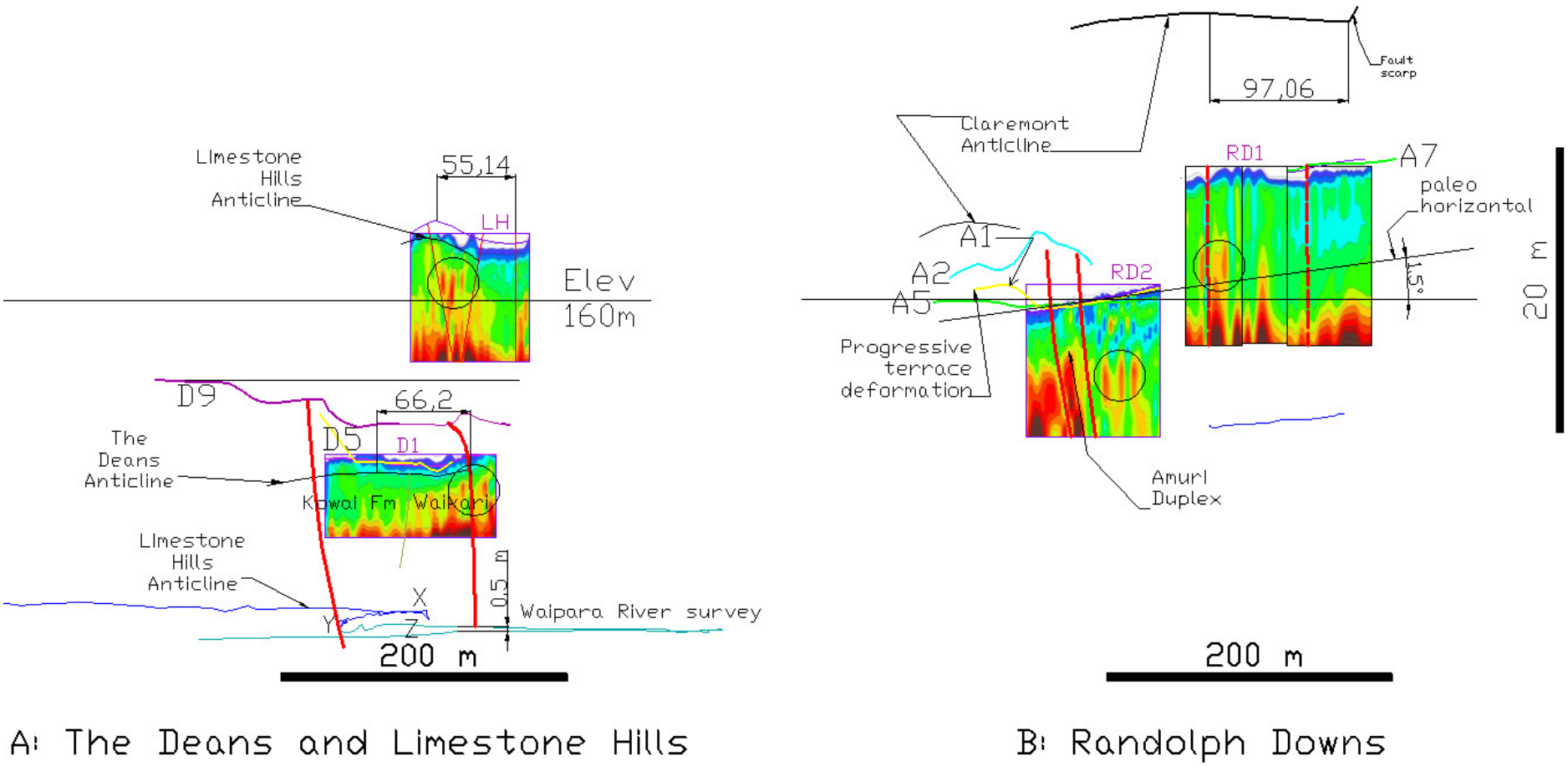

Figure 6-22: An east-facing across site correlation of the Boby's Stream MASW profiles with detailed geomorphological surveys and structural interpretations. All dipping features exaggerated in the section view by 5x VE. Regional surface gradient is to the east. A back pocket supplement to this diagram shows both plan and elevation views and the location of topographic profiles.

The sensitivity of bedrock rivers to neotectonics is well documented (Bull, 2007; Burbank and Anderson, 2001). The Dalethorpe study confirmed previous local studies such as Litchfield *et al.* (2003) that have indicated the structural sensitivity of Torlesse river profiles and further suggests that fluvio-tectonic correlations can be made at a very detailed scale despite inherent noise. Detailed river profiling thus formed a key component of this section of the study. The detailed thalweg profile of the Waipara River was surveyed over approximately 2 km, starting near the confluence with Boby's Stream and ending on the downstream side of The Deans meander loop as the river emerges into the alluvial plain. The data are integrated with MASW and mapping in Figure 6-22A and a standard long river profile is included at Figure 6-23. Both are marked with key points that are referred to in the text.

The topographic survey data quality is excellent and reflects the structure well. The river is clearly not in dynamic equilibrium and Figure 6-23 clearly shows that the profile over the entire surveyed reach is broadly convex and comprises a series of smaller convexities. Interpretation of the thalweg profile is aided by examination of the integrated AutoCAD model (Figure 6-22A), which shows the Waipara River approaching Limestone Hills, where it encounters the Limestone Hills Anticline. The anticline is clearly imaged by the surfer corrected MASW profile LH, along with several smaller faults. The river bed 100 m upstream of Limestone Hills is presently clean bedrock, stripped even of gravel veneer.

After crossing the Limestone Hills Anticline the river immediately encounters The Deans Anticline as it rounds the meander bend under outcrop LHa (point X). The Deans anticline is an actively growing structure that is immediately apparent on the terraces of The Deans Point bar, where it warps the terrace surface (Detail B – Map 2) and causes drainage to become trapped at the base of the terrace riser, contributing to the active erosion in the gullies on the east side of the Point bar. The Deans Anticline is clearly imaged by the MASW profile D1 and its width can be seen by examining the highest (D9) topographic profile at The Deans. The profile steps down southward across a flight of three terraces, of which only the bottom two have their gradients clearly affected by anticlinal warping.

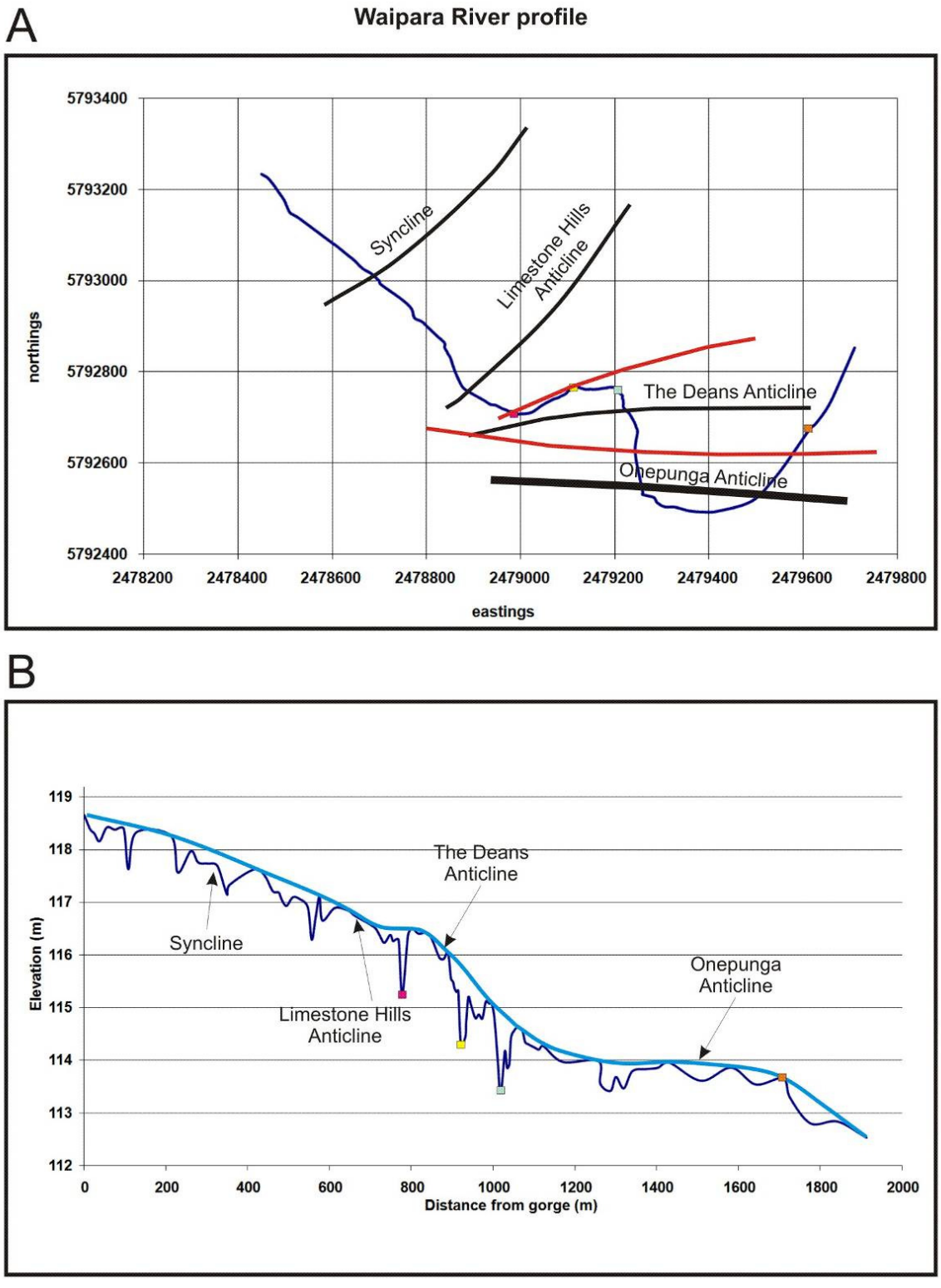

Figure 6-23: Detailed map (A) and profile (B) view of the thalweg of the Waipara River for 2 km south of the gorge. The profile (B) includes both the surveyed river bed (dark blue) and the approximate water level (light blue) Coloured markers are placed along the meander between The Deans and Limestone Hills to allow the reader to correlate between map and profile views.

The Waipara River is temporarily deflected by the anticline and drops down the face of the rising limb, becoming entrenched behind a forward splay of the Boby's Stream Fault at point Y, a deep hole. Unlike the clean bedrock upstream of Limestone Hills the river bed through the reach on the northern side of The Deans Anticline is characterised by steep reaches separated by deep sandy pools. The steepest reach of the river is the X-Y reach where the river is chasing down the fault. The river then crosses the fault and flows across the face of the anticline before executing a sharp meander turn and successfully crossing the crest of the anticline at point Z, which coincides with the ancestral normal fault trace annotated on Map 2 and seen in Figure 6-20 . After cresting the anticline the reach does not steepen but remains relatively flat and sandy. MASW velocity trends suggest that this may be due to a footwall syncline that is developing against the active fault strand.

After crossing the active fault trace the river becomes almost billiard table smooth, falling only 0.5 m in the next 600 m as it cuts a wide meander across the crest of the Onepunga Anticline, occupying the full width of its bed on the downstream side as it has for >90 years (Figure 6-24). The Onepunga Anticline is the major structure that dominates the hanging wall of the Boby's Stream Fault (see Section AA' on Map 2).

Figure 6-24: Photograph c.1918 looking east across The Deans meander bend directly along the crest of the Onepunga Anticline. Although tree growth precludes taking a comparative photograph, the river can be seen to occupy the full width of its bed as it does today. Judging from the scale of the buildings, of which the main house in the background and the woolshed in the foreground are still existing, at least a metre or two of downcutting has since occurred along the front of the homestead. Photo by permission of Ian Turnbull, The Deans.

Only a very limited amount of river profiling was possible in Boby's Stream, as the river is now mostly overgrown and line of sight is not possible for surveying. A differential GPS survey failed due to errors in setting up base stations. A number of topographic profiles were surveyed on the terraces around the MASW profiles and these are presented together with the small section of stream profile in Figure 6-22B.

On first inspection, the MASW surveys at Randolph Downs do not appear to have encountered any fold structures, despite the study area being immediately along strike from the relatively large amplitude Claremont Anticline (Campbell, JK 1995 – unpublished data), which is being uplifted by compression of Waipara Greensand within the same fault block as that across which the RD2 line was run. Topography, however, suggests otherwise. The RD2 line and topographic profile A2 are run on the downstream side of an abandoned meander where the paleoflow direction would have been to the north. Topographic profile A5 is run on the upstream side of the same meander, where the gradient would originally have been opposite to that on the A2/RD2 side. The two gradients should originally have been approximately bisected by a horizontal line. The bisector of that line is now inclined at 1.5° to the north, suggesting folding or tilting of that amount since abandonment of the surface.

The tilting appears to be confirmed by the progressive rotation of terrace remnants at the northern end of topographic profiles A1 and A2. There is, however, an enigmatic bulge north of the Amuri duplex in profile A5 that is responsible for an ephemeral swamp on the surface. The nature of this bulge is not immediately clear but it could be accounted for if deformation was occurring independently on either side of the Amuri duplex. The explanation favoured here is to map the Claremont anticline as veering away to follow the en echelon trend of the other secondary folds. The tilting south of the Amuri Duplex is probably being driven by the main Onepunga Anticline (see Section AA', Map 2).

A final point highlighted by the circles drawn on the MASW sections on the correlation diagrams is the peaky velocity characteristics seen in almost every case around the fault-zones. If these are not processing artefacts this suggests that local stress fields and hydrogeological processes are controlling velocity characteristics adjacent to the faults.

6.5 Discussion

This site was significantly different from the greywacke surveys at Dalethorpe in several ways and provided a useful test of the resolution of the MASW technique as well as an

opportunity to refine it. Faults are definitely not as clearly defined in these units as in greywacke except in exceptional circumstances. It was also not always possible with these surveys to reliably determine the transition from cover material (mainly greywacke gravels) into weathered bedrock. Both of these problems are due to a large overlap in the relative velocities of the units. Gravel wedges at The Deans, however, stood out clearly, even against Kowai Formation, and were very weakly dispersive. It is thus considered likely that almost any normally dispersive unit could be discriminated from gravels, which is a useful characteristic in many situations. In this study, only the Conway and Loburn Formations are considered likely to be problematic if a gravel wedge is present. Faults within or juxtaposing Loburn, Conway or Waipara units may not be distinguishable on the basis of S-wave velocities but may nevertheless be detectable by surface wave surveys through direct examination of the survey records.

Data acquisition using a 0.5 m geophone spacing was successfully applied and shown to compar favourably with 1 m spacings. The fundamental mode discrimination is not greatly affected but higher mode contamination is reduced. In addition, the re-running of the RD2 survey necessitated the use of planted rather than streamer-mounted geophones. The re-run survey produced exceptional results in comparison to the original streamer survey, although as previously shown in Figure 6-15, the heavily tussocked site was totally unsuitable for streamer acquisition, even after mowing. The relative merits of planted over streamer-sled-coupled surveys are better illustrated by comparing the penetration depths achieved for the RD2, D1 and D2 surveys. Over lithologically similar ground, the penetration depth using planted geophones at RD2 was twice that achieved using the streamer on the short grass along line D1. RD2 penetration was also slightly greater than, but similar to, the penetration depth achieved using the streamer on a well-compacted driveway (line D2). Survey acquisition using planted geophones in the soft ground at RD2 was less than 10 minutes slower than a streamer survey, although it was made easier by the use of a well-practised team and the towed streamer to set geophone spacings. The author's commercial MASW experience is that planting geophones in compacted ground is much more difficult. This suggests that the use of planted geophones should be considered wherever ground conditions are appropriate, so as to optimize survey results.

The quarry survey was disappointing although it did show the utility of MASW over fill material. The technique is clearly almost useless over a velocity inversion such as is

mapped at the quarry. This is in stark contrast to the results achieved on RD2 where the dip of the fault plane was imaged because the velocity contrast across the fault did not interfere with normal dispersion.

6.6 Conclusions

This study area has illustrated the difficulty in discriminating the effects of cataclasis from primary lithological variation in soft rock. Whilst it was not possible to test every lithological combination it can be safely stated that not only can cataclasis not be discriminated where rock strength is low but, for the lowest strength rocks, primary lithological variation may not always be apparent. Nevertheless, most of the surveys produced good results. Faults in weak units such as Loburn Formation were identified on raw records even though they were not seen in the final profile. Even the presence of a low velocity layer in the immediate subsurface inferred from higher mode domination is useful data and in almost every case valuable knowledge can be quickly gained with a surface wave survey. Once again the key to maximum utility of the technique was integration of geophysical, geological, geotechnical and detailed geomorphological data.

7 APPLICATION OF MASW AT THE TAIERI RIDGE

7.1 Introduction

As outlined in the introductory chapter, the New Zealand plate boundary system accommodates 37 mm/yr of convergence on an azimuth of 071° according to the NUVEL-1A global plate motion model of DeMets *et al* (DeMets et al., 1994). This convergence is obliquely partitioned into 35 mm/yr of strike slip and 10 mm/yr dip slip along the 55° striking Alpine Fault. These rates are incompatible with complete accommodation on the Alpine Fault itself, which has significantly lower Quaternary strike slip rates of only 27±5 mm/yr and dip slip rates that decline southward from the full 10 mm/yr in the Mt Cook area to almost nil at Jackson Bay (Norris and Cooper, 2001).

The southern dip slip deficit is accommodated in a wide zone of active deformation across Otago. Norris and Nichols (Norris and Nichols, 2004) documented a modern contraction rate in Otago that requires 15 m of Holocene shortening, of which some 8 - 10 m are unaccounted for. One candidate structure identified for accommodation of some of this strain is the Taieri Ridge (Figure 7-1), where uplift has been documented but evidence for fault activity is still equivocal. This chapter presents the results of application of the MASW technique to re-processing of a High Resolution Reflection (HRR) seismic investigation of the inferred fault on the eastern side of the Taieri Ridge.

7.1.1 Scope and objectives

The main objective of this study is to prove the utility of MASW to locate and define the extent of fault-zones in several typical New Zealand settings, and to define within-zone variability that is readily correlated with measurable rock properties and with the distribution of surface deformation (Section 1.1). In order to meet that objective it is necessary with the final site to demonstrate that sound subsurface structural and geotechnical inferences can be taken from MASW. In the blind interpretation exercise presented below, the HRR seismic data are supplemented only by published material and by trench and topographic data collected along the seismic line by Kilner (Kilner, in prep) prior to the incorporation of the Sheehy Road site into the present study. No site visit has yet been undertaken.

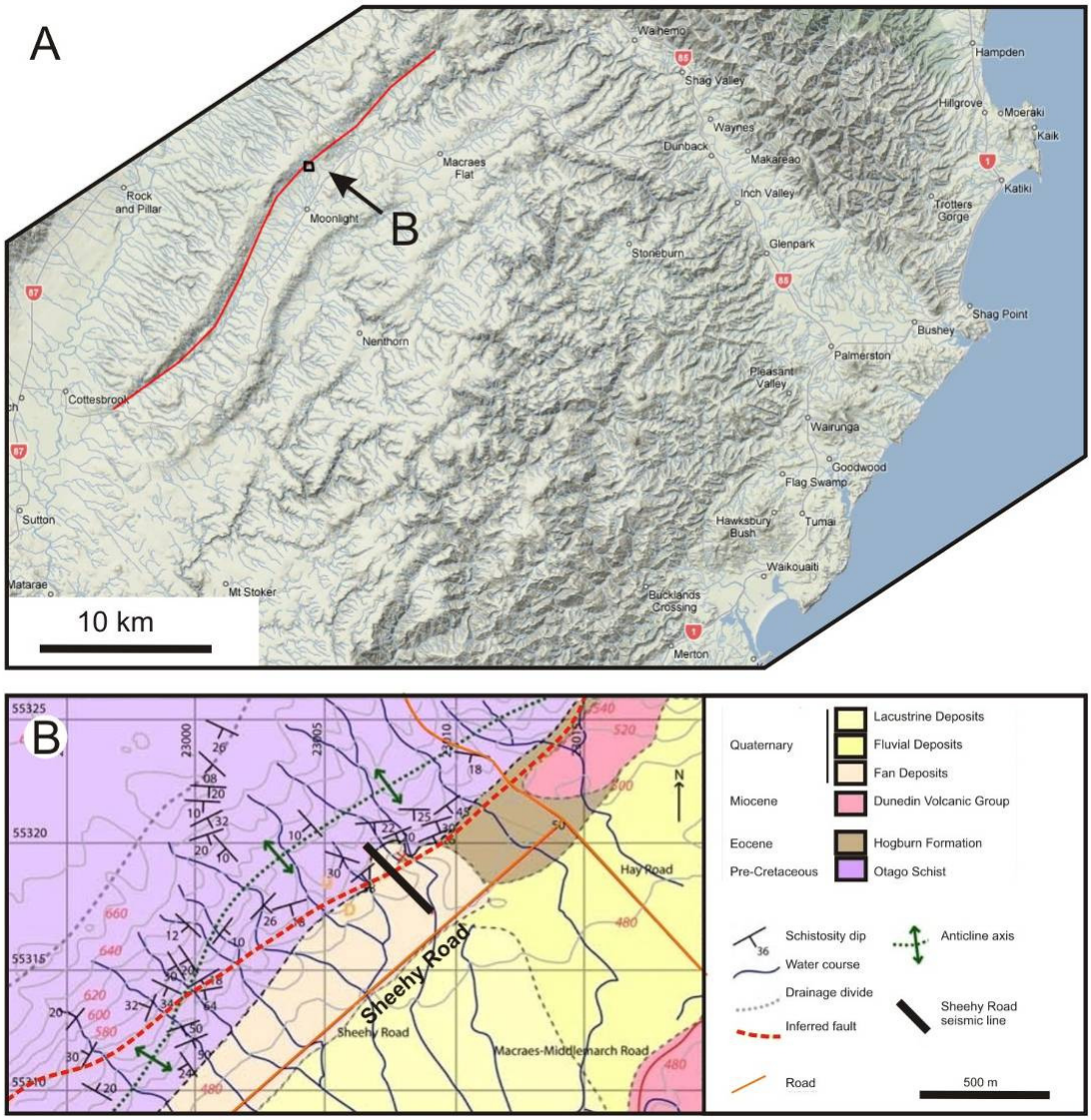

Figure 7-1: (A) Google topographic map showing the location of the Taieri Ridge and study area and (B) geological map (after (Kilner et al., 2007)) of the Sheehy Road Field area on the southeastern side of the Taieri Ridge

Section 7.2 presents observations of the wavefield and dispersion characteristics of the component records from processing of the seismic data. The results of the MASW surveys are presented in a similar format to that used in previous chapters and are correlated with existing trench and topographic data. Interpretations include the location and extent of the fault-zone, the likely geotechnical character of the subsurface and the likely extent of surface deformation. The area of interpretation is restricted to the interfluve on which the seismic survey was run. It should be noted that, whilst this site increases the range of lithologies encountered in this study, these 'new' lithologies potentially introduce greater uncertainty in the post-processing, pre-ground truthing interpretation of the results. This disadvantage to the selection of this site over previously considered sites, which juxtaposed Torlesse greywacke with Tertiary soft rocks, is

outweighed by the opportunity presented for a true blind survey that favourably exposes the MASW technique to a wider selection of potential users. Prior to final discussion and conclusions, a novel variation from the standard MASW investigation is presented, termed Swept Frequency Imaging (SFI). The SFI image is compared with the HRR and MASW imaging. The final discussion in this chapter then centres around the implications of MASW for the application of surface wave seismic methods across active fault-zones.

7.1.2 Site geology and geomorphology

The Taieri Ridge is a young, relatively low and little modified structure in a set of northeast trending, westward dipping faults and folds that step out across eastern Otago, subparallel to the Alpine Fault. The faults and folds form a number of parallel asymmetric ranges that generally step down in elevation to the east and include, in eastward order, the Dunstan Range, the Raggedy Range, the Rough Ridge Group, the Rock and Pillar Range and the Taieri Ridge (Figure 1-3 and Norris and Nichols, 2004). Strong circumstantial evidence, in particular the work of Norris and Nichols who documented c. 8 m of Holocene uplift on the Taieri Ridge using Optically Stimulated Luminescence dating immediately adjacent to the study area, has led to a thrust fault being inferred along the eastern side of the Taieri Ridge (Norris and Nichols, 2004). Deformation on the Taieri Ridge fault is believed to extend out of the schist basement into the Quaternary fans and outwash slopes of remobilized debris that are deposited over remanant Tertiary units by the many streams that drain the eroding structure (Figure 7-1, Figure 7-2). Unfortunately, geomorphic evidence of deformation is thoroughly obscured by anthropogenic land use (Kilner et al., 2007). The central and eastern Otago region is afflicted by a lack of unequivocal field evidence of range scale faulting and the Taieri Ridge is no exception. Little unequivocal evidence of Holocene displacements has been documented on Otago faults and none of that on the Taieri Ridge (Norris and Nichols, 2004). This study aims to help redress this situation by providing reliable constraints on the location of the fault for paleoseismic trenching.

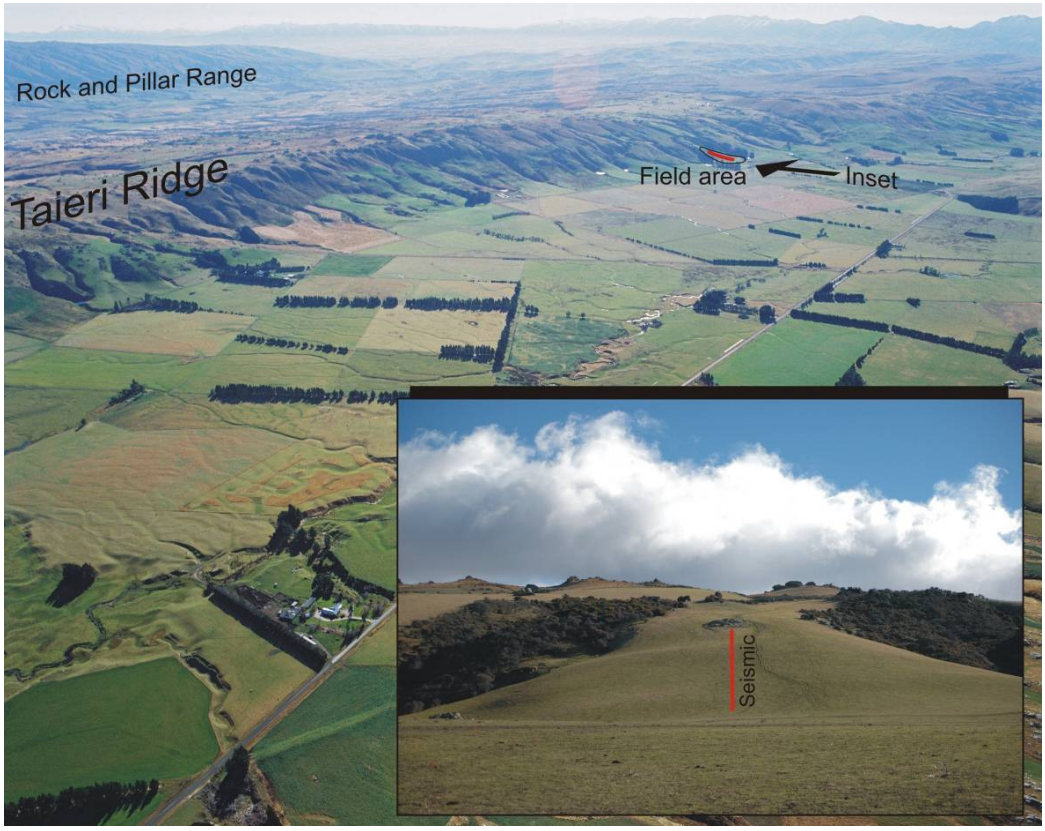

Figure 7-2: Oblique aerial photo looking north showing the Taieri Ridge with the parallel Rock and Pillar Range structure in the background. Inset detail shows field area and location of seismic line. The uphill extent of the line stopped in the hanging wall of the inferred fault at the outcropping schist. Main photo by Lloyd Homer (used with permission of GNS Science). Inset photo by Jeremy Kilner.

7.1.2.1 High Resolution Reflection Seismic

The structure of the Taieri Ridge recently came under the scrutiny of Otago MSc student, Jeremy Kilner (in prep; 2007). Kilner aimed to document paleoseismic evidence of fault activity on the Taieri Ridge, constraining the deformation and targeting trenching activity using a range of geophysics including HRR seismic, ground penetrating radar and a magnetic survey. Similarly to this study, his use of geophysics was motivated by the difficulty targeting invasive techniques where geomorphic expression is absent or, at best, ambiguous. He also wished to derive wider details of the near fault surface structure. The processing and results of the seismic survey are summarised below. For further details of the seismic and an account of the other geophysics used, see Kilner (in prep).

The HRR survey was carried out using a Seistronix RAS-24, 48 channel seismograph. The geophones were 30 Hz vertical geophones at 0.5 m geophone spacing. The selected sampling interval of 0.25 ms yields a Nyquist frequency of 0.5/0.00025 or 2 kHz, an order of magnitude higher than the expected frequencies of 100 – 150 Hz for HRR. The data were processed in Globe Claritas seismic processing suite and a processing flow is shown in Figure 7-3. A refraction static model was produced (Figure 7-4) to determine the near

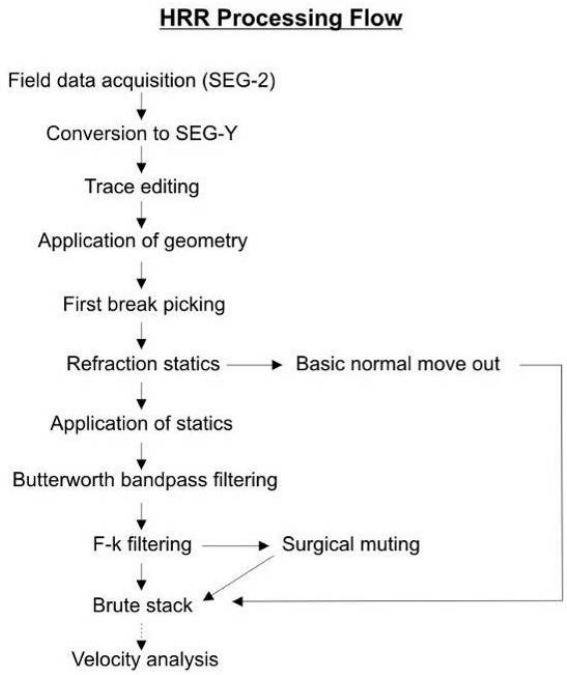

Figure 7-3: HRR processing flow leading to production of final stacked section (after Kilner et al. (Kilner et al., 2007))

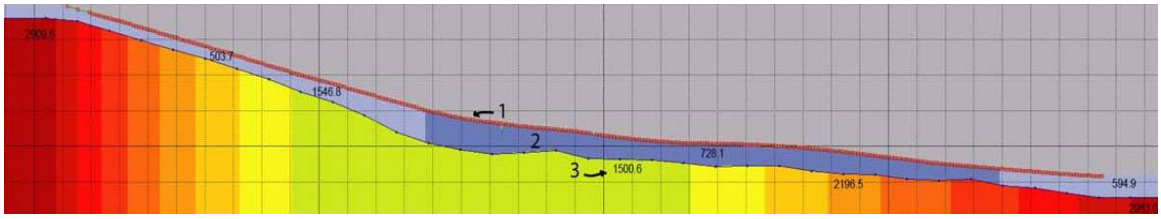

Figure 7-4: Refraction static model showing (1) surface topography, (2) 'weathering' layer thickness and velocity, and (3) second layer velocity.

surface velocities. The statics were applied to remove the effect of variable thickness and velocity in the weathering zone. Somewhat ironically, removal of ground roll was difficult. Surface, refraction and air waves must be removed or reduced to enhance the reflection hyperbola. Various strengths of surgical mutes were applied to shot gathers to remove the ground roll, but these commonly resulted in processing artefacts. Other difficulties included deconvolution to remove multiples, and differentiating between reflections and refractions. The completed seismic sections (Figure 7-5) are Common Depth Point (CDP) stacks that include both reflection and refraction events due to the difficulty separating them. This may have been due to the survey aperture being constrained by the desire for closely spaced geophones, leading to a dearth of far offset data. Stacking both reflection and refraction data are not standard practice but is based on

the theory that both will occupy the same region in space on the shot gather and will therefore stack where the subsurface interface is located (Kilner et al., 2007).

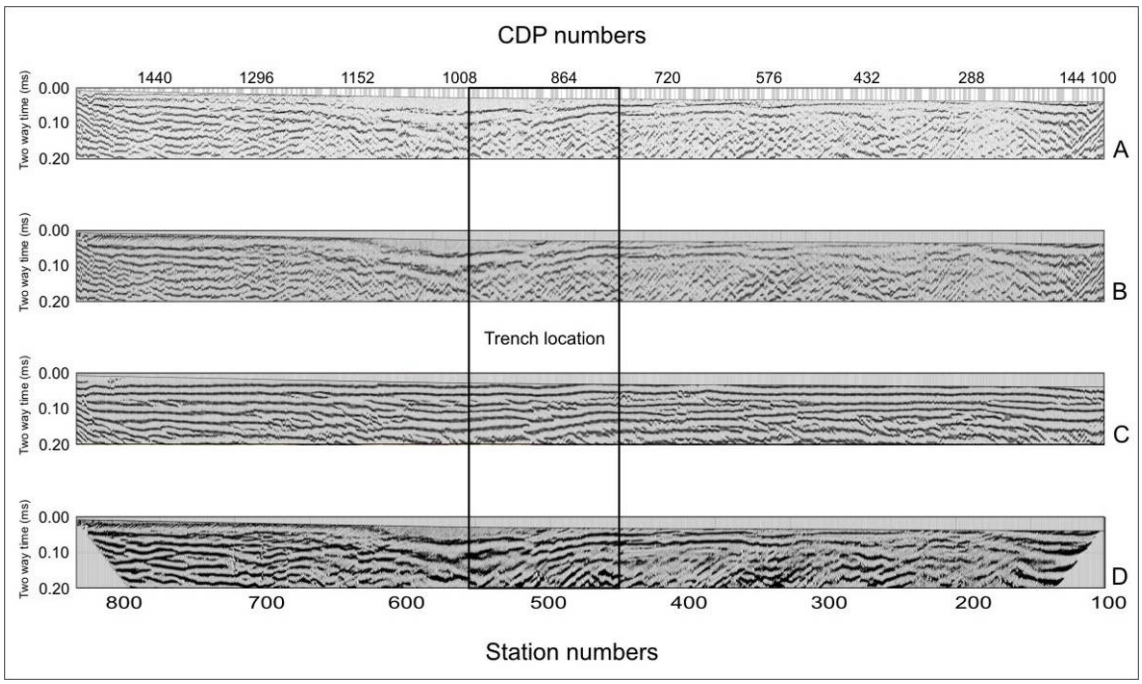

Figure 7-5: CDP stacks that use a basic velocity model based on the refraction statics in Figure 7-4. A: stack with no muting or f-k filtering. B: stack with surgical mute designed to remove ground roll. C: stack B with f-k filter applied. D: stack with severe mute to remove groundroll but no f-k filtering.

7.1.2.2 Trenching

A trench was excavated to investigate the Taieri Ridge fault prior to the site's incorporation as part of this study (Figure 7-6) (Kilner, in prep). The trench was sited based on interpretation of geophysical investigations including the HRR survey and GPR and magnetic surveys. Most of the lithologies exposed in the trench were heavily altered and the extent of alteration made interpretation and logging difficult. Some of the contacts marked in the log are based on a combination of distant and closeup logging. The surface profile on the trench log may also be misleading due to piling of topsoil on an unvegetated surface next to the trench when the trench was opened.

These difficulties aside, the structure exposed in the trench (Figure 7-6) definitely appeared to be only secondary to the inferred main Taieri Ridge structure. Abundant evidence of small scale faulting was observed in the trench, with apparent offsets up to 15cm observed throughout the grey and purple igneous clays at the base of the Dunedin Volcanics and in the mottled orange/grey siltstone of the Hogburn Formation. The massive grey clay between 22 and 33 m contained numerous striations and may accommodate some displacements that cannot be easily quantified. The remanant

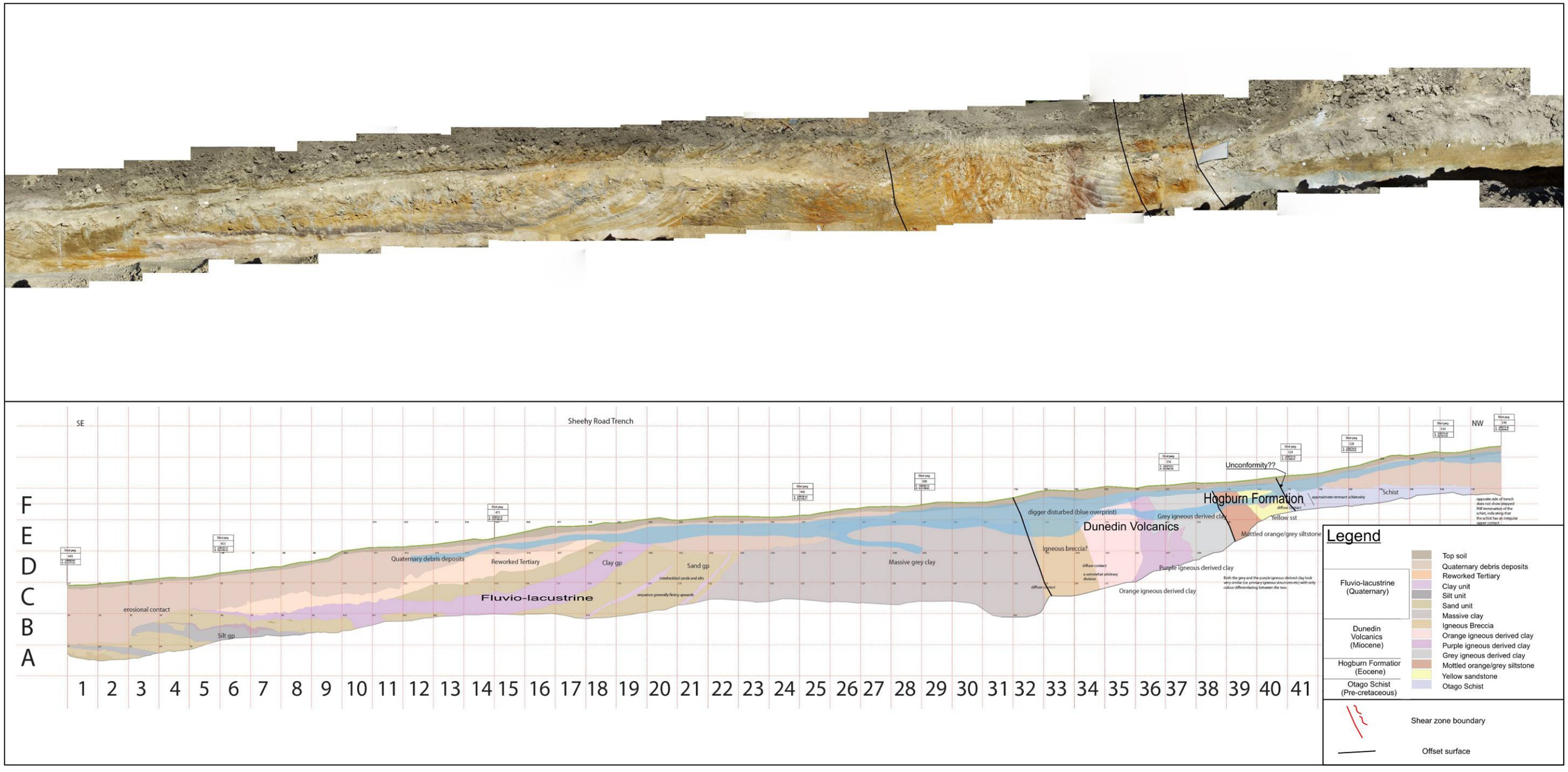

Figure 7-6. Trench photo panorama and log (modified after Kilner (2008)) for Sheehy Road Trench 1. This trench was sited on the basis of interpretation of the HRR survey described in 7.3.2. As predicted by the results of the MASW survey the major Taieri Ridge fault was not located although abundant evidence of minor faulting was seen southeast of the unconformity.

schistosity in the schist exposed at the NW end of the trench, however, dipped uphill, some 90° away from the schistosity in the outcrop that marked the NW end of the survey line (see Figure 7-2). The outcrop schistosity was typical of the area in that it roughly paralleled the slope and unconformity. The schist in the trench appeared to be in-situ and, like the outcrop, its schistosity also paralleled the unconformable contact with the overturned Hogburn formation. The change in fabric orientation is suggestive of a major fault or fold between the trench and the outcrop, which is less than 60 m away. Clearly, the first trench failed to locate the fault, but the initial choice of HRR was fortuitous in that its acquisition parameters favoured reprocessing of the raw seismic files using MASW.

7.2 MASW survey

7.2.1 Data collection and processing

The HRR survey was shot in both directions at the Sheehy Road site to locate and image the fault inferred by Norris and Nichols (Norris and Nichols, 2004) (Figure 7-7). SEG2 (raw seismic data) files from the SE to NW survey were selected that conformed to the required shot spacing for the MASW survey. The files were then formatted and manipulated in the Surfseis field setup utility to produce KGS files with appropriate survey geometry. The HRR and effective MASW acquisition parameters are spelt out in Table 7-1. The geophones used for the Sheehy Road survey were planted 30 Hz geophones rather than the sled mounted 8 Hz geophones used elsewhere in this study. Cultural and environmental noise sources are unknown, but are likely to have included livestock and wind.

7.2.2 Dispersion curve extraction

The seismic records were analyzed and dispersion curves were extracted following the methodology outlined in Chapter 3. The survey was processed both as a single record survey and as a fixed source walkaway (FSW) survey. The records had been collected with a 0m near offset so the first 10 traces were cut leaving a 38 trace 18.5 m aperture array centred 14.5 m from source. The resulting 5 m near offset is only half of the

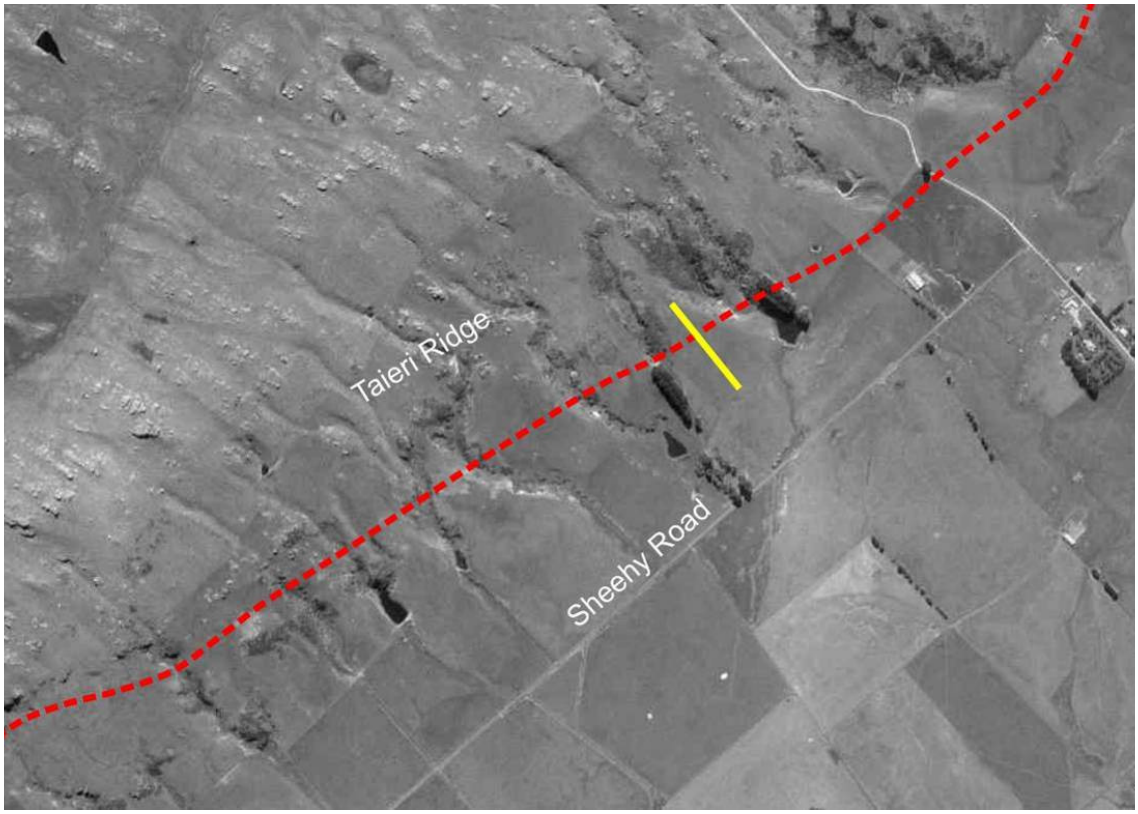

Figure 7-7. Sheehy Road survey line location (yellow) relative to the inferred fault (dotted red). No scarp is developed in the survey area.

Table 7-1. Acquisition parameters for Taieri Ridge HRR survey and effective parameters for MASW surveys.

Survey line	HRR	MASW	MASW a
Acquisition	48	38	86
Walkaway construction	NA	None	FSW
Aperture/ Array dimension (D)	23 m	18.5 m	40.5 m
Near offset (x1)	0 m and 23 m	5 m	5 m
Shot spacing	2 dx (1 m)	10 dx (5 m)	10 dx (5 m)
Sampling interval (ms)	0.25	0.25	0.25
Recording time (ms)	1510	1000	1000
Pre-amp gain	12db	12db	12db
Number of records	>590	65	65
Survey length	364 m	320 m	320 m

minimum 10 m proposed by Park *et al.* (Park et al., 2005a). The object of using a longer near offset is to maximize the wavelength of planar Rayleigh waves recorded by the survey, so this provided an opportunity to see what effect an overly short near offset

actually had on the processing. In fact the effect was minimal, probably due to the relatively high natural frequency of the geophones. The swept frequency records showed that no coherent surface waves were typically recorded with frequencies less than around 20 Hz and at that frequency there were no indications of near field effects. The proximity of the entire array to the source actually led to greater coherency of high frequencies whilst reducing the potential for far field higher mode contamination. For an explanation of near and far field effects see Appendix A.

The overtone dispersion images generated from the 38 channel survey were dominated by coherent surface wave energy although dispersiveness and phase velocity varied systematically along the line. The first seven records evaluated at the downhill (eastern) end of the line (centre stations 27-97) were strongly dispersive with high phase velocities and a high signal to noise ratio (Figure 7-8A). Structurally, these records should all be well into the footwall given that the trench indicated that the fault is uphill of station 530.

The phase velocities declined abruptly over the next 10 m through records 8 and 9. Subsequent records, including those of the section of the line subsequently trenched, displayed weakly dispersive, low phase-velocity trends until much farther down the line at records 46-7, centred on stations 574-584. The overtone (dispersion) image for the records approaching records 46-7 displayed the trend common to the middle of the line (Figure 7-8B) but with progressively increasing dominance of a high phase-velocity [higher?] mode (Figure 7-9). The frequency at which this mode dominated reduced with successive records until the fundamental mode could no longer be clearly seen. Record 46 marked the re-emergence of the fundamental mode with sharply increased dispersiveness and phase-velocity . The change in character was maintained until the end of the line (Figure 7-8C) and was accompanied by increased body wave contamination leading to apparently excessive Rayleigh wave phase velocities (lower records - Figure 7-9). The decline and re-emergence of fundamental mode, together with increased body wave contamination and the subsequent presence of a clearly separated and strong higher mode is markedly similar to observations on Dalethorpe Lines 3 and 7 over elevated bedrock on the hanging wall of the MDT fault.

A

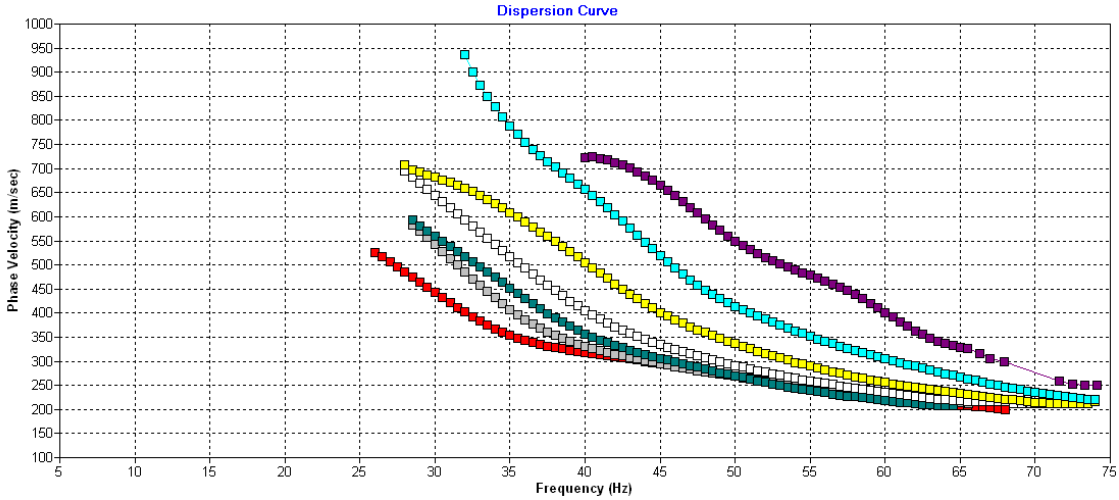

B

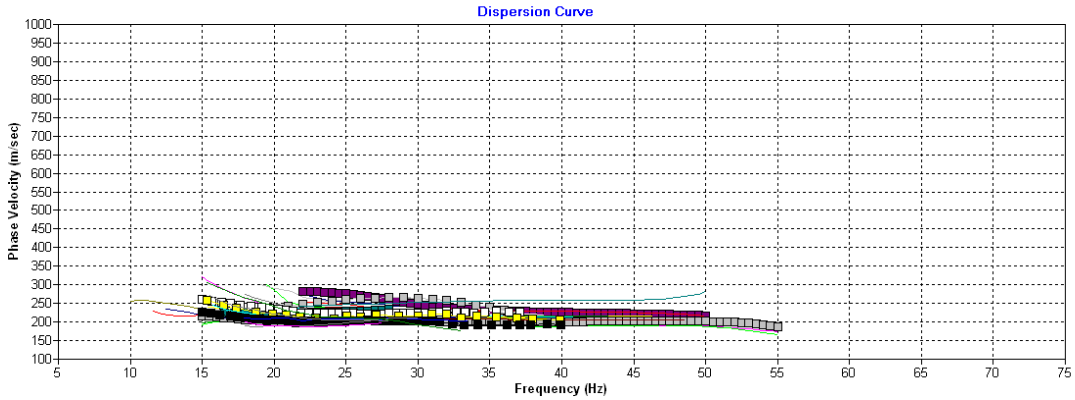

C

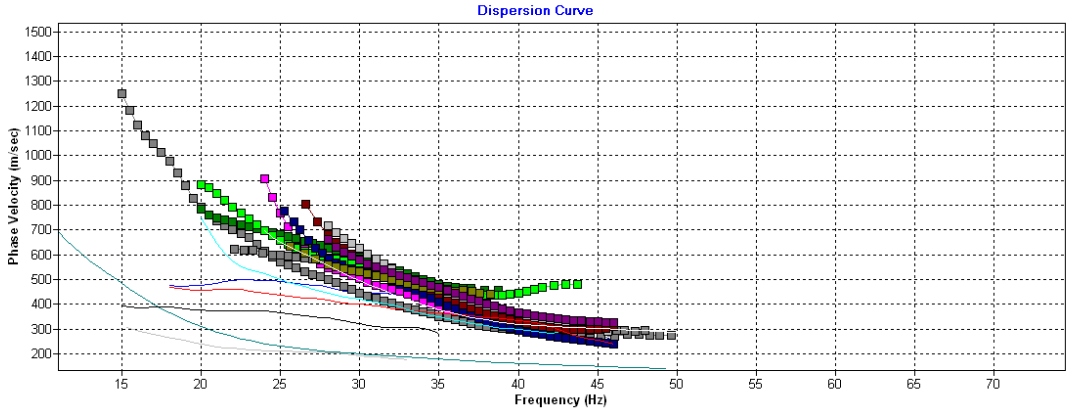

Figure 7-8: Dispersion curves for the A) start [east], B) middle and C) end [west] of the seismic line. A systematic shift can be observed, that relates to changes in the character of the subsurface.

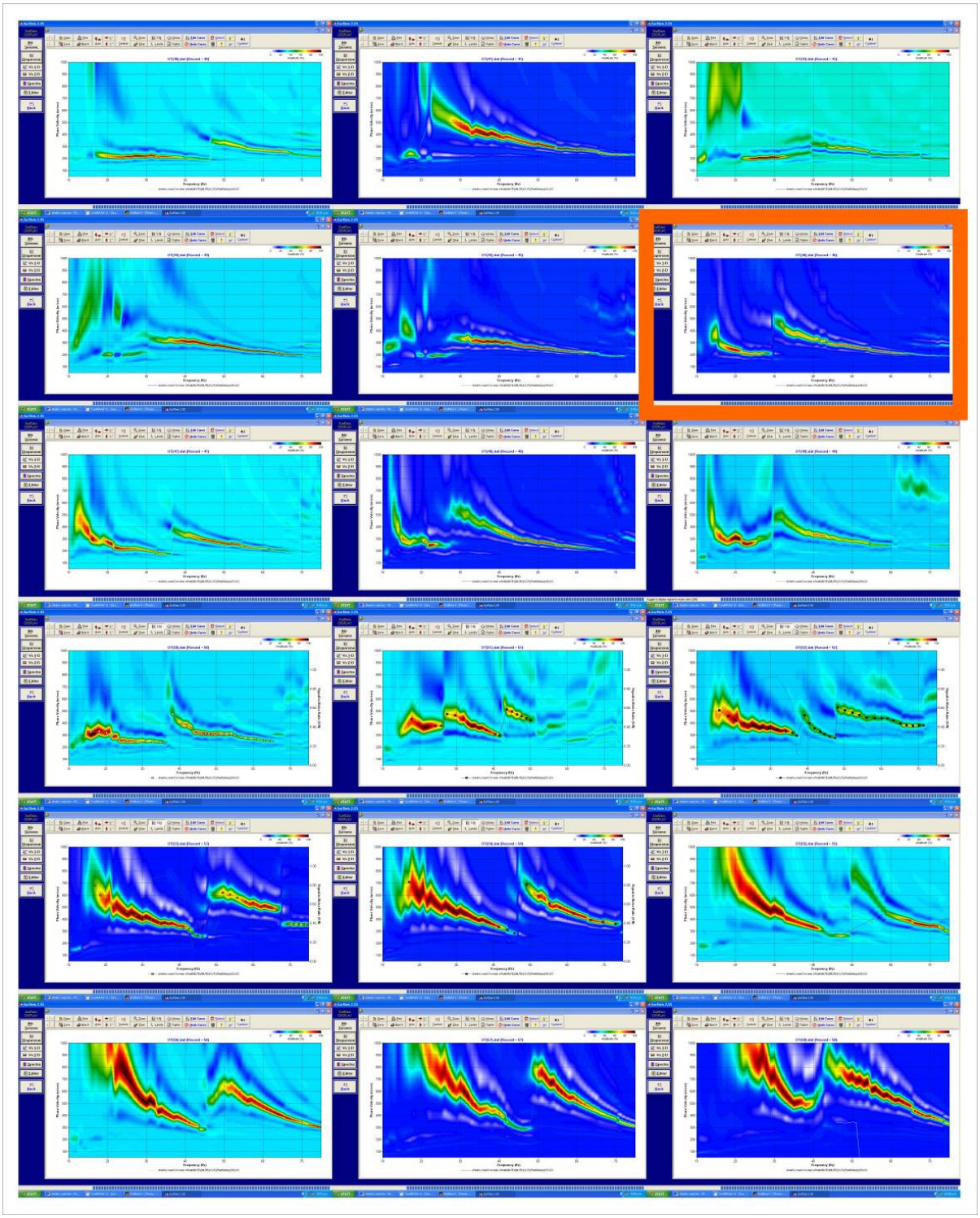

Figure 7-9: Raw unprocessed dispersion images either side of record 46 (outlined), showing the change in character between record 40 (top left) and record 58 (bottom right). Record 41 (top centre) is located at the western end of the trench where schist was uncovered and shows higher mode completely dominating fundamental mode dispersion. Aside from that, the fundamental mode is progressively swamped by higher mode dispersion before re-emerging with a much more strongly dispersive character.

7.2.3 2D S-wave velocity sections, interpretations and correlations

The dispersion curves were inverted and 2D Vs sections are presented for both first and second processings of the single shot records, as well as for the FSW records (Figure 7-10). As was found at the Dalethorpe and Boby's Stream sites, FSW records facilitated modal separation and provided a stable result. In this case, however, the single shot records were reprocessed using the FSW records as a guide with significantly improved results. Dispersion could be picked to slightly lower frequencies for the FSW, so the FSW record is slightly deeper. Overall, the velocities were typically less than 350 m/s in the central section and less than 800 m/s elsewhere. S-wave propagation velocities parallel to the foliation of schist are very similar to the S-wave velocities observed in Torlesse greywacke at low confining pressures, although S-wave splitting does occur (Okaya et al., 1995)(***Figure 7-11***). In this instance the fabric orientation is dipping slightly in the opposite direction to the direction of S-wave propagation at the NW end of the line. This orientation should be relatively fast. The fault should therefore be imaged as juxtaposition of a high velocity rock mass (schist) with a much lower velocity material (Tertiary and Quaternary strata). The highest velocities at the NW end of the line can be confidently inferred to represent schist of the same orientation as the outcrop. If the S-wave velocities in weathered schist are also similar to those in Torlesse greywacke (Table 4-2), which is a reasonable assumption (Fumal, 1978), the transition into completely weathered, outcrop-oriented schist can be inferred to occur at the 550 m/s contour. This velocity boundary, which may represent the Taieri Ridge Fault, is located at station 580 (Figure 7-10).

Unlike the outcrop at the NW end of the seismic line, the fabric orientation of the schist in the trench is almost normal to the S-wave propagation direction. S-waves propagating through schist at this orientation would probably travel at up to 35% lower velocities than the S-waves at the NW end of the line (Okaya et al., 1995). This suggests velocities of only 350 m/s for completely weathered schist, which may explain the failure of the S-wave velocity profile to differentiate between the soft rocks and the schist exposed in the trench. The presence of the schist is disguised by its fabric orientation.

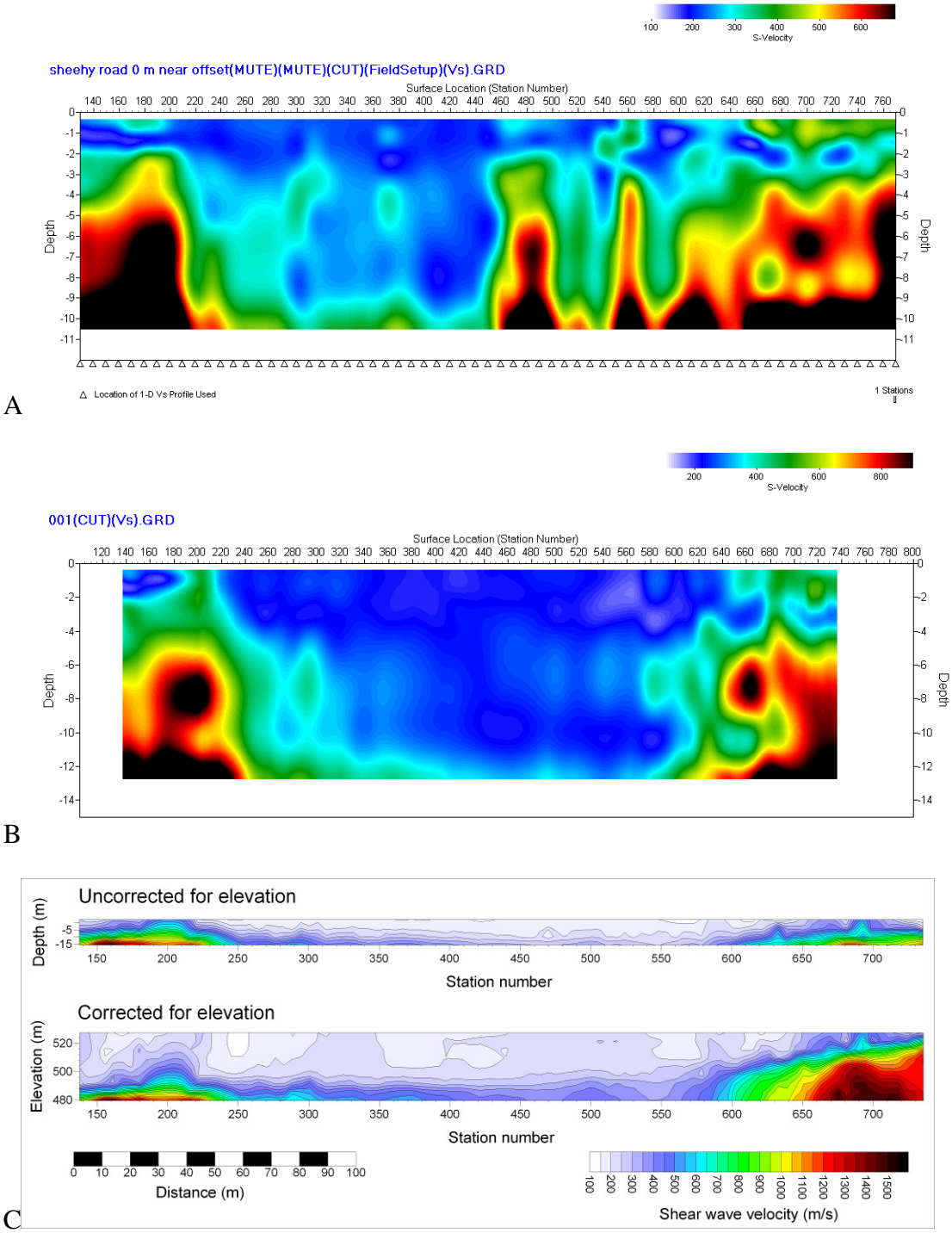

Figure 7-10. Comparison of MASW profiles derived from the same seismic data but using single shot and walkaway configurations. A) 5m offset 38 channel single shot survey with higher mode contamination. B) 5 m offset 86 channel FSW survey. C) 5 m offset 38 channel reprocessed in the light of B and contoured in Surfer8 to produce a crudely 'elevation corrected' profile.

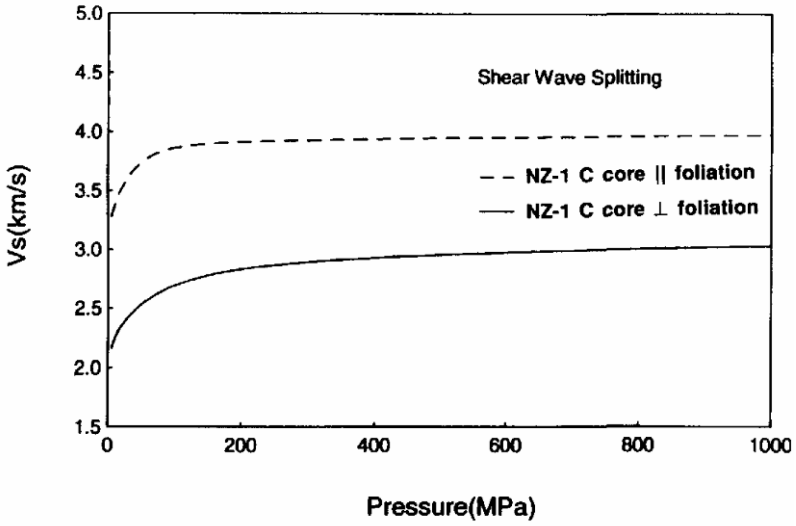

Figure 7-11: S-wave velocities indicating the potential for S-wave splitting in Alpine Schist (after (Okaya et al., 1995)). The anisotropy and velocities of the NZ1 Alpine Schist mylonite are very similar to the NZ 3 and 4 Haast Schist. Even at low pressures, propagation parallel to foliation is approximately 1 km/s faster than propagation perpendicular to foliation. This has implications for the planning, execution and interpretation of MASW in a schistose setting.

An intriguing component of the MASW profiles is the presence of a high velocity field at the SE end of the line. The high velocities fall in line with several NE trending doglegs in the streams draining the Taieri Ridge. This suggests that both the streams and the high velocities reflect the presence of an unmapped structure in the near surface, a structure to which the streams are reacting. The most likely candidates for the source of this velocity high are either an igneous body or near surface bedrock. No igneous body was mapped in that area during the magnetic survey carried out by Kilner (2008). Also, the velocities and the vertical velocity gradient are markedly similar to the velocities in the schist at the NW end of the line. Until proven otherwise the high velocity body is interpreted as in situ schist, possibly the riser of a bedrock strath cut by the ancestral river and subsequently in-filled.

7.3 Correlations

7.3.1 Geomorphology

High quality geomorphological data for this site are limited to total station elevations determined for the HRR seismic stations. Even so, the data are interesting. Visual examination of the slope profile surveyed at single station intervals (0.5 m spacings, Figure 7-12) suggests a break in slope at station 550, 5 m uphill of the trench. Gradient indices, however, show that the slope is changing rapidly over the 540-580 interval before attaining its stable maximum value at station 580. This is the same location at which the

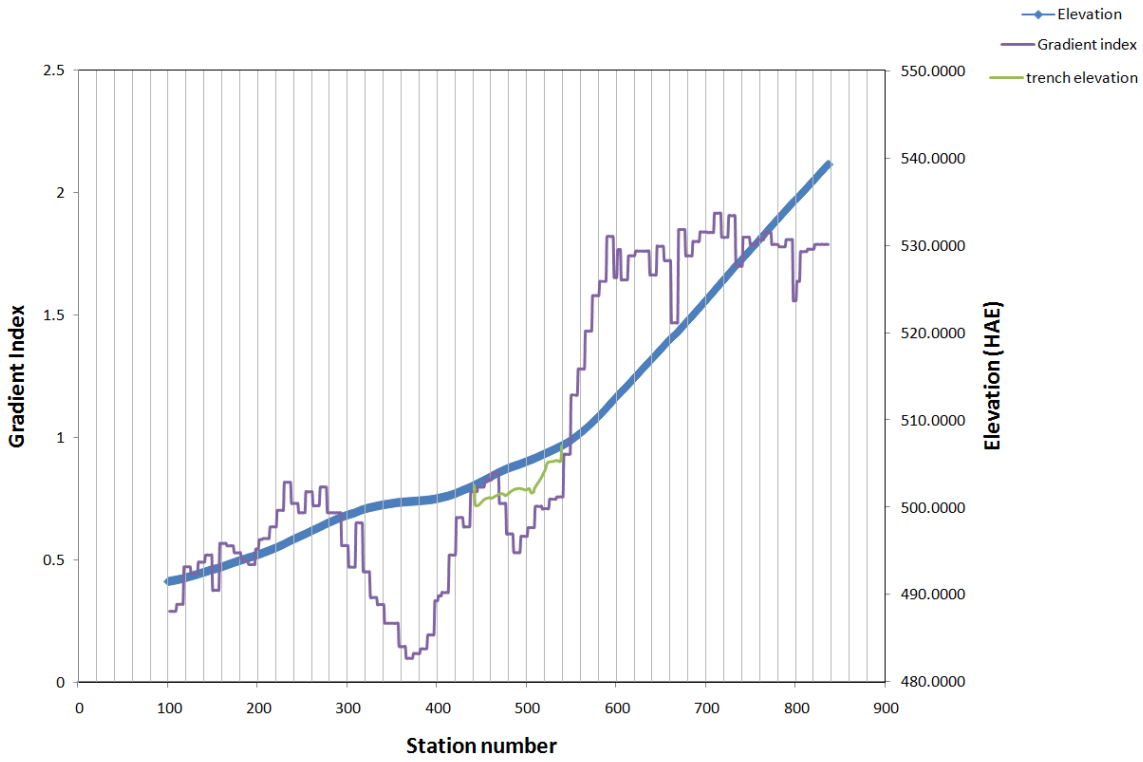

Figure 7-12. Sheehy road seismic line station-to-station gradients indexed against the end-to-end gradient of the line.

transition across the fault into weathered schist is inferred in the previous section. This break in slope has previously been mapped by Norris and Nichols (Norris and Nichols, 2004) as the unconformity separating the schist from the overlying Hogburn Formation. Unfortunately, this interpretation cannot be discounted on the basis of the MASW profiles alone, as the nature of MASW is such that dips are smeared. In particular, velocity inversions such as would be expected where high velocity schist overrides low velocity strata along a low to moderately dipping fault plane are likely to be poorly represented by the inversion, hindering structural interpretation.

7.3.2 High Resolution Seismic Reflection Survey

Little of value is gained by correlating the MASW profiles with the original HRR survey. The two survey types image at very different scales and most HRR surveys are not interpretable in the top 10 m (Finnemore, pers. comm). There is, however, an apparent correlation of the southeastern high S-wave velocity zone with the closest approach to the surface of the first high amplitude reflection. If the reflection is not a processing artefact, the correlation lends weight to the interpretation of the high S-wave velocities as near surface schist bedrock.

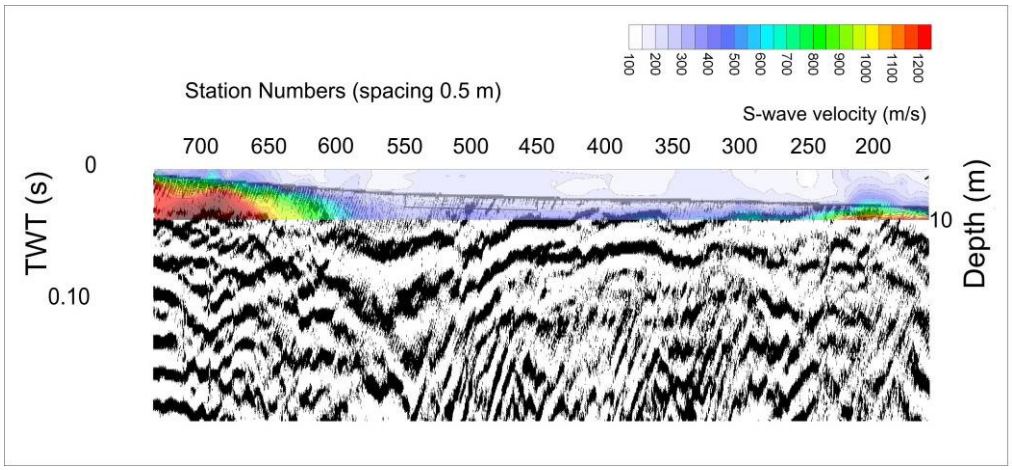

Figure 7-13: Correlation of the elevation corrected MASW profile with the original HRR profile.

7.4 Swept Frequency imaging

As a wave propagates, an apparent attenuation accumulates because reflections from individual fractures interfere with the propagating wave. This seismic response to fracturing provides a means of inferring fracture density from variations in seismic velocity in a media (Boadu and Long (Boadu and Long, 1996)). Suppose, however, that rather than computing the numbers it was possible to view the location of the attenuating fracture by directly examining the trace-to-trace coherence and amplitudes of transmitted surface waves in the subsurface. Surface wave swept frequency records (SFRs), produced in Surfseis from impulsive shot records, may provide just such an opportunity.

Examination of SFRs is an integral part of MASW processing that facilitates determination of the optimum offset range and also allows for examination of lateral variability in the subsurface (Chapter 3 and Appendix A). During the processing of the Taieri Ridge data it became apparent that anomalous low amplitude zones affecting a range of frequencies in one record could often also be observed in an adjacent record, offset by a number of traces equivalent to the shot offset. In some but not all instances these low amplitude zones separated areas of the subsurface with significant lateral velocity variation. It is possible that these low amplitude zones are caused by leaky modes or channel waves, interfering with the fundamental mode in the offset-time (*x-t*) domain. Leaky modes are multiply reflected and constructively interfering dispersive waves propagating in a waveguide. Part of the energy is reflected each time a compressional wave hits the waveguide wall, while the rest is converted to compressional or shear energy that radiates out of the waveguide, hence the term ‘leaky’. A channel wave is a wave that is propagated and confined in low velocity layer. Such interference with the

fundamental mode is generally difficult to deal with in studies such as this but the distribution of the interference may be interesting in and of itself.

A single-trace-per-channel composite SFR of part of the Taieri Ridge line was produced using screenshots pasted in Corel Draw. This exercise was undertaken as a means to further understanding exactly how the dispersion and ultimately the 2D inversion were being affected by the presence and distribution of the low amplitude zones. It also provided an opportunity to ascertain whether these apparently systematic variations in the SFRs reflected systematic variations in the subsurface, as it seemed reasonable to assume that they would do. The composite SFR, termed a swept frequency image (SFI), is presented in Figure 7-14 along with its interpreted counterpart.

The same simple rationale that underpins MASW allows an SFI to be interpreted as a 2D image of near surface elastic variability. That rationale can be summarized as follows (Park et al., 1999a). Frequency is inversely related to depth through wavelength. SFRs display the phase velocity of each frequency component of the record in increasing or decreasing frequency order. Within the SFR, the phase velocity and attenuation characteristics at each frequency reflect the average elastic properties of the subsurface down to approximately half the wavelength. That is to say, the velocities of the lower frequencies (longer wavelengths) are controlled by the S-wave velocities of the deeper layers in the subsurface. Higher frequencies similarly reflect S-wave velocities closer to the surface.

The images in Figure 7-14 were constructed from a swept frequency record produced by convolution of the shot records with a linear upsweeping function from 20-100 Hz. The swept frequency record had a mild automatic gain control applied. Every third SFR from the footwall end of the trench to the hanging wall (NW) end of the line was screenshot and pasted into Corel Draw. A 5 m shot spacing meant that only 10 traces per record were required to yield the one trace per station image so the screenshot was trimmed to leave only the last 30 of the 38 traces in the record. A composite one-trace-per-station SFR was then created by joining the resulting bitmaps along their boundaries. The stepped appearance results from the somewhat arbitrary strategy employed for placing contiguous bitmaps, which was to maintain the linearity of the lowest frequency event in the record. Because an upsweeping SFR had been used, the bitmaps were mirrored around a horizontal line to place the high frequencies at the top. The result was an image with a

A

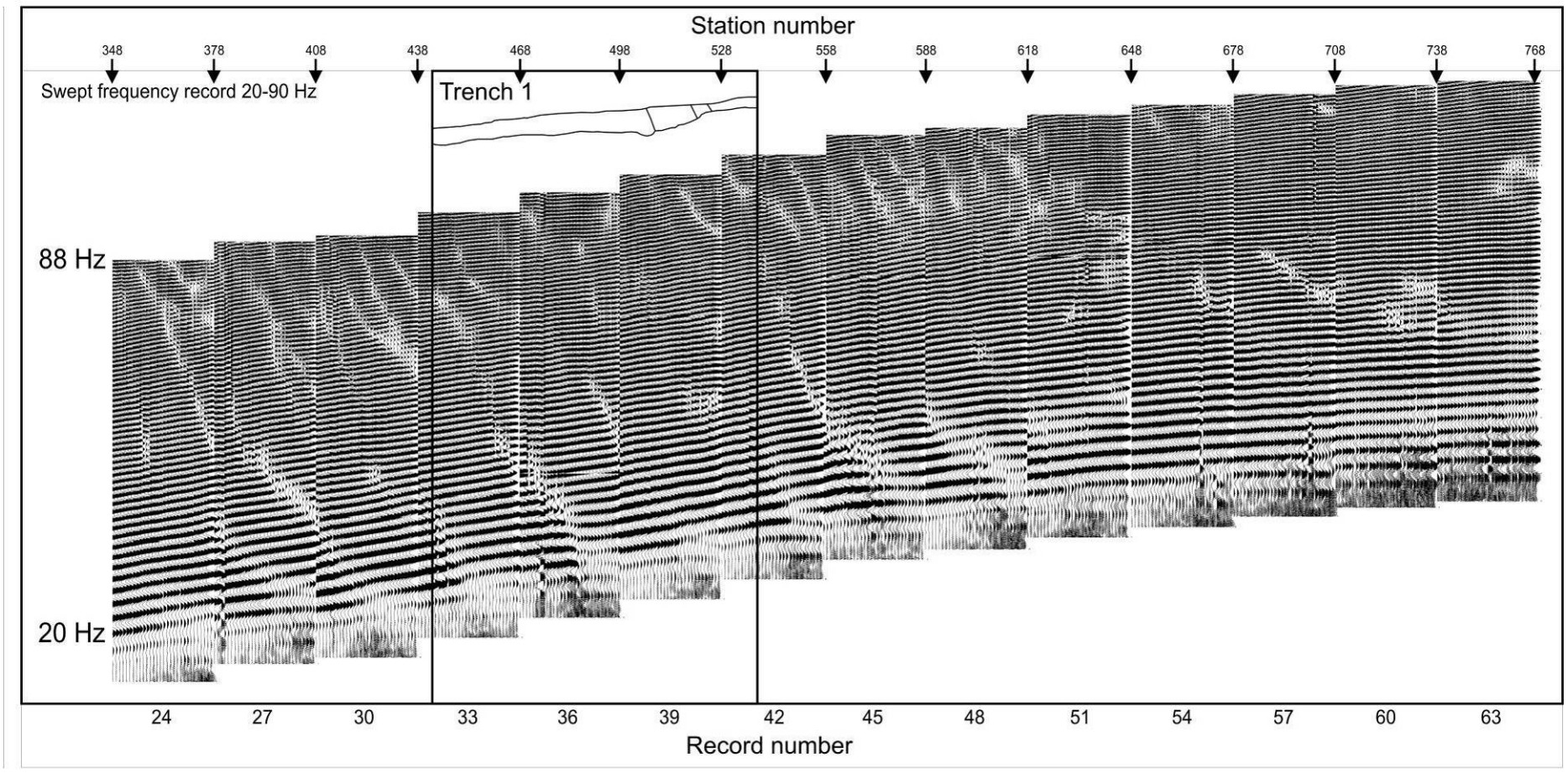

B

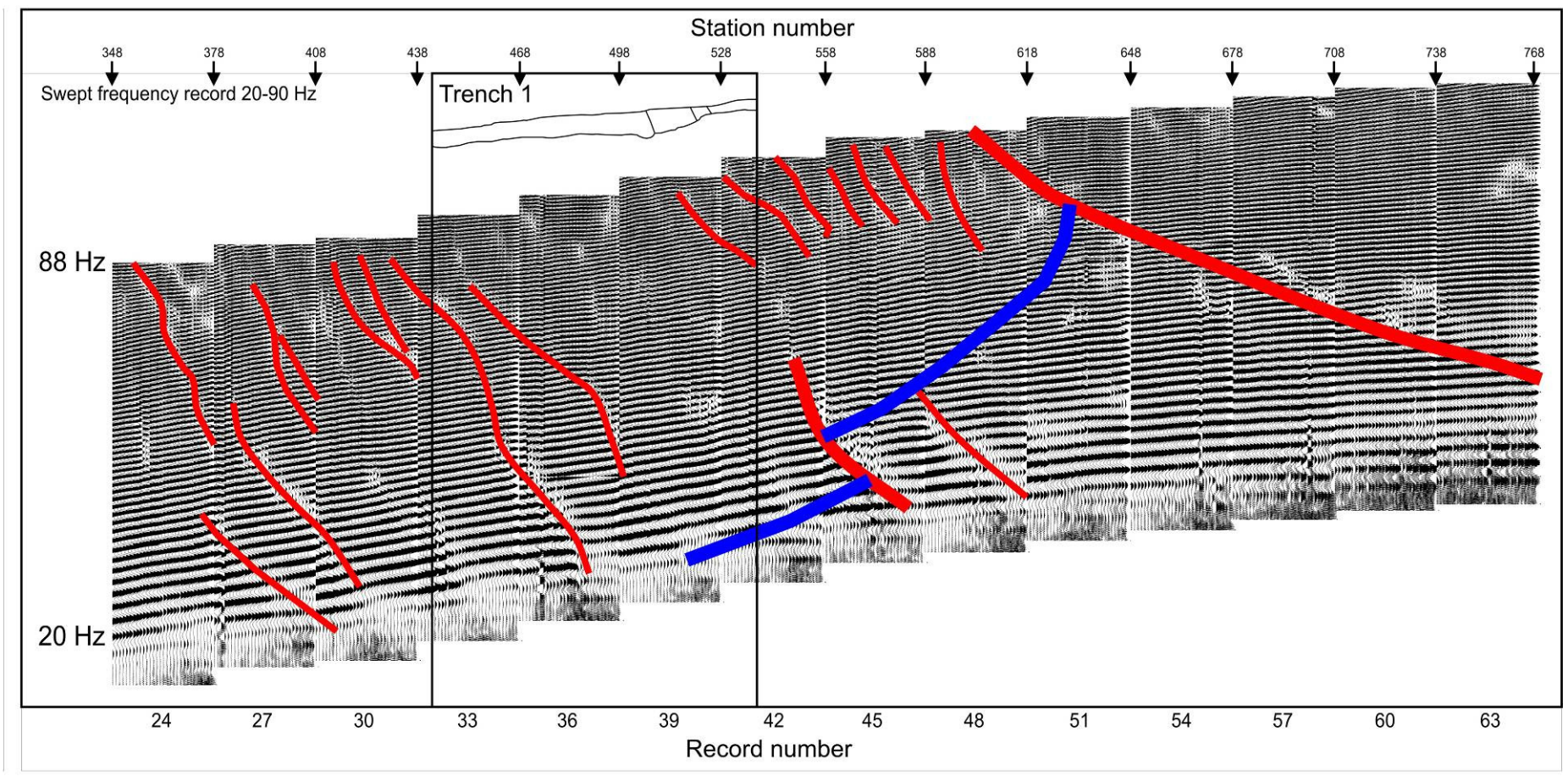

Figure 7-14: Swept frequency image of the northwest end of the Taieri Ridge seismic line A) without and B) with interpretation. The black seismic lines are surface wave events of the frequency scaled on the left of the image. The slope of the line is inversely proportional to the velocity of the event. Red lines are faults or shears, whilst the blue line is a velocity-based pick of the location of the unconformity. The lateral location of the trench is shown, together with the location of major unit boundaries observed in the trench. For discussion see text.

true distance or station horizontal scale and a frequency vertical scale of indeterminate depth.

Several features stand out immediately on examination of Figure 7-14A and the overall appearance of the image is strikingly structural. The most obvious lateral variation is the abundance of near surface low amplitude zones in the southeast and their abrupt disappearance shortly after station 588. The clean and fast Rayleigh waves east of station 588 do not immediately extend to depth. Rather, the clarity of the SFR increases in depth with each subsequent record. The base of the clear zone is marked by a low amplitude zone that is reasonably continuous between records and dips to the NW. Below that low amplitude zone is an almost mirror image continuation of the clean fast Rayleigh waves that both dips and declines in coherence to the southeast. It is my contention that the low amplitude zones contributing to this image can be structurally interpreted as the interference of reflections from structural surfaces with the propagating Rayleigh waves, as suggested in the first paragraph of this section.

On this basis, an interpretation of the SFI is presented in Figure 7-14B. The shears and faults are picked visually but the unconformity is picked by vertically exaggerating the image and picking the break in slope between lower (Tertiary) and higher (schist) velocities. Deformation is distributed mainly in the footwall of the NW dipping Taieri Ridge fault, just as predicted by Norris and Nichols (Norris and Nichols, 2004). The exact dip of the fault is difficult to determine due to the indeterminate vertical scale, but can be estimated by calculating ½ the wavelength at the point where the fault leaves the image. The velocity at that point is approximately 600 m/s at a frequency of approximately 30 Hz. This gives a calculated wavelength of 600/30 or 20 m and a ½ wavelength depth of approximately 10 m. Over a distance of 35 m this translates to a dip of only 16 degrees in the near surface, which may go some way to explaining the difficulty seeing the fault on the HRR seismic sections.

The SFI is also correlated strongly with the trench in Figure 7-14, and to much better effect than the standard MASW profiles. The trench profile is shown together with the location of the two major structural boundaries observed in the trench. The presence in the SFI image of only two major low amplitude zones in the immediate vicinity of the trench,

and the strong correlation of both zones with the structure in the trench, lends weight to the veracity of this technique.

The SFI technique is not completely without precedent. Park *et. al.* (Park et al., 1999a) presented a technique for void detection based on examination of a swept frequency record to which a dynamic linear moveout (DLMO) had been applied based on a reference location. The application of DLMO corrects for the offset effect by flattening out the velocity slope of events in an SFR. If a particular frequency range in a shot gather has velocity characteristics that are different to those reflected by the reference dispersion curve, the 'correction' will be over (for higher velocities) or under (lower velocities). Park *et. al.* (Park et al., 1999a) stacked the constituent traces of the DLMO corrected records and output the stacked traces. The resulting stacked section clearly delineated a void in the subsurface.

The effect of the DLMO and stacking process, however, is not only to flatten out velocity events in similarly dispersive shot gathers. Additionally, frequencies with phase velocities similar to the reference location will have large stacked amplitudes due to constructive interference, whilst frequencies with different phase velocities will have weak stacked amplitudes due to destructive interference. The degree of attenuation is related to the extent to which the velocities are anomalous compared to the reference location. Essentially, the DLMO process highlights anomalous areas with respect to the reference location with little regard for local subtle anomalies. The stacked section at Figure 7-15 has been constructed in the manner of Park *et al.* (Park et al., 1999a) with the reference dispersion curve taken from the NW (hanging wall) end of the line. It shows clearly the variance of the footwall velocities from those on the hanging wall but obscures almost all of the detail that is visible in the SFI section created from the raw SFRs.

7.5 Discussion

Ideally, the results and interpretations presented here should be field tested and the test results also presented here. Unfortunately, the planned trench that was the main objective of the ground truthing exercise has not yet been dug due to landowner-requested delays caused by a drought. Although both the Kilner thesis and this one have now been submitted, the trench will probably still go ahead, as it is still relevant to ongoing research

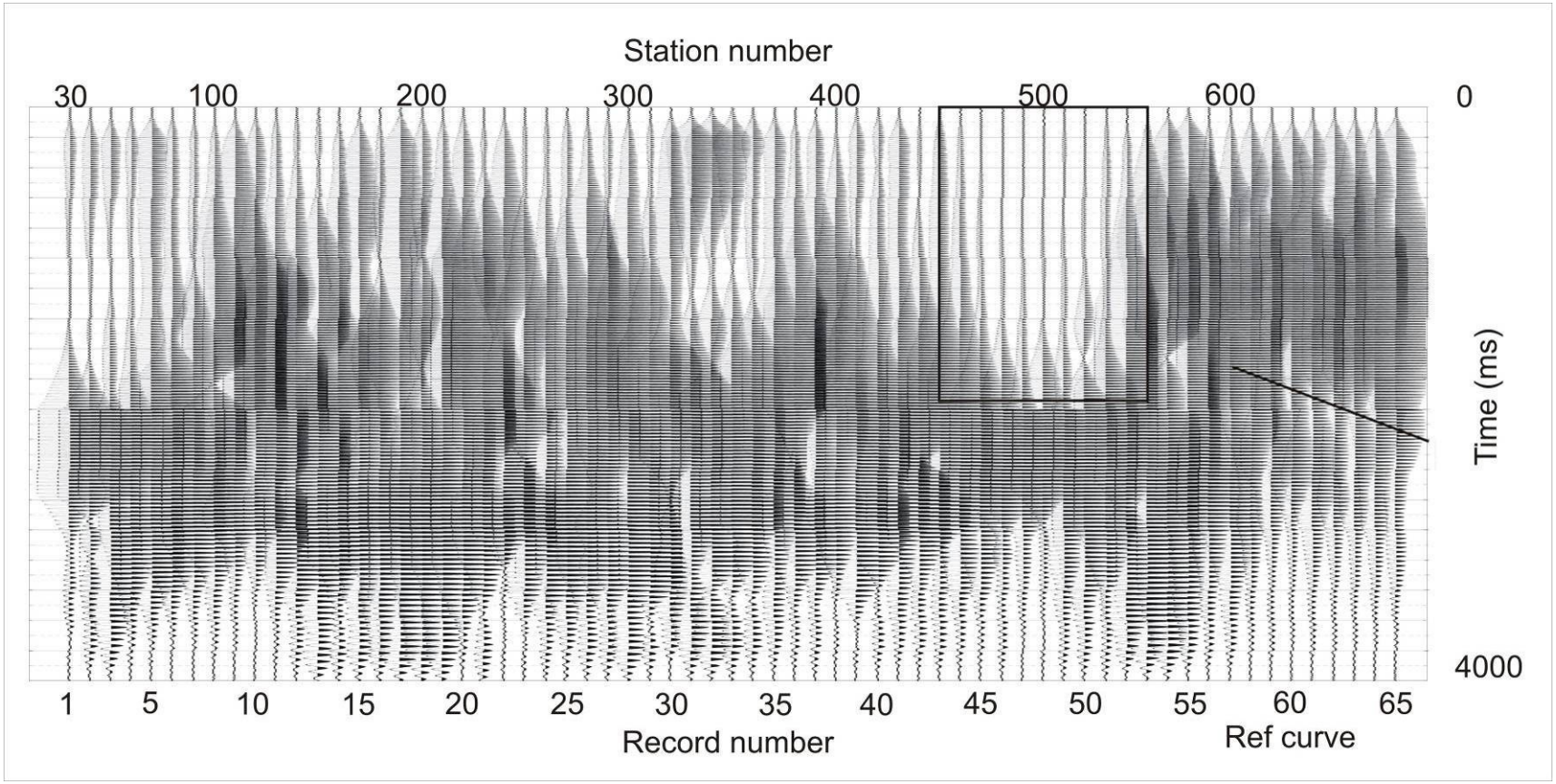

Figure 7-15: Dynamic Linear Moveout (DLMO) stacked section of the Taieri Ridge seismic line. Rectangle is trench location and line indicates possible imaging of faulting.

at the University of Otago. When excavation finally begins it will be sited on the basis of the interpreted MASW. It is my intention to follow through on this site by continuing with the ground truthing after submission of this thesis, including the full spectrum of geotechnical and crosshole seismic investigations. The results will be appended to this document at that stage.

This survey highlights both the promise and the limitations of MASW. One clear limitation is the potential for structural features to be disguised by non-preferred orientation of anisotropic rock fabric. This problem may have disguised the presence of schist in the trenched section of the seismic line. The problem may have been amplified by the weathering of the schist pre-decreasing the otherwise high velocity of the schist so that the velocity in the slow direction was indistinguishable from the lower velocities of Tertiary and Quaternary units. It seems possible that survey planning may need to take account of local fabric orientation to avoid inadvertently blurring velocity boundaries.

Another limitation that has been repeatedly encountered in this study is the difficulty in identifying and removing higher mode contamination of the fundamental mode surface wave signal. The problem is common with fundamental mode inversion techniques such as this (O'Neill and Matsuoka, 2005), particularly over faults (Nagai et al., 2005) and some authors recommend full-wavefield modelling where the subsurface is anything other than normally dispersive (Forbriger, 2003a, b). Figure 7-9 is the first time in this study in which completely unprocessed dispersion images were produced and viewed simultaneously for a critical series of records rather than processing record by record. This strategy proved very informative and was used to good effect to guide dispersion curve extraction. In particular, it was useful to aid identification of the fundamental mode on the dispersion image. What was immediately apparent was that signal that may have otherwise been discarded as higher mode is actually fundamental mode signal characteristic of a separate lithology coexisting in the subsurface within the array aperture. MASW is not equipped to deal well with a dispersion curve that includes both ‘fundamental mode’ dispersion trends, because it models the lateral velocity changes that create the trends as vertical velocity changes, typically resulting in an apparent velocity inversion. O’Neill and Matsuoka (O'Neill and Matsuoka, 2005) modelled several situations that may lead to ‘modal’ jumps and concluded that full wavefield modelling may provide a better option where the surface is not normally dispersive.

An investigation of the relative merits or otherwise of full wavefield modelling is beyond the scope of this study, which rather aims to investigate the utility of MASW. The SFI technique related in this chapter, however, may provide a cheap and cheerful under the table method of accounting for all the variability in the surface wavefield.

8 DISCUSSION, CONCLUSIONS AND RECOMMENDATIONS FOR FURTHER RESEARCH

This final chapter presents a general summary and discussion of points arising from the study. It begins by addressing the extent to which the study objectives have been met. To this end, the first section discusses the utility of the technique for the location of discrete and disseminated faulting. That is followed by discussions of the extent to which within-zone variability in S-wave velocities can, and has, been correlated with measurable rock properties and with the distribution of ground deformation. Having summarized the utility of the technique, the fundamental strengths and weaknesses are addressed, along with strategies for dealing with problems arising from these. Other matters discussed include the technical and fiscal potential of MASW as a tool for fault-zone planning, and promising photogrammetric geomorphic analysis techniques being developed at the University of Canterbury's Geospatial Research Centre. It draws conclusions and makes recommendations for further work.

8.1 Utility of the MASW technique

An understanding of the relationship between past, ongoing and future ground motion, local geology and natural hazards fuels a desire to predict the ground response to seismic and aseismic deformation, whether for building design or for land use zonation. This study has investigated the utility of MASW as a tool in this regard and the results are discussed here.

8.1.1 Fault location

The results of this study demonstrate that, in most circumstances, both discrete offsets and zones of faulting and damage can be imaged effectively using MASW. Discrete minor fault offsets were best imaged in hard rock lithologies such as Torlesse greywacke, where vertical and lateral velocity gradients are steepest. The greater the vertical gradient, the greater the lateral contrast where the velocity gradient is offset. Damage zones were similarly best imaged in Torlesse greywacke due to the greater influence of cataclasis on hard rock S-wave velocity. Where damage zones are imaged in soft rocks, they should be considered a minimum indication of the true extent. The ability of an experienced MASW

practitioner to make improved determination based on raw and swept frequency record characteristics should not be overlooked when using the MASW technique.

8.1.2 Geotechnical S-wave variability correlations

8.1.2.1 Discrimination of cataclasis

This study has shown that the S-wave velocities of the lithologies studied are affected to varying degrees by shearing and cataclasis, and that the primary determinant of how S-wave velocities will react to cataclasis is intact rock strength. Below a 20 MPa threshold the S-wave velocities are dominated by rock strength whilst above that threshold the influence of cataclasis and fracturing increases logarithmically. The results of the Taieri Ridge survey, however, suggest that where rocks are juxtaposed from either side of the threshold it may be difficult to discriminate the effects of cataclasis from primary lithological variation. This may be exacerbated by S-wave splitting. Cataclasis in Torlesse greywacke appeared to reduce Rayleigh wave dispersion, so sudden temporary decreases in vertical velocity gradient may provide useful pointers to the presence of cataclased rock masses.

8.1.2.2 Lithological discrimination

In general, gravels are readily distinguished by their low S-wave velocities where they overlie a suitably stiff substrate but less so where they overlie softer lithologies. Similarly, the hard rock lithologies such as greywacke and schist are readily discriminated from Tertiary and Quaternary cover sediments as seen at Taieri Ridge. Discrimination within the cover sediments is less simple because of the large degree of overlap in the velocity ranges. Despite the overlap, however, discrimination is possible because units with similar velocity ranges show different velocity gradient characteristics. The Kowai Formation unit in the meander point bar at The Deans, for instance, can be differentiated from the juxtaposed Waikari Formation based on its weathering-related vertical velocity gradient, despite the great degree of overlap in their near surface S-wave velocities. This type of permanent change in vertical velocity gradient should be differentiated from temporary changes indicative of cataclasis.

The differential vertical velocity gradients described above may be due to changes in effective stress or porosity with depth, and may also be due to long term water table effects (Fumal, 1978). These are factors that may become laterally variable in an active

tectonic setting, where stress regimes may change over metres to tens of metres. The survey over Loburn Formation, for instance, was unusual in that it showed a variable velocity increase towards and around the fault-zone that may be attributable to localised stress or water regime factors. This suggests that, for the weakest lithologies at least, S-wave profile interpretation may not always be intuitive because primary lithological velocity characteristics may be overprinted by tectonically induced velocity increases.

The predicted near surface S-wave velocities from Chapter 6 are reproduced below and expanded to include all the encountered lithologies from Boby's Stream along with Torlesse greywacke.

Table 8-1: Summary table of predicted S-wave velocities for all lithologies encountered in this study.

Unit	$V_{s\,min}$ (m/s)	$V_{s\,max}$ (m/s)
Torlesse greywacke	500	1100
Weka Pass Limestone	302	593
Mt Brown sandstone	227	596
Amuri Limestone	202	628
Waikari Formation	190	563
Waipara Greensand	130	594
Loburn Formation	98	2-300
Conway Formation	47	2-300
Kowai Formation	150-200	<450?

8.1.2.3 Transferring between different scales of investigation

A particular issue with laboratory analysis has been the scale-dependence of S-wave velocities. This apparent dispersion between laboratory and survey investigation wavelengths is dealt with here by correlating fracture-related percentage-declines in velocity rather than absolute velocities. This strategy is valid in this instance because the basic lithological character of most investigation sites will be reasonably well constrained. For example, the Taieri Ridge Fault, though its exact location was unknown, could be confidently stated to emplace basement schist against or over Tertiary and Quaternary

sediments. The survey can thus be interpreted if the likely near-surface velocity ranges of these mapped lithologies are known, and geotechnical parameters can be inferred based on lateral velocity declines. Recall however, from Section 8.1.2.1 above, that interpretation of the Taieri Ridge MASW survey is complicated by the juxtaposition of lithologies from either side of the 20 MPa rock-strength-threshold.

8.1.3 S-wave velocity, geomorphology and ground deformation

Earthquakes such as the Chi-Chi earthquake of 1999 have demonstrated the importance of avoiding areas of ongoing or off-plane deformation (eg Kelson et al., 2001). MASW has proven very useful in this regard. The Springfield Fault-zone at Dalethorpe has a long history of accumulation of seismic and aseismic deformation over a wide zone. The correlation of MASW and detailed surveying at that site was extremely strong and facilitated demarcation of a wide zone of seismic and aseismic deformation that extended over more than 200 m. This included verified identification of 2.5 m of aseismic warping within the wedge, imaging of multiple flexural shear zones in the footwall of the Main Upstream Thrust, and an apparent velocity response to a parasitic anticline in the Bell Hill Fault footwall syncline. Soft rock deformation zones at the Boby's Stream sites were also imaged, including fault angle depressions and anticlinal warping as at The Deans, although as mentioned above none of the Boby's Stream lines was long enough to reveal a stable out-of-zone velocity signature. Overall, this study clearly demonstrates that integration of topographically corrected MASW, with detailed geomorphological surveying, should be considered the most desirable and rewarding strategy at sites where ongoing off-plane deformation is suspected.

The data accumulated in this study provided an opportunity for a comparative evaluation of the distribution and style of strain, surface deformation and fault zonation between the three test sites. All three were thrust faults with the Boby's Stream being an oblique thrust. Both Dalethorpe and Boby's Stream surveys showed evidence of damage concentration in the hanging wall. The S-wave velocities in the soft rock at Taieri Ridge were virtually featureless and very little could be determined about the style of strain from the standard MASW profile. Swept frequency imaging, however, provided much greater details about the internal structure and unlike the other two areas, showed that the coseismic strain was mainly disseminated through a wide zone in the footwall.

8.1.4 Topography

The use of surface wave surveys is considered questionable where significant topography, of a smaller scale length than the array aperture, is encountered along the survey line. In this study a successful survey was run across a fault scarp of more than 1 m. Topographic correction of S-wave velocity profiles is however, essential to map subsurface structure in such challenging terrain and the use of Surfer8 added significant value to the results. Despite uncertainty about the geometric validity of the correction technique, it appears to have been successful. In order to minimise problems and the likelihood of erratic surface wave behaviour the survey should be oriented where possible to avoid the true dip of the scarp by crossing it obliquely.

Although ongoing deformation was imaged using standard MASW at these two sites, it is apparent that the amplitude of deformation imaged was greater at Dalethorpe, where the calculated recurrence interval suggests that deformation rates are slow compared to those at Boby's Stream. It thus seems reasonable to suggest that the potential for imaging aseismic deformation is a function not only of the rate of the deformation process, but also of the rate at which processes, such as in ground weathering or alteration, can smear the tectonic velocity signature. Once again it seems that resolution is likely to be better in hard rock lithologies like Torlesse greywacke.

Potentially the most exciting deformation mapping in this study is provided by the swept frequency image of the Taieri Ridge Fault. That image apparently shows a zone of disseminated deformation forward of the main fault that extends beyond the 150 m of footwall imaged using that technique. The validity of swept frequency imaging is not yet verified but this is expected to change after paleoseismic trenching is undertaken at the site.

8.2 Fundamental strengths and weaknesses of the MASW technique

8.2.1 Strengths

Possibly the greatest strength of the MASW technique lies in its combination of versatility, speed, simplicity and interpretability. Surface waves will propagate through even the weakest material and all they require to do so is a half-space. Their propagation is not significantly challenged by subsurface utilities or structures (Miller et al., 1999b). Large datasets can be acquired rapidly with a single vehicle and a crew of three.

Processing is simple, especially in comparison to other seismic techniques. Both the images and the numbers have numerous end-user uses beyond the fault-zone location itself. For instance, this study has shown how strongly S-wave velocities reflect the elastic properties of the subsurface, and the relationships developed will be useful in a variety of engineering end user applications, such as foundation design for large structures. MASW surveys are already being undertaken in lieu of drilling for wind turbine foundation design.

8.2.2 Relative strengths: A comparison with other geophysical methods

During the course of this study, MASW has been favourably compared with a range of other geophysical techniques. Of the two other seismic techniques (conventional seismic reflection by ETH Zurich at Dalethorpe and High Resolution Reflection (HRR) seismic by Kilner, (2008) at Taieri Ridge), the conventional reflection data were discarded and the HRR sections were misleading and difficult to both process and interpret. The reprocessing of the HRR data, however, allowed a direct comparison with MASW that highlighted several points. Firstly, the HRR provides greater penetration than the MASW but the near surface resolution is lacking. The MASW on the other hand provides good near surface resolution but does not image any structure at depth. In this respect, it fills in the interpretation of the poorly resolved top 10 m of the HRR section. Given the demonstrated compatibility of the techniques in terms of data acquisition parameters, the two should be considered complementary.

Crice (2005) referred to MASW as 'the wave of the future', and compared the revolution consequent on its development with the paradigm shift that followed the development of resistivity tomography. Both techniques are simply applied and resistivity has already been used effectively in active fault investigations (eg Similox-Tohon et al., 2006). The electrical techniques used previously on these study sites, however, fare poorly in a comparison with MASW. For instance, the results of the Dalethorpe resistivity survey was ambiguous and difficult to interpret, probably because they are not related to the elastic properties of the subsurface, which vary across a fault-zone due to lithological and cataclastic contrasts. The technique may, however, fare better in the soft rock lithologies.

GPR surveys produced excellent images both at Dalethorpe and on the Claremont property at the western end of the Boby's Creek site but the data are limited in terms of penetration and end use. Additionally, the time taken to acquire and process a GPR survey

is greater for a given area and the results are far from guaranteed, especially where they may be affected by cultural noise such as buried services or by unsuitable subsurface conditions such as conductive clays. The Claremont GPR surveys, however, show that GPR does work well in areas where lateral velocity contrasts are minimal, whilst the RD1 line clearly showed the limitations of MASW in such conditions. In such instances, joint application and interpretation of GPR or other electrical methods and MASW may be advisable so as to achieve the best results. In most cases, MASW should at the very least be considered as a wider reconnaissance tool.

8.2.3 Inherent weaknesses

Interpretation of gross lithology from seismic velocities is not unusual in geophysics (e.g. Christensen and Fountain, 1975; Fountain and Christensen, 1989). These interpretations are, however, made at a much larger scale than this study and are based on the distribution of compressional and S-wave velocities in the crust or mantle. In this study, no recourse is available to compressional wave velocities, so lithological interpretation must be made based on sound geological mapping and field and laboratory geotechnical analysis of the units in the study area. Previous studies are valuable but, unless a unit is known to be regionally homogenous, they should be locally validated to account for basin or regional scale property variations.

The greatest weakness of MASW, however, is systematic, namely the requirement for a fundamental mode dispersion to be extracted, often from a record plagued by propagation of higher mode Rayleigh waves (eg Nasseri-Moghaddam, 2006). In a fault-zone, this problem is compounded by wavefield scattering. Strategies should be investigated and employed to minimise these problems and thus optimise the utility of the technique. For instance, Nagai *et al*. (2005) recommend the use of a processing technique called Common Mid Point Cross Correlation (CMPCC) to minimise scattering. This technique is not possible within the Surfseis software utilities but might be worth considering for users with access to a suitable seismic processing suite.

8.3 Techniques and strategies

Apart from novel processing techniques, the first recourse of an MASW practitioner is to optimise data acquisition. Strategies in this regard are discussed in the following subsections.

8.3.1 Survey geometry

Selection of appropriate survey geometry is obviously a key step toward a successful survey. Based on accumulated experience, the best approach in a fault-zone setting is to acquire data over a shorter offset range. The near offset is better to be too short than too long. The former limits penetration, but the latter invites higher mode contamination, of which the practitioner will have no knowledge until processing begins.

In ideal circumstances survey geometry selection should follow site calibration; however this is often not practical as it may take up to half a day on site. In general, the array aperture should be minimised to reduce potential velocity variability below the array and to improve the resolution. If more channels are available they should be spaced more closely. This is even more important if swept frequency imaging is considered. Attempts to produce swept frequency records for Dalethorpe were inconclusive, probably because of the wider geophone spacing. If a larger aperture is desired in order to record longer wavelengths, the use of walkaways should be considered. Both the Dalethorpe and Taieri Ridge surveys benefited from the use of walkaway records to visually mute higher modes in the offset-time domain.

It is virtually impossible to recommend a single survey geometry for each lithology. The Taieri Ridge data, however, was of particularly high quality and reasonably simple to process across both hard and soft rock lithologies. This dataset was cropped from the original 0 m near offset to an effective near offset of 5 m, so this should be considered a good starting point. For further information on survey parameters the interested reader should see Park *et al*. (2005a)

8.3.2 Equipment and software

Several improvements to the Surfseis software would be useful, such as a CMPCC processing utility to reduce wavefield scattering and better focus the fundamental mode energy (Nagai *et al*, 2005). An equally useful improvement would be inclusion of a visually-guided f-k domain filter such as the bow slice filter of Park *et al*. (2002) with which to filter higher modes. Inclusion of these options would go some way to reducing the effects of two major sources of systematic noise in surface wave surveys. In the meantime it may be worth pre-processing to perform these steps in a separate software

package prior to dispersion curve extraction. This was briefly attempted using Visual Sunt but little time was available to learn a separate software package.

A significant equipment choice is that of streamer-mounted versus planted geophones. The improvement in penetration using planted rather than sled-mounted geophones at Boby's Stream (see section 6.5), together with the dominance of surface wave energy seen in the Taieri Ridge data (section 7.2), makes a clear case for the preferred use of planted geophones, especially when the survey substrate is grassy.

8.3.3 Noise

Even the best obtainable record contains noise. In addition, systematic noise can make MASW processing difficult in proximity to a fault (e.g. Ivanov, 2006 and this study). The prevalent noise types in all the records analyzed in this study were body wave and higher mode contamination, backscattered surface waves and diffractions. Surface wave diffractions occur where abrupt changes in bedrock topography, perhaps due to a fault, create point sources in the subsurface (Xia et al., 2007). Although diffractions constitute noise, they are still useful indicators of points of interest. Xia *et al.* (2007) for instance, derived a Rayleigh wave travel time equation from which the depth to a diffractor can be determined. The same applies to other systematic noise. In this study, for instance, identification of backscatter was the only method by which the location of a major fault in Loburn Formation mudstone could be identified.

Each noise sources poses its own challenges and noise can not be completely eliminated during data acquisition. The key to success is correct selection of field parameters, disciplined methodology and thorough pre-processing. Once acquired, most records can be enhanced by analyzing the noise in a swept frequency record to determine velocities for application of f-k filtering. This approach proved effective in remediation of most noise sources.

8.4 Potential contribution of the MASW technique to fault-zone planning

The Guideline published by the Parliamentary Commissioner for the Environment (Kerr et al., 2003) defines a fault avoidance zone 20 m either side of the known fault trace or likely rupture zone, with provision to reduce or expand this distance based on the zone of intense deformation (section 1.3.4). This purely geomorphic approach creates difficulties, especially given New Zealand's rapid rates of landscape evolution, which this study has

shown may disguise surface features formed by active folding and recent ruptures. The Dalethorpe study shows that geomorphology is too subjective to use alone with any confidence. Selective erosion by the river and poor bedrock exposure in the modern river conspired to conceal the Main Downstream Thrust prior to the application of MASW. That fault is located much more than 20 m from the previously mapped fault. Similarly, the swept frequency imaging at Taieri Ridge shows deformation extending well beyond a 20 m fault avoidance zone. This is of course, assuming that the fault could be accurately located. It seems amply clear that designation of fault avoidance zones needs a more scientific basis.

MASW shows great potential for addressing these problems. This study has calibrated the technique in nine lithologies, providing the capability to infer subsurface structure and zonation independently of fault exposure. It can thus be used at a range of scales within these lithologies to define the variability and extent and/or boundaries of the fault-affected zone. This capability appears to be unimpaired by degradation or burial of the fault trace. The calibrated MASW technique thus promises to provide the clear guidance called for by the BOE Report (Williams, 2001). MASW is thus an economic, rapid and, most importantly, scientifically informed method of land planning, regulation and risk avoidance in relation to active faults, which will provide cost benefits for insurers, planners, and developers.

8.4.1 Cost

This paper would be incomplete without mention of the fiscal merits of MASW. The Dalethorpe MASW surveys, which took 24 man-hours to survey and should take around 100 hours to process for an experienced practitioner, provide an image of the subsurface structure that can be applied confidently over at least 42 hectares. A single trench to bedrock across the width of the fault-zone would have occupied a 12 tonne digger for 2 days at a cost of around NZ$>2000.00. Borehole drilling and logging at a suitable scale would be significantly more expensive and this cost would be substantially increased if downhole geophysics were employed. A non-invasive geophysical method that has been shown to provide cost-effective and relevant geological, geotechnical and site hazard data for design and planning is therefore extremely attractive. MASW has been shown to fulfil these requirements and should be strongly considered when planning for development on, and adjacent to, active faults.

8.5 Unmanned aerial vehicles for geomorphic mapping

A considerable amount of time is expended in carrying out a detailed geomorphic analysis using EDM or even GPS surveying without any guarantees of continuous coverage. Photogrammetric geomorphological analysis techniques are being developed by the Geospatial Research Centre New Zealand (GRCNZ) that bear directly on the resolution with which geomorphic analyses can be carried out without incurring large financial and time expenses. These include the creation of <30cm digital terrain models using calibrated aerial photography acquired at high resolution by unmanned aerial vehicles (UAVs). A full morning of theodolite surveying was required at The Deans to produce a 25 cm contour map of around 2 hectares using a state-of-the-art semi robotic total station. The same undertaking with a standard theodolite would take at least double that time. A full morning of UAV flights would comprehensively cover as much as 2 km^2 at a much higher resolution. This approach must add confidence and value for money to airphoto interpretation, field mapping and detailed geomorphic analysis. Whilst discussion of photogrammetric techniques is outside the scope of this document, considerable time was expended early in the project investigating their potential. It is unfortunate that the GRCNZ was in its infancy at that time as their data acquisition capabilities would have added significant value to this study.

8.6 Conclusions

It is perhaps slightly ironic that ground roll, the property responsible in such large part for earthquake destruction, can be exploited to image the offending structures. This study has integrated geological, geotechnical, geomorphological and geophysical data to calibrate MASW as a fault-zone planning tool for the detection, characterization and zonation of geological hazards associated with active faulting and folding in a wide range of hard and soft rock lithologies. It has shown that, apart from fault detection, S-wave velocities derived from MASW are also extremely sensitive to within zone variability in deformation in the subsurface. In particular, MASW has proven remarkably effective at detecting damage zones and fault-related folds in hard and intermediate rock types. These are structures that cause much of the off-plane deformation that has been shown to cause severe coseismic structural damage (eg Kelson *et al*., 2001).

The MASW method provides a low-cost scientific basis for fault-zone planning that is in complementary to, and if necessary independent of, geomorphological interpretation, thus

making a valuable contribution to New Zealand's fault risk management practices. Whilst a study of this scope is clearly invaluable given sufficient time and funding, in situations where these resources are limited a surface wave survey should be the first choice as a mapping and planning tool. Suitably acquired data can be multiply processed as MASW in the first instance followed by targeted SFI or HRR. These seismic methods should be preferred in every instance over electrical methods because they provide a measure of the elastic properties of the subsurface, which is more directly relevant to fault-zone planning than electrical characteristics.

8.7 Recommendations for future research

A valuable corollary of this study was the use of MASW to aid reconstruction of the geometry and hence uplift and paleoseismic history of the Dalethorpe pop-up wedge (section 5.2). The strength of the results is constrained partly by the limitations on dating the relevant datum surfaces. This is an aspect of the study that deserves further work, as does the geometry and kinematics of the fault at depth, and its relationship to other range front faults including the adjacent Bell Hill Fault. As it stands, the Dalethorpe component of this study only included limited speculative discussion of the role of the Bell Hill Fault. The latter clearly displaces the younger A surface downstream of the Springfield Faults and thus appears to have ruptured more recently than the Main Upstream or Downstream thrusts of the Springfield Fault Dalethorpe. Research is clearly needed to constrain the role of the Bell Hill Fault and the timing of the last rupture, as these factors have implications for understanding late Holocene base level changes, the reversal of river slip off and the paleoseismicity of the fault complex as a coherent system. Any investigation of the history of the Bell Hill Fault should also attempt to account for the enigmatically underfit nature of the present Hawkins River system and the source of the late Pleistocene flows in the basin.

This study has shown with limited data that a threshold UCS exists, beyond which fracture density supersedes intact rock strength as the primary control on S-wave velocity. A study should be designed to further investigate this threshold. If such a study were to incorporate a wide range of lithologies that are relevant to New Zealand and representative of an equally wide range of UCS values, it may prove possible to derive empirical relationships from which gross lithology can be inferred given geological context and S-wave velocity characteristics.

Sites at the lower resolution of MASW should be further investigated in order to refine the potential for fault location in poor ground. This investigation should be integrated with other geophysical techniques such as resistivity tomography to determine the point at which electrical methods become as useful as MASW.

Finally, a saying from the author's childhood would have us believe that there is 'more than one way to skin a cat' and the surface wave cat is no exception. Crice (2005), in his 'Wave of the Future' editorial, suggested that surface wave surveys will lead to a new era in geophysics because of their usefulness, interpretability and potential productivity. If swept frequency imaging can be practically and theoretically validated, and if it can be given a user friendly automated graphical user interface, it could prove to be yet another way to skin the surface wave cat and thus another step toward Crice's wave of the future.

9 REFERENCES

Anderson, J.G., Lee, Y., Zeng, Y., and Day, S., 1996, Control of strong motion by the upper 30 meters: Bulletin of the Seismological Society of America., v. 86, p. 1749-1759.

Andrews, P.B., Speden, I.G., and Bradshaw, J.D., 1976, Lithological and paleontological content of the Carboniferous-Jurassic Canterbury Suite, South Island, New Zealand. : New Zealand Journal of Geology and Geophysics v. 19, p. 791-819.

Andrus, R.D., and Stokoe, K.H., 2000, Liquefaction resistance of soils from shear-wave velocity: Journal of Geotechnical and Geoenvironmental Engineering, v. 126, p. 1015-25.

ASTM, 1980, Standard method of test for unconfined compressive strength of rock core specimens D-2938-79, Annual book of ASTM standards, Part 19, ASTM, p. 440-443.

Babaie, H.A., Hadizadeh, J., and Babaei, A., 1995, Self-similar cataclasis in the Saltville thrust zone, Knoxville, Tennessee: Journal of Geophysical Research, v. 100.

Bagde, M.N., Raina, A.K., Chakraborty, A.K., and Jethwa, J.L., 2002, Rock mass characterization by fractal dimension: Engineering Geology, v. 63, p. 141-155.

Becker, J., Saunders, W., and Van Dissen, R., 2005, Planning for the development of land on or close to active faults: A study of the adoption and use of the Active Fault Guidelines: Lower Hutt, New Zealand, Institute of Geological & Nuclear Sciences Limited.

Behr, Y., Townend, J., Savage, M., and Bannister, S., 2007, Ambient noise imaging of New Zealand's geological roots, Geological Society of New Zealand Miscellaneous Publication 123A, p. 10.

Benjumea, B., Hunter, J.A., Aylsworth, J.M., and Pullan, S.E., 2003, Application of high-resolution seismic techniques in the evaluation of earthquake site response, Ottawa Valley, Canada: Tectonophysics, v. 368, p. 193-209.

Boadu, F.K., 1997, Fractured rock mass characterization parameters and seismic properties: Analytical studies: Journal of Applied Geophysics, v. 37, p. 1-19.

—, 2000, Predicting the transport properties of fractured rocks from seismic information: numerical experiments: Journal of Applied Geophysics, v. 44, p. 103-113.

Boadu, F.K., and Long, L.T., 1996, Effects of fractures on seismic-wave velocity and attenuation: Geophysical Journal International, v. 127, p. 86-110.

Boore, D.M., 2004a, Can site response be predicted?: Journal of Earthquake Engineering, v. 8, p. 1-41.

—, 2004b, Ground motion in Anchorage, Alaska, from the 2002 Denali fault earthquake: Site response and Displacement Pulses.: Bulletin of the Seismological Society of America, v. 94, p. S72-S84.

Brabhaharan, P., Davey, R., O'Riley, F., and Wiles, L., 2005, Earthquake Risk Assessment Study: Part 1 - Review of Risk Assessment Methodologies and Development of a Draft Risk Assessment Methodology for Christchurch: Christchurch, New Zealand, Environment Canterbury Report U04 / 108.

Branner, J.C., 1911, Impressions regarding the relations of surface geology to intensity in the Mendoza, Valparaiso, Kingston and San Francisco earthquakes.: Bulletin - Seismological Society of America, v. 1, p. 38-43.

Brown, E.T., 1981, Rock Characterisation, Testing and Monitoring. ISRM Suggested Methods: Oxford, Pergammon Press.

BSSC, 2006, The 2003 NEHRP Recommended Provisions For New Buildings And Other Structures. Part 1: Provisions (FEMA 450)

Building Seismic Safety Council.

Buch, F., 2008, Seismic Response of Little Red Hill - Towards an understanding of topographic effects on ground motion and rock slope failure: Christchurch, University of Canterbury.

Bull, W.B., 1990, Stream-terrace genesis: implications for soil development: Geomorphology, v. 3, p. 351-367.

—, 1991, Geomorphic responses to climate change.: New York, Oxford University Press, 326 p.

—, 1996, Global climate change and active tectonics: effective tools for teaching and research: Geomorphology, v. 16, p. 217-232.

—, 2007, Tectonic Geomorphology of Mountains.: Oxford, UK, Blackwell.

Burbank, D., Meigs, A., and Brozovic, N., 1996, Interactions of growing folds and coeval depositional systems: Basin Research, v. 8, p. 199-223.

Burbank, D.W., and Anderson, R.S., 2001, Tectonic Geomorphology, Blackwell Science, 273 p.

Campbell, J., 2008, Geotechnical characterisation of stone roof and floor material. Spring Creek Coal Mine, West Coast, New Zealand. [BSc Honours thesis]: Christchurch, University of Canterbury.

Campbell, J.K., Nicol, A., and Howard, M.E., 2003, Long-term changes to river regimes prior to late Holocene coseismic faulting, Canterbury, New Zealand: Journal of Geodynamics, v. 36, p. 147-168.

Chelidze, T., and Gueguen, Y., 1990, Evidence of fractal fracture: International journal of rock mechanics and mining sciences & geomechanics abstracts, v. 27, p. 223-225.

Christensen, N.I., and Fountain, D.M., 1975, Constitution of the lower continental crust based on experimental studies of seismic velocities in granulite: Geol. Soc. Am. Bull., v. 86, p. 227-236.

Corboz, P., 2004, High Resolution Geophysical Surveying at the Springfield Fault, New Zealand: Imaging a buried active fault zone, Institute of Geophysics, Zurich, Switzerland, p. 62.

Cowan, H.A., 1992, Structure, seismicity and tectonics of the Porters Pass-Amberley Fault Zone, North Canterbury, New Zealand. : Christchurch, New Zealand., University of Canterbury.

Cowan, H.A., Nicol, A., and Tonkin, P.L., 1996, A comparison of historical and paleoseismicity in a newly formed fault zone and a mature fault zone, north Canterbury, New Zealand: Journal of Geophysical Research, v. 101, p. 6021-6036.

Crampin, S., McGonigle, R., and Bamford, D., 1980, Estimating crack parameters from observations of P-wave velocity anisotropy: Geophysics, v. 45, p. 361-375.

Crice, D., 2005, MASW, the wave of the future: Journal of Environmental and Engineering Geophysics, v. 10, p. 77-79.

DBHNZ, 2007, New Zealand Building Code Handbook (Third Edition), Department of Building and Housing, Wellington, p. 220.

DeMets, C., Gordon, R.G., Argus, D.F., and Stein, S., 1994, Effect of recent revisions to the geomagnetic reversal time scale on estimates of current plate motions: Geophysical Research Letters, v. 21, p. 2191-2194.

Dor, O., Rockwell, T.K., and Ben-Zion, Y., 2006, Geological observations of damage asymmetry in the structure of the San Jacinto, San Andreas and Punchbowl faults in Southern California: A possible indicator for preferred rupture propagation direction: Pure and Applied Geophysics, v. 163, p. 301-349.

Dorman, J., and Ewing, M., 1962, Numerical inversion of seismic surface wave dispersion data and crust-mantle structure in the New York-Pennsylvania area: Journal of Geophysical Research v. 67, p. 5227-5241.

Duan, B., and Oglesby, D.D., 2005, The dynamics of thrust and normal faults over multiple earthquake cycles: Effects of dipping fault geometry: Bulletin of the Seismological Society of America, v. 95, p. 1623-1636.

Duffy, B., Finnemore, M., and King, M., 2008, MASW investigation of turbine sites at Te Rere Hau Windfarm, Palmerston North: Christchurch, Connell Wagner.

ECAN, 1998, Canterbury Regional Policy Statement: Christchurch, Environment Canterbury, p. 242-257.

—, 2006, CRPS Scoping Report, Environment Canterbury, Christchurch, p. 25.

Ekström, G., Stein, R.S., Eaton, J.P., and Eberhart-Phillips, D., 1992, Seismicity and Geometry of a 110-km-Long Blind Thrust Fault 1. The 1985 Kettleman Hills, California, Earthquake.: Journal of Geophysical Research, v. 97, p. 4843-4864.

Evans, S.T., 2000, Paleoseismic analysis of the Springfield Fault, Central Canterbury., Unpublished B.Sc. (Hons.) thesis. University of Canterbury.

Forbriger, T., 2003a, Inversion of shallow-seismic wavefields: I. Wavefield transformation: Geophysical Journal International, v. 153, p. 719-734.

—, 2003b, Inversion of shallow-siesmic wavefields: II. Inferring subsurface properties from wavefield transforms: Geophysical Journal International, v. 153, p. 735-752.

Fountain, D.M., and Christensen, N.I., 1989, Composition of the continental crust and upper mantle: A review: Geophysical Framework of the Continental United States, v. 172, p. 711-742.

Fumal, T.E., 1978, Correlations between seismic wave velocities and physical properties of near-surface geologic materials in the southern San Francisco Bay region, California., U.S. Geol. Surv.

Gao, F., Xie, H., and Wu, J., 1999, Fractal analysis of the relation between rock damage and rock fragmentation: Yanshilixue Yu Gongcheng Xuebao/Chinese Journal of Rock Mechanics and Engineering, v. 18, p. 503-506.

Gao, F., Zhong, W., Li, L., and Xie, H., 2004, Fractal and statistical analysis of strength of jointed rocks: Yanshilixue Yu Gongcheng Xuebao/Chinese Journal of Rock Mechanics and Engineering, v. 23, p. 3608-3612.

Gettemy, G.L., Tobin, H.J., Hole, J.A., and Sayed, A.Y., 2004, Multi-scale compressional wave velocity structure of the San Gregorio Fault zone: Geophysical Research Letters, v. 31.

Ghosh, A., and Daemen, J.J.K., 1993, Fractal characteristics of rock discontinuities: Engineering Geology, v. 34, p. 1-9.

Ghosh, D.K., and Srivastava, M., 1991, Point-load strength: an index for classification of rock material: Bulletin - International Association of Engineering Geology, v. 44, p. 27-33.

Gokceoglu, C., and Aksoy, H., 2000, New approaches to the characterization of clay-bearing, densely jointed and weak rock masses: Engineering Geology, v. 58, p. 1-23.

Green, A.G., 2004, Seismic Reflection Survey of the Springfield Fault at Dalethorpe, ETH Zurich.

Guccione, M.J., Mueller, K., Champion, J., Shepherd, S., Carlson, S.D., Odhiambo, B., and Tate, A., 2002, Stream response to repeated coseismic folding, Tiptonville Dome, New Madrid Seismic Zone: Geomorphology, v. 43, p. 313-349.

Habimana, J., Labiouse, V., and Descoeudres, F., 2002, Geomechanical characterisation of cataclastic rocks: Experience from the Cleuson-Dixence project: International Journal of Rock Mechanics and Mining Sciences, v. 39, p. 677-693.

Hamdi, E., and du Mouza, J., 2005, A methodology for rock mass characterisation and classification to improve blast results: International Journal of Rock Mechanics and Mining Sciences, v. 42, p. 177-194.

Haney, M.M., Snieder, R., Sheiman, J., and Losh, S., 2005, Geophysics: A moving fluid pulse in a fault zone: Nature, v. 437, p. 46.

Hart, E.W., and Bryant, W.A., 1997, Fault Rupture Hazard Zones in California: Alquist-Priolo Earthquake Fault Zoning Act with Index to Earthquake Fault Zones Maps, Californian Department of Conservation, Division of Mines and Geology p. 47.

Hobbs, B.E., 1993, The significance of structural geology in rock mechanics, *in* Hudson, ed., Comprehensive Rock Engineering, Volume 1: Oxford, Pergamon, p. 25-62.

Hoek, E., and Brown, E.T., 1980, Underground excavations in rock.: London, Institution of Mining and Metallurgy.

—, 1997, Practical estimates of rock mass strength: International Journal of Rock Mechanics and Mining Sciences, v. 34, p. 1165-1186.

Hoek, E., Marinos, P., and Benissi, M., 1998, Applicability of the geological strength index (GSI) classification for very weak and sheared rock masses. The case of the Athens Schist Formation: Bulletin of Engineering Geology and the Environment, v. 57, p. 151-160.

Hoek, E., Wood, D., and Shah, S., 1992 A modified Hoek-Brown criterion for jointed rock masses, *in* Hudson, J.A., ed., Proceedings of the rock mechanic symposium. International Society of Rock Mechanics Eurock'' 92: London, British Geotechnical Society, p. 209-214.

Howard, M., Nicol, A., Campbell, J., and Pettinga, J., 2005, Holocene paleoearthquakes on the strike-slip Porters Pass Fault, Canterbury, New Zealand: New Zealand Journal of Geology & Geophysics, v. 48, p. 59-74

ISRM, 1979, Suggested methods for determining the uniaxial compressive strength and deformability of rock materials: International Journal of Rock Mechanics & Mining Sciences, v. 16, p. 135-140.

—, 1985, Suggested Method for Determining Point Load Strength: International Journal of Rock Mechanics and Mining Sciences, v. 22, p. 53-60.

Ivanov, J., Miller, R.D., Lacombe, P., Johnson, C.D., and Lane Jr, J.W., 2006, Delineating a shallow fault zone and dipping bed rock strata using multichannal analysis of surface waves with a land streamer: Geophysics, v. 71.

Ivanov, J., Park, C.B., Miller, R.D., and Xia, J., 2005, Analyzing and filtering surface-wave energy by muting shot gathers: Journal of Environmental and Engineering Geophysics, v. 10, p. 307-322.

Ivanov, J., Park, C.B., Miller, R.D., Xia, J., and Overton, R., 2001, Modal separation before dispersion curve extraction by MASW method, Proceedings of the SAGEEP: Denver, Colorado.

Joh, S.H., Kim, D.S., Kang, T.H., Kim, K.S., Ha, H.S., Chang, H.S., and Jo, C.H., 2006, Comparison of surface-wave techniques in the spatial profiling of subsurface stiffness, Geotechnical Special Publication, p. 188-195.

Kanamori, H., and Brodsky, E., 2004, The physics of earthquakes: Reports on Progress in Physics, v. 67 p. 1429-1496.

Karastathis, V.K., Ganas, A., Makris, J., Papoulia, J., Dafnis, P., Gerolymatou, E., and Drakatos, G., 2007, The application of shallow seismic techniques in the study of active faults: The Atalanti normal fault, central Greece: Journal of Applied Geophysics, v. 62, p. 215-233.

Kelson, K.I., Kang, K.H., Page, W.D., Lee, C.T., and Cluff, L.S., 2001, Representative Styles of Deformation along the Chelungpu Fault from the 1999 Chi-Chi (Taiwan) Earthquake: Geomorphic Characteristics and Responses of Man-Made Structures: Bulletin of the Seismological Society of America, v. 91, p. 930-952.

Kerr, J., Nathan, S., Van Dissen, R., Webb, P., Brunsdon, D., and King, A., 2003, Planning for Development of Land on or Close to Active Faults: A guideline to assist resource management planners in New Zealand, Ministry for the Environment.

KGS, 2003, SurfSeis Introduction - Multichannel Analsysis of Surface Waves, Kansas Geological Survey.

Kilner, J.W., in prep, Geophysical imaging of Eastern Otago Active Fault Structures. Unpublished MSc thesis: Dunedin, University of Otago.

Kilner, J.W., Norris, R.J., and Gorman, A.R., 2007 Seismic Imaging of Eastern Otago Active Fault Structures, Geosciences '06: Palmerston North, New Zealand, Geological Society of New Zealand Miscellaneous Publication 123A: p.43.

King, G.C.P., and Vita-finzi, C., 1981, Active folding in the Algerian earthquake of 10 October 1980: Nature, v. 292, p. 22-26.

King, M.S., Myer, L.R., and Rezowalli, J.J., 1986, Experimental studies of elastic- wave propagation in a columnar- jointed rock mass: Geophysical Prospecting, v. 34, p. 1185-1199.

King, M.S., Shakeel, A., and Chaudhry, N.A., 1997, Acoustic wave propagation and permeability in sandstones with systems of aligned cracks: Geological Society Special Publication, p. 69-85.

Leary, P.C., and Henyey, T.L., 1985, Anisotropy and fracture zones about a geothermal well from P-wave velocity profiles.: Geophysics, v. 50, p. 25-36.

Leucci, G., and De Giorgi, L., 2006, Experimental studies on the effects of fracture on the P and S wave velocity propagation in sedimentary rock ("Calcarenite del Santo"). Engineering Geology, v. 84, p. 130-142.

Lin, C.P., Chang, C.C., and Chang, T.S., 2004, The use of MASW method in the assessment of soil liquefaction potential: Soil Dynamics and Earthquake Engineering, v. 24, p. 689-698.

Litchfield, N.J., Campbell, J.K., and Nicol, A., 2003, Recognition of active reverse faults and folds in North Canterbury, New Zealand, using structural mapping and geomorphic analysis: New Zealand Journal of Geology and Geophysics, v. 46, p. 563-579.

Litchfield, N.J., and Norris, R.J., 2000, Holocene motion on the Akatore Fault, south Otago coast, New Zealand.: New Zealand Journal of Geology & Geophysics, v. 43, p. 405-418.

Losh, S., and Haney, M.M., 2006, Episodic Fluid Flow in an Aseismic Overpressured Growth Fault, Northern Gulf of Mexico, *in* Abercrombie, R., McGarr, A., Kanamori, H., and Di Toro, G., eds., Earthquakes: Radiated Energy and the Physics of Faulting. Geophysical Monograph 170: Washington, DC, American Geophysical Union, p. 199-205.

Louie, J.N., 2001, Faster, Better: Shear-Wave Velocity to 100 Meters Depth from Refraction Microtremor Arrays: Bulletin of the Seismological Society of America, v. 91, p. 347-364.

Lu, B., Chen, J.P., Ge, X.R., and Wang, S.L., 2005, Fractal geometry study on structure of jointed rock mass: Yanshilixue Yu Gongcheng Xuebao/Chinese Journal of Rock Mechanics and Engineering, v. 24, p. 461-467.

Marinos, P., and Hoek, E., 2001, Estimating the geotechnical properties of heterogeneous rock masses such as flysch: Bull Eng Geol Env, v. 60, p. 82-92.

Miller, R.D., Park, C.B., Ivanov, J., Xia, J., Laflen, D.R., and Gratton, C., 2000, MASW to investigate anomalous near surface materials at the Indian Refinery in Lawrenceville, Illinois, Kansas Geol. Surv. Open File Rept. 2004-4: Lawrence, Kansas, p. 48.

Miller, R.D., Xia, J., Park, C.B., and Ivanov, J.M., 1999a, MASW to investigate subsidence in the Tampa, Florida area, Volume Open-file Report 99-33., Kansas Geological Survey

—, 1999b, Multichannel analysis of surface waves to map bedrock: Leading Edge (Tulsa, OK), v. 18, p. 1392-1396.

Moseley, M.P., and Schumm, S.A., 2001, Gravel bed rivers - the view from the hills, *in* Moseley, M.P., ed., Gravel-Bed Rivers V, New Zealand Hydrological Society.

Mukerji, T., Mavko, G., Mujica, D., and Lucet, N., 1995, Scale-dependent seismic velocity in heterogeneous media: Geophysics, v. 60, p. 1222-1233.

Nagai, K., O'Neill, A., Sanada, Y., and Ashida, Y., 2005, Genetic algorithm inversion of Rayleigh wave dispersion from CMPCC gathers over a shallow fault model: Journal of Environmental and Engineering Geophysics, v. 10, p. 275-286.

Nakagawa, S., Nihei, K.T., and Myer, L.R., 2002, Elastic wave propagation along a set of parallel fractures: Geophysical Research Letters, v. 29, p. 31-1.

Nasseri-Moghaddam, A., 2006, Study of the effect of lateral inhomogeneities on the propagation of Rayleigh waves in an elastic medium [PhD thesis]: Waterloo, University of Waterloo.

Nasseri-Moghaddam, A., Phillips, C., Cascante, G., and Hutchinson, D.J., 2005, Detection of underground cavites using MASW test, Proceedings, Annual Conference - Canadian Society for Civil Engineering, Volume 2005.

Nicol, A., 1992, Tectonic structures developed in Oligocene limestones: implications for New Zealand plate boundary deformation in North Canterbury: New Zealand Journal of Geology and Geophysics, v. 35, p. 353-362.

—, 1993, Haumurian (c.66-80 Ma) half-graben development and deformation, mid Waipara, north Canterbury, New Zealand: New Zealand Journal of Geology & Geophysics, v. 36, p. 127-130.

Nicol, A., Alloway, B.V., and Tonkin, P.L., 1994, Rates of deformation, uplift and landscape development associated with active folding in the Waipara area of North Canterbury, New Zealand.: Tectonics, v. 13, p. 1327-1344.

Nicol, A., and Campbell, J.K., 2001, The impact of episodic fault-related folding on late holocene degradation terraces along Waipara River, New Zealand: New Zealand Journal of Geology and Geophysics, v. 44, p. 145-155.

Norris, R.J., and Cooper, A.F., 2001, Late Quaternary slip rates and slip partitioning on the Alpine Fault, New Zealand: Journal of Structural Geology, v. 23, p. 507-520.

Norris, R.J., and Nichols, R., 2004, Strain accumulation and episodicity of fault movement in Otago., EQC research report, NZ EQC, 01/445.

O'Neill, A., and Matsuoka, T., 2005, Dominant higher surface-wave modes and possible inversion pitfalls: Journal of Environmental and Engineering Geophysics, v. 10, p. 185-201.

Oglesby, D.D., Archuleta, R.J., and Nielsen, S.B., 1998, Earthquakes on dipping faults: The effects of broken symmetry: Science, v. 280, p. 1055-1059.

Okaya, D., Christensen, N., Stanley, D., and Stern, T., 1995, Crustal anisotropy in the vicinity of the Alpine Fault Zone, South Island, New Zealand: New Zealand Journal of Geology and Geophysics, v. 38 p. 579-583.

Ouchi, S., 1985, Response of alluvial rivers to slow active tectonic movement: Geological Society of America Bulletin, v. 96, p. 504-515.

Park, C.B., 2003, Surfseis Multichannel Analysis of Surface Waves - MASW users Manual, Lawrence, Kansas Geological Survey.

—, 2006, Surfseis: Active and Passive MASW - users manual v2.0: Kansas Geological Survey, Lawrence, Kansas.

Park, C.B., and Miller, R.D., 2006, Roadside passive MASW: Proceedings of the SAGEEP, April 2-6, 2006, Seattle, Washington.

Park, C.B., Miller, R.D., and Ivanov, J., 2002, Filtering surface waves, Proceedings of the SAGEEP 2002: Las Vegas, Nevada

Park, C.B., Miller, R.D., and Miura, H., 2005a, Optimum Field Parameters of an MASW survey: http://www.kgs.ku.edu/Geophysics2/Pubs/Pubs/PAR-02-03.pdf, Kansas Geological Survey.

Park, C.B., Miller, R.D., Ryden, N., Xia, J., and Ivanov, J., 2005b, Combined use of active and passive surface waves: Journal of Engineering and Environmental Geophysics, v. 10, p. 323-334.

Park, C.B., Miller, R.D., and Xia, J., 1998, Imaging dispersion curves of surface waves on multi-channel record, 68th Annual International Meeting of the Society of Exploration Geophysicists, Expanded Abstracts, p. 1377-1380.

—, 1999a, Detection of near surface voids using surface waves, Symposium on the Application of Geophysics to Engineering and Environmental Problems (SAGEEP 99): Oakland, California, p. 281-286.

—, 1999b, Multichannel analysis of surface waves: Geophysics, v. 64, p. 800-808.

Park, C.B., Miller, R.D., Xia, J., and Ivanov, J., 2004, Imaging dispersion curves of passive surface waves: Society of Exploration Geophysics Expanded Abstracts v. NSG 1.6.

Park, C.B., Miller, R.D., Xia, J., Ivanov, J., Sonnichsen, G.V., Hunter, J.A., Good, R.L., Burns, R.A., and Christian, H., 2005c, Underwater MASW to evaluate stiffness of water-bottom sediments: Leading Edge (Tulsa, OK), v. 24, p. 724-728.

Parrales, R., Dahlin, T., and Rubi, C., 2003, Site investigation with combined methods in a faulted area in Managua, Nicaragua - a pre-study, 9th Meeting of Environmental and Engineering Geophysics: Prague, Czech Republic.

Perrin, N.D., 2008, pers. comm, Engineering Geologist, Geological and Nuclear Sciences: Wellington.

Pettinga, J., Yetton, M.D., Van Dissen, R.J., and Downes, G., 2001, Earthquake source identification and characterisation for the Canterbury Region, South Island, New Zealand.: Bulletin of the New Zealand Society for Earthquake Engineering, v. 34, p. 282-317

Philip, H., and Meghraoui, M., 1983, Structural analysis and interpretation of the surface deformations of the El Asnam earthquake of October 10, 1980 (Mediterranean area): Tectonics, v. 2, p. 17-49.

Protodyakonov, M.M., 1969, Method of determining the strength of rocks under uniaxial compression, *in* Protodyakonov, M.M., Koifman, M.I., and others, eds., Mechanical properties of Rocks (Translated from Russian): Jerusalem, Israel Program for Scientific Translations, p. 1-8.

Rasolofosaon, P.N.J., Rabbel, W., Siegesmund, S., and Vollbrecht, A., 2000, Characterization of crack distribution: Fabric analysis versus ultrasonic inversion: Geophysical Journal International, v. 141, p. 413-424.

Rhazi, J., Hassaim, M., Ballivy, G., and Hunaidi, O., 2002, Effects of concrete non-homogeneity on Rayleigh waves dispersion: Magazine of Concrete Research, v. 54, p. 193-201.

Rix, G.J., and Leipski, E.A., 1991, Accuracy and resolution of surface wave inversion, Geotechnical Special Publication, p. 17-32.

Ruegg, J.C., Kasser, M., Tarantola, A., Lepine, J.C., and Chouikrat, B., 1982, Deformations associated with the El Asnam earthquake of 10 October 1980: Geodetic determination of vertical and horizontal movements: BULLETIN OF THE SEISMOLOGICAL SOCIETY OF AMERICA, v. 72, p. 2227-2244.

Ryden, N., and Park, C.B., 2005, Seismic joint analysis for non-destructive testing of asphalt and concrete slabs, Geotechnical Special Publication, p. 991-1000.

Seshunarayana, T., Senthil Kumar, P., Sampath Rao, V., Mysaih, D., Satish Kumar, K., and Pavan Kishore, P., 2008, Multichannel analysis of surface waves reveals shear zones and fractures in a shallow granite basement: Wailapally watershed near Hyderabad: Journal of the Geological Society of India, v. 71, p. 261-265.

Shakeel, A., and King, M.S., 1998, Acoustic wave anisotropy in sandstones with systems of aligned cracks: Geological Society Special Publication, p. 173-183.

Similox-Tohon, D., Sintubin, M., Muchez, P., Verhaert, G., Vanneste, K., Fernandez, M., Vandycke, S., Vanhaverbeke, H., and Waelkens, M., 2006, The identification of an active fault by a multidisciplinary study at the archaeological site of Sagalassos (SW Turkey): Tectonophysics, v. 420, p. 371-387.

Soule, F., 1907, The earthquake and fire and their effects on structural steel and steel-frame buildings, *in* Gilbert, G.K., Humphrey, R.L., Sewell, J.S., and Soule, F., eds., The San Francisco earthquake and fire of April 18, 1906 and their effects on structures and structural materials., United States Geological Survey, Bulletin 324, p. 131-158.

Speight, R., 1928, The Geology of the Malvern Hills, New Zealand Department of Scientific and Industrial Research Geological Memoirs 1, p. 72.

Statistics-New-Zealand, 2004, Projected Population of Regional Councils, http://www.stats.govt.nz/NR/rdonlyres/59607657-FD15-42E6-99A0-922BCA943B88/15230/spp01base06updatealltables.xls, accessed 30 January 2008, Volume 2008, Statistics New Zealand.

Stephenson, W.J., Louie, J.N., Pullammanappallil, S., Williams, R.A., and Odum, J.K., 2005, Blind shear-wave velocity comparison of ReMi and MASW results with boreholes to 200 m in Santa Clara Valley: Implications for earthquake ground-motion assessment: Bulletin of the Seismological Society of America, v. 95, p. 2506-2516.

Stokoe, K.H., Wright, S.G., Bay, J.A., and Roesset, J.M., 1994, Characterization of geotechical sites by SASW method: Geophysical characterization of sites, p. 15-25.

Szlavin, J., 1974, Relationships between some physical properties of rock determined by laboratory test: International Journal of Rock Mechanics and Mining Sciences Geomechanics Abstracts, v. 11, p. 57-66.

Szwedzicki, T., 1998, Indentation hardness testing of rock: International Journal of Rock Mechanics and Mining Sciences, v. 35, p. 825-829.

Tomeh, A.A., Alyateem, S., Malik, H., and Malone, B., 2006, Geophysical surveying and data simulation application to geotechnical investigations: A cost effective approach for developing economical foundation engineering design criteria, GeoCongress 2006: Geotechnical Engineering in the Information Technology Age, Volume 2006, p. 98.

Tonkin, P.L., pers. comm., Soil scientist and senior fellow, Department of Geological Sciences, University of Canterbury.

Tonkin, P.L., and Almond, P., 1998, Using Loess soil stratigraphy to reconstruct the late Quaternary history of piedmonts adjacent to large strike-slip faults, South Island, New Zealand: Geological Society of New Zealand Miscellaneous Publication, v. 101A, p. 227.

Tu, X.B., Wang, S.J., and Yue, Z.Q., 2005, Fractal fragmentation of weathered rock and its application in engineering geology: Yanshilixue Yu Gongcheng Xuebao/Chinese Journal of Rock Mechanics and Engineering, v. 24, p. 587-595.

Turk, N., and Dearman, W.R., 1986, Correction Equation on the influence of length to diameter ratio on the uniaxial compressive strength of rocks: Engineering Geology, v. 22, p. 293-300.

Vincent, P.D., Tsoflias, G.P., Steeples, D.W., and Sloan, S.D., 2006, Fixed-source and fixed-receiver walkaway seismic noise tests: A field comparison: Geophysics, v. 71, p. W41-W44.

Wallace, L.M., Beavan, J., McCaffrey, R., Berryman, K., and Denys, P., 2007, Balancing the plate motion budget in the South Island, New Zealand using GPS, geological and seismological datas: Geophysical Journal International, v. 168, p. 332-352.

Wells, D.L., and Coppersmith, K.J., 1994, New Empirical Relationships among Magnitude, Rupture Length, Rupture Width, Rupture Area, and Surface Displacement: Bulletin of the Seismological Society of America, v. 84, p. 974-1002.

Williams, M., 2001, Building on the Edge: The Use and Development of Land on or Close to Fault Lines: Wellington, Office of the Parliamentary Commissioner for the Environment, p. 38 pp.

Worthington, M.H., 1984, An introduction to geophysical tomography: First Break, v. 2, p. 20-26.

Wulff, A.M., Raab, S., and Huenges, E., 2000, Alteration of seismic wave properties and fluid permeability in sandstones due to microfracturing: Physics and Chemistry of the Earth, Part A: Solid Earth and Geodesy, v. 25, p. 141-147.

Xia, J., Chen, C., Tian, G., Miller, R.D., and Ivanov, J., 2005, Resolution of high-frequency Rayleigh-wave data: Journal of Environmental and Engineering Geophysics, v. 10, p. 99-110.

Xia, J., Miller, R.D., and Park, C.B., 1999, Estimation of near-surface shear-wave velocity by inversion of Rayleigh waves: Geophysics, v. 64, p. 691-700.

Xia, J., Miller, R.D., Park, C.B., Hunter, J.A., Harris, J.B., and Ivanov, J., 2002, Comparing shear-wave velocity profiles inverted from multichannel surface wave with borehole measurements: Soil Dynamics and Earthquake Engineering, v. 22, p. 181-190.

Xia, J., Miller, R.D., Park, C.B., and Tian, G., 2003, Inversion of high frequency surface waves with fundamental and higher modes: Journal of Applied Geophysics, v. 52, p. 45-57.

Xia, J., Nyquist, J.E., Xu, Y., Roth, M.J.S., and Miller, R.D., 2007, Feasibility of detecting near-surface feature with Rayleigh-wave diffraction: Journal of Applied Geophysics, v. 62, p. 244-253.

Xie, H., 1993, Fractals in Rock Mechanics: Rotterdam, A.A. Balkema, 453 p.

Xie, H., and Chen, Z., 1988, Fractal geometry and fracture of rock: Lixue xuebao, v. 4, p. 255-264.

Xu, C., and Butt, S.D., 2006, Evaluation of MASW techniques to image steeply dipping cavities in laterally inhomogeneous terrain: Journal of Applied Geophysics, v. 59, p. 106-116.

Yielding, G., Jackson, J.A., King, G.C.P., Sinvhal, H., Vita-Finzi, C., and Wood, R.M., 1981, Relations between surface deformation, fault geometry, seismicity, and rupture characteristics during the El Asnam (Algeria) earthquake of 10 October 1980: Earth and Planetary Science Letters, v. 56, p. 287-304.

Yousif, H.M.K., 1987, The application of remote sensing to geomorphological neotectonic mapping in North Canterbury: Christchurch, New Zealand, University of Canterbury.

Yunmin, C., Han, K., and Ren-Peng, C., 2005, Correlation of shear wave velocity with liquefaction resistance based on laboratory tests: Soil Dynamics and Earthquake Engineering, v. 25, p. 461-469.

Zhang, S.X., and Chan, L.S., 2003, Possible effects of misidentified mode number on Rayleigh wave inversion: Journal of Applied Geophysics, v. 53, p. 17-29.

Zhu, Z., and Toksooz, M.N., 2003, Crosshole seismoelectric measurements in borehole models with fractures: Geophysics, v. 68, p. 1519-1524.

Zinszner, B., Meynier, P., Cabrera, J., and Volant, P., 2002, Ultrasonic, sonic and seismic waves velocity in shale from Tournemire tunnel. Impact of anisotropy and natural fractures: Oil and Gas Science and Technology v. 57, p. 341-353.

APPENDIX A. THE GEOPHYSICAL PRINCIPLES OF MASW

Introduction

Geophysical detection of near surface features such as faults is challenging due to the inherent complexity and variability of the material properties. MASW is a multichannel, high- frequency, surface-wave technique that has been shown to provide a reliable indication of S-wave velocities in different geological settings including faults (this study and Ivanov et al., 2006). MASW is a three stage process comprising Rayleigh-wave acquisition and dispersion curve extraction followed by inversion of a v_s profile from the dispersion curves. This appendix will introduce the reader to Rayleigh-waves and then outline the methodology for processing MASW. Integrated with the methodology are a review of the underlying geophysical principles and a discussion of potential pitfalls at each stage of the process. The order in which the method is presented is reversed from the order in which MASW is carried out. In order to step systematically through the process of surface wave acquisition, dispersion curve extraction and inversion it would be necessary to constantly refer forwards to the next stage. This is because each stage of the MASW process is very much dependent on the success and quality of the previous stage. Therefore, in order to avoid unnecessary repetition I begin with the inversion process, before moving on to dispersion curve extraction and data acquisition.

Rayleigh-waves, which are the principal component of ground roll, account for up to 70% of the energy in a seismic survey (Park et al., 1999b). Ground roll is made up of low velocity and frequency, large amplitude waves that travel near the ground surface. The depth of penetration of a Rayleigh-wave depends directly on its wavelength, with the longer wavelengths penetrating deeper. These long wavelength waves are thus more controlled by the elastic properties of the deeper layers and exhibit higher phase velocities. Conversely, short wavelength velocities reflect the elastic properties closer to the surface and travel more slowly. This property of wavelength [frequency] dependent velocity is known as signal dispersion and is controlled in varying degrees by S-wave velocity, layer thickness, P-wave velocity, and density (Xia *et al*., 1999).

Rayleigh-waves propagate as different modes, a mode being a packet of acoustic energy that propagates in one direction whilst confined in the other two directions. In the case of Rayleigh-waves they are confined to the air/earth interface. Different modes of Rayleigh-waves have different motions relative to the travel direction and therefore different

propagation velocities at a given frequency. Of these modes, fundamental mode Rayleigh-waves (anticlockwise motion) are the slowest and so appear closest to the origin in a frequency v phase velocity (dispersion) plot.

Surface wave inversion

Inversion of S-wave velocities from Rayleigh-wave dispersion curves is the final step in a seismic technique known as Multichannel Analysis of Surface Waves (MASW). The acronym MASW is used here as far as possible without commercial connotations, although it is commonly associated with the Surfseis brand of software from Kansas Geological Survey. This software is used throughout this study and much of the procedure outlined here is specific to Surfseis. Many researchers in the field have, however, developed their own analysis and inversion software and this study cites liberally from amongst their publications. For this reason MASW is taken to mean any process based on multichannel surface wave acquisition, dispersion curve extraction and subsequent inversion by modal dispersion modelling. Where the technique applied or study cited uses other than an active source and equi-spaced linear receiver array, or where inversion is of dispersion curves other than fundamental mode Rayleigh-waves, this will be clearly stated in the text.

The concept of determining S-wave velocity by inverting surface wave dispersion curves is not new and was originally tried by Dorman and Ewing (1962). More recently, Xia *et al* (1999) modelled the contribution of each of the parameters mentioned above to fundamental mode Rayleigh-wave phase velocity (Figure A-1). They found, both for their models and in field-testing, that S-wave velocity is the dominant parameter at frequencies >5 Hz. The low sensitivity of Rayleigh-wave phase velocity to P-wave velocity and density allows these parameters to be estimated to within 25% without significant adverse affect on the convergence of model and inversion. Definition of a layer model by division of the subsurface into layers of constant velocity removes layer thickness as a variable, leaving S-wave velocity as the only remaining variable. S-wave velocities can thus be derived by inverting Rayleigh-wave dispersion data to fit a layer model with fixed estimates of layer thickness, Poisson's ratio or P-wave velocity and density. Once individual dispersion curves are inverted, the resulting 1D profiles are interpolated to construct a 2D S-wave velocity profile.

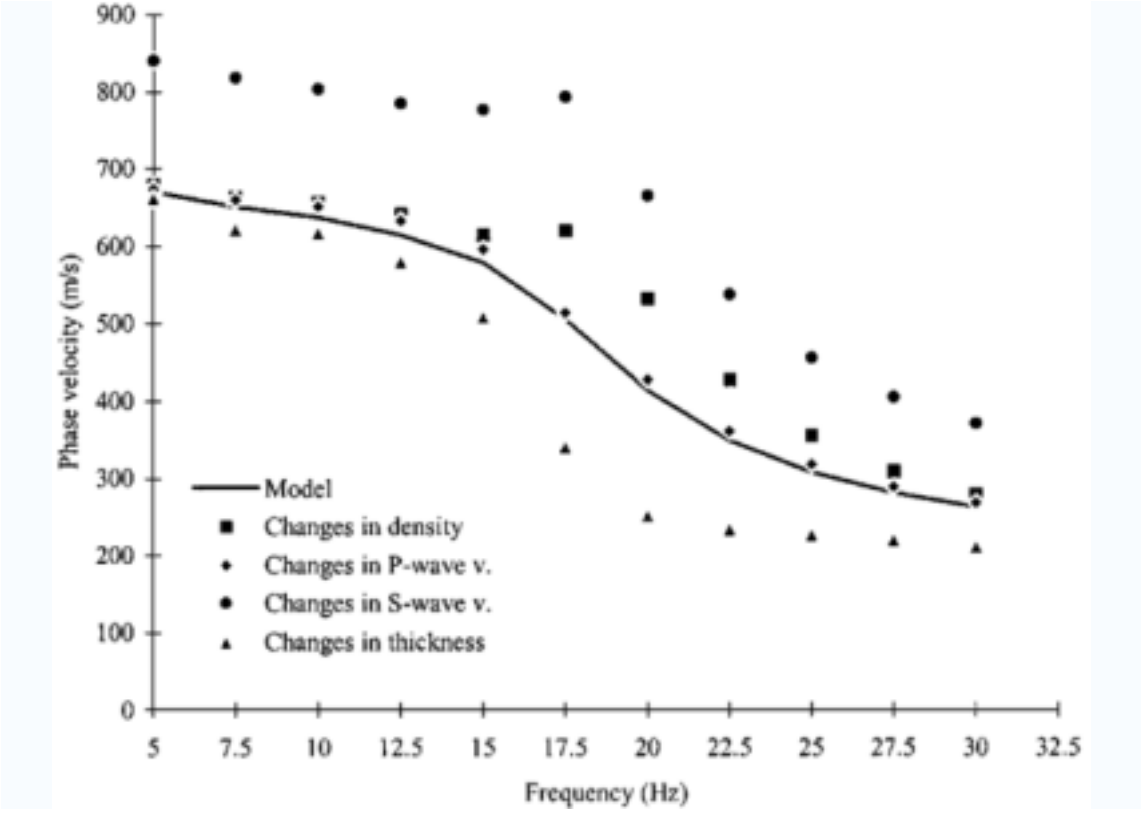

Figure A-1: The effect on Rayleigh-wave phase velocities of 25% change in density (squares), P-wave velocity (diamonds), S-wave velocity (circles) and layer thickness (triangles) in a layered earth model). S-wave velocity can be seen to dominate the dispersion curve, whilst P-wave velocity has little effect (after Xia et al., 1999).

The validity of an inversion of a fundamental mode Rayleigh-wave dispersion curve is heavily dependent on the accuracy of the curve (O'Neill and Matsuoka, 2005; Xia et al., 2003; Zhang and Chan, 2003). A well picked fundamental mode dispersion curve (Figure A-2 A) will invert to a model that closely resembles the earth model, but if the dispersion curve is inaccurate at any point along its length a partly or completely spurious S-wave velocity profile can result (Figure A-2 B and D). Fundamental mode records are susceptible to contamination by body-waves and higher mode Rayleigh-waves, which can affect the dispersion curve over the affected frequency range. This may result in a temporary reversal in the slope of the dispersion curve (Figure A-2 B), or a temporary or permanent jump to a higher mode, which may result in dispersion discontinuities (O'Neill and Matsuoka, 2005). Of these, the slight slope change shown in Figure A-2 is more problematic. This is because an inaccuracy that causes a standard deviation of only 4-5 m/s in Rayleigh-wave phase velocity over a specific frequency range may be un-noticable but produce an S-wave velocity misfit of 100% compared to the earth model (Figure A-2 D). Zhang *et al.* (2003) observed that cross-mode mixing of up to 40% at middle to high frequencies made little difference to the inverted result, but anything more than 5%

mixing at low frequencies adversely affected the inverted model. Mixing of <10% dramatically reduced penetration depth whilst higher mixing ratios produced similarly reduced penetration depth and significantly higher velocities within those penetration depths.

Xia *et al*. (2003) suggest several strategies for dealing with this problem during fundamental-mode-only inversion. One option is to reduce the layering resolution of the model. Reducing the number of layers smoothes out artifacts of the dispersion inaccuracy in the inversion compared with a larger number of layers. Another strategy is to avoid over-forcing the fit of the model with potentially inaccurate data. If the inversion is forced to conclude at an error that is less than the difference between the inaccurate and accurate data, the inverted S-wave velocity profile will be skewed toward the erroneous data (Figure A-2 B). The best fit with the [erroneous] dispersion curve does not necessarily produce the best fit with the earth model.

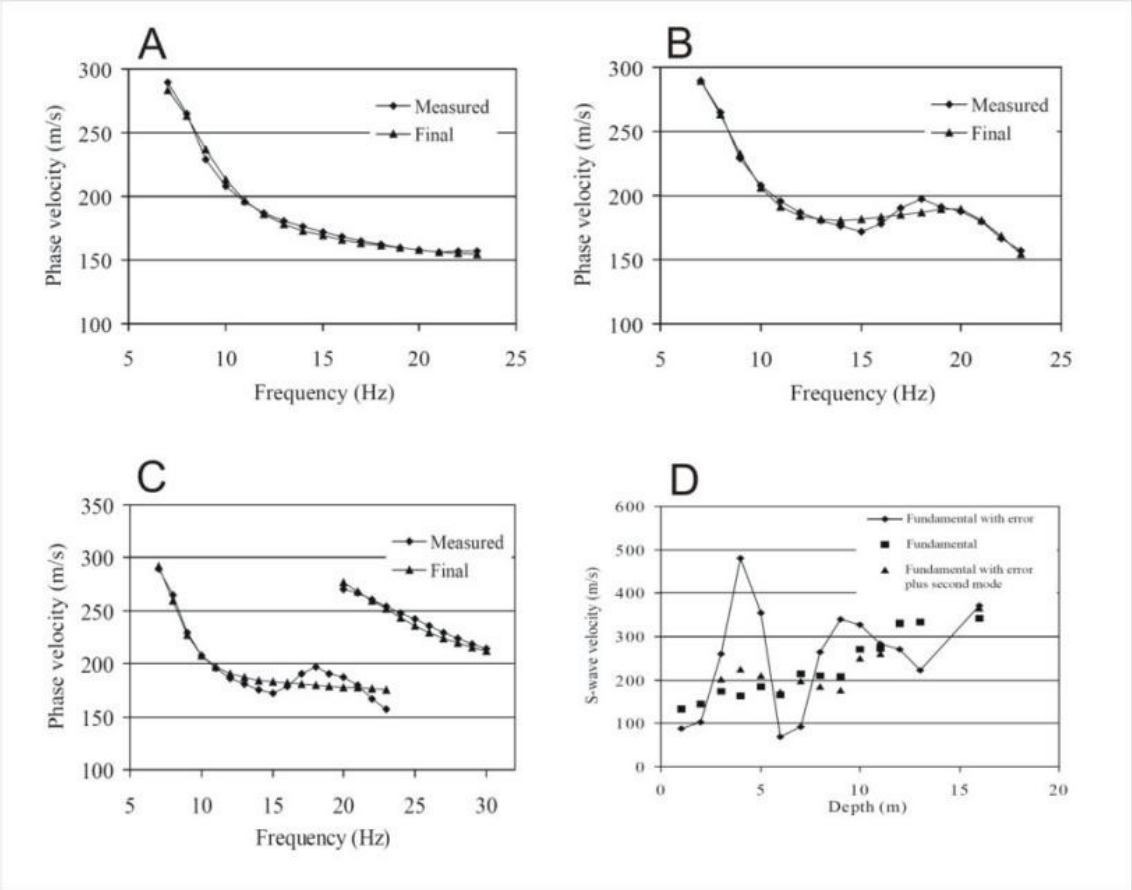

Figure A-2. An example from Xia et al. (2003) illustrating the effect of fundamental dispersion curve error on the inverted model. 'Measured' curves are extracted from the shot record, whilst 'Final' curves are calculated from the final S-wave velocity model. A) Accurate fundamental mode dispersion curve. B) Erroneous fundamental mode dispersion curve with higher mode and body wave contamination deliberately introduced between 13-19 Hz. C) As B but with the inclusion of higher mode data from 20-30Hz. D) The erroneous fundamental mode data produces an irrational profile (diamonds) except where it is supplemented by the higher mode dispersion curve (triangles). In the latter case, the S-wave velocity model closely follows that of the accurate fundamental mode curve (squares).

Xia *et al*'s (2003) main proposal, however, was an alternative approach based on inverting both fundamental and higher mode Rayleigh-waves (Figure A-2 C). Higher mode Rayleigh-waves are even more strongly dependent on S-wave velocity than are fundamental mode Rayleigh-waves. This means that a small change in S-wave velocity at a given wavelength produces a many times larger standard deviation in the phase velocity of the higher mode than that of the fundamental mode. An erroneous fundamental mode dispersion curve forced to terminate inversion with a small error will draw the model towards the erroneous data. Inclusion of the higher modes, however, will increase the *overall* error as the fundamental mode inversion strays past the true model toward a best fit with the erroneous data. The higher modes therefore stabilize the inversion procedure. As an added advantage, Xia *et al.* (2003) showed numerically that higher modes respond to S-wave velocity variations at a greater depth than fundamental mode Rayleigh-waves of an equal wavelength. Higher modes therefore 'see' deeper. On this basis a new mode of inversion that includes higher modes and restricts the user to a maximum of a five layer model has been incorporated in the latest version of Surfseis. The inversion is applied directly to the overtone image and can account for up to four modes during the inversion (Park, 2006). This utility was not used in this study due to the requirement for good quality records.

Dispersion curve extraction

Prior to inversion, shot records must be processed to image the dispersion and, depending on the inversion mode, to extract fundamental mode dispersion curves. This is the key manual processing stage in the production of a 2D S-wave velocity profile. Surfseis applies a wavefield transformation developed by Park *et al.* (1998) to generate a dispersion (overtone) image. A multichannel coherency measure is applied to a decomposed (swept frequency) record in the offset-frequency domain and used to calculate phase velocity with frequency. These two variables plotted together make up a dispersion curve.

Fundamental mode dispersion curves must reflect the dispersive character of planar-propagating fundamental-mode Rayleigh waves only. However, the majority of field records contain distinct higher and leaky modes and channel waves, which interfere with the fundamental mode in the offset-time (x-t) domain (Figure A-3). Leaky modes are multiply reflected and constructively interfering dispersive waves propagating in a [borehole] waveguide. Part of the energy is reflected each time a compressional wave hits

the waveguide wall, while the rest is converted to compressional or shear energy that radiates out of the waveguide, hence the term 'leaky'. A channel wave is a wave that is propagated and confined in low velocity layer. Such interference with the fundamental mode is difficult to deal with in studies such as this because lateral inhomogeneity in the subsurface requires the use of a short receiver spread, an issue that will be covered shortly. Interference may therefore be so severe that no dispersion curves can be reliably extracted from the raw shot gather.

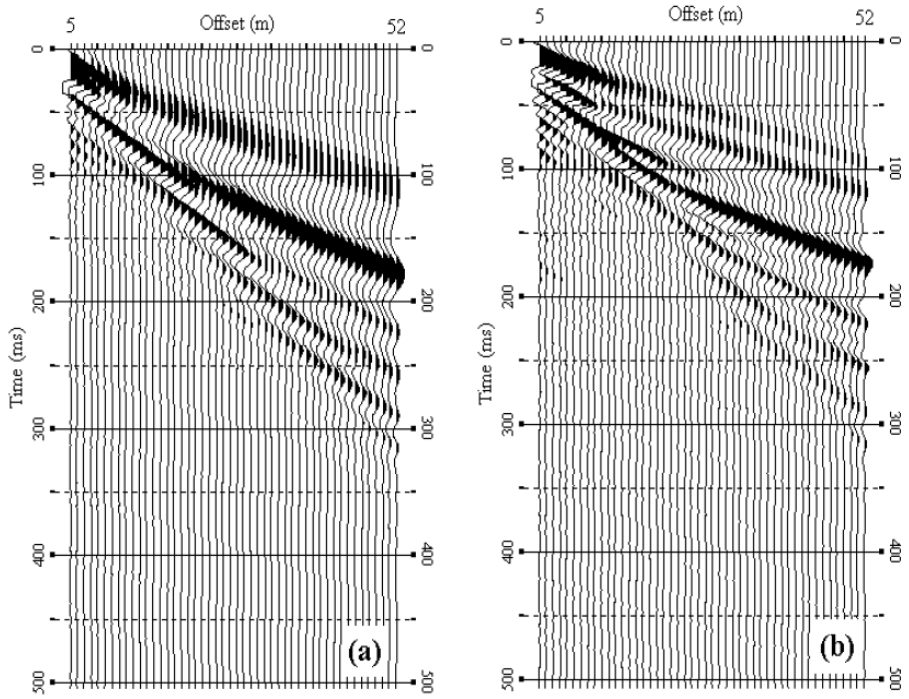

Figure A-3: Synthetic shot gathers with a) fundamental mode only and b) fundamental and first higher modes. The higher mode is assigned overall energy of approximately 2 x fundamental mode (after (Park et al., 2002)).The low frequency fundamental mode events overlap with the higher mode events, whilst the higher frequencies of fundamental mode inhabit a lower velocity field in the x-t domain.

If fundamental and higher modes are not separable the dispersion curves generated from a raw shot record cannot be interpreted as fundamental mode (Forbriger, 2003a, b; Ivanov et al., 2005; Ivanov et al., 2001; O'Neill and Matsuoka, 2005; Park et al., 2002; Zhang and Chan, 2003). A non-MASW solution to this problem is to substitute modal dispersion modelling with full-wavefield modelling (e.g. Forbriger, 2003a; Forbriger, 2003b). This is recommended by O'Neill and Matsuoka (2005) where the energy jumps more than one mode a time, or where leaky mode contributions are observed. The latter is typically due to a steep non-linear velocity gradient in the upper 2 m underlain by homogenous material and can be distinguished by the phase velocity of the higher mode exceeding the S-wave velocity of the model. This study, however, focuses on the use of MASW, so this section

will outline the strategies used for pre-processing and enhancing the record prior to dispersion curve extraction and hence improving modal dispersion modelling.

Modal separation may be undertaken in the *x-t* domain by directly muting the interfering wavefields if the raw shot gather clearly displays different surface wave velocity trends (Figure A-3, Figure A-4) (Ivanov et al., 2005; Ivanov et al., 2001). The size of the mute taper is inconsequential because surface wave analysis is focused on the low frequency spectrum. Muting the faster arrival time ranges to remove higher modes will also mute lowest frequency fundamental mode surface waves because the velocity fields of fundamental and higher modes typically overlap at higher phase velocities. To mitigate this effect it is necessary to extract the dispersion curve twice. The first extraction is performed on the dispersion image of the un-muted record and the second extraction is from the muted dispersion image. The dispersion curves are then combined, retaining the low frequency component of the former and the high frequency component of the latter (Ivanov et al., 2005).

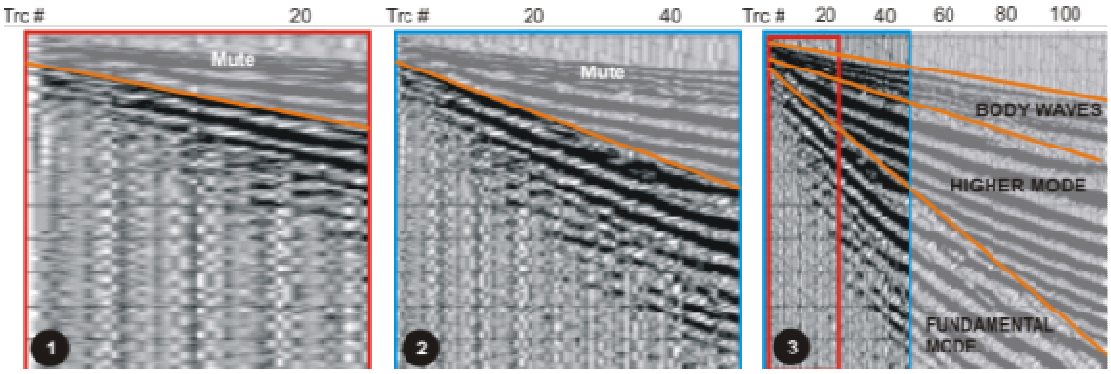

Figure A-4: Muting of higher modes in the x-t domain. 'Records' 1 and 2 have been cut from record 3 (Red and blue boxes). The longer the array, the easier to visually identify and mute the velocity fields dominated by higher mode and body waves. Note, however, that the higher mode dominated velocity field will still contain the low frequency (high velocity) component of fundamental mode Rayleigh-waves. This problem is addressed by the dispersion curve extraction technique of Ivanov et al.(Ivanov et al., 2005).

Alternatively, modal separation may be undertaken in the frequency-wavenumber (*f-k*) domain (Park et al., 2002). Two techniques, known as velocity (or pie-slice or fan) filtering and polygonal filtering, are commonly used to filter shot records in the *f-k* domain. The velocity filter is less than ideal for separation of surface wave modes because the lower frequency fundamental mode commonly has velocities overlapping those of the higher modes (Figure A-5). Park *et al.* (2002) developed an improved version of polygonal filtering known as bow slice filtering. Their method defines the rejecting zone in f-k space by a narrow curved shape (bow slice – Figure A-5) that follows a trajectory in f-k space. The trajectory is predefined using dispersion information of the higher mode

obtained by overtone analysis (discussed below), resulting in specific rejection of the higher mode only.

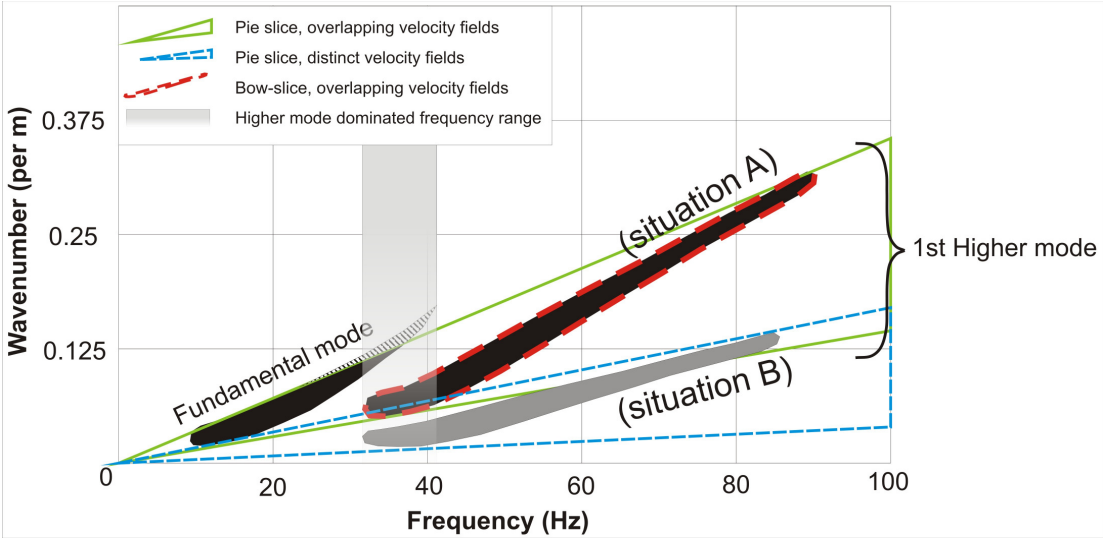

Figure A-5. Application of velocity (pie slice) and bow-slice (polygonal) filters in the f-k domain. The amplitude spectrum for fundamental mode and higher mode (A) (inside the green slice) is that of Figure A-3 (b). Application of a velocity filter in situation (A) will remove all but the higher frequency components (hatched) of the fundamental mode wavefield, due to the overlapping velocities of fundamental and higher modes at low frequencies. Although the velocity filter works better in situation (B), the same result in both situations could be more quickly achieved by muting in the x-t domain. The bow slice filter, however, is defined by a band around a rejection zone that follows a trajectory in f-k space, thus avoiding the fundamental mode entirely. It should work well in both situations (Modified from Park et al., 2002).

The f-k filtering utility in Surfseis presently includes only velocity filters, which must be applied without viewing the data in the *f-k* domain. Several of the records produced in this study were imported into VisualSunt for *f-k* filtering. The nature of the records was such that, for most, there was no obvious modal separation visible even in the *f-k* domain. In some records the overall surface wave velocity trend was clear but in others even that was largely buried by wavefield scattering. Broad filtering polygons were therefore defined on the basis of the better quality records and applied to all the records. This removed the body-waves and back-scatter and generally resulted in a dramatic improvement in dispersion curve extraction using the muting technique of Ivanov *et al.*(2005), outlined above.

Dispersion curve extraction and inversion are particularly problematic where data are acquired in faulted areas with large lateral velocity contrasts. The contrasts lead to wavefield scattering and dispersion discontinuities that are not accounted for by inversion modeling, which assumes a layered stack (Nagai et al., 2005). Nagai *et al.* used numerical modeling to quantify some of the systematic errors that occur due to the layering assumption. They observed that their dispersion curves, extracted from cross-correlated common-mid-point (CMPCC) gathers, displayed characteristic low frequency phase

velocity reversals as the survey crossed the fault. Specifically they noted that spreads centred over a layered subsurface, or equally centred over a discontinuity, produced smooth dispersion curves. Wavefield scattering was suppressed by the CMPCC processing. On the other hand, spreads that asymmetrically overhung a fault produced aberrant dispersion curves. This suggests that dispersion curve behaviour could be used to infer subsurface structure prior to inversion if CMPCC processing is used rather than raw shot gathers.

Although dispersion analysis is the standard surface wave processing procedure, a pre-dispersion-curve indication of subsurface structure may be provided by examination of diffracted surface waves in the raw shot gather (Xia et al., 2007). Faults create point sources in the subsurface and so generate diffractions. The Rayleigh-wave diffraction arrival time t_x becomes a linear function of x and v at far offsets from the diffractor (whose position is marked by the apex of the diffraction hyperbola) so that

$$t_x = \frac{1}{v}[d + x]$$

where t_x is the diffraction arrival time at the distance x from the apex of the diffraction hyperbola and d is the horizontal distance from the source to the apex of the diffraction hyperbola. This allows simple estimation of the diffraction velocity. The value derived for v can then be substituted directly in Xia *et al.*'s Rayleigh-wave diffraction travel time equation

$$t_x = \frac{1}{v}\left[d + (x^2 + h^2)^{\frac{1}{2}}\right]$$

and solved for the depth h to the diffractor (Figure A-6). Xia *et al.* verified the relationship using a vertical fault model on which the Rayleigh-wave diffractions were enhanced by *f-k* filtering.

Early surface-wave-inversion verification studies appeared to indicate that the number of points on a dispersion curve need only be greater than the number of layers in an inversion profile (Rix and Leipski, 1991) . More recent modelling, however, suggests that a small sampling interval over a wide frequency range is essential for accurate inversion and that the quality of dispersion curve extracted is particularly important in achieving a strong match. Zhang and Chan (2003) found two factors to be most complicit in degrading the quality of the inversion. The first of these is dispersion curve sampling interval. The accuracy of inversion models is heavily dependent on using a small

sampling interval over a wide frequency range in the overtone analysis. The closer the sampling interval, the better the correlation they obtained between the model and the inverted section (Figure A-7). This was especially true where the model contained a low velocity layer at depth. Dispersion curve sampling interval should therefore be minimized in the processing of fault-zone surveys.

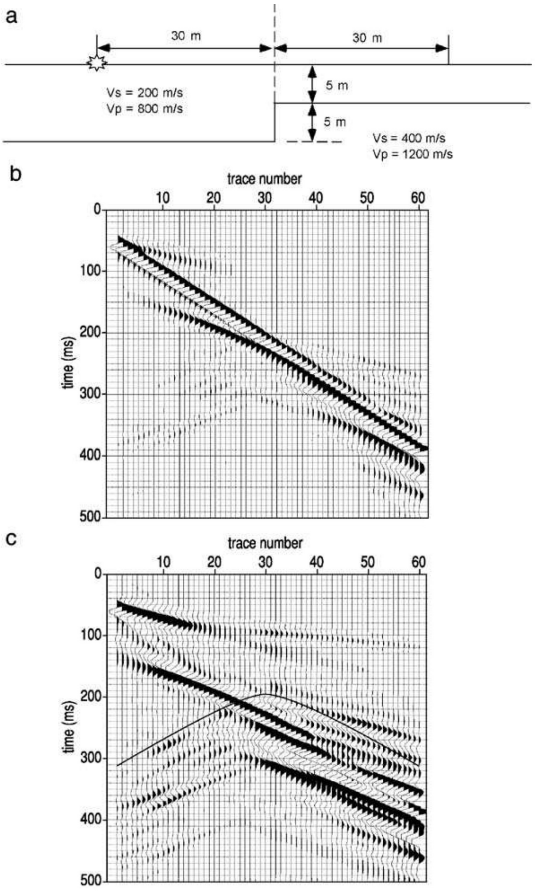

Figure A-6: a) A vertical fault model with a source on the left side of the fault. b) A synthetic shot gather due to the fault model. c) FK filtered data with a diffraction traveltime curve. c = 190 m/s and tx = 0.237 s are the average phase velocity and the travel time at x = 14 m, respectively (after (Xia et al., 2007))

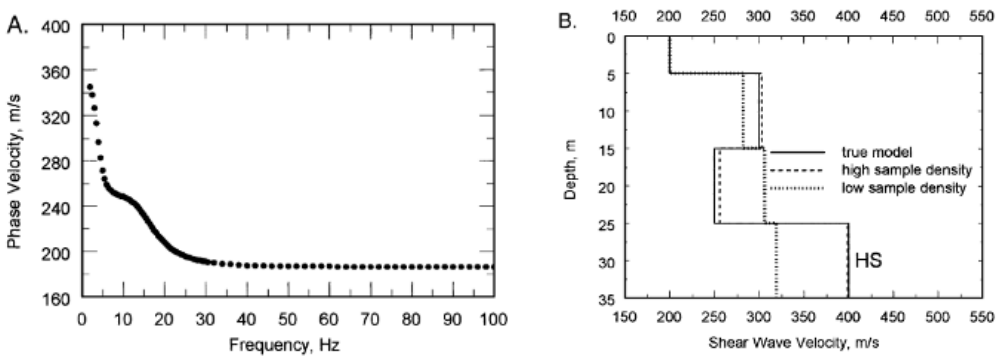

Figure A-7: A) Dispersion curve generated forwardly from a model containing a low velocity layer at a depth of 15-25 m. B) The low sample density (5Hz) dispersion curve fails to produce the low velocity layer whilst the higher sample density (1Hz) is in good agreement with the model (Zhang and Chan, 2003).

Data acquisition

The first step in an MASW survey is to acquire broadband high frequency (>5 Hz) planar fundamental mode Rayleigh-wave records. The data acquisition may be carried out in either active (Park et al., 1999b) or passive modes. Passive data can be collected in remote ((Park et al., 2004)- outside the scope of this study) or roadside (Park and Miller, 2006) modes, or a passive roadside survey may be supplemented by an active source (Park et al., 2005b). Only active source surveys were successfully used in this study.

For active surveys optimal data collection is greatly aided by correct selection of field parameters (Figure A-8:), a subject covered extensively by Park *et al*. (1999b) and again by Park *et al*. (2005a), although the latter is specific to 'typical' soil sites.

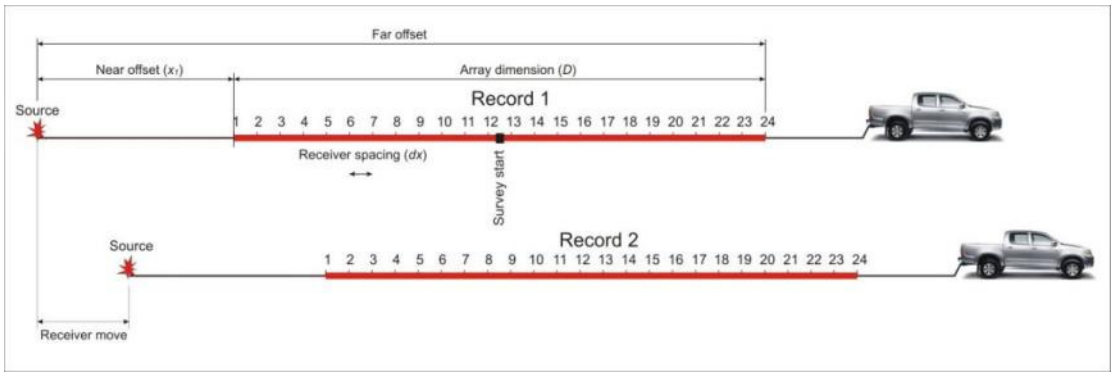

Figure A-8: MASW survey geometry using a land streamer. Key acquisition parameters are illustrated and selection of these is discussed in the text.

Prior to deploying a survey, little can be selected other than an appropriate source and receiver array and it is here that the flexibility of MASW becomes immediately apparent. A wide variety of sources are useful, including swept frequency sources (e.g. vibroseis) and impulsive sources such as sledgehammer and plate or rubber band accelerated weight drops (RAWD). Selection of an appropriate source is a key requirement to ensure delivery of enough energy. Impulsive sources are cheaper and more convenient so are used in all active MASW surveys in this study. An 8 kg sledgehammer and plate was chosen as a seismic source and the signal recorded with a 24 channel string of 4.5 Hz sled-mounted vertical geophones. This source and receiver setup should maximise investigation depth (Park et al., 2005a).

On-site survey preparation should begin with a full wavefield survey to determine the optimal survey geometry. The near offset x_1 (Figure A-8:) is a critical parameter as it determines the position of the receiver array in the wavefield and therefore the impact of

near or far field effects. Near field effects are caused by cylindrical rather than planar propagation of Rayleigh-waves proximal to the source (Figure A-9:) and lead to lack of energy and linear coherence in the lower frequency component of a record. The longer a wavelength, the further it must travel before becoming planar. The reliable investigation depth is approximately given by

$$z_{max} = C_1 / (2\ f_1) = ½\ \lambda_{max}$$

where C_1 is phase velocity for the lowest frequency analyzed (f_1) and λ_{max} is the maximum wavelength recorded (Rix and Leipski, 1991). It follows that the objective with MASW is to record low frequencies or long wavelengths whilst not recording non-planar waves. The Surfseis inversion is stable down to a lower bound of 5 Hz (Xia *et al*., 1999).

Far field effects are caused by contamination of the record due to attenuation of the higher frequency fundamental mode waves at far offsets (Park et al., 1999b). At excessive offsets higher mode surface waves dominate over fundamental mode surface waves and this typically limits the array dimension *D* (Figure A-8:). The uppermost frequency reliably imaged is usually given by the velocity and frequency of the highest uncontaminated frequency recorded (f_{max}) (Stokoe et al., 1994) such that

$$H1 \geqslant 0.5\ \lambda_{min} = 0.5 C_{min} / f_{max}$$

where C_{min} and λ_{min} are phase velocity and wavelength, respectively, which correspond to a particular f_{max}. Although the final inverted S-wave velocity profile may have shallow layers thinner than H1, any calculated S-wave velocity value for these layers should be considered unreliable.

By convolving a full wavefield shot gather with a sweeping linear stretch function (Park et al., 1999b) and examining the swept frequency record (Figure A-10), a near offset can be selected that minimizes near and far field effects over a useful range of wavelengths. As the reliable investigation depth is approximately ½ λ_{max}, optimizing the near offset maximizes the investigation depth.

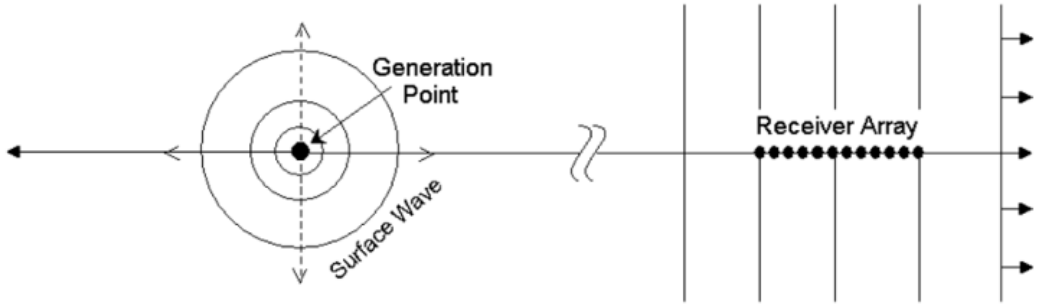

Figure A-9: Rayleigh wave propagation away from a generation point. Near to the source the wavefront is cylindrical, whilst further away it becomes planar (after Park and Miller, (Park and Miller, 2006))

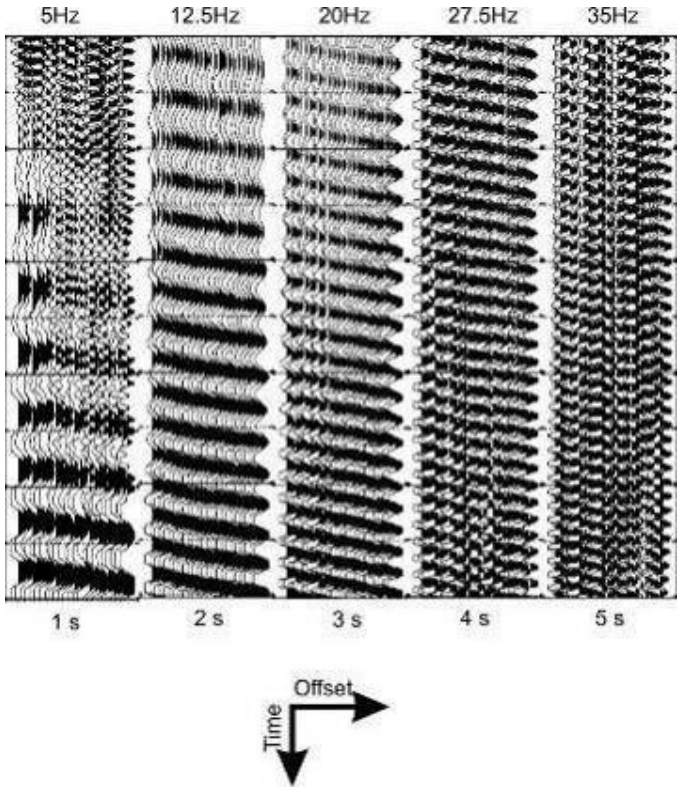

Figure A-10. A 5 s long swept frequency display of a shot gather collected using an 8 kg sledgehammer at Dalethorpe. Traces can be seen to be strongly coherent from about 10 Hz through to about 30 Hz where far field effects are established. The dispersion should therefore be imaged from 10-30 Hz.

If an MASW receiver spread is too short, the resulting dispersion curve is an apparent dispersion, which may not be purely fundamental mode. A long array dimension D (Figure A-8) is therefore necessary to obtain fundamental mode dispersion by methods such as Ivanov *et al.* (Ivanov et al., 2005). The length required may be even greater at sites where the S-wave velocity does not vary linearly with depth (Lin and Lin, 2007). This, coupled with the requirement to obtain maximum wavelengths, means that a receiver spread cannot generally be kept short enough to avoid violating the 'horizontally layered medium' assumption (Xia *et al.*, 1999) when investigating a faulted substrate or

one with significant bedrock topography. As a result, it is likely that long array dispersion curves for such sites will be interpreted as vertical variation of S-wave velocity, when their character is actually attributable to lateral inhomogeneity. This trade-off between the need for lateral spatial resolution (small spreads) and long wavelengths to yield investigation depths (large spreads) threatens the applicability of MASW in fault investigation.

One countermeasure explored in this study is construction of a walkaway record. Two methods of walkaway construction are compared in this study (Figure A-11). One method is to construct a fixed receiver walkaway (FRW) with a source moveout (Figure A-11 A). The other method creates a fixed source walkaway (FSW) using a receiver moveout (Figure A-11 B). If the study site is comprised of laterally homogeneous layering both methods should produce identical source-to-reciever offset-sorted seismograms. Lateral velocity field variations, however, will cause variations between the display produced by a FSW or a FRW. This is because the FSW survey collects 48 channels over a 48 receiver spread. It therefore records faithfully the changes in wavefield caused by increased source-receiver offset. The same change is merely approximated by an FRW survey, which collects 48 channels of velocity data beneath a spread of 24 receivers, assuming lateral homogeneity across the survey length (Vincent et al., 2006). Unaccounted for lateral variation of the subsurface may therefore induce static errors when synthesizing walkaway records using the FRW method. For the purposes of this study FSWs proved useful in conjunction with short receiver spacings to facilitate removal of higher modes despite going on to process only the first half of the record.

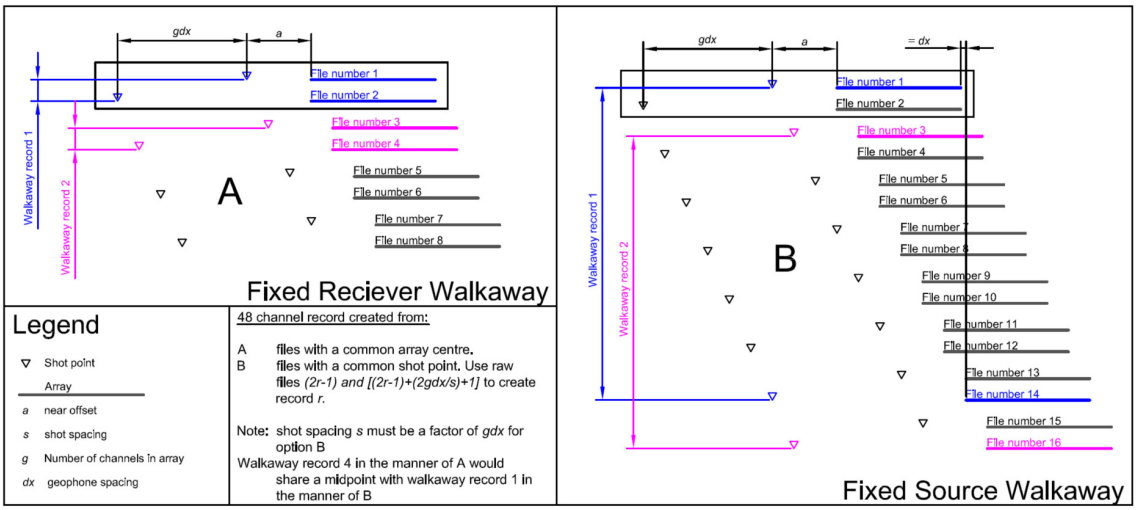

Figure A-11: Construction of 48 channel walkaway records by concatenation of A) files with a common mid-point and differing offsets (Fixed Receiver Walkaway) and B) files with a common shot point (Fixed Source Walkaway).

APPENDIX B. DISPERSION CURVE GRADING

Two criteria are used to judge the quality of a dispersion curve (Park, 2003)(p.9.17). The first is the signal to noise ratio and the second is the general dispersion trend. The most objective approach is to use the dispersion curve to apply a dynamic linear moveout to the swept frequency record derived from the shot record from which the curve was extracted. This has the effect, for a good dispersion curve, of flattening out the slope of the individual frequency event velocities. This is, however, a labour intensive approach. Apart from applying a DLMO, the following represents a subjective scale that I have found useful for grading dispersion curves.

0	No data or no dispersion curve extractable	+/- Records falling in these categories should not be used
1	Poor quality dispersion curve extracted after much processing. Lowest confidence level.	
2	Strong diffractions and scattered wavefield. Modal jumps reflect strong lateral contrasts in S-wave velocity. S-wave sounding unreliable.	
3	Significant Rayleigh wave phase velocity pull up observed. Filtering adversely affects dispersion curve extraction. Potential for significant higher mode or body wave contamination at a range of depths.	- Strong likelihood of elevated velocities at all depths. Use with caution. + Halfspace and near surface velocities significantly perturbed. Perturbation may mildly contaminate the middle depths
4	Some unusually high Rayleigh wave phase velocities or abnormal dispersion observed at either end of the curve. Possibly inflated velocities nearest the surface (due to higher mode contamination) or in the halfspace (due to body wave contamination). Otherwise confident.	- filtering difficult and of limited success but only halfspace and shallowest velocities considered likely to be excessive + filtering removed most contamination but near surface and halfspace velocities remain higher than those typically observed.
5	Normally dispersive overtone image. Good SNR. No evidence of signal contamination. Highest confidence level.	- significant filtering to remove contamination but good result acheived + no filtering was necessary

BACK POCKET CONTENTS

Map 1: Tectonic Geomorphology and Structure of the Upper Hawkins Basin, Dalethorpe (1:5000)

Map 2: Geology and Geomorphology of the Boby's Creek Study area (1:5000)

Figure 6-20 supplement: An east-facing across site correlation of the Boby's Stream MASW profiles with detailed geomorphological surveys and structural interpretations. All dipping features exaggerated in the section view by 5x VE. Regional surface gradient is to the east.

Compact Disc 1: Data, figures and documents